Alma Mater Studiorum – Università di Bologna

DOTTORATO DI RICERCA IN

SCIENZE DELLA TERRA

Ciclo XXX

Settore Concorsuale: 04/A1

Settore Scientifico Disciplinare: GEO/07

Multi-stage metasomatism in a mantle wedge and exhumation mélange: New insights from the peridotites of the Ulten Zone (Eastern Alps, Italy)

Presentata da: Bibiana Förster

Coordinatore Dottorato

Prof. Giulio Viola

Supervisore

Dott. Roberto Braga

Co-Supervisore

Dott.ssa Sonja Aulbach

Esame finale anno 2018

Abstract

Convergent plate boundaries are geologic "crossroads" where petrogenetic processes mediated by different liquids overlap one after another. Coupling between the subducting plate and the overlying mantle wedge generates corner flow in the latter, with flux of hot mantle from beneath. Towards the subduction channel, metamorphic reactions in subducting crust release fluids that rise into the overlying mantle wedge, producing metasomatism and/or partial melting. This highly complex geological setting is the place of fundamental mass exchange between different earth's reservoirs, with consequences on the long-term cycling of elements between solid earth and the atmosphere. The study of mantle wedge processes relies on the availability of ultramafic rocks now exposed in exhumed roots of orogenic belts. A key area where it is possible to have at hands this peculiar material is the Ulten Zone (UZ), a tectonic unit of the Italian Eastern Alps. The UZ contains lenses of ultramafic rocks (peridotites and pyroxenites) which are incorporated in high-grade Upper Austroalpine crustal rocks (gneisses and migmatites). The peridotites derive from a mantle wedge, were incorporated in a crustal slab during continental subduction in the course of the Variscan orogeny, and subsequently exhumed in a crust-mantle mélange. The complex pre-Alpine tectono-metamorphic history is documented by a variety of mineral assemblages and microstructures and the peridotites display the progressive transition from coarse-grained spinel lherzolite with protogranular-porphyroclastic textures towards fine-grained recrystallized garnet-amphibole peridotite with granoblastic-porphyroclastic texture to fine-grained retrogressed spinel-amphibole peridotite.

This PhD work aims to shed light on conditions and timing of individual melt-mediated and fluid-mediated metasomatic stages affecting the UZ peridotites during their involvement in the Variscan cycle and to contribute to the understanding of the element cycle during crust-mantle interaction in a continental collisional setting. A comprehensive dataset was obtained by detailed petrographic, elemental and multi-isotope analyses on whole-rocks and metasomatic phases of new peridotite samples, including the first analyses of the carbon contents in UZ peridotites, combined analysis of radiogenic isotopes (Nd-Sr-Hf-Pb) and carbon isotopes on whole-rocks as well as the first analysis of the stable-isotope (carbon and oxygen) composition of carbonates. In combination with information from the literature, the main findings can be summarized as follows:

The multi-stage evolution of the UZ is mirrored by their decoupled major-element and trace-element compositions. Whole-rock major-element compositional trends combined with the concentrations of HREE below the depleted mantle indicate that the UZ peridotites derive from protoliths that were subjected to partial melting and subsequent refertilization. Hafnium and Nd T_{CHUR} model ages of peridotites with depleted major-element compositions and with depleted Hf-isotope compositions yield broadly consistent Proterozoic ages > 1 Ga, which may indicate initial formation of these peridotites by depletion of a primitive mantle during the assembly of the supercontinent Rodinia. A Sm-Nd isochron age of 409 ± 38 Ma corresponds to the onset of the Variscan orogeny and may constrain the timing of isotopic re-equilibration after the Proterozoic partial melting event. Refertilization was likely induced by interaction of the protoliths of the UZ peridotites with rising metasomatic liquids from deeper parts of the subduction zone during residence in an early hot supra-subduction zone mantle wedge. Inclusions of dolomite in primary spinel from coarse-grained protogranular peridotites are interpreted as an early generation of dolomite which formed in the high-temperature spinel-stability field from the metasomatic liquids, likely mafic carbonated melts carrying recycled crustal components, during the refertilization stage. The radiogenic Pb isotopic composition of the

UZ peridotites further indicates that the mantle source of the protoliths contained mixed recycled crustal components.

Because of corner flow, the spinel-facies peridotites were transported closer to the slab-mantle interface and entered the garnet-stability field due to pressure increase. Here, the peridotites were subjected to multi-stage interaction with aqueous fluids released from the crustal slab, resulting in the formation of hydrous phases, such as amphibole, and enrichment in incompatible trace elements (LREE, LILE, U, addition of unradiogenic Nd and radiogenic Sr) in fine-grained recrystallized peridotites, while coarse-grained peridotites largely escaped hydration and recrystallization. At this stage, discrete dolomite grains formed as inclusions in garnet and in the matrix of fine-grained garnet-bearing peridotite simultaneously with amphibole and apatite, indicating that the crustal slab-derived fluid carried a carbon-component. The dolomite occurrence in the garnet-amphibole peridotite assemblage suggests that the peridotites experienced maximum pressures of ca. 1.9 GPa at ca. 900°C.

The study of U-Pb geochronology and trace element characteristics of zircon reveals valuable information on the timing and conditions of fluid-peridotite interactions during the retrograde evolution of the UZ crust-mantle mélange. Zircon in fine-grained garnet-amphibole peridotite and in a phlogopite-rich rock from the peridotite-crust contact zone records *T* of ca. 600-700°C (determined by Ti-in-zircon geothermometry) and yield an age of ca. 333 Ma, which was previously interpreted as the age of peak *P-T* conditions. Our data, conversely, reflect the time of formation of the crust-mantle contact zones at low-*T* (and *P*) conditions prevailing during late-stage exhumation. This implies that the influx of crust-derived aqueous fluids into garnet-facies peridotites occurred prior to 333 Ma, before the peridotite entrainment into the crustal slab. Zircon grew from aqueous fluid/s released from crystallizing leucosome during emplacement of the peridotites into the crustal host rocks and formation of the crust-peridotite contact zones. The occurrence of zircon together with elevated HFSE concentrations and coupled Sr and Hf isotopic compositions in the fine-grained peridotites indicate that the late crust-derived aqueous fluid carried HFSE.

Tectonic uplift and exhumation in a crust-peridotite mélange brought the peridotites to crustal levels, where different peridotite portions interacted with fluids sourced from different adjacent lithologies. This is mirrored by highly variable stable-isotope compositions of carbonates in UZ peridotites, which distinguish the UZ in a southwestern (SW) domain with less negative carbonate $\delta^{13}C$ (from -11.1‰ to -0.03‰) and a northeastern (NE) domain with carbonates displaying more negative $\delta^{13}C$ (from -16.8‰ to -5.7‰), indicating that the fluids carried different carbon-isotope signatures. Importantly, retrograde magnesite is observed in peridotites from the NE domain only, which also contain higher carbon concentrations (up to 0.181 wt. % oxidized carbon) than peridotites from the SW domain. The generally light carbon isotopic composition of the carbonates suggests that the carbon was sourced in the crustal host rocks.

Finally, the UZ peridotites show incipient to high degrees of late serpentinization which, in dolomite-bearing peridotites, was accompanied by formation of calcite-brucite intergrowths as a product of fluid-mediated dolomite breakdown according to the reaction $CaMg(CO_3)_2 + H_2O \rightarrow CaCO_3 + Mg(OH)_2 + CO_2$. The dissolved carbon species released into the migrating serpentinization fluid may be responsible for (1) the precipitation of calcite in serpentinization-related veinlets, as observed in all UZ peridotites, and (2) the formation of reduced carbon through redox reactions, since all UZ peridotites contain reduced carbon (up to 0.124 wt. %) in concentrations similar to carbonate carbon. Total carbon concentrations in UZ peridotites range from 0.013 to 0.280 wt. %, suggesting that mantle-wedge peridotites can store crust-derived carbon via various processes involving melt/fluid-rock interaction, and that carbon is ultimately mobilized to crustal levels during exhumation of an orogenic crust-peridotite association.

In summary, the study provides new insights into the sequence of metasomatic events in the evolution of the UZ peridotites and the origin and nature of involved metasomatic agents during crust-mantle interaction in a collisional setting.

Table of contents

Structure of the thesis

Chapter 1 introduces the thematic framework for this PhD thesis and introduces the geological context of the Ulten Zone and its lithologies. A description of the research aims of this PhD work is given, as well as an overview of research activities and of the analytical techniques performed to approach these aims during the PhD studies.

Chapter 2 deals with the multi-stage evolution of the peridotites by discussing combined results of whole-rock elemental and isotopic analyses. This chapter provides the first multi-isotope analysis on peridotite whole-rocks, including the radiogenic isotopes Nd-Hf-Sr-Pb. The aim is to constrain the various melt-mediated and fluid-mediated processes acting upon the peridotites during their evolution.

Chapter 3 presents the study of zircons in peridotites, combining zircon U-Pb geochronology and geochemistry. The results help to better constrain the sequence of events in the geodynamic history of the Ulten Zone in the context of crust-mantle coupling in a collisional setting. The capability of subduction-related aqueous fluids to mobilize high field strength elements (HFSE) is furthermore discussed.

Chapter 4 focuses on a comprehensive petrographic study in order to identify multiple carbonate phases in the peridotites, providing insights into the cycling of carbon between crust and mantle and the capability of mantle-wedge derived rocks to store carbon. This chapter was published during the PhD activities and is reported unchanged in this thesis. Therefore, later new findings from other research activities presented in other chapters are not considered in this chapter.

Chapter 5 deals with the carbon contents and carbon isotopic composition of peridotite whole-rocks as well as with the stable-isotope (carbon and oxygen) composition of carbonates in the Ulten Zone peridotites. The origin of carbon and possible mechanisms of carbon cycling in a subduction- and exhumation-related tectonic setting are discussed in the light of carbon transfer between crust and mantle.

Chapter 6 summarizes the main findings obtained during this PhD work and presents general conclusions.

1 Introduction

1.1 Subduction zones: Key settings for element transfer between the Earth's reservoirs

Subduction of crustal material to depths of the Earth's mantle at convergent plate margins is a key mechanism in the global mass transfer and element cycle. The transfer of crustal material into the mantle in subduction-to-collision zones contributes to the occurrence of chemical heterogeneities of mantle portions and ultimately affects the output from the mantle to the atmosphere through volcanism and degassing. The occurrence of these two output processes are controlled by numerous factors during subduction, such as increasing pressure and temperature, dependent on the depth and subduction angle, and the presence and/or generation of fluids and melts. Fluids and melts released from the descending crustal slab in the course of subduction can migrate into the overhanging mantle portion, the mantle wedge, and modify its chemical composition. The subduction-modified mantle wedge is the source rock for melts generated in volcanic arcs related to a convergent plate margin. Therefore, fluid- and melt-mediated metasomatism of mantle wedge plays a key role in mass transfer and element cycling and is, thus, of particular interest for geologists.

1.1.1 Metasomatic agents in continental subduction zones: Element carriers during crust-mantle interaction

In contrast to subduction of hydrated oceanic crust, subduction of drier continental crust is usually not related to coeval production of arc magmas (e.g. Rumble et al., 2003; Zheng, 2012), but postcollisional magmatism produces a variety of igneous rocks in continental collision orogens and their adjacent active continental margins (Zhao et al., 2013 and references therein). Therefore, the fate of the subducted crustal material recycled into the mantle, the mechanisms of its reworking and the potential of recycled crust to source magmatism is of crucial importance for the understanding of the mass transfer between the Earth's reservoirs. In this context, the interface between the subducting slab and the overlying mantle wedge is the tectonic key site where substantial mass transfer occurs, mediated by aqueous fluids, silicate melts, carbonatitic liquids or supercritical fluids. The occurrence of these liquids, which are characterized by different capabilities of mobilizing elements (e.g. Kessel et al., 2005; Bebout, 2007, 2013; Zheng & Hermann, 2014; Poli, 2015), are related to the dehydration and/or partial melting of different rock types at variable pressure (*P*) and temperature (*T*) conditions in the subduction zone. Fluids released from dehydration and from breakdown of nominally anhydrous minerals can trigger partial melting of the subducting continental slab at supersolidus *P*-*T* conditions (Zheng & Hermann, 2014). While crust-derived aqueous fluids at subsolidus conditions are the carriers for LILE (large ion lithophile elements), hydrous melts are capable of mobilizing LREE (light rare earth elements) from the subducting rocks (Zheng & Hermann, 2014 and references therein). These trace element compositions are characteristic for the individual slab agents and thus, enrichment in LILE, moderate enrichment in LREE and depletion of HFSE (high field strength elements) is typical for migmatic leucosomes which formed from partial melts of subducted ultrahigh-pressure metamorphic rocks (Zheng & Hermann, 2014). The depletion of HFSE in subduction fluids has been ascribed to the low solubility of HFSE-bearing minerals in aqueous fluid at subduction zone conditions (Audetat & Keppler, 2005; Tropper & Manning, 2005), but several experimental studies have demonstrated that HFSE mobility can increase in alkali-rich fluids and in the presence of ligands (Cl and F) in the fluid and/or silicate melt (Jiang et al., 2005; Wilke et al., 2012; Louvel et al., 2013 and references therein). In synthesis, fluid-mediated and melt-mediated interaction of mantle-wedge peridotites at the slab-mantle interface in a continental subduction setting and during migration of the slab agent through the mantle wedge carries the crustal signature into the mantle and accounts for substantial element recycling. The peridotites derived from the mantle wedge record these processes by cryptic and/or modal metasomatism.

1.1.2 Orogenic peridotites from the mantle wedge: Recorders of element transfer from crust to mantle

Although numerous studies on mantle xenoliths in intra-plate volcanic rocks exist (e.g. Arai & Ishimaru, 2008; Ionov, 2010) which can represent metasomatized mantle portions and/or source rocks for melts, the availability of mantle-wedge samples directly derived from a subduction-to-collision zone to study crust-mantle interaction is limited. Therefore, the mantle wedge remains the least understood portion in the "subduction factory" (Scambelluri et al., 2006; Kelemen & Manning, 2015). Orogenic peridotites, which derive from a mantle wedge involved in a continent-continent collisional setting (e.g. Brueckner, 1998; Brueckner & Medaris, 2000), are captured by the subducting crustal slab due to tectonic movement, and are subsequently exhumed. Such peridotites can reside in host crustal rocks as mantle-wedge slices and provide, when exposed at the surface, favorable conditions for studying the formation as well as the evolution of the mantle in the context of fluid- and/or melt-assisted interaction with subducted crustal material. These orogenic peridotites often show the transition from spinel- to garnet peridotite and can therefore record high-pressure (H*P*) and ultrahigh-pressure (UH*P*) conditions related to different subduction depths, for example in the Western Gneiss Region (Scambelluri et al., 2008, 2010a; Vrijmoed et al., 2013), the Dabie-Sulu orogen (Zhang et al., 2007, 2011; Chen et al., 2015), Monte Duria (Hermann et al., 2006), North Qaidam (Chen et al., 2017 and references therein), the Bohemian Massif (e.g. Liati & Gebauer, 2009) as well as in the alpine orogenic belt (e.g. Ulten Zone, Godard et al., 1996; Nimis & Morten, 2000, and Cima di Gagnone, Scambelluri et al., 2014).

1.2 Why study Ulten Zone peridotites? – Aims of the present work

The present PhD thesis deals with the ultramafic rocks, mainly peridotites and minor pyroxenites, from the Ulten Zone tectonic unit in the Italian Eastern Alps. The peridotites have been suggested to derive from a supra-subduction zone mantle wedge, slices of which were incorporated in a subducting crustal slab during the Variscan orogeny (e.g. Godard et al., 1996). These rocks give insights into the mechanisms of crustal metasomatism at the slab-mantle interface from subduction to exhumation. Several comprehensive petrographic and geochemical studies have previously focused on unraveling the crust-to-mantle mass transfer recorded by the Ulten Zone peridotites during their evolution from inner parts of a mantle wedge to emplacement into the crustal host rocks and subsequent exhumation. However, several fundamental questions remain open, namely (1) the geochemical and isotopic signature of the mantle wedge prior to the main metasomatic event, (2) the significance of some metasomatic accessory minerals like carbonates and zircon, (3) the carbon content of the mantle-wedge peridotites sampled in the Ulten Zone. The aim of this PhD work is to shed more light on these open questions to help unravel the origin of chemical heterogeneities in a subcontinental lithospheric mantle subjected to intense metasomatism by multiple agents (fluids/melts) during subduction and exhumation related to the Variscan plate convergence.

In order to approach this aim, this PhD work comprises whole-rock Hf-Nd-Sr-Pb analyses and a detailed study of metasomatic accessory minerals in the Ulten Zone peridotites, having available a new and large sample set that allows comprehensive characterization of these rocks. While previous studies focused largely on samples from a few localities in the Ulten Zone, an extended sample set from different localities can provide a bigger picture of the Ulten Zone history. Isotopic work was reported previously (Rost & Brenneis, 1978; Gebauer & Grünenfelder, 1978; Thöni, 1999; Tumiati et al., 2003) but there has been a general lack of detailed investigation of the metasomatic stages by means of radiogenic isotopes. Similarly, the metasomatic history of the Ulten Zone peridotites is largely based on incompatible element geochemistry of minerals, mostly amphibole (e.g., Rampone & Morten, 2001). First attempts to discuss the origin of metasomatic accessory minerals, such as carbonates and zircon, were reported previously (e.g. Braga & Sapienza, 2007; Marocchi et al., 2009; Sapienza et al., 2007, 2009) but a detailed study of these accessory minerals is lacking. Thus, a new multi-isotope approach on these minerals, combined with petrographic and mineral-chemistry analyses (major and trace elements), will elucidate carbonation-decarbonation reactions in a mantle wedge and the involvement of silica- and HFSE-rich metasomatic fluids in post-Variscan times.

1.3 The Ulten Zone tectonic unit and its geologic setting

1.3.1 Tectonic context of the Ulten Zone

The Ulten Zone (UZ), or in some publications referred to as "Ulten-Nonsberg Zone", is a pre-Alpine basement unit (Figure 1.1; e.g. Morten et al., 1976; Martin et al., 1993; Martin et al., 1998) belonging to the Austroalpine system in the Eastern Alps located in the north of the Alpine Periadriatic lineament (Figure 1.1). The basement units in the Eastern Alps were interpreted to reflect a pre-Carboniferous and Carboniferous history in the process of the amalgamation of several continental microplates which were located between the Gondwana and Laurussia plate margins. The convergence and collision of Gondwana and Laurussia resulted in ocean closure and oblique continent-continent collision, the so-called Variscan orogeny, going on from pre-Devonian times up to ca. 330 Ma in the Carboniferous (Neubauer & Handler, 2000; Ranalli et al., 2005). Ocean closure was accompanied by Paleozoic oceanic subduction and the continental collision resulted in subsequent Late Paleozoic continental crust underplating (Neubauer & Handler, 2000). After the Variscan orogenic cycle, Permian to Jurassic lithospheric attenuation and rifting resulted in the opening of small oceanic basins belonging to the Tethys ocean (Martin et al., 1998; Ranalli et al., 2005). The subsequent Alpine history of the uppermost Austroalpine units preserving the Variscan tectono-metamorphic overprint (e.g. Martin et al., 1998 and references therein) is related to late Cretaceous to Tertiary tectonic rearrangement during the oblique convergence of the Adria microplate towards the paleo European plate margin, and collision (Godard et al., 1996; Martin et al., 1998). The present-day structural location of the UZ as a crustal-scale "push-up" structure is the result of uplift due to Cretaceous emplacement of basement units and Tertiary strike-slip movements along the Tonale and Giudicarie faults (Godard et al, 1996).

1.3.2 Geologic setting of the Ulten Zone

The UZ belongs to the pre-Mesozoic Tonale nappe (Figure 1.1) which forms a narrow NE-SW oriented belt and is delineated in the northwest from the adjacent Austroalpine Campo-Ortler nappe by the Peio Line and separated from the Southalpine domain by the North Giudicarie Line in the southeast and the Tonale Line (Insubric Line) in the south (Martin et al., 1998). The Tonale nappe consists of two major units, the Ulten unit and the Tonale unit, which can be distinguished in terms of their lithologies (Figure 1.1). The Ulten unit consists mainly of higher grade basement rocks and can be divided into two zones based on the metamorphic grade: (1) the UZ which defines the northeastern part of the Ulten unit and is mainly composed of highly-deformed paragneisses and orthogneisses and nebulitic and stromatic migmatites (Martin et al., 1993; Hauzenberger et al., 1996; Godard et al., 1996 and references therein) and (2) the southwestern part of the Ulten unit which is, relative to the UZ basement, characterized by a lower metamorphic grade and more intense retrogression (Martin et al., 1998). In the UZ, lenses of ultramafic rocks (peridotite ± pyroxenite; e.g. Herzberg et al., 1977; Rost & Brenneis, 1978; Morten & Obata, 1983; Obata & Morten, 1987), often up to hundreds of meters in length, are embedded in the foliated high-grade metamorphic crustal basement (Obata & Morten, 1987; Godard et al., 1996). The ultramafic rocks are generally located at the boundary between the underlying strongly-foliated garnet-kyanite gneisses and the overlying stromatic to nebulitic migmatites (Godard et al., 1996; Martin et al., 1998; Del Moro et al., 1999). The "hybrid" gneiss-peridotite and migmatite-peridotite contact zones consist of hydrous mineral assemblages (Tumiati et al., 2003; Marocchi et al., 2009, 2010), but the crust-peridotite contacts are rarely exposed at the surface (Obata & Morten, 1987). Occasionally, the crustal rocks expose bodies of amphibolized eclogites and metagabbros (Godard et al., 1996; Martin et al., 1998) of variable size.

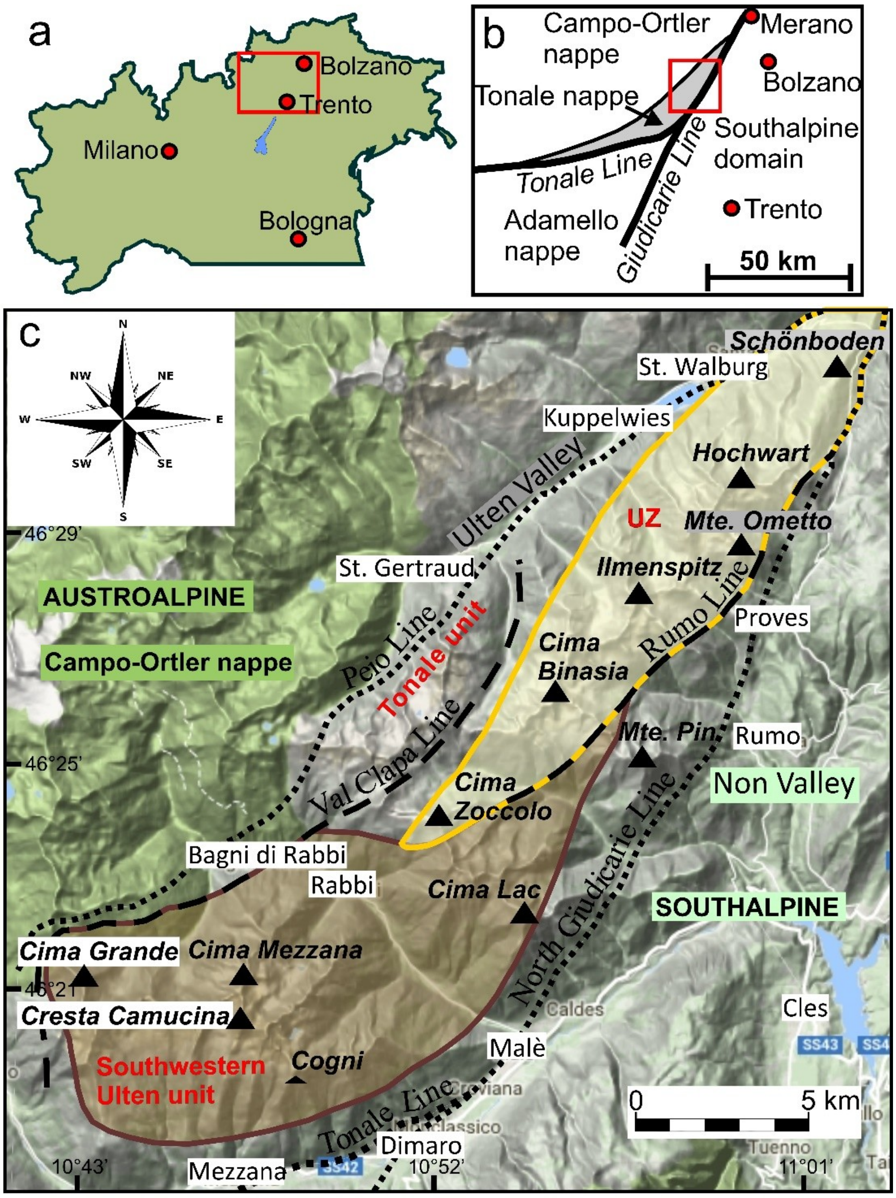

Figure 1.1. Map of the Ulten Zone (UZ). (a) Location of the UZ in the Italian Eastern Alps; (b) Location of the UZ belonging to the Tonale nappe as a fragment of the Paleozoic Variscan belt north of the Insubric Lineament; (c) Map of the Ulten unit composed of the UZ in the northeastern area (yellow marked field) and a southwestern domain (brown marked field). The Ulten unit and the adjacent Tonale unit compose the Tonale nappe. Geologic map redrawn after Godard et al. (1996), terrain map taken from earth3dmap.com.

1.3.3. The lithologies of the Ulten Zone

Despite the Alpine tectonic movements, the pre-Alpine evolution of the UZ lithologies is still well-preserved by parageneses and fabrics (Godard et al., 1996; Hauzenberger et al., 1996; Ranalli et al., 2005). As the focus of this PhD study is on the peridotites, their origin and evolution, the peridotite occurrences will be treated more in detail, whereas the other UZ rock types will be described more briefly.

1.3.3.1 The Ulten Zone ultramafic rocks

Several earlier studies (e.g. Herzberg et al., 1977; Rost & Brenneis, 1978; Morten & Obata, 1983; Obata & Morten, 1987) carried out the first attempts to describe the mineralogic composition and petrographic occurrence of the peridotites and pyroxenites and to discuss their origin. These observations were followed by numerous reports (Godard et al., 1996; Susini & Martin, 1996; Rampone & Morten, 2001; Scambelluri et al., 2006; Marocchi et al., 2007; Sapienza et al., 2009; Scambelluri et al., 2010b; Braga & Bargossi, 2014) dealing with the petrographic characterization of these rocks.

1.3.3.2 Peridotites

The peridotites include both harzburgitic and lherzolitic compositions (Obata & Morten, 1987). They can be classified into two groups, based on their grain size (Obata & Morten, 1987): a relatively undeformed coarse type of lherzolitic composition with a grain size up to a few cm, and a harzburgitic fine type with grain sizes from 0.2 to 1 mm displaying variable degrees of mylonitic deformation. The fine type is more abundant than the coarse type (Obata & Morten, 1987) and it was interpreted to reflect a transition from coarse protogranular spinel lherzolites via coarse porphyroclastic spinel-garnet lherzolites to fine-grained granoblastic-porphyroclastic garnet-amphibole peridotites (Herzberg et al., 1977; Obata & Morten, 1987).
The main mineral assemblage of the coarse type consists of large kinked olivine (up to 5 mm grain size) and orthopyroxene (enstatite, 2-4 mm grain size) showing undulose extinction, smaller clinopyroxene (diopside, 0.7-2 mm) and dark brown Cr-Al spinel (0.6-1 mm). Spinel occurs disseminated in the peridotite matrix, as exsolutions in pyroxenes and as intergrowths with orthopyroxene (Braga & Bargossi, 2014). Fine-grained recrystallized parts between the large grains occasionally contain amphibole, which can also occur along pyroxene grain boundaries as secondary phase (Obata & Morten, 1987; Scambelluri et al., 2010b). Diopside occurs as exsolutions in enstatite and contains, in turn, exsolution lamellae of enstatite and spinel (Obata & Morten, 1987). Rarely, garnet was observed in the coarse type peridotite in reaction coronas around spinel and in granoblastic aggregates in equilibrium with neoblastic pyroxene and olivine (Scambelluri et al., 2010b), as well as in thick exsolution lamellae together with pyroxenes, amphibole and spinel in coarse enstatite and diopside (Obata & Morten, 1987; Scambelluri et al., 2010b). Often coarse type peridotites show the transition from the protogranular texture to a porphyroclastic structure. Porphyroclastic peridotites contain porphyroclasts of kinked olivine, enstatite and diopside up to 5 mm in size, showing undulose extinction (Obata & Morten, 1987). Orthopyroxene porphyroclasts contain exsolution lamellae of clinopyroxene, which in turn contains orthopyroxene exsolutions when it appears as porphyroclasts. Neoblasts of pyroxene and olivine can occur and olivine neoblasts contain spinel inclusions, while olivine porphyroclasts are inclusion-free (Obata & Morten, 1987). In this transitional type large spinel grains are surrounded by garnet and fine-grained recrystallized garnet-bearing domains contain neoblastic edenitic-pargasitic amphibole and/or hornblende but no spinel (Obata & Morten, 1987; Scambelluri et al., 2010b). In these recrystallized parts clinopyroxene was locally observed, whereas dolomite and apatite form a stable assemblage with olivine, orthopyroxene, amphibole and garnet.

The fine type peridotites can be divided into a garnet-bearing and a garnet-free assemblage. In general, the fine-grained peridotites are mainly harzburgites showing a variety of mineral assemblages and textures from porphyroclastic to tabular or mosaic equigranular (Obata & Morten, 1987). The main mineral assemblage usually consists of granoblastic olivine + orthopyroxene ± clinopyroxene ± garnet ± amphibole ± spinel ± chlorite (Obata & Morten, 1987). Amphibole occurs as pargasite, brownish green magnesiohornblende and colorless tremolite, indicating multi-stage amphibole growth; zoning is often observed, displaying a compositional transition from pargasite and magnesiohornblende in the core to tremolite grain rims (Obata & Morten, 1987; Braga & Bargossi, 2014). Spinel may occur as inclusions in amphibole, dispersed as accessory phase in the peridotite matrix or as inclusions in garnet (Obata & Morten, 1987).

The garnet-bearing fine-grained peridotites are composed of strongly hydrated assemblages characterized by large amounts of modal amphibole (up to 23 vol. %; Obata & Morten, 1987; Rampone & Morten, 2001). Garnet occurs both as large porphyroblastic grains (up to 2-3 mm size) containing vermicular grains of Cr-spinel, and as small grains in textural equilibrium with olivine, pyroxenes, amphibole and possibly spinel. These smaller garnet grains are usually spinel-free but can contain inclusions of olivine, pyroxenes and dolomite (Obata & Morten, 1987). Rarely, garnet occurs as euhedral to rounded porphyroblasts that can be as large as 9 cm, include pargasitic amphibole and are often in textural contact to pargasitic-edenitic amphibole (Tumiati et al., 2003, 2007). Garnet is often rimmed by retrograde kelyphites consisting of symplectitic spinel + orthopyroxene + clinopyroxene ± amphibole and orthopyroxene ± amphibole ± clinopyroxene assemblages. Occasionally, garnet is completely replaced by amphibole-spinel aggregates often including pre-garnet spinel grains (Susini & Martin, 1996; Martin et al., 1998; Godard & Martin, 2000; Tumiati et al., 2003). Garnet-bearing peridotites may also contain phlogopite, dolomite and apatite, and dolomite rarely occurs as large grains (Obata & Morten, 1987; Morten & Trommsdorff, 2003; Sapienza et al., 2009).

Fine-grained chlorite-bearing peridotites display strong deformation and a tabular or mosaic equigranular texture. Retrograde chlorite occurs in textural equilibrium with olivine, orthopyroxene and amphibole, whereas spinel is a rare phase in this assemblage, indicating that chlorite is the dominant stable Al-phase (Obata & Morten, 1987; Marocchi et al., 2007). Chlorite porphyroblasts can contain spinel relics and relict olivine and orthopyroxene porphyroclasts were observed (Marocchi et al., 2007). Amphibole in this peridotite type appears as euhedral pargasite in textural equilibrium with olivine and orthopyroxene and as elongated tremolite which often forms aggregates together with chlorite (Marocchi et al., 2007). While garnet is absent in this peridotite type and no pseudomorphs after garnet were observed, secondary phases, such as serpentine, opaque minerals and talc are present (Marocchi et al., 2007).

1.3.3.3 Pyroxenites

Pyroxenites occur in veins and dykes, cutting the peridotites, and consist of garnet-amphibole websterite and garnet-amphibole clinopyroxenite (Morten & Obata, 1983). Websterites contain clinopyroxene megacrysts (up to 6 cm) with orthopyroxene and garnet exsolutions, situated within an equigranular mosaic matrix composed of orthopyroxene + clinopyroxene + amphibole + garnet + spinel. Clinopyroxenite consists of diopside + Mg-hornblende + garnet with accessory ilmenite (Morten & Obata, 1983; Braga & Bargossi, 2014). The pyroxenites form dm-wide bands concordant with the foliation of the peridotite host rock (Morten & Obata, 1983; Godard et al., 1996).

1.3.3.4 The Ulten Zone crustal rocks

The UZ basement mostly consists of strongly foliated gneisses (garnet-kyanite paragneiss and orthogneiss) and migmatites (e.g. Godard et al., 1996; Hauzenberger et al., 1996; Martin et al., 1998; Del Moro et al., 1999; Bargossi et al., 2003; Braga et al., 2007a). The migmatites are geometrically superposed on the garnet-kyanite-bearing gneisses and crop out in the higher parts of the mountains (Godard et al., 1996;

Bargossi et al., 2003). The ultramafic bodies are situated at the migmatite-gneiss boundary. The garnet-kyanite gneisses consist of large garnet and kyanite grains (up to several cm) set in a foliated mylonitic matrix that is formed by mm-to-cm sized layers of alternating quartz-feldspathic layers (aggregates of quartz + albitic plagioclase ± orthoclase-rich alkali feldspar) and mica-rich films (aggregates of biotite ± muscovite; Godard et al., 1996; Hauzenberger et al., 1996; Martin et al., 1998; Bargossi et al., 2003; Braga et al., 2007b). Rutile, apatite, monazite, zircon and graphite occur as accessory phases in the garnet-kyanite gneisses (Braga et al., 2007b). Upward the mountain crests, these gneisses grade into migmatites which display different textures and occur as stromatic, nebulitic and massive leucosomes with associated garnet- and kyanite-rich fels interpreted as restitic rocks (Bargossi et al., 2003). Stromatic and nebulitic migmatites consist mainly of quartz + plagioclase ± alkali feldspar + garnet + kyanite + biotite + muscovite, whereas the restitic rocks are formed of garnet + kyanite and minor quartz + biotite ± plagioclase ± rutile ± amphibole + sulfides (Del Moro et al., 1999; Bargossi et al., 2003). Orthogneisses appear intercalated between paragneisses and migmatites, displaying generally a garnet-free quartz-plagioclase mineral assemblage and a garnet-bearing assemblage of quartz + plagioclase + alkali feldspar. Both orthogneiss types contain accessory phases such as biotite, muscovite ± zircon ± rutile (Del Moro et al., 1999; Braga et al., 2007b). Occasionally, lenses of amphibolites occur as intercalations within the migmatites and gneisses and rarely display relics of an eclogite paragenesis (Hauzenberger et al., 1996; Godard et al., 1996; Del Moro et al., 1999). Late leucocratic veins, dykes and pods (up to tens of meters thickness) cut both the peridotites and crustal rocks and consist of plagioclase + quartz + biotite ± restitic garnet and kyanite (Martin et al., 1998; Del Moro et al., 1999; Marocchi et al., 2009). Trondhjemitic pods and lenses are often observed at the crust-peridotite contact and are always associated with phlogopite- and anthophyllite-rich reaction bands (Marocchi et al., 2009).

1.3.3.5 The Ulten Zone crust-peridotite contact rocks

The rocks forming the contact zones between host gneisses/migmatites and peridotite lenses, especially in the Hochwart/Vedetta Alta area, were reported in Godard et al. (1996) and studied in detail by Tumiati et al. (2003, 2007) and Marocchi et al. (2009, 2010, 2011). These contact zones were interpreted to be of metasomatic origin and are characterized by variable mineralogical compositions and reflect fluid-assisted metasomatic reactions between the crustal rocks and the peridotite.

The contact zones between gneiss and peridotite occur as phlogopite-rich to tremolite-anthophyllite-rich cm-sized reaction bands, locally associated to thinner bands of talc-chlorite-serpentine-rich rocks (Marocchi et al., 2009, 2010). Contact rocks which are mainly composed of phlogopite are called phlogopitite (modal phlogopite > 90 vol. %) and can contain accessory phases such as tourmaline, zircon and apatite (Marocchi et al., 2009, 2010). The contact between migmatites and peridotites is often exposed as thick, dm-sized bands, marked by the occurrence of phlogopitites and actinolite-tremolite-phlogopite ± chlorite-bearing rocks (Godard et al., 1996; Tumiati et al., 2003). So-called amphibolites contain Mg-hornblende + phlogopite + plagioclase with accessory quartz, Cl-apatite, zircon and allanite-(Ce) (Tumiati et al., 2003). These bands can also include phases such as cm-sized tourmaline, allanite and chlorian varieties of ferrokinoshitalite and apatite (Tumiati et al., 2007). Also mm-to-cm-sized bands of talc + clinochlore + serpentine were observed at the interface between migmatites and peridotites (Tumiati et al., 2007).

1.3.4 Evolution of the Ulten Zone peridotites

Numerous studies have dealt with the petrologic and geotectonic evolution of the UZ crustal basement and the incorporated ultramafic bodies. Based on geochronological and petrologic approaches it was concluded that the UZ represents a fragment of the Paleozoic Variscan belt (e.g. Godard et al., 1996).

Several possible scenarios on the geodynamic setting and evolution of the UZ have been suggested in the past decades, with initially particular interest on the transition from spinel peridotite to garnet peridotite. Based on these works and due to extended sample sets, more recent studies (e.g. Braga & Sapienza, 2007; Marocchi et al., 2007, 2009, 2010, 2011; Sapienza et al., 2007, 2009) spotlighted also the significance of crust-peridotite interaction during "post-garnet" stages on the retrograde exhumation path of the UZ crust-mantle association. However, the mechanism of peridotite emplacement into crustal rocks in the context of the geodynamic evolution of the UZ is still not fully understood and remains matter of debate. The mantle wedge-derived ultramafic rocks overlying a continental subducting zone were incorporated into the crustal slab during (1) deep subduction at (near-UH*P*) peak conditions (Nimis & Morten, 2000; Tumiati et al., 2003) or (2) during exhumation after peak conditions (Scambelluri et al., 2006). According to scenario (1), a two-stage exhumation model was suggested (Ranalli et al., 2005), in which the crust-peridotite association was uplifted along the subduction channel after peridotite insertion at peak conditions during ongoing subduction. This model suggests that exhumation was driven by upward buoyancy of the crustal material and subsequently by slab break-off with lithospheric extension. Although the most recent studies on UZ ultramafic rocks and the metasomatic hybrid contacts favor the subduction-channel model for the evolution of the UZ (Rampone & Morten, 2001; Marocchi et al., 2007, 2009, 2010, 2011; Tumiati et al., 2003, 2007; Scambelluri et al., 2006, 2010a), the lack of diagnostic UH*P* phases in the metamorphic UZ rocks led Braga & Massonne (2008) conclude that models involving lithospheric delamination cannot be ruled out in the context of the UZ evolution. In contrast to the subduction scenario, several works suggested that crustal thickening during the Variscan continent-continent collision was followed by lithospheric delamination, i.e. lower crustal material was detached from the crustal slab, and subsequent crustal thinning lead to upwelling of hot asthenospheric mantle (Braga et al., 2007a; Perchuk et al., 2007; Braga & Massonne, 2008). Detachment of lower crust due to lithospheric delamination during late stages of Variscan orogeny was also suggested to explain the predominance of felsic rocks in the Variscan basement (Wittenberg et al., 2000) and discussed in further studies (e.g. Massonne, 2005).

In the context of the subduction-channel scenario, the highly variable petrographic characteristics of UZ peridotites have been interpreted to record their complex tectono-metamorphic history: at pre-Variscan times (Petrini & Morten, 1993), high-temperature spinel lherzolites ($T \approx 1200°C$ and $P \leq 1.5$ GPa) were intruded by hot ($T > 1400°C$) upwelling subduction-related hydrous melts from deeper levels of the mantle wedge containing recycled crustal material (stage 1, Figure 1.2; Nimis & Morten, 2000; Scambelluri et al., 2006). Interaction of the primary coarse-grained protogranular spinel lherzolite with these melts resulted in cryptic metasomatism (enrichment in LILE and LREE; Scambelluri et al., 2006). The coarse spinel peridotites were then transported to greater depths close to the slab-wedge interface due to corner flow and were transformed into garnet-amphibole peridotites within the mantle wedge (Nimis & Morten, 2000; Scambelluri et al., 2006). The transformation and recrystallization into fine-grained garnet-amphibole peridotites was ascribed to eclogite-facies conditions, i.e. pressure increase up to ca. 2.7 GPa and temperature decrease to 825-900°C (stage 2, Figure 1.2; Nimis & Morten, 2000), accompanied by infiltration of crust-derived (carbon-bearing) aqueous fluids (Rampone & Morten, 2001; Scambelluri et al., 2006; Marocchi et al., 2007; Tumiati et al., 2007; Sapienza et al., 2009). A slab-derived hydrous COH-fluid enriched in incompatible trace elements was released from *in-situ* partial melting and migmatization of the metapelites and acted as the agent responsible for peridotite metasomatism, i.e. the garnet + amphibole-facies recrystallization (Rampone & Morten, 2001; Tumiati et al., 2003; Scambelluri et al., 2006; Marocchi et al., 2007; Sapienza et al., 2009). Fluid metasomatism in the UZ peridotites resulted in the modal increase of amphibole (up to 23%, Rampone & Morten, 2001) and formation of other metasomatic phases, such as carbonates (Obata & Morten, 1987; Sapienza et al., 2009), apatite and phlogopite (Rampone & Morten, 2001; Scambelluri et al., 2006). Moreover, it promoted enrichment in LILE (Ba, K, Sr, LREE) as well as in Cs, Pb and U and strong enrichment of LILE over HFSE (Zr, Y, Ti, Nb) in amphibole in the amphibole-rich fine-type peridotites (Rampone & Morten, 2001; Scambelluri et al., 2006). However, it remains matter of debate whether hydration and recrystallization (and pressure peak metamorphism) of the peridotites occurred while they were still residing in the mantle wedge before entrapment in the host gneisses at early stages of exhumation (Tumiati et al., 2003; Scambelluri et al., 2006) or, in contrary, peridotites and gneisses reached the metamorphic peak together during subduction after tectonic peridotite incorporation into crustal rocks (Tumiati et al., 2003, 2007; Figure 1.2). The first scenario would require that rising crust-derived partial melts interact with the mantle-wedge peridotites, leading to crystallization of a metasomatic orthopyroxene-rich layer and the liberation of a residual aqueous fluid enriched in incompatible trace elements (Scambelluri et al., 2006). In this case, the aqueous fluid would migrate upwards into the mantle wedge where it would lead to amphibole formation in the peridotites. However, large-scale formation of orthopyroxene has not been observed in the UZ, leading Rampone & Morten (2001) to suggest that the metasomatizing aqueous fluid was liberated through the crystallization of leucosomes after the migmatization of the metapelites. Moreover, the second scenario was supported by Sm-Nd isotopic data revealing common isotopic homogenization of crustal and ultramafic rocks at ca. 330 Ma, most likely when the wedge-derived peridotites were already incorporated in the crustal host rocks (Tumiati et al., 2003, 2007). This age was also interpreted to reflect the time of the garnet-facies metamorphism of the peridotites and partial melting of the subducted metapelites (Tumiati et al., 2003, 2007; Figure 1.2). However, the suggested scenarios are in conflict since hydration of the peridotites related to leucosome crystallization would require lower *P-T* conditions (below the wet metapelite solidus) than those inferred for the H*P* garnet-facies stage (> 800°C, see above). This discrepancy was observed also by Marocchi et al. (2009, 2010), who studied the "hybrid" crust-peridotite contact zones, the development of which was ascribed to fluid-mediated crust-peridotite interaction at low *P-T* conditions in the course of the exhumation of the crust-peridotite mélange (stage 3, Figure 1.2). While Tumiati et al. (2003, 2007) related their formation to fluid-mediated crust-peridotite interaction at the H*P* garnet-stage at ca. 330 Ma, Marocchi et al. (2009, 2010) suggested that the contacts formed at ca. 660-700°C and <1.2 GPa (stage 3; Figure 1.2). Thus, Marocchi et al. (2010) stated that the emplacement of the peridotites into the host crustal rocks and the coeval hydration by crust-derived aqueous fluids is not consistent with peak metamorphism and rather must be related to a low-pressure stage during exhumation. Nevertheless, obtained *P-T* conditions for the equilibration of carbonated hydrous peridotites (Braga & Sapienza, 2007; Sapienza et al., 2007, 2009; Malaspina & Tumiati, 2012) are partly lower than the peak-*P-T* from Nimis & Morten (2000; stage 4, Figure 1.2). Although the depth and timing of peridotite incorporation into the crustal host rocks as well as the *P-T* path of peridotites and crustal rocks remain matter of debate, it is evident that all UZ rock types share their exhumation history beginning at ca. 330 Ma (Tumiati et al., 2003, 2007).

The retrograde evolution of the garnet peridotites is documented by the occurrence of kelyphites of variable composition which formed as a result of the transition from H*P* garnet peridotite to low-pressure spinel peridotites (Godard & Martin, 2000). Furthermore, ongoing infiltration of crust-related aqueous fluids during exhumation led to retrogression of the peridotites to chlorite-amphibole peridotite (Obata & Morten, 1987; Scambelluri et al., 2006; Braga & Sapienza, 2007; Marocchi et al., 2007). Based on the lack of garnet relics and garnet pseudomorphs as well as of HREE fractionation of amphibole and chlorite and positive Eu anomaly in rocks and minerals, Marocchi et al. (2007) demonstrated that at least some of the chlorite-amphibole peridotites did not have garnet-bearing precursors (Figure 1.2). These authors therefore conclude that peridotites with different *P-T* trajectories were captured by crustal host rocks which have originated from different crustal levels. The composition of the crust-derived aqueous fluid(s) did not change during exhumation (Scambelluri et al., 2006) but it has been shown by thermodynamic modeling that the CO_2-content of the fluid phase increased, although potentially only locally (Braga & Sapienza, 2007). The two-stage model for the exhumation of the crust-mantle mélange consists of a first fast buoyancy-driven stage and a second slow stage related to slab break-off during ongoing subduction (Ranalli et al., 2005). This model, however, considers only exhumation from subduction depths >100 km and peridotite insertion into the crustal rocks at peak metamorphic conditions. However, after possible slab break-off, lithospheric attenuation and rifting in the course of the opening of the Alpine Tethys, the subduction process finished and the UZ was no longer involved in subduction (Ranalli et al., 2005).

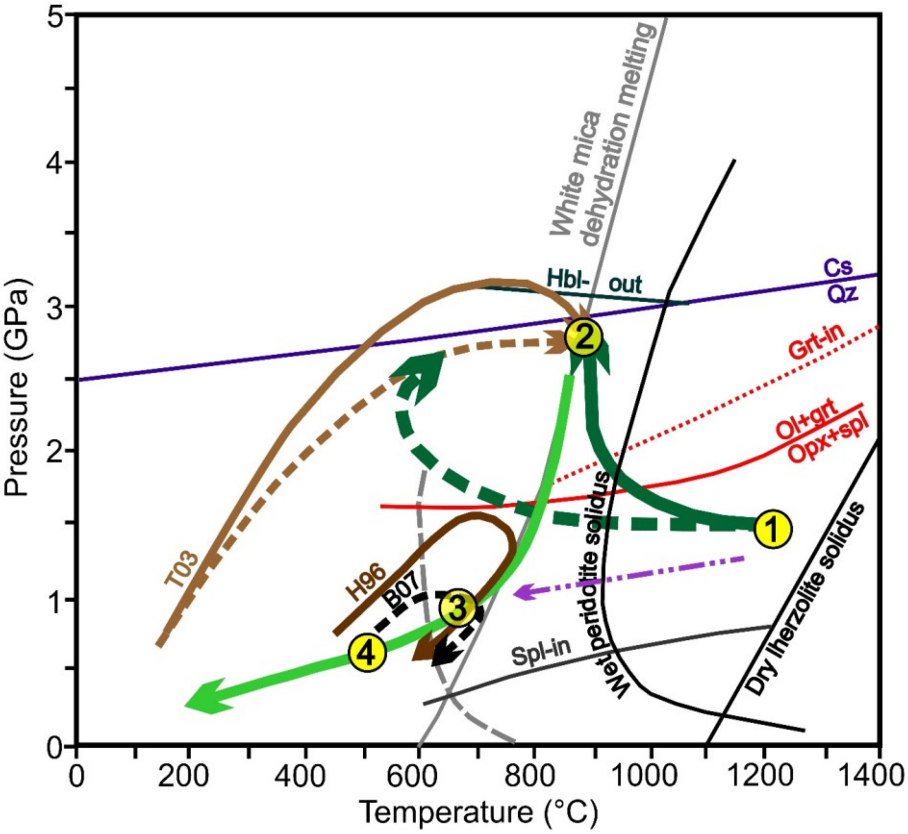

Figure 1.2. Pressure-Temperature (*P-T*) evolution for Ulten Zone crustal rocks and peridotites with main metasomatic events after Tumiati et al. (2003), Marocchi et al. (2009) and Sapienza et al. (2009). Dark green thick full and stippled lines show possible peridotite *P-T* paths starting at stage 1 (spinel stage) at high temperatures. Insertion of peridotites into crustal host rocks occurs either during subduction (dashed line; Nimis & Morten, 2000) or at the beginning of the common exhumation (full line; Scambelluri et al., 2006). Stage 2 shows the high-pressure stage with transformation of spinel peridotite into garnet-bearing peridotite, accompanied by influx of crust-derived aqueous fluids and dolomite formation (Sapienza et al., 2009). This stage marks also the start of the common exhumation of the crust-peridotite association at ca. 330 Ma (Tumiati et al., 2003). Stage 3 marks the formation of the hybrid crust-peridotite contact zones and the pressure-temperature conditions for peridotite emplacement into the crustal rocks suggested by Marocchi et al. (2009). Stage 4 marks further hydration of the peridotites at low pressure and temperatures and further dolomite formation (Sapienza et al., 2009). Purple stippled-dotted line indicates path of chlorite peridotites which possibly never equilibrated at garnet-facies conditions (Marocchi et al., 2007). Proposed *P-T* paths for crustal rocks: T03 (Tumiati et al., 2003), H96 (Hauzenberger et al., 1996) and B07 (Braga et al., 2007a). Red stippled grt-in curve as in Marocchi et al. (2009), full red curve opx+spl → ol+grt as in Tumiati et al. (2003). Gray stippled line indicates the solidus for H_2O-saturated metapelites. Mineral abbreviations after Whitney & Evans (2010).

1.4 Sampling campaign and sample preparation

In order to address the open questions discussed in section 1.2, a comprehensive sampling of new peridotites ± pyroxenites from ultramafic localities in the UZ was carried out. Some of these localities had not been studied before. The extended sample set of UZ peridotites enabled a correlation between petrologic observations and the locality in the UZ.

1.4.1. Field work and sampling

The aim of the sampling campaign was to sample peridotite localities in all parts of the UZ. Beforehand I searched the localities of the peridotite outcrops using new geologic maps where the UZ is displayed on the 1:50000 sheets "Rabbi" and "Appiano/Eppan", and the digital map catalogue CARGBrowser (CARG: Geological CARtography; http://gis2.provinz.bz.it/carg/ClientServlet?CMD=Init) provided by the Provincia Autonoma di Bolzano – Alto Adige where it is possible to zoom in to a 1:5000 map scale. I compared the geologic maps with road and trail maps of the region to investigate the location of the ultramafic lenses and their accessibility. The UZ virtually encloses the mountain range Le Maddalene in Trentino (Italy), located between the Ulten, the Non and the Rabbi Valley (Figure 1.1c). The ultramafic outcrops occur at ca. 2000 m altitude and are accessible from those valleys. During the 3-weeks field campaign I studied ultramafic rocks of 12 localities, most of them not studied before, and sampled more than 150 new hand specimens. Table 1.1 shows the coordinates of the localities, the type of peridotite exposure (*in-situ* vs. boulders/debris fan) and the observed petrographic types.

Table 1.1 Sample localities and peridotite occurrences studied during the field campaign.

Sample locality	Peridotite field occurrence	Latitude	Longitude	Altitude	Peridotite types
Bichlalm	*In-situ* + boulders	46°28'52''	10°55'37''	2300	Fine
Klapfbergalm	Road cut *in-situ*	46°27'36''	10°54'52''	1950	Fine grt
	Below road *in-situ*	46°27'36''	10°54'52''	1950	
	Debris flow, boulders	46°27'14''	10°54'31''	2040	
Kornigl	*In-situ* + boulders	46°30'47''	11°01'54''	2180	Coarse + fine
	Debris field	46°30'57''	11°01'59''	2100	
Malga Binasia	*In-situ* + boulders	46°26'41''	10°56'28''	2240	Coarse + fine
Malga Masa Murada	*In-situ*	46°27'	10°57'	2000	Not investigated in detail
Malga Preghena	*In-situ* + boulders	46°25'18''	10°53'29''	2100	Coarse + fine grt
	In-situ + boulders	46°24'47''	10°53'08	2300	
Malga Zoccolo	Debris field + *in-situ*	46°24'38''	10°52'47''	2100	Coarse + fine
Monte Ometto	*In-situ*	46°29'37''	11°00'20''	2150	Coarse + fine
	Boulder	46°29'34''	11°01'30''	2060	
Samerbergalm	*In-situ?*/debris field?	46°29'35''	10°59'29''	2130	Coarse grt + fine grt
Schönboden	*In-situ*	46°31'45''	11°02'13''	2100	Coarse + fine grt
Schöngrubspitz	*In-situ*	46°30'48''	11°01'56''	2235	Highly altered
Walschgrube/Pfandlalm	*In-situ*	46°31'	11°00'	1970	Fine grt
Laghetti di Grumi	No peridotite	46°26'36''	10°58'12''	2090	No peridotite

grt: garnet

The ultramafic rocks occur as lenses of sizes from meter to 100-meter scale, embedded in the crustal host rocks, and consist of peridotites ± pyroxenites. The chosen specimens from each locality are representative of the variable petrographic characteristics. Fine-grained spinel peridotite occurs in all studied localities whereas coarse-grained spinel peridotite was found in seven of the studied peridotite bodies (Table 1.1; Figure 1.3), in agreement with the early observations by Obata & Morten (1987), indicating that the fine-grained type is much more abundant than the coarse-grained type in the studied localities. Coarse-grained undeformed peridotite often occurs as “lenses” within the fine-grained mylonitic peridotite (Figure 1.4). It is noteworthy that coarse-grained peridotite occurs only in peridotite bodies which are located along the southeastern flank of the UZ (Figure 1.3). While coarse-grained garnet-bearing peridotite was observed in the locality Samerbergalm only, fine-grained garnet-bearing peridotites were found in five localities (Table 1.1; Figure 1.3). Other five outcrops across the UZ contain garnet-free peridotites (Table 1.1; Figure 1.3) but pseudomorphs after garnet were partly observed. Some ultramafic bodies exhibit pyroxene aggregates and/or pyroxene veins.

It is interesting to note that the new geologic maps indicate a peridotite exposure close to the Laghetti di Grumi but extensive field observations could not confirm the presence of peridotite in this locality (Table 1.1).

Figure 1.3. Sketch of the Ulten Zone with the peridotite localities examined during the field campaign. The ovals (not in scale) mark the sampled localities and the different observed peridotite types in terms of their texture (coarse-grained vs. fine-grained) and mineral assemblage (garnet-bearing vs. garnet-free). The peridotite-bearing localities Schöngrubspitz and Malga Masa Murada are not shown because they were not examined in detail and only a few samples were taken. Grt: garnet.

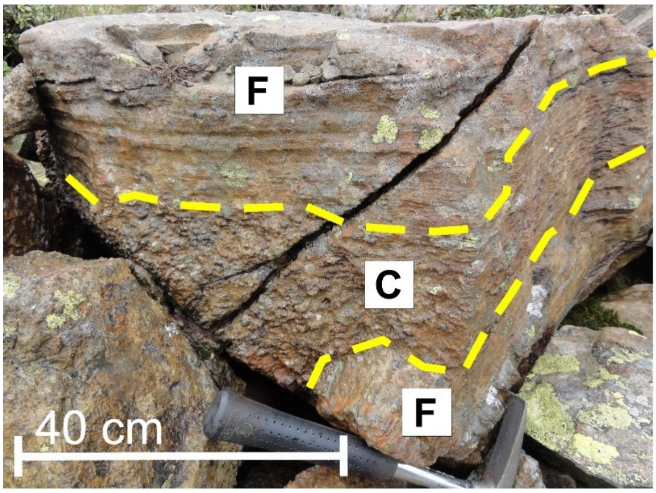

Figure 1.4. Photograph of an Ulten Zone peridotite boulder from Malga Binasia, consisting of a coarse-grained part (C) embedded in fine-grained deformed peridotite (F).

1.4.2 Sample preparation

The new collected hand specimens were cut to obtain unaltered parts of the rocks. Selected samples were cut into cm-sized blocks that were used for thin-section preparation and into blocks that were used for the production of whole-rock powder. The blocks for thin sections were selected in a way that the thin sections were representative for the rocks and possibly included also special features in the rock, such as veins, large porphyroclasts and/or different rock domains. Regarding the blocks selected for whole-rock powder production it was taken care of that these blocks are representative of the homogeneous mineral composition of the rock and that they do not contain veins and/or different rock domains (different mineral assemblages). Thin sections were mainly produced at the Goethe University Frankfurt and partly at the Universities of Parma and Bologna. Whole-rock powders were obtained by crushing the blocks into granulate using a mechanical rock crusher and by grinding the granulate using a vibratory agate disc mill.

1.5 Petrography

Petrographic characterization of >150 new peridotite samples (Table A1 in Appendix) from the abovementioned studied localities across the entire UZ sampled during the field campaign as well as of further samples from a “in-house” sample set was carried out on thick sections (~100 µm) using an optical transmitted light microscope and an energy-dispersive (EDS) scanning electron microscope (SEM; Philips 515B, 5 µm spot size, 15 kV voltage) at the Dipartimento di Scienze Biologiche, Geologiche ed Ambientali of the University of Bologna (Italy). The new petrographic study confirms that the UZ peridotites display highly variable petrographic characteristics, as reported previously (e.g. Obata & Morten, 1987) and summarized in section 1.3.3.2. According to the classification of the peridotites into a coarse type and a fine type, introduced by Obata & Morten (1987), in the present study the peridotites are grouped into coarse-grained spinel peridotite and coarse-grained garnet-bearing peridotite as well as fine-grained garnet-bearing and fine-grained garnet-free peridotite (Table A1, Appendix). The transition from protogranular coarse-grained peridotite to recrystallized fine-grained peridotite is represented by a porphyroclastic type, whose texture and grain size is highly variable: from more coarse-grained with recrystallized fine-grained domains between the coarse minerals to peridotites with a fine-grained matrix and relic porphyroclasts. Weakly deformed coarse-grained spinel peridotites can be mainly found with fine-grained domains of fractured olivine and orthopyroxene between the coarse minerals, progressing into a porphyroclastic texture and also with granoblastic aggregates of these minerals (Figure 1.5a). Instead, the coarse-grained garnet-bearing peridotites largely display a protogranular texture with partly fine-grained recrystallized domains between the coarse grains. These rocks represent former spinel peridotites where coronitic garnet overgrew spinel that now appears in a vermicular structure (Figure 1.5b).

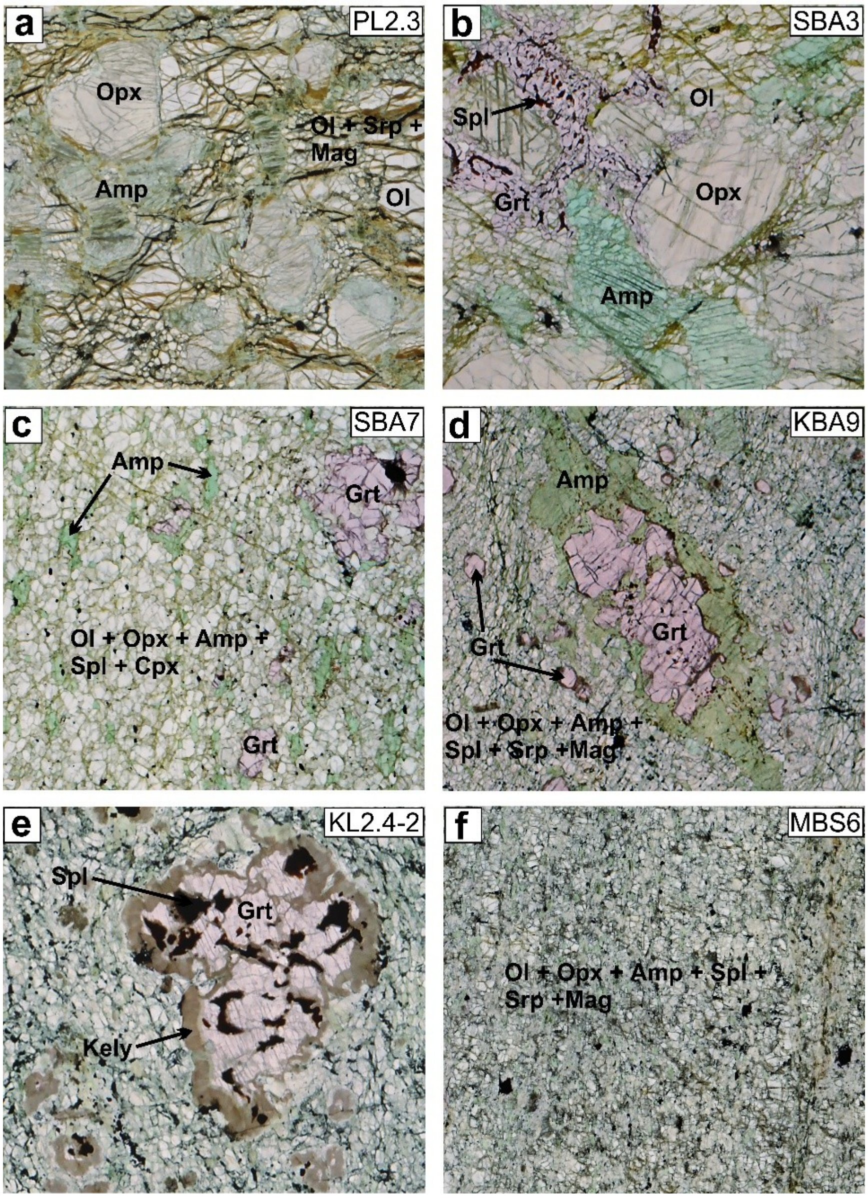

Figure 1.5. Details of thin-section scans of Ulten Zone peridotites. (a) Coarse-grained spinel peridotite displaying the transition from a protogranular to a porphyroclastic texture with large opx, ol and amp and fine-grained domains of ol and opx. Ol is partly replaced by serpentine veins associated to mag. (b) Coarse-grained peridotite showing a protogranular texture of partly fractured ol, opx and amp with anhedral coronitic grt rimming vermicular spl. (c-e) Fine-grained grt-amp peridotites with a granoblastic-porphyroclastic texture. Some samples are only little serpentinized (c), whereas most samples show stronger serpentinization, visible from the high abundance of opaque minerals which occur in the serpentine veins. (d,e). Anhedral grt is often associated with amp (d), can contain spl and is often rimmed by kelyphite (e) and occasionally completely replaced by kelyphite. (f) Fine-grained grt-free spl peridotite with an equigranular-granoblastic texture showing mylonitic deformation and strong serpentinization. This peridotite type often contains pseudomorphs after grt. Height of the scan details corresponds to 1 cm in the thin section. Kely: kelyphite, other mineral abbreviations after Whitney & Evans (2010).

These peridotites contain secondary amphibole and minor serpentine veins, displaying only minor serpentinization. The fine-grained garnet-bearing peridotites display a granoblastic-porphyroclastic mylonitic deformed texture (Figure 1.5c-e). These are recrystallized hydrated garnet-amphibole peridotites with variable modes of amphibole and they are often crosscut by serpentine veins in various modal abundance. Clinopyroxene is either present as a minor phase in the matrix or is absent in these peridotites. Garnets occur in variable size and can contain vermicular spinel. Often, garnets are overgrown by a kelyphitic corona and are in textural equilibrium with amphibole (Figure 1.5c-e). Many of the fine-grained garnet-amphibole peridotites display an oriented texture of the matrix grains and amphiboles often occur vein-like in the matrix (Figure 1.5c,d). Orthopyroxene sometimes occurs as porphyroclasts in the matrix (Table A1, Appendix). The serpentine veins often contain Fe-oxide and form a mesh texture in the peridotites, replacing olivine. Fine-grained garnet-free peridotites display mainly a equigranular-granoblastic matrix and are highly retrogressed (Figure 1.5f). They contain highly abundant amphibole, are strongly serpentinized and occasionally contain porphyroclasts of orthopyroxene. Occasionally occurring pseudomorphs after garnet indicate that these peridotites once equilibrated in the garnet-stability field and garnet was completely replaced by secondary kelyphite. Some fine-grained peridotites that do not contain garnet or garnet pseudomorphs did probably never reach garnet stability (Marocchi et al., 2007). The peculiar occurrence of non-primary peridotite phases, such as carbonates and zircon, in some peridotite samples will be treated in detail in the following chapters.

1.6 Analytical techniques

A brief description of the performed analyses and used analytical techniques is given here. The detailed conditions for the analyses will be reported in the following chapters. Table A2 in the Appendix lists the analyses performed on the individual samples.

1.6.1 Bulk-rock major-element and trace-element analyses

Analyses of bulk-rock compositions of selected peridotite samples were carried out at ActLabs (Ontario, Canada). Whole-rock major and trace elements were analyzed by ICP-MS (inductively-coupled plasma mass spectrometry) using a Perkin Elmer Sciex ELAN 6000, 6100 or 9000. Some trace element analyses for selected samples for radiogenic isotope analyses were repeated with lower detection limits, using the analytical package “UT-4M ‘Near Total’ Digestion ICP/MS”. The whole-rock contents of carbon and sulfur were carried out by solid state infrared absorption using an Eltra CS-800 or CS-2000 Carbon/Sulfur analyzer. Concentration of FeO in the whole rocks was determined by titration.

1.6.2 Bulk-rock radiogenic isotope analyses

Chemical extraction of the elements Sr, Nd, Pb and Hf from whole-rock powders of selected peridotite samples was performed by multi-step column chromatography in the clean-lab facilities at Géosciences Montpellier of the University of Montpellier II (France). After the separation process, aliquots of each element were taken and measured preliminarily, in order to ascertain whether the extracted elemental amount is measurable by ICP-MS. The final isotope analyses were carried out using the ThermoScientific Neptune Plus ICP-MS at ENS Lyon (France).

1.6.3 Zircon U-Pb geochronology and zircon and garnet trace-element composition

In-situ analyses of trace element compositions in zircon and garnet and U-(Th-)Pb age determinations on zircons in thick sections (~100 µm) were performed by Laser ablation (LA)-ICP-MS at Géosciences Montpellier at the University of Montpellier II (France), using a MicroLAS QPLUS laser coupled to a Thermo Element XR ICP-MS.

1.6.4 Bulk-rock oxidized and reduced carbon concentrations

Analyses of the concentrations of oxidized carbon (carbonate carbon) and reduced carbon were performed on whole-rock powders of selected ultramafic samples using a LECO RC-412 Multiphase Carbon Determinator at the Institute of Physical Geography of the Goethe University Frankfurt am Main (Germany). The total carbon content in a sample was determined from the analysis of the emitted CO_2 via infrared spectrometry after combustion of a powder sample. The heating was ramped up first to 550°C and then up to 1000°C. The concentration of reduced carbon was then calculated as the difference between the analyzed concentrations of total carbon and oxidized carbon (in weight percent).

1.6.5 Bulk-rock total-carbon concentration and carbon isotopic composition

Analyses of total carbon concentration and carbon-isotope composition in whole-rock powders of selected ultramafic rock samples were carried out at the Dipartimento di Fisica e Scienze della Terra of the University of Ferrara (Italy) using EA-IRMS (elemental analysis isotope ratio mass spectrometry).

1.6.6 Stable-isotope (carbon and oxygen) composition of carbonates in bulk rock

In order to dissolve the carbonates in ultramafic rocks and to obtain CO_2 gas, whole-rock powders were mixed with phosphoric acid at 72°C. Analyses of the carbon and oxygen isotopic composition of bulk carbonate in the whole-rock samples were then performed on CO_2 gas released from carbon dissolution using a Finnigan MAT 252 magnetic sector isotope ratio MS connected to a GasBench II system at the Department of Earth and Environmental Sciences of Lehigh University (USA).

1.7 References

1. Audetat, A., Keppler, H. (2005). Solubility of rutile in subduction zone fluids, as determined by experiments in the hydrothermal diamond anvil cell. Earth and Planetary Science Letters 232, 393-402.
2. Arai, S., Ishimaru, S. (2008). Insights into petrological characteristics of the lithosphere of mantle wedge beneath arcs through peridotite xenoliths: a review. Journal of Petrology 49, 665-695.
3. Bargossi, G.M., Bondi, M., Mordenti, A., Morten, L. (2003). The abundances of 55 elements and petrovolumetric models of the crust in the Non and Ulten Valley (Site 3). In: F.P. Sassi (Ed.). The abundance of 55 elements and petrovolumetric models of the crust in 9 type areas from the crystalline basements of Italy, with some geophysical and petrophysical data, Accademia Nazionale delle Scienze detta dei XL, Scritti e Documenti, Roma, 163-196.
4. Bebout, G.E. (2007). Metamorphic chemical geodynamics of subduction zones. Earth and Planetary Science Letters 260, 373-393.
5. Bebout, G.E. (2013). Metasomatism in subduction zones of subducted oceanic slabs, mantle wedges, and the slab-mantle interface. In: D.E. Harlow, H. Austrheim (Eds.). Metasomatism and the chemical transformation of rock, Springer Berlin Heidelberg, 289-349.

6. Braga, R., Massonne, H.-J., Morten, L. (2007a). An early metamorphic stage for the Variscan Ulten Zone gneiss (NE Italy): evidence from mineral inclusions in kyanite. Mineralogical Magazine 71(6), 691-702.
7. Braga, R., Bargossi, G.M., Mair, V., Marocchi, M., Sapienza, G.T., Bondi, M. (2007b). Garnet peridotites, pyroxenites and migmatites from the Ulten Zone: A tribute to Lauro Morten. Mitteilungen der Österreichischen Mineralogischen Gesellschaft 153, 243-261.
8. Braga, R., Sapienza, G.T. (2007). The retrograde evolution of a dolomite-bearing hydrous peridotite from the Ulten Zone (Italian Alps). GeoActa 6, 37-45.
9. Braga, R., Massonne, H.-J. (2008). Mineralogy of inclusions in zircon from high-pressure crustal rocks from the Ulten Zone, Italian Alps. Periodico di Mineralogia 77, 43-64.
10. Braga, R., Bargossi, G.M. (2014). Crust-mantle relationships close at hands – Walking through the Ulten-Nonsberg orogenic lower crust. Periodico semestrale del Servizio Geologico d'Italia – ISPRA e della Società Geologica Italiana, Geological Field Trips 6, 46 p.
11. Brueckner, H.K. (1998). Sinking intrusion model for the emplacement of garnet-bearing peridotites into continent collision orogens. Geology 26, 631-634.
12. Brueckner, H.K., Medaris, L.G. (2000). A general model for the intrusion and evolution of "mantle" garnet peridotites in high-pressure and ultra-high-pressure metamorphic terranes. Journal of Metamorphic Geology 18, 123-133.
13. Chen, Y., Su, B.X., Guo, S. (2015). The Dabie-Sulu orogenic peridotites: progress and key issues. Science China: Earth Sciences 58, 1679-1699.
14. Chen, R.-X., Li, H.-Y., Zheng Y.-F., Zhang, L., Gong, B., Hu, Z., Yang, Y. (2017). Crust-mantle interaction in a continental subduction channel: evidence from orogenic peridotites in North Qaidam, Northern Tibet. Journal of Petrology 58, 191-226.
15. Del Moro, A., Martin, S., Prosser, G. (1999). Migmatites of the Ulten Zone (NE Italy), a record of melt transfer in deep crust. Journal of Petrology 40, 1803-1826.
16. Gebauer, D., Grünenfelder, M. (1978). U-Pb dating of alpine-type garnet-peridotites example: Val Ultimo (Eastern Alps, northern Italy). U.S. Geological Survey Open-File Report OF 78-0701, 135-137.
17. Godard, G., Martin, S., Prosser, G., Kiénast, J.R., Morten, L. (1996). Variscan migmatites, eclogites and garnet-peridotites of the Ulten zone, Eastern Austroalpine system. Tectonophysics 259, 313-341.
18. Godard, G., Martin, S. (2000). Petrogenesis of kelyphites in garnet peridotites: a case study from the Ulten zone, Italian Alps. Journal of Geodynamics 30, 117-145.
19. Hauzenberger, C.A., Höller, W., Hoinkes, G. (1996). Transition from eclogite to amphibolite-facies metamorphism in the Austroalpine Ulten Zone. Mineralogy and Petrology 58, 111-130.
20. Hermann, J., Rubatto, D., Trommsdorff, V. (2006). Sub-solidus Oligocene zircon formation in garnet peridotite during fast decompression and fluid infiltration (Duria, Central Alps). Mineralogy and Petrology 88, 181-206.
21. Herzberg, C., Riccio, L., Chiesa, S., Fornoni, A., Gatto, G.O., Gregnanin, A., Piccirillo, E.M., Scolari, A. (1977). Petrogenetic evolution of a spinel-garnet lherzolite in the Austridic crystalline basement from Val Clapa (Alto Adige, northern Italy). Memorie degli Istituti di Geologia e Mineralogia dell'Università di Padova 30, 3-28.
22. Ionov, D.A. (2010). Petrology of mantle wedge lithosphere: new data on supra-subduction zone peridotite xenoliths from the andesitic Avacha volcano, Kamchatka. Journal of Petrology 51, 327-361.
23. Jiang, S.-Y., Wang, R.-C., Xu, X.-S., Zhao, K.-D. (2005). Mobility of high field strength elements (HFSE) in magmatic-, metamorphic-, and submarine-hydrothermal systems. Physics and Chemistry of the Earth 30, 1020-1029.

24. Kelemen, P.B., Manning C.E. (2015). Reevaluating carbon fluxes in subduction zones, what goes down, mostly comes up. Proceedings of the National Academy of Sciences 112, E3997-E4006.
25. Kessel, R., Schmidt, M.W., Ulmer, P., Pettke, T. (2005). Trace element signature of subduction-zone fluids, melts and supercritical liquids at 120-180 km depth. Nature 437, 724-727.
26. Liati, A., Gebauer, D. (2009). Crustal origin of zircon in a garnet peridotite: a study of U-Pb SHRIMP dating, mineral inclusions and REE geochemistry (Erzgebirge, Bohemian Massif). European Journal of Mineralogy 21, 737-750.
27. Louvel, M., Sanchez-Valle, C., Malfait, W.J., Testemale, D., Hazemann, J.-L. (2013). Zr complexation in high pressure fluids and silicate melts and implications for the mobilization of HFSE in subduction zones. Geochimica et Cosmochimica Acta 104, 281-299.
28. Malaspina, N., Tumiati, S. (2012). The role of C-O-H and oxygen fugacity in subduction-zone garnet peridotites. European Journal of Mineralogy 24, 607-618.
29. Marocchi, M., Hermann, J., Morten, L. (2007). Evidence for multi-stage metasomatism of chlorite-amphibole peridotites (Ulten Zone, Italy): Constraints from trace element compositions of hydrous phases. Lithos 99, 85-104.
30. Marocchi, M., Mair, V., Tropper, P., Bargossi G.M. (2009). Metasomatic reaction bands at the Mt. Hochwart gneiss-peridotite contact (Ulten Zone, Italy): insights into fluid-rock interaction in subduction zones. Mineralogy and Petrology 95, 251-272.
31. Marocchi, M., Hermann, J., Tropper, P., Bargossi, G.M., Mair, V. (2010). Amphibole and phlogopite in "hybrid" metasomatic bands monitor trace element transfer at the interface between felsic and ultramafic rocks (Eastern Alps, Italy). Lithos 117, 135-148.
32. Marocchi, M., Marschall, H.R., Konzett J., Tropper P., Ludwig, T., Mair, V., Bargossi, G.M. (2011). Metasomatic tourmaline in hybrid contact-bands between gneiss and peridotite in the Ulten Zone of the Eastern Italian Alps: Chemistry and boron isotopic composition. The Canadian Mineralogist 49, 245-261.
33. Martin S., Morten L. and Prosser G. (1993). Metamorphic and structural evolution of the Spl- to Grt-peridotites and surrounding basement rocks from the Nonsberg area. In: L. Morten (Ed.). Italian Eclogites and Related Rocks, Rendiconti della Accademia Nazionale Quaranta, XIII, 237-251.
34. Martin S., Godard G., Prosser G., Schiavo A., Bernoulli D. and Ranalli, G. (1998). Evolution of the deep crust at the junction Austroalpine/Southalpine: the Tonale Nappe. Memorie di Scienze Geologiche (Padova) 50, 3-50.
35. Massonne, H.-J. (2005). Involvement of crustal material in delamination of the lithosphere after continent-continent collision. International Geology Review 47, 792-804.
36. Morten L., Bargossi G.M. and Landini Bargossi F. (1976). Notizie preliminari sulle metamorfiti della Val di Rumo, Val di Non, Trento. Mineralogica et Petrographica Acta 21, 137-144.
37. Morten, L., Obata, M. (1983). Possible high-temperature origin of pyroxenite lenses within garnet peridotite, northern Italy. Bulletin de Minèralogie 106, 775-780.
38. Morten, L., Trommsdorff, V. (2003). Metamorphism and textures of dry and hydrous garnet peridotites. In: D.A. Carswell, R. Compagnoni (Eds.). Ultrahigh Pressure Metamorphism. EMU Notes in Mineralogy 5, Chapter 5, 1-209.
39. Neubauer, F., Handler, R. (2000). Variscan orogeny in the Eastern Alps and Bohemian Massif: How do these units correlate? Mitteilungen der Österreichischen Geologischen Gesellschaft 92, 35-59.
40. Nimis, P., Morten, L. (2000). P-T evolution of "crustal" garnet peridotites and included pyroxenites from Nonsberg area (upper Austroalpine), NE Italy: from the wedge to the slab. Journal of Geodynamics 30, 93-115.
41. Obata, M., Morten, L. (1987). Transformation of spinel lherzolite to garnet lherzolite in ultramafic lenses of the Austridic Crystalline Complex, Northern Italy. Journal of Petrology 28, 599-623.

42. Perchuk, L.L., Gerya, T.V., Parfenova, O.V., Podgornova, S.T. (2007). Metamorphic rocks of the Samerberg Complex, Eastern Alps: 2. P-T paths and the problem of a geodynamic model. Petrology 15, 397-415.
43. Petrini, R., Morten, L. (1993). Nd-isotopic evidence of enriched lithospheric domains: an example from the Nonsberg area, eastern Alps. Terra Abstract 4, 19-20.
44. Poli, S. (2015). Carbon mobilized at shallow depths in subduction zones by carbonatitic liquids. Nature Geoscience 8, 633-637.
45. Rampone, E., Morten, L. (2001). Records of crustal metasomatism in the garnet peridotites of the Ulten Zone (Upper Austroalpine, Eastern Alps). Journal of Petrology 42, 207-219.
46. Ranalli, G., Martin, S., Mahatsente, R. (2005). Continental subduction and exhumation: an example from the Ulten Unit, Tonale Nappe, Eastern Austroalpine. In: D. Gapais, J.P. Brun, P.R. Cobbold (Eds.). Deformation Mechanisms, Rheology and Tectonics: from Minerals to the Lithosphere. Geological Society, London, Special Publications 243, 159-174.
47. Rost, F., Brenneis, P. (1978). Die Ultramafite im Bergzug südlich des Ultentals, Provinz Alto Adige (Oberitalien). Tschermaks Mineralogische und Petrographische Mitteilungen 25, 257-286.
48. Rumble, D., Liou, J.G., Jahn, B.M. (2003). Continental crust subduction and ultrahigh pressure metamorphism. In: R.L. Rudnick (Ed.). Treatise on Geochemistry 3, 293-319.
49. Sapienza, G.T., Braga, R., Marocchi, M., Bargossi, G.M., Bondi, M. (2007). P-T and density constraints on a chlorite-amphibole-peridotite (Ulten Zone, Italy). Ofioliti 32, 83-84.
50. Sapienza, G.T., Scambelluri, M., Braga, R. (2009). Dolomite-bearing orogenic garnet peridotites witness fluid-mediated carbon recycling in a mantle wedge (Ulten Zone, Eastern Alps, Italy). Contributions to Mineralogy and Petrology 158, 401-420.
51. Scambelluri, M., Hermann, J., Morten, L., Rampone, E. (2006). Melt- versus fluid-induced metasomatism in spinel to garnet wedge peridotites (Ulten Zone, Eastern Italian Alps): clues from trace element and Li abundances. Contributions to Mineralogy and Petrology 151, 372-394.
52. Scambelluri, M., Pettke, T., Van Roermund, H.L.M. (2008). Majoritic garnets monitor deep subduction fluid flow and mantle dynamics. Geology 36, 59-62.
53. Scambelluri, M., Van Roermund, H.L.M., Pettke, T. (2010a). Mantle wedge peridotites: Fossil reservoirs of deep subduction zone processes: Inferences from high and ultrahigh-pressure rocks from Bardane (Western Norway) and Ulten (Italian Alps). Lithos 120, 186-201.
54. Scambelluri, M., Rampone, E., Braga, R., Malaspina, N. (2010b). The Variscan garnet peridotites from the Eastern Alps (Ulten Zone): records of subduction metasomatism in the mantle wedge. In: M. Beltrando, A. Peccerillo, M. Mattei, S. Conticelli, C. Doglioni (Eds.). Journal of the Virtual Explorer, Electronic Edition 36, paper 28.
55. Scambelluri, M., Pettke, T., Rampone, E., Godard, M., Reusser, E. (2014). Petrology and trace element budgets of high-pressure peridotites indicate subduction dehydration of serpentinized mantle (Cima di Gagnone, Central Alps, Switzerland). Journal of Petrology 55, 459-498.
56. Susini, S., Martin, S. (1996). Microstrutture nelle peridotiti della Serie d'Ultimo (Austroalpino superiore, Alpi Orientali). Atti Ticinesi di Scienze della Terra 4, 47-63.
57. Thöni, M. (1999). A review of geochronological data from the Eastern Alps. Schweizer Mineralogische und Petrographische Mitteilungen 79, 209-230.
58. Tropper, P., Manning, C.E. (2005). Very low solubility of rutile in H_2O at high pressure and temperature, and its implications for Ti mobility in subduction zones. American Mineralogist 90, 502-505.
59. Tumiati, S., Thöni, M., Nimis, P., Martin, S., Mair, V. (2003). Mantle-crust interactions during Variscan subduction in the Eastern Alps (Nonsberg-Ulten Zone): geochronology and new petrological constraints. Earth and Planetary Science Letters 210, 509-526.

60. Tumiati, S., Godard, G., Martin, S., Klötzli, U., Monticelli, D. (2007). Fluid-controlled crustal metasomatism within a high-pressure subducted mélange (Mt. Hochwart, Eastern Italian Alps). Lithos 94, 148-167.

61. Vrijmoed, J.C., Austrheim, H., John, T., Hin, R.C., Corfu, F., Davies, G.R. (2013). Metasomatism in the ultrahigh-pressure Svartberget garnet-peridotite (Western Gneiss Region, Norway): implications for the transport of crust-derived fluids within the mantle. Journal of Petrology 54, 1815-1848.

62. Whitney, D.L., Evans, B.W. (2010). Abbreviations for names of rock-forming minerals. American Mineralogist 95, 185-187.

63. Wilke, M., Schmidt, C., Dubrail, J., Appel, K., Borchert, M., Kvashnina, K., Manning, C.E. (2012). Zircon solubility and zirconium complexation in $H_2O+Na_2O+SiO_2 \pm Al_2O_3$ fluids at high pressure and temperature. Earth and Planetary Science Letters 349-350, 15-25.

64. Wittenberg, A., Vellmer, C., Kern, H., Mengel, K. (2000). The Variscan lower continental crust: evidence for crustal delamination from geochemical and petrophysical investigations. In: W. Franke, V. Haak, O. Oncken, D. Tanner (Eds.). Orogenic processes: quantification and modeling in the Variscan Belt. Geological Society, London, Special Publications 179, 401-414.

65. Zhang, R.Y., Li, T., Rumble, D., Yui, T.-F., Li, L., Yang, J.S., Pan, Y., Liou, J.G. (2007). Multiple metasomatism in Sulu ultrahigh-P garnet peridotite constrained by petrological and geochemical investigations. Journal of Metamorphic Geology 25, 149-164.

66. Zhang, Z.M., Dong, X., Liou, J.G., Liu, F., Wang, W., Yui, F. (2011). Metasomatism of garnet peridotite from Jiangzhuang, southern Sulu UHP belt: constraints on the interactions between crust and mantle rocks during subduction of continental lithosphere. Journal of Metamorphic Geology 29, 917-937.

67. Zhao, Z.-F., Dai, L.-Q., Zheng, Y.-F. (2013). Postcollisional mafic igneous rocks record crust-mantle interaction during continental deep subduction. Scientific Reports 3, 3413.

68. Zheng, Y.-F. (2012). Metamorphic chemical geodynamics in continental subduction zones. Chemical Geology 328, 5-48.

69. Zheng, Y.-F., Hermann, J. (2014). Geochemistry of continental subduction-zone fluids. Earth, Planets and Space 66, 93.

2 Evolution of orogenic mantle from wedge to exhumation: Implications from trace elements and radiogenic isotope geochemistry of peridotites from the Ulten Zone

2.1 Introduction

Orogenic peridotites, which were involved in continental subduction, are capable of recording processes in Earth's mantle, such as partial melt extraction and/or reaction with mantle melts or fluids, and may add to our understanding of the origin and evolution of the subcontinental lithospheric mantle (SCLM). Such peridotites usually record subduction-related processes which resulted in mineralogical and chemical modification through reactions with metasomatic agents (fluids and/or melts) released by the subducting crustal slab. Due to the complex evolution of orogenic peridotites, from residence in the SCLM via involvement in a continental subduction zone to exhumation in a crust-peridotite association, it is difficult to decipher the different evolutionary stages and the associated element mobility. Orogenic peridotites reveal largely fertile whole-rock major element compositions similar to the primitive mantle (PM) but depleted compositions have also been observed (Bodinier & Godard, 2014). The fertile compositions are attributed to refertilization of an initially depleted SCLM due to interaction with silicate melts, rather than low degrees of melt depletion (Le Roux et al., 2007; Xiong et al., 2015).

The study of radiogenic isotope systematics of orogenic peridotite whole-rock compositions may give insights into the nature and timing of depletion and of melt- and fluid-mediated processes in a supra-subduction zone mantle-wedge and in a tectonic mélange of crustal and wedge-derived ultramafic rocks in an orogenic setting. For this purpose, trace elements are conventionally classified according to their different affinities for aqueous fluids and melt: the fluid-mobile large ion lithophile elements (LILE, e.g. Cs, Ba, Pb, Rb and Sr) and, less so, the light rare earth elements (LREE) usually partition into aqueous fluids, whereas the high field strength elements (HFSE, e.g. Nb, Ta, Zr, Hf) and heavy REE (HREE) can be mobilized by melts. Accordingly, enrichment of LILE and LREE relative to HFSE in orogenic peridotites has been interpreted to reflect a crustal origin of the metasomatic agent, which carried the incompatible elements into the mantle wedge (e.g. Rampone & Morten, 2001; Scambelluri et al., 2006, 2010; Xiong et al., 2015). For example, the strong enrichment in LILE over HFSE in amphibole-rich fine-grained garnet peridotites from the Ulten Zone (UZ) has been ascribed to crustal metasomatism through influx of a COH-fluid derived from the crustal slab (e.g. Rampone & Morten, 2001). Such crustal metasomatism has been observed also in other orogenic peridotites, such as those from the Western Gneiss Region (Scambelluri et al., 2008, 2010; Vrijmoed et al., 2013), the Dabie-Sulu orogen (Zhang et al., 2007, 2011; Chen et al., 2015), Monte Duria (Hermann et al., 2006) and North Qaidam (Chen et al., 2017 and references therein). However, enrichment of LREE in peridotites may also result from chromatographic effects during migration of the metasomatic agent (Scambelluri et al., 2006 and references therein). In addition, recent work increasingly shows that trace elements traditionally viewed as fluid-immobile can be mobilized depending on the availability of appropriate ligands in the fluid (Zhang et al. 2007; Vrijmoed et al. 2013; Chen et al. 2015). Nevertheless, if Hf is demonstrated to be fluid-immobile in the samples under investigation, the Lu-Hf system may provide insights into melt-mediated processes, whereas experiments show that the Rb-Sr, U-Pb and Sm-Nd radiogenic isotope systems are more sensitive to processes involving aqueous fluids (Kessel et al., 2005). Combining radiogenic isotope data of whole-rock peridotites with elemental and petrographic constraints not only gives insights into fluid-mediated crustal metasomatism, but also allows for unraveling melt- and/or fluid-mediated processes in the mantle wedge preceding crust-mantle coupling.

In this study we present the results of whole-rock characterization of UZ peridotites using major element and trace element compositions as well as the first combined Sr-Nd-Hf-Pb isotopic data-set for this locality, with the aim to shed more light on the different evolutionary stages and to unravel the geochemical signature of the involved metasomatic agents acting upon the UZ peridotites.

2.2 Sample material and petrography

Samples are listed in Table 2.1 and scans of thin sections of representative samples are shown in Figure 2.1. They were collected from eight peridotite outcrops during a field campaign in 2015 and samples from mount Hochwart were taken from an "in-house" sample set available at University of Bologna. Additional samples used in the present study were characterized by Ionov et al. (2017).

Table 2.1 Provenance and summary of petrographic data for Ulten Zone peridotites and WR analyses performed in this study.

Sample	Locality	Type	Pseudomorphs after grt	Alteration degree	Performed analyses	
					WR major and trace elements	WR radiogenic isotope analyses
KBA8	Klapfbergalm	Fine grt		Low	x	
KL1.2-1	Klapfbergalm	Fine spl	Yes	Low	x	
KL2.2	Klapfbergalm	Fine spl	Yes	Medium	x	
Ko2C	Kornigl	Coarse spl		High	x	
Ko2F	Kornigl	Fine spl	(Yes)	High	x	
MBS2	Malga Binasia	Coarse spl		Medium	x	x
MBS6	Malga Binasia	Fine spl		Medium	x	x
MOL1.3	Monte Ometto	Fine spl		High	x	
MOL1.5	Monte Ometto	Coarse spl		Low	x	x
P10A	Hochwart	Fine spl	Yes	Low	x	
P10B	Hochwart	Fine grt		Low	x	
P10C	Hochwart	Fine grt		Low	x	
P11	Hochwart	Fine grt		Low	x	
PL1.1	Malga Preghena	Coarse spl		High	x	
PL1.6	Malga Preghena	Fine grt		High	x	
PRE-A	Malga Preghena	Coarse spl		High	x	
SB3.4	Schönboden	Fine grt		Medium	x	
MR141B	Samerbergalm	Fine spl	Yes	Low	x	
SBA2	Samerbergalm	Coarse grt		Low	x	
SBA4	Samerbergalm	Fine grt		Low	x	x
WG1	Walschgrube	Fine grt		High	x	
WG4	Walschgrube	Fine grt		Low	x	x
ULT8	*Poinella/Seefeld*	*Coarse grt*		*Low*	-	x
LP6	*Lago Poinella*	*Coarse spl*		*Medium*	*Ionov et al. (2017)*	x
LP8	*Lago Poinella*	*Coarse spl*		*Low*	-II-	x
U8	*Seefeld*	*Fine grt*		*Low*	-II-	x
U13	*Seefeld*	*Fine grt*	*Yes*	*High*	-II-	x
U15	*Seefeld*	*Fine grt*	*Yes*	*Low*	-II-	x

Mineral abbreviations after Whitney & Evans (2010)

Italics: samples were previously reported in Ionov et al. (2017)

The samples selected for this study show a variety of petrographic characteristics, typical for the UZ, and are classified regarding their textural type (coarse-grained vs. fine-grained) and their mineral facies (spinel vs. garnet) according to the classification by Obata & Morten (1987). The sample set comprises coarse-grained spinel peridotites with protogranular-porphyroclastic texture (Figure 2.1a,b), some of which contain coronitic garnet (Figure 2.1c), fine-grained garnet-amphibole peridotites (Figure 2.1d-f) as well as fine-grained garnet-free peridotites (Figure 2.1g,h) with mylonitic granoblastic-porphyroclastic textures. All samples contain amphibole in variable amounts and display alteration in variable degrees (Table 2.1), with the strongest alteration shown by some of the fine-grained peridotites by a dense mesh of crosscutting veins consisting of serpentine and opaque minerals (Figure 2.1). Garnet in the fine-grained garnet-amphibole peridotites has variable sizes, may contain spinel and often has a kelyphitic corona. Some of the fine-grained garnet-free peridotites contain subrounded aggregates of amphibole ± chlorite ± spinel, which are presumably pseudomorphs after garnet (Table 2.1). The mineral assemblage of the coarse-grained peridotite MOL1.5 is different from the other coarse-grained samples since it contains a high abundance of dolomite (± magnesite) and amphibole (see thesis chapter 4).

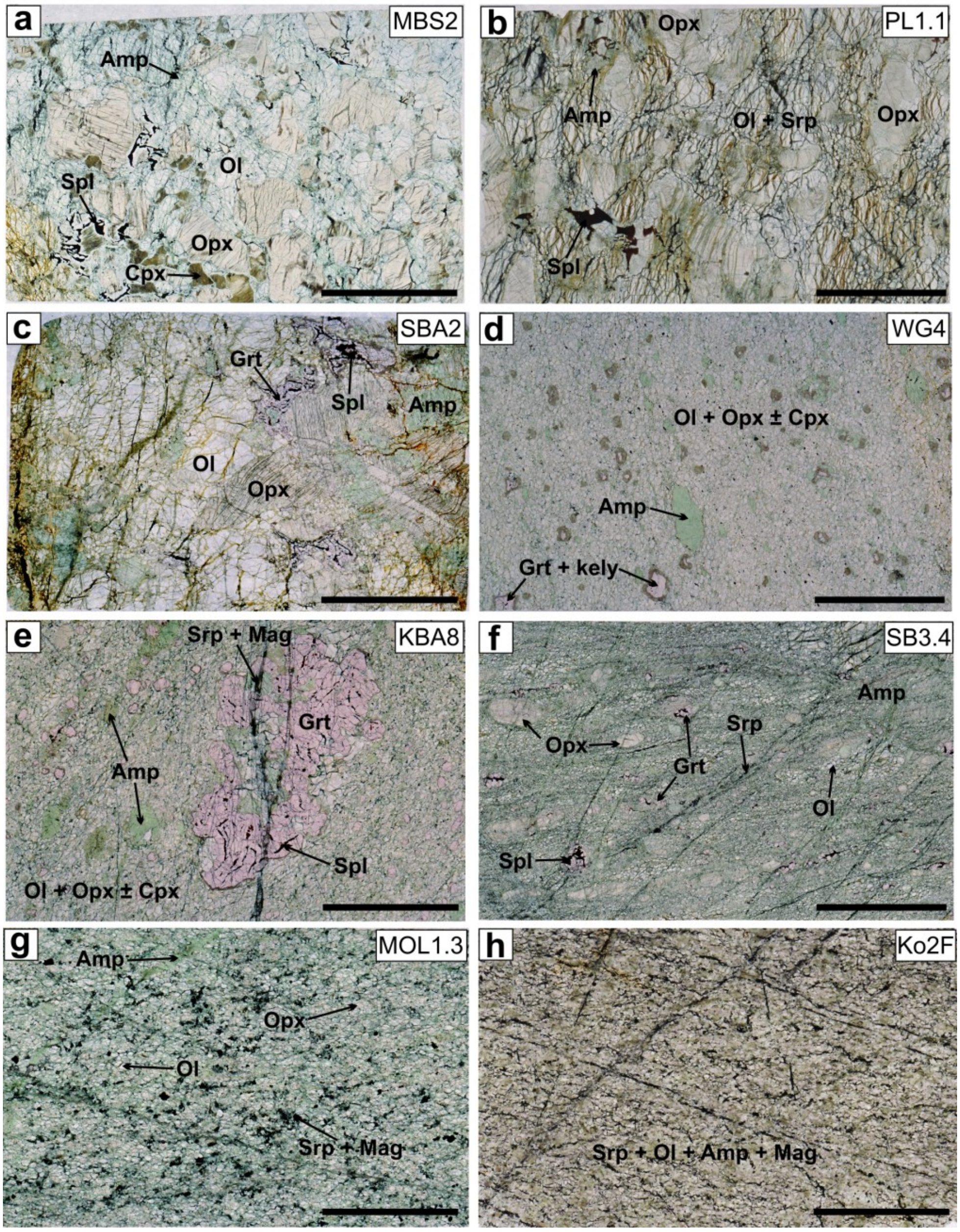

Figure 2.1. Thin section scans of Ulten Zone (UZ) peridotites selected for this study. The samples are representative for the different petrographic/textural types: (a,b) coarse-grained protogranular-porphyroclastic spinel peridotites with veins of serpentine and Fe oxide indicating serpentinization-related olivine recrystallization; (c) coarse-grained protogranular-porphyroclastic peridotite with coronitic garnet; (d,e) fine-grained mylonitic porphyroblastic garnet-amphibole peridotites with porphyroblasts of garnet and amphibole; (f) fine-grained mylonitic porphyroclastic peridotite with opx porphyroclasts and abundant crosscutting veins of serpentine and magnetite; (g,h) fine-grained mylonitic spinel-amphibole peridotites with abundant crosscutting serpentine veins. Scale bars denote 1 cm. Mineral abbreviations after Whitney & Evans (2010).

2.3 Analytical methods

2.3.1 Bulk-rock major element and trace element analyses

Analyses of major and trace elements were performed on whole-rock powder at Activation Laboratories (Ontario, Canada) with the analytical package "4Lithores" using a Perkin Elmer Sciex ELAN 6000/6100/9000. Whole-rock major-element compositions were analyzed by ICP-AES (inductively-coupled plasma atomic emission spectroscopy), concentration of FeO was determined by titration. Whole-rock trace-element compositions were analyzed by ICP-MS (inductively-coupled plasma mass spectrometry). Some trace element analyses for selected samples for radiogenic isotope analyses were repeated with lower detection limits, using the analytical package "UT-4M 'Near Total' Digestion ICP/MS". Detailed information of analytical techniques and detection limits are reported on the laboratory website (www.actlabs.com). Precision and accuracy for trace element analyses are within 10%.

2.3.2 Analyses of bulk-rock radiogenic isotopes (Sr-Nd-Hf-Pb)

Chemical purification of the elements Sr, Nd, Pb and Hf from whole-rock powders was achieved by multi-step column chromatography in the clean-lab facilities at Géosciences Montpellier of the University of Montpellier (France) and following the methods described in Bosch et al. (2008). Sample powders were weighted in order to obtain ca. 100-200 ng of Sr, Nd, Hf and Pb in the final solutions, according to their elemental concentrations. A duplicate of sample SBA4 was taken for later reproducibility control. A leaching step for Nd, Sr and Pb using 6 N HCl was performed for 1 hour on a hot plate at 95°C before acid digestion. After leaching, the residues were rinsed three times by centrifugation with Milli-Q H_2O. All samples, including Hf, were subsequently dissolved using a mixture of HNO_3 and HF on a hot plate at 140°C in Teflon beakers. After evaporation to dryness, a second attack of dissolution was performed on the residues using 2 ml of HNO_3 on a hot plate.

For Hf chemical purification, HCl was added to dried residues for substitution of the N ion by the Cl ion. After centrifugation with 0.5 N HCl, the samples were loaded in HCl-conditioned columns and attacked using 8 ml of a mixture of HCl 0.5 M and Hf 0.22 M. The procedure for Hf extraction followed the method described in Connelly et al. (2006), including a purification step using 0.85 ml of the mixture HNO_3 3.5 M + H_3BO_3 0.06 M and the subsequent Hf elution step by column chromatography using 6 ml of HNO_2 1 M + HF 0.35 M.

For Pb separation, 0.5 ml of 8 N HBr was added to dry residues and the samples were subsequently installed on a hot plate at 100°C. For column chromatography, an anion exchange resin (AG1X8, 200-400 mesh) was used, and samples were loaded into HBr-conditioned columns with 0.5 N HBr and subsequently eluted in 1 ml 6 N HCl.

For Sr separation, samples were loaded with HCl in HCl-conditioned columns with Sr Eichrom resin (Pin et al., 1994) and subsequently 6 ml of 1.5 N HCl and 10 ml of 2.5 N HCl were added. Strontium was eluted after several steps of HNO_3 addition. Neodymium separation was performed by several steps of HCl addition and elution.

After the separation process, aliquots of each element were taken and measured preliminarily, in order to ascertain whether the extracted elemental amount is measurable by ICP-MS and to determine the dilution factor for dilution with HNO_3 for isotope analyses. Analyses of Sr, Nd, Hf and Pb were carried out using the ThermoScientific Neptune Plus Multi-Collector ICP-MS (MC-ICP-MS) at the École Normale Supérieure de Lyon (ENSL, France). For Pb analyses, internal standard normalization was carried out, using the Tl normalization method described by White et al. (2000).

2.4 Results

2.4.1 Bulk-rock major element composition

Whole-rock major and trace element analyses were analyzed on five coarse-grained protogranular-porphyroclastic spinel peridotites, one coarse-grained peridotite with coronitic garnet, nine fine-grained garnet-amphibole peridotites and six fine-grained garnet-free spinel-amphibole peridotites. Whole-rock major element compositions and LOI data are listed in Table 2.2 and illustrated in Figure 2.2. Measured Fe_2O_3 was recalculated to FeO, which prevails in mantle peridotites. The LOI values range from 0.25 to 7.72 wt. % and conform to the alteration and hydration degrees of the peridotites observed during petrographic investigation. The oxide covariation diagrams presented in Figure 2.2 show a wide scatter for the new samples, overlapping with the range of the other UZ peridotites (literature data). The compositions of the new UZ peridotites are compared here with those for subduction-related orogenic peridotites from Cima di Gagnone (Scambelluri et al., 2014) and for subduction-related peridotite xenoliths from the Avacha volcano in Kamchatka (Ionov, 2010). The peridotites from Cima di Gagnone display highly variable major-element compositions interpreted to record refertilization of a depleted SCLM. These peridotites experienced, likewise to the UZ peridotites, enrichment by crustal fluids, but document a main enrichment due to alteration by seawater-derived fluids prior to subduction (Scambelluri et al., 2014). In contrast, the Avacha peridotites are embedded in arc lavas and have been reported to derive from a hot and shallow supra-subduction zone mantle wedge which experienced high degrees of partial melting (Ionov, 2010).

2.4.2 Bulk-rock trace element composition

Trace element compositions of the UZ peridotites are listed in Table 2.3. Whole-rock trace element patterns normalized to primitive mantle are shown in Figure 2.3 according to the different petrographic/textural types. The coarse-grained spinel peridotites and one garnet-bearing coarse-grained peridotite show U-shaped REE patterns with enrichment of La and Ce but depletion in less incompatible LREE and MREE relative to the HREE (Figure 2.3a), whereas the fine-grained garnet-amphibole peridotites display enrichment in LREE relative to MREE (La_N/Sm_N = 0.94 to 6.39), and limited MREE/HREE fractionation (Gd_N/Yb_N = 0.56 to 1.22; Figure 2.3b). Similar LREE-enrichment is observed in the fine-grained garnet-free spinel-amphibole peridotites containing pseudomorphs after garnet (Table 2.1). In contrast, the two samples (MOL1.3 and MBS6) that do not exhibit garnet pseudomorphs have distinctly lower REE abundances relative to the other garnet-free samples (Figure 2.3c). All UZ peridotites show enrichment in incompatible elements (Rb, Ba, Th, U and Pb) and depletion in more compatible elements (below depleted mantle (DM), Figure 2.3d-f). Positive correlations with Al_2O_3, a measure of the degree of fertility of depletion in peridotite, are shown by the moderately incompatible elements Lu and V (Figure 2.4a), and are independent of the petrographic type. In contrast, correlations of Al_2O_3 with the compatible elements Ni and Co are less clear and none are observed with more incompatible trace elements. Covariation plots of individual trace elements show that the concentrations of incompatible trace elements, such as La (as example for LREE, Figure 2.4b), Sr and Ba (as example for LILE, Figure 2.4b,c), are dependent on the petrographic type. In accordance with previous studies (e.g. Rampone & Morten, 2001; Scambelluri et al., 2006; Marocchi et al., 2007; Sapienza et al., 2009; Ionov et al., 2017), fine-grained peridotites are more strongly enriched in the incompatible elements than the coarse-grained peridotites. A general positive correlation of Th and U and Th/U ratios <DMM (Figure 2.4d) are consistent with fluid-mediated enrichment in U. Trace element abundances in the peridotites are not correlated to the sample localities in the UZ.

Table 2.2 Major oxides and LOI for whole-rock peridotites of the Ulten Zone in wt. %.

Sample	SiO_2	TiO_2	Al_2O_3	$Cr_2O_3^{calc}$	FeO^{total}	MnO	MgO	CaO	Na_2O	K_2O	NiO^{calc}	P_2O_5	Total	Fe_2O_3	Mg#	LOI
KBA8	43.99	0.081	3.08	0.33	8.01	0.130	40.98	2.91	0.23	0.02	0.211	0.020	100.00	1.78	0.837	0.97
KL1.2-1	44.25	0.082	2.64	0.31	7.78	0.127	41.27	3.03	0.27	0.03	0.200	0.021	100.00	1.20	0.841	1.92
KL2.2	44.98	0.039	2.29	0.36	7.75	0.130	41.01	2.94	0.18	0.03	0.292	<dl	100.00	1.18	0.841	3.11
Ko2C	46.21	0.054	3.71	0.45	7.97	0.129	37.66	3.11	0.36	0.06	0.294	<dl	100.00	2.76	0.825	5.88
Ko2F	44.90	0.052	2.72	0.41	8.34	0.126	40.48	2.31	0.24	0.09	0.284	0.055	100.00	3.10	0.829	7.72
MBS2	45.95	0.023	2.79	0.41	7.46	0.131	40.87	2.06	0.06	0.04	0.198	<dl	100.00	1.67	0.846	2.64
MBS6	43.20	0.035	1.50	0.34	8.10	0.122	45.14	1.20	0.08	0.04	0.229	<dl	100.00	1.30	0.848	2.53
MOL1.3	43.39	0.021	1.52	0.31	7.42	0.122	45.65	1.18	0.12	0.03	0.241	<dl	100.00	1.99	0.860	4.22
MOL1.5	46.82	0.035	2.91	0.44	8.08	0.132	38.95	2.00	0.28	0.10	0.243	<dl	100.00	3.09	0.828	1.50
P10A	45.35	0.034	2.42	0.42	8.13	0.135	40.75	2.27	0.16	0.03	0.294	<dl	100.00	1.46	0.834	0.25
P10B	45.64	0.038	2.72	0.42	8.11	0.135	39.69	2.71	0.20	0.04	0.285	<dl	100.00	0.81	0.830	0.62
P10C	44.88	0.033	2.99	0.44	8.13	0.139	40.44	2.50	0.14	0.02	0.279	<dl	100.00	1.27	0.833	0.34
P11	45.16	0.075	2.37	0.35	7.85	0.130	41.33	2.10	0.21	0.10	0.275	0.041	100.00	1.82	0.840	0.39
PL1.1	42.51	0.020	1.83	0.23	8.28	0.132	44.76	1.95	0.06	<dl	0.219	<dl	100.00	2.82	0.844	5.76
PL1.6	44.72	0.065	3.08	0.35	7.80	0.134	40.34	3.02	0.20	0.05	0.210	0.021	100.00	2.29	0.838	5.08
PRE-A	44.71	0.028	2.26	0.29	7.55	0.130	42.13	2.59	0.10	<dl	0.209	<dl	100.00	2.54	0.848	6.07
SB3.4	43.78	0.051	2.97	0.30	8.29	0.134	41.48	2.56	0.19	0.03	0.198	<dl	100.00	2.15	0.833	2.88
MR141B	45.65	0.044	2.43	0.35	8.22	0.128	40.03	2.60	0.22	0.03	0.285	0.021	100.00	1.39	0.830	1.92
SBA2	45.04	0.047	2.16	0.24	8.37	0.141	41.15	2.38	0.16	<dl	0.291	0.010	100.00	1.35	0.831	0.46
SBA4	43.56	0.054	2.13	0.35	8.30	0.131	43.36	1.66	0.15	0.03	0.275	<dl	100.00	1.66	0.839	0.40
WG1	44.91	0.044	2.32	0.33	8.61	0.143	40.91	2.25	0.18	0.02	0.284	<dl	100.00	1.97	0.826	5.53
WG4	43.08	0.079	2.54	0.35	8.17	0.131	43.04	2.08	0.23	0.05	0.234	0.010	100.00	1.76	0.840	0.87
Avg. UZ	44.67	0.047	2.52	0.35	8.03	0.131	41.43	2.34	0.18	0.05	0.251	0.025	100.00	1.88	0.837	

Oxides are recalculated to 100% anhydrous composition.

FeO^{total} is recalculated as total iron from measured FeO and Fe_2O_3.

$Cr_2O_3^{calc}$ and NiO^{calc} are recalculated from Cr and Ni trace element concentrations.

Mg# = MgO/(MgO+FeO). LOI, loss of ignition.

dl: detection limit.

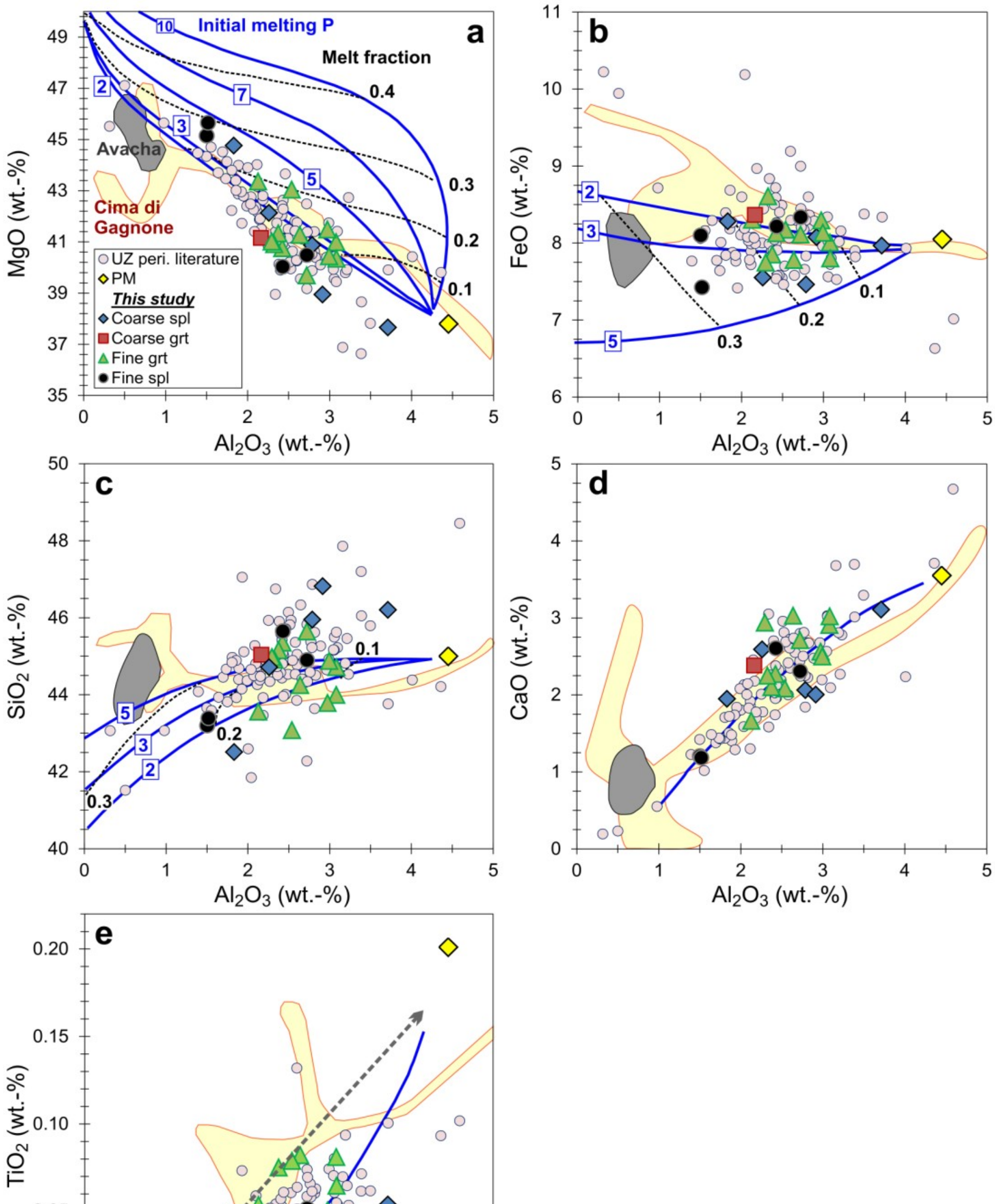

Figure 2.2. Whole-rock co-variation plots of major oxides (a) MgO, (b) FeO, (c) SiO_2, (d) CaO and (e) TiO_2 vs. Al_2O_3 in UZ peridotites in this study compared to literature data for UZ peridotites (Herzberg et al., 1977; Rost & Brenneis, 1978; Obata & Morten, 1987; Bondi et al., 1992; Bargossi et al., 2003; Marocchi et al., 2007, 2009; Tumiati et al., 2007; Sapienza et al., 2009; Gudelius, 2015; Ionov et al., 2017). Shown for comparison are subduction-related peridotite xenoliths from the Avacha volcano in Kamchatka (Ionov, 2010) and from Cima di Gagnone (Scambelluri et al., 2014). The reported compositions are recalculated to 100% anhydrous peridotite. Primitive mantle (PM) compositions after McDonough & Sun (1995). Full blue lines labeled with squares in (a-c) show model residues with initial melting pressures in GPa, black dotted lines indicate melt fractions (Herzberg, 2004). Full blue lines in (d,e) indicate model melting residues for isobaric batch melting calculated by Niu (1997). Dashed arrow in (e) indicates a straight mixing line which would be the result of peridotite refertilization.

Table 2.3 Trace element concentrations in Ulten Zone whole-rock peridotites determined by ICP-MS (in ppm).

	KBA8	KL1.2-1	KL2.2	Ko2C	Ko2F	MBS2	MBS6	MOL1.3	MOL1.5	P10A	P10B	P10C	P11	PL1.1	PL1.6	PRE-A	SB3.4	MR141B	SBA2	SBA4	WG1	WG4	dl
Sc	13	11	11	15	12	14	8	8	13	12	14	16	10	10	14	12	13	13	13	11	11	12	1
V	65	65	60	68	55	62	36	38	71	57	67	58	56	42	66	53	63	61	55	45	54	56	5
Cr	2240	2050	2400	2860	2530	2690	2280	2000	3000	2780	2830	3000	2380	1470	2290	1850	2020	2320	1620	2350	2110	2350	20
Co	99	93	103	98	99	92	102	106	93	110	106	107	100	96	95	90	93	104	109	110	101	107	1
Ni	1640	1530	2210	2140	2030	1500	1750	1810	1890	2250	2190	2170	2130	1610	1560	1540	1510	2170	2220	2130	2090	1820	20
Cu	20	40	<dl	3680	<dl	<dl	<dl	<dl	<dl	20	20	20	20	30	30	<dl	10	<dl	10	20	30	10	10
Zn	50	50	40	2430	60	50	70	40	90	50	60	70	50	<dl	50	40	50	60	70	50	50	60	30
Rb	<dl	<dl	2	2	3	1.6*	1.2*	1	1.5*	2	2	2	2	<dl	1	<dl	<dl	2	<dl	1.2*	1	1.3*	1/0.1*
Sr	23	37	30	15	28	3*	16*	14	10*	23	26	25	48	5	39	5	8	22	3	15*	19	21*	2/1*
Y	2.2	1.6	1.3	2	1.7	0.8	0.6	<dl	1.5	1.6	1.7	2	2.7	0.8	1.9	1.2	1.6	1.5	1.7	1.4	3.2	1.6	0.5
Zr	9	7	3	2	3	3	3	5	4	7	3	3	16	2	13	5	5	2	<dl	5	1	8	1
Nb	0.3	0.4	0.6	0.6	0.7	<dl	<dl	<dl	0.5	0.7	0.7	0.6	1.1	<dl	<dl	<dl	<dl	0.6	<dl	0.4	0.4	<dl	0.2
Cs	<dl	0.1	0.6	0.2	0.3	0.2	0.1	<dl	0.2	0.2	0.2	0.2	0.2	<dl	0.2	<dl	0.1	0.3	0.3	<dl	0.3	<dl	0.1
Ba	43	73	71	20	72	9	23	19	19	49	51	48	89	7	93	16	23	46	17	37	55	51	2
La	0.42	0.85	2.22	1.33	2.27	<dl	0.87	1.22	0.64	2.06	2.02	1.89	3.37	0.48	2.18	1.33	0.70	2.19	0.50	0.75	3.47	1.47	0.05
Ce	1.50	2.31	3.93	2.05	4.12	<dl	1.59	1.93	1.51	3.71	3.72	3.16	6.05	0.58	4.26	1.65	1.21	4.30	0.65	1.84	5.18	2.59	0.05
Pr	0.22	0.34	0.41	0.21	0.50	<dl	0.15	0.16	0.16	0.39	0.40	0.32	0.72	0.04	0.49	0.13	0.14	0.49	0.08	0.22	0.52	0.27	0.01
Nd	1.04	1.66	1.53	0.77	1.89	<dl	0.53	0.44	0.73	1.44	1.46	1.10	3.02	0.06	1.77	0.34	0.56	1.50	0.47	0.84	1.72	1.29	0.05
Sm	0.28	0.38	0.33	0.21	0.41	<dl	0.11	0.04	0.18	0.26	0.35	0.29	0.51	0.02	0.38	0.06	0.13	0.30	0.20	0.16	0.34	0.27	0.01
Eu	0.093	0.140	0.085	0.081	0.095	0.007	0.034	0.017	0.043	0.061	0.088	0.081	0.044	0.016	0.098	0.022	0.050	0.093	0.049	0.065	0.093	0.092	0.005
Gd	0.34	0.41	0.20	0.24	0.31	0.05	0.12	0.05	0.15	0.14	0.19	0.20	0.37	0.06	0.30	0.11	0.19	0.23	0.17	0.19	0.30	0.27	0.01
Tb	0.06	0.05	0.04	0.05	0.05	0.01	0.02	<dl	0.04	0.03	0.04	0.04	0.06	0.01	0.05	0.03	0.04	0.04	0.04	0.03	0.07	0.05	0.01
Dy	0.38	0.30	0.22	0.34	0.27	0.11	0.09	0.06	0.26	0.23	0.29	0.32	0.39	0.11	0.33	0.20	0.28	0.26	0.29	0.23	0.44	0.31	0.01
Ho	0.08	0.06	0.05	0.08	0.06	0.03	0.02	0.01	0.05	0.05	0.07	0.08	0.09	0.03	0.07	0.04	0.06	0.06	0.07	0.05	0.10	0.06	0.01
Er	0.27	0.19	0.16	0.29	0.21	0.09	0.06	0.05	0.15	0.21	0.22	0.26	0.27	0.10	0.21	0.14	0.19	0.18	0.23	0.17	0.31	0.19	0.01
Tm	0.042	0.030	0.026	0.050	0.036	0.017	0.010	0.010	0.026	0.033	0.038	0.045	0.040	0.015	0.034	0.025	0.028	0.032	0.041	0.025	0.048	0.027	0.005
Yb	0.29	0.19	0.18	0.36	0.24	0.12	0.06	0.08	0.18	0.21	0.24	0.29	0.26	0.10	0.24	0.18	0.19	0.22	0.28	0.17	0.35	0.18	0.01
Lu	0.044	0.028	0.028	0.053	0.038	0.021	0.010	0.013	0.027	0.031	0.036	0.045	0.037	0.015	0.035	0.027	0.029	0.033	0.044	0.026	0.051	0.028	0.002
Hf	0.2	0.1	0.2	0.2	0.2	<dl	<dl	<dl	0.1	0.3	0.2	0.1	0.4	<dl	0.3	<dl	<dl	0.1	0.1	<dl	0.2	0.1	0.1
Ta	0.06	0.04	0.29	0.28	0.27	<dl	0.02	<dl	0.51	0.31	0.29	0.30	0.58	<dl	0.02	<dl	<dl	0.32	0.28	<dl	0.29	0.02	0.01
Pb	<dl	<dl	<dl	128	<dl	0.2*	0.8*	<dl	1.4*	<dl	<dl	5	5	<dl	<dl	<dl	<dl	<dl	<dl	0.8*	<dl	1.9*	5/0.1*
Th	0.08	0.11	0.25	0.29	0.38	<dl	0.13	0.18	0.13	0.43	0.33	0.33	0.48	0.10	0.58	0.16	0.18	0.37	0.16	0.14	0.80	0.13	0.05
U	0.04	0.07	0.14	0.15	0.13	0.03	0.16	0.09	0.07	0.17	0.16	0.15	0.46	0.05	0.17	0.07	0.06	0.18	0.06	0.07	0.11	0.10	0.01
Th/U	2.00	1.57	1.79	1.93	2.92	na	0.81	2.00	1.86	2.53	2.06	2.20	1.04	2.00	3.41	2.29	3.00	2.06	2.67	2.00	7.27	1.30	5

dl: detection limit.

*Results from trace element analyses using Total Digestion ICP/MS with lower detection limits for Rb, Sr and Pb.

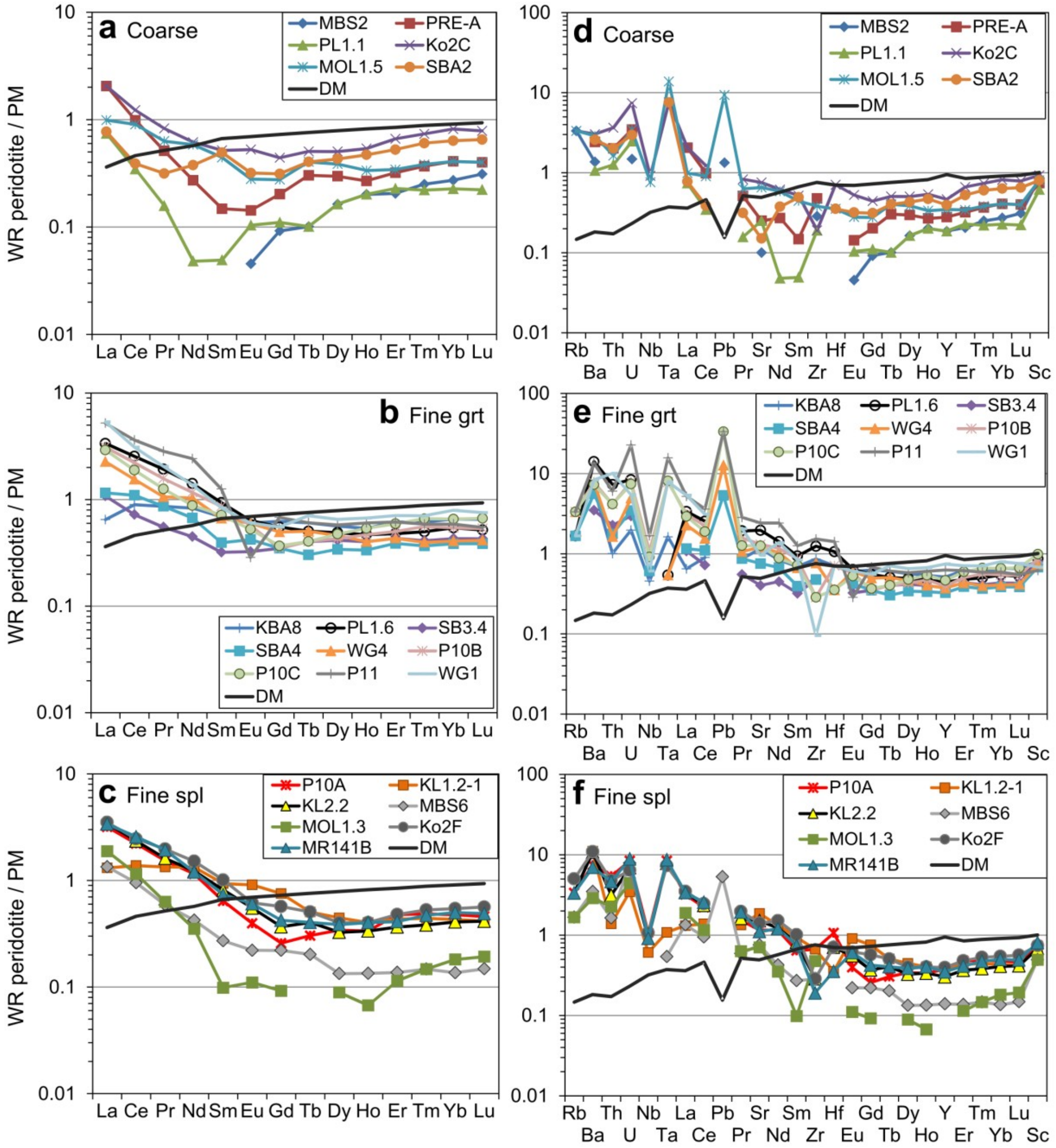

Figure 2.3. Primitive mantle-normalized (McDonough & Sun, 1995) trace element abundances of whole-rock UZ peridotites for (a,d) coarse-grained spinel peridotites and one coarse-grained garnet peridotite; (b,e) fine-grained garnet-amphibole peridotites and (c,f) fine-grained garnet-free peridotites. Left column: REE patterns, right column: extended trace element patterns. Note that the exceptionally high Pb concentration of the coarse-grained sample Ko2C is not shown in (d). Depleted mantle (DM) composition after Salters & Stracke (2004).

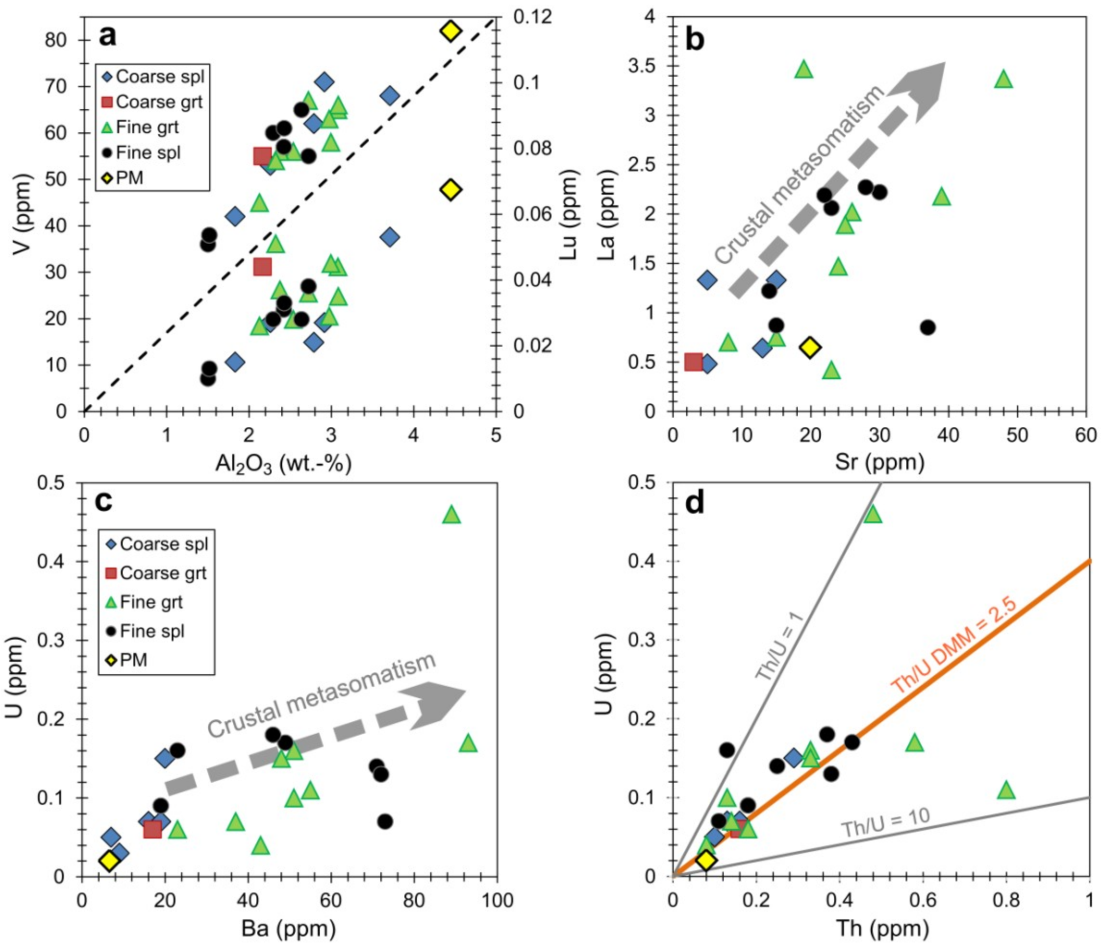

Figure 2.4. Covariation plots of selected trace elements for Ulten Zone peridotites. (a) Al_2O_3 vs. V and Lu shows positive correlations, consistent with the moderately incompatible behavior of V and Lu (representative for HREE) during melt extraction. (b) Sr vs. La shows a general positive correlation emphasized by the fine-grained hydrated peridotites which generally exhibit elevated concentrations of Sr and La relative to the coarse-grained peridotites. (c) Ba vs. U shows a positive correlation in the coarse-grained peridotites as well as in the fine-grained peridotites which are enriched in Ba compared to the former. (d) Th vs. U shows a general positive correlation in all peridotites which mostly exhibit Th/U ratios <DMM, consistent with fluid-mediated enrichment in U. DMM ratio from Workman & Hart (2005), PM from McDonough & Sun (1995).

2.4.3 Bulk-rock isotopic compositions

Whole-rock isotopic compositions for Nd, Sr and Hf are reported in Table 2.4, Pb isotopic compositions are listed in Table 2.5. Isotope covariation plots and isochron diagrams are shown in Figures 2.5-2.8. Present-day isotopic compositions were determined for four coarse-grained spinel peridotites, one coarse-grained garnet-bearing peridotite, five fine-grained garnet-amphibole peridotites and one fine-grained spinel peridotite from the UZ. ^{176}Hf/^{177}Hf was determined on only seven samples due to the low concentration of Hf in some samples (Table 2.4). The UZ peridotites display highly variable isotopic ratios with ^{176}Hf/^{177}Hf ranging from 0.282873 to 0.283743 (εHf = +3.49 to + 34.28) and ^{143}Nd/^{144}Nd ratios between 0.512127 and 0.514377 (εNd = -9.97 to +33.92). The most radiogenic Hf isotopic composition is shown by the coarse-grained sample MOL1.5, whereas the fine-grained peridotites are characterized by less radiogenic compositions (Figure 2.5a). Interestingly, sample MOL1.5 and another coarse-grained sample LP6 have unradiogenic Nd compositions, whereas another coarse-grained sample LP8 shows a highly radiogenic Nd composition (Figure 2.5b). The fine-grained samples have a narrower compositional range in the Sm-Nd isochron diagram, at unradiogenic Nd compositions. Calculated Depleted Mantle model ages $T_{DM,Nd}$ range from 342 Ma for sample LP8 to 1439 Ma for the fine-grained spinel-bearing peridotite MBS6 (Table 2.4), while $T_{DM,Hf}$ are highly variable and seem implausible (Table 2.4). Calculated Nd T_{CHUR} model ages range from 238 Ma (sample WG4) to 1444 Ma (sample MOL1.5), while plausible Hf T_{CHUR} model ages were only obtained for three fine-grained garnet-amphibole peridotites (1155 Ma for sample U8, 1325 Ma for sample U13 and 1658 Ma for sample WG4; Table 2.4). Strontium isotopic compositions are also highly variable (^{87}Sr/^{86}Sr from 0.704348 to 0.714340) with the most radiogenic compositions exhibited by coarse-grained sample MBS2 (Figure 2.5c). The ^{206}Pb/^{204}Pb ratio ranges from 17.5771 to 18.7152, ^{207}Pb/^{204}Pb varies between 15.5512 and 15.6486 and ^{208}Pb/^{204}Pb ranges from 37.5035 and 38.5408 (Table 2.5). The UZ peridotites show variable Pb isotopic compositions with three fine-grained garnet-amphibole peridotites displaying less radiogenic Pb compositions compared to the other samples (Figure 2.5d-f).

Initial isotopic compositions were calculated for 330 Ma, the inferred time of isotopic homogenization of all UZ rock types associated with peridotite insertion into the crustal host rocks (Tumiati et al., 2003), although it is not ascertained that this age applies to all petrographic types which are potential recorders of different metasomatic events in the UZ evolution.

Age calculations were performed using *Isoplot* (Ludwig, 2008) on the new samples in this study and in previous studies (Tumiati et al., 2003; Gudelius, 2015). In the Lu-Hf isochron diagram, combined fine-grained garnet-amphibole peridotites define a linear correlation, yielding a poorly defined age of 786 ± 300 Ma, with an initial ε_{Hf} of +3.41 (MSWD = 1837), implying imperfect isotopic homogenization during interaction of a depleted mantle with melts or fluids at this time. The coarse-grained peridotites which define a linear correlation in the Sm-Nd isochron diagram at relatively radiogenic Nd compositions (excluding the outlying less radiogenic samples LP6 and MOL1.5) yield an age of 409 ± 38 Ma, with an initial ε_{Nd} of +6.42 (MSWD = 60) (Figure 2.6a). The fine-grained samples form a trend towards unradiogenic Nd at relatively invariable Sm-Nd, precluding regression and also casting doubt on the geological meaning of calculated model ages. The coarse-grained samples which define a linear correlation in the ^{206}Pb/^{204}Pb vs. ^{207}Pb/^{204}Pb space, yield a poorly defined age of 1539 ± 810 Ma (MSWD = 3826) (Figure 2.6b), which is similar (1394 ± 330 Ma, MSWD = 3907) when considering all samples (coarse-grained and fine-grained).

Table 2.4 Whole-rock Sm-Nd-, Rb-Sr- and Lu-Hf-isotope composition for Ulten Zone peridotites.

Sample	LP6	LP8	MBS2	MOL1.5	ULT8	SBA4	U8	U13	U15	WG4	MBS6
Type	Coarse spl	Coarse spl	Coarse spl	Coarse spl	Coarse grt	Fine grt	Fine grt	Fine grt	Fine grt	Fine grt	Fine spl
Measured ratio											
^{143}Nd/^{144}Nd (± 2σ)	0.512127 (± 3)	0.513915 (± 9)	0.514377 (± 15)	0.512186 (± 5)	0.513801 (± 5)	0.512501 (± 13)	0.512465 (± 2)	0.512348 (± 8)	0.512383 (± 2)	0.512529 (± 1)	0.512319 (± 8)
Sm (ppm)^1	0.027	0.013	<dl	0.18	na	0.16	0.265	0.089	0.220	0.27	0.11
Nd (ppm)^1	0.17	0.01	<dl	0.73	na	0.84	1.59	0.51	1.07	1.29	0.53
^{147}Sm/^{144}Nd (calculated)	0.092254	0.554852	na	0.149081	na	0.115163	0.100625	0.106319	0.124545	0.126546	0.125485
εNd	-9.97	24.91	33.92	-8.81	22.68	-2.67	-3.37	-5.65	-4.97	-2.13	-6.23
$t_{DM,Nd}$ (Ma)^2	1286	342	na	2273	na	1007	926	1141	1314	1090	1439
$t_{CHUR,Nd}$ (Ma)^2	747	544	na	1444	na	257	275	489	539	238	684
^{87}Sr/^{87}Sr (± 2σ)	0.707707 (± 3)	0.706978 (± 6)	0.714340 (± 3)	0.707466 (± 55)	0.705394 (± 3)	0.705906 (± 3)	0.704348 (±6)	0.707590 (± 3)	0.710107 (± 3)	0.705728 (± 3)	0.707518 (± 3)
Rb (ppm)^1	0.38	0.16	1.6	1.5	na	1.2	0.64	0.36	1.68	1.3	1.2
Sr (ppm)^1	5.5	4.2	3	10	na	15	26.7	11.2	37.8	21	16
^{87}Rb/^{86}Sr (calculated)	0.203223	0.106346	1.543249	0.434039	na	0.231487	0.069502	0.092384	0.128795	0.179127	0.217019
^{176}Hf/^{177}Hf (± 2σ)	na	na	na	0.283743 (± 17)	na	0.282986 (± 10)	0.283145 (± 16)	0.282911 (± 16)	0.282873 (± 8)	0.282985 (± 6)	0.282997 (± 42)
Lu (ppm)^1	0.022	0.026	0.021	0.027	na	0.026	0.015	0.013	0.031	0.028	0.010
Hf (ppm)^1	0.005	0.006	<dl	0.1	na	<dl	0.042	0.046	0.128	0.1	<dl
εHf	na	na	na	34.28	na	7.50	13.11	4.85	3.49	7.45	7.89
^{176}Lu/^{177}Hf (calculated)	0.579079	0.653756	na	0.038487	na	na	0.050216	0.038681	0.034234	0.039913	na
$t_{DM,Hf}$ (Ma)^2	na	na	na	-40825	na	418	-741	24872	4260	-40571	403
$t_{CHUR,Hf}$ (Ma)^2	na	na	na	9025	na	-344	1155	1325	4884	1658	-362
Age-corrected ratio (330 Ma)					na						
^{143}Nd/^{144}Nd$_i$	0.511927	0.512716	na	0.511864	na	0.512252	0.512248	0.512119	0.512114	0.512256	0.512048
εNd$_i$	-5.57	9.82	na	-6.81	na	0.76	0.68	-1.84	-1.93	0.83	-3.23
^{87}Sr/^{86}Sr$_i$	0.706753	0.706479	0.707092	0.705427	na	0.704819	0.704022	0.707156	0.709502	0.704887	0.706498
εSr$_i$	37.64	33.75	42.46	18.82	na	10.18	-1.14	43.38	76.69	11.14	34.03
^{176}Hf/^{177}Hf$_i$	na	na	na	0.283506	na	na	0.282835	0.282672	0.282661	0.282738	na
εHf$_i$	na	na	na	33.15	na	na	9.40	3.66	3.26	5.99	na

[1] Elemental abundances taken from ICP-MS trace element analyses reported in Table 3.

[2] tDM is depleted mantle model age; tCHUR is Chondritic Uniform Reservoir model age.

Decay constants for ^{147}Sm = 6.54 x 10^{-12} a^{-1} (Lugmair & Marti, 1978), for ^{87}Rb = 1.42 x 10^{-11} a^{-1} (Steiger & Jäger, 1977) and for ^{176}Lu = 1.865 x 10^{-11} a^{-1} (Nir-El & Lavi, 1998).

Present-day CHUR values are ^{143}Nd/^{144}Nd = 0.512638, ^{147}Sm/^{144}Nd = 0.1967 (Jacobsen & Wasserburg, 1980), ^{87}Sr/^{86}Sr = 0.7045, ^{87}Rb/^{86}Sr = 0.0847 (McCulloch & Black, 1984; DePaolo, 1988), ^{176}Hf/^{177}Hf = 0.282774, ^{176}Lu/^{177}Hf = 0.0332 (Blichert-Toft & Albarède, 1997).

Present-day DM values are ^{143}Nd/^{144}Nd = 0.513151, ^{147}Sm/^{144}Nd = 0.2135 (Blichert-Toft & Puchtel, 2010), ^{176}Hf/^{177}Hf = 0.283294, ^{176}Lu/^{177}Hf = 0.03933 (Vervoort & Blichert-Toft, 1999).

All errors 2σ relate to the last significant digits.

na: not available.

Table 2.5 Whole-rock U-Pb-isotope composition of Ulten Zone peridotites.

Sample	Th (ppm)[1]	U (ppm)[1]	Pb (ppm)[1]	$^{206}Pb/^{204}Pb$ (± 2σ)	$^{238}U/^{206}Pb$ (calculated)	$^{207}Pb/^{204}Pb$ (± 2σ)	$^{235}U/^{207}Pb$ (calculated)	$^{208}Pb/^{204}Pb$ (± 2σ)	$^{232}Th/^{208}Pb$ (calculated)	Age-corrected ratio (330 Ma)		
										$(^{206}Pb/^{204}Pb)_i$	$(^{207}Pb/^{204}Pb)_i$	$(^{208}Pb/^{204}Pb)_i$
U8	0.146	0.043	0.603	18.2938 (± 2)	0.2551	15.5930 (± 2)	0.0020	38.2672 (± 6)	0.4132	18.280	15.592	38.260
U13	0.099	0.045	2.933	17.5771 (± 3)	0.0551	15.5571 (± 4)	0.0004	37.5769 (± 15)	0.0573	17.574	15.557	37.576
U15	0.304	0.192	3.686	17.6604 (± 6)	0.1869	15.5590 (± 7)	0.0015	37.5035 (± 22)	0.1407	17.651	15.558	37.501
LP6	0.056	0.037	1.046	18.4885 (± 2)	0.1261	15.6199 (± 2)	0.0010	38.3706 (± 5)	0.0916	18.482	15.620	38.369
LP8	0.006	0.009	0.941	18.2318 (± 2)	0.0337	15.6028 (± 2)	0.0003	38.2159 (± 4)	0.0107	18.230	15.603	38.216
MOL1.5	0.130	0.070	1.400	18.4157 (± 3)	0.1793	15.6138 (± 4)	0.0014	38.3822 (± 8)	0.1582	18.406	15.613	38.380
MBS2	<dl	0.030	0.200	18.7152 (± 2)	0.5379	15.6486 (± 2)	0.0043	38.5408 (± 5)	na	18.687	15.647	na
MBS6	0.130	0.160	0.800	18.3996 (± 5)	0.7172	15.6230 (± 6)	0.0057	38.3023 (± 21)	0.2769	18.362	15.621	38.298
SBA4	0.140	0.070	0.800	17.6917 (± 2)	0.3138	15.5512 (± 2)	0.0025	37.5116 (± 8)	0.2982	17.675	15.550	37.507
WG4	0.130	0.100	1.900	18.4151 (± 2)	0.1887	15.6199 (± 2)	0.0015	38.2811 (± 5)	0.1166	18.405	15.619	38.279
ULT8	na	na	na	18.4494 (± 2)	na	15.6149 (± 2)	na	38.4645 (± 5)	na	na	na	na

[1] Elemental abundances taken from ICP-MS trace element analyses reported in Table 3.

Decay constants for $^{238}U = 1.55125 \times 10^{-10}\ a^{-1}$, for $^{235}U = 9.8485 \times 10^{-10}\ a^{-1}$ and for $^{232}Th = 4.9475 \times 10^{-11}\ a^{-1}$ (Holmes, 1946; Houtermans, 1946).

All errors 2σ relate to the last significant digits.

na: not available.

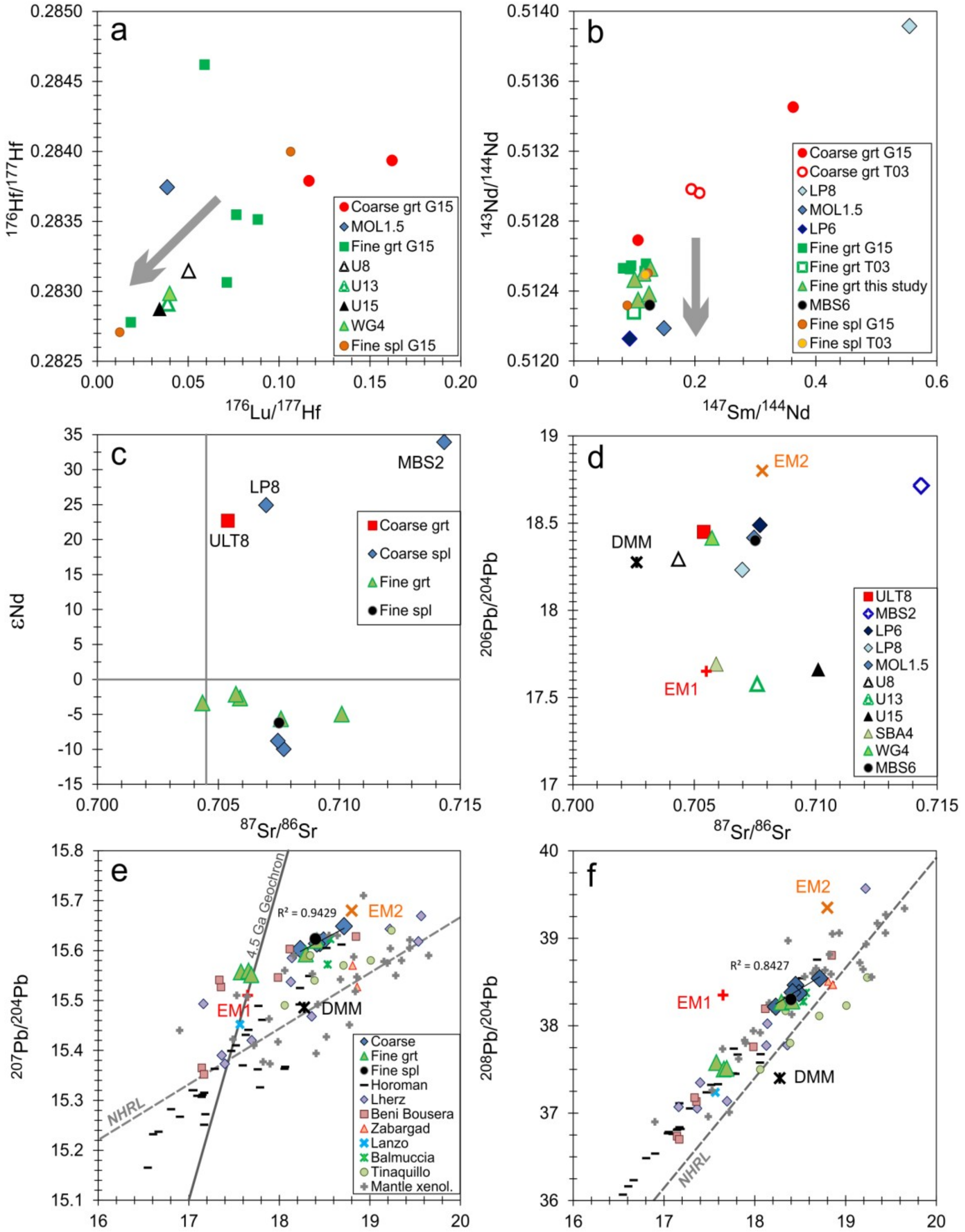

Figure 2.5. Covariation plots of whole-rock isotope compositions from this study. (a) ^{176}Hf/^{177}Hf vs. ^{176}Lu/^{177}Hf, (b) ^{143}Nd/^{144}Nd vs. ^{147}Sm/^{144}Nd, (c) εNd vs. ^{87}Sr/^{86}Sr, (d) ^{206}Pb/^{204}Pb vs. ^{87}Sr/^{86}Sr, (e) ^{207}Pb/^{204}Pb vs. ^{206}Pb/^{204}Pb, (f) ^{208}Pb/^{204}Pb vs. ^{206}Pb/^{204}Pb. In (a) and (b) data for UZ peridotites from previous studies are shown for comparison and extension of the sample set. Data from Tumiati et al. (2003; T03) and Gudelius (2015; G15). Arrows mark addition of unradiogenic Hf and Nd to the fine-grained peridotites and partly coarse-grained peridotites. In (e) and (f) Pb isotopic data of worldwide orogenic peridotites (Horoman (Japan): Malaviarachchi et al., 2008; Lherz (France), Beni Bousera (Morocco), Zabargad (Red Sea) and Lanzo (Italy): Hamelin & Allègre, 1988; Balmuccia (Italy): Mukasa & Shervais, 1999; Tinaquillo (Venezuela): Choi et al., 2007) and mantle xenoliths (South Korea: Choi et al., 2005; Spitsbergen (Norway): Ionov et al., 2002; Massif Central (France): Zangana et al., 1997; Canada: Schmidberger et al., 2001; Hungary and Romania: Rosenbaum et al., 1997) is shown for comparison. DMM values are taken from Workman & Hart (2005), EM1 and EM2 from Hart (1988). NHRL = Northern Hemisphere Reference Line (Hart, 1984).

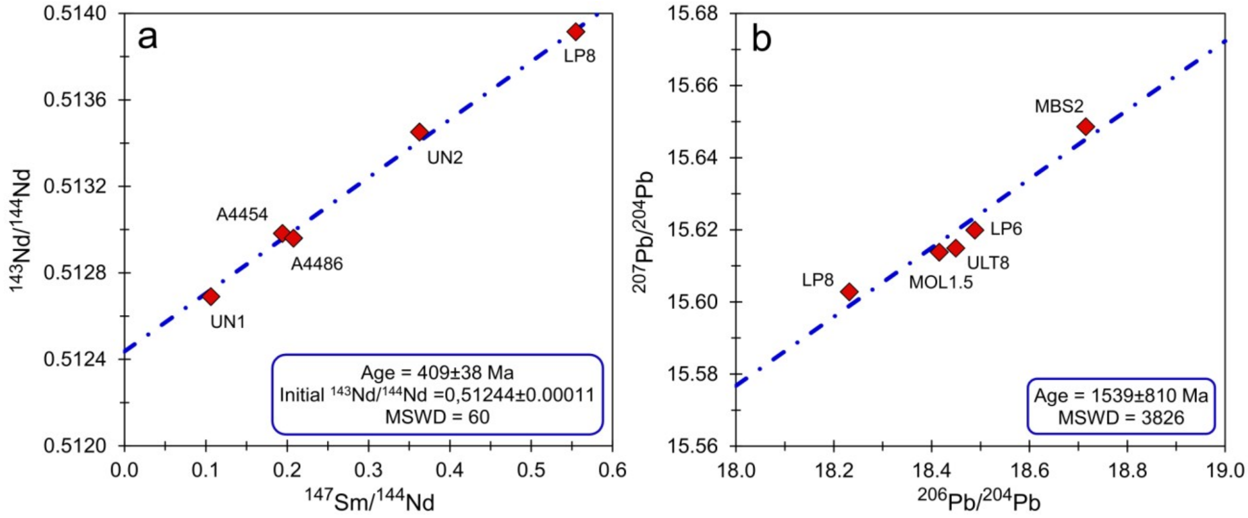

Figure 2.6. (a) Sm-Nd isochron of coarse-grained Ulten Zone peridotites examined in this study (LP8) and from Tumiati et al. (2003; A4454 and A4486) and Gudelius (2015; UN1 and UN2). (b) Plot of ^{207}Pb/^{204}Pb vs. ^{206}Pb/^{204}Pb of coarse-grained peridotites which define a linear correlation and were taken for age calculation.

2.5 Discussion

2.5.1 Conditions and timing of melt depletion and refertilization of UZ peridotites

According to the observations by Rampone & Morten (2001), the major-element variability of the UZ peridotites (Figure 2.2) is not correlated with the different petrographic types (coarse- vs. fine-grained) and metamorphic assemblages (garnet-bearing vs. garnet-free). These authors interpreted the variability to reflect primary compositional heterogeneities, i.e. different degrees of fertility/depletion of the mantle protoliths. The compositional trends exhibited by the UZ peridotites in terms of major elements (Figure 2.2) conform to trends which have been interpreted to reflect an origin as residues after various degrees of partial melting (Bodinier & Godard, 2014). Accordingly, all UZ peridotites have HREE compositions <DM (Figure 2.3), indicating apparent variable degrees of melt depletion. A tracer for melt extraction is the contents of Al_2O_3 (Pearson et al., 2003; Ionov & Hofmann, 2007). Ionov et al. (2017) interpreted the melt extraction trend of the UZ peridotites to show a moderately refractory character since the samples represent neither fertile (3.3 to 4.8 wt. % Al_2O_3) nor highly refractory (< 1 wt. % Al_2O_3) peridotites. These authors suggest that the protoliths of the UZ peridotites were formed by melt extraction, by ca. 10-20 % of polybaric melting in upwelling mantle beginning at 2-4 GPa during garnet stability and ending close to the surface in the stability field of spinel. The positive correlations of Al_2O_3 and the moderately incompatible trace elements, such as V and Lu (Figure 2.4a) likely preserve the records of low to moderate degree of melt extraction (Ionov et al. (2017). In contrast, fertile compositions of orogenic peridotites from the Western Gneiss region and from North Qaidam have been attributed to refertilization of highly depleted subcontinental mantle due to interaction with percolating silicate melts of basaltic composition (Beyer et al., 2006; Shi et al., 2010; Xiong et al., 2015).

More recently, the variability of the UZ peridotite whole-rock major-element composition has been interpreted to record refertilization, in which peridotites in the hot and shallow depleted mantle experienced interaction with a hydrous mafic melt, leading to enrichment in Li, some LILE and LREE in minerals forming the early spinel-facies assemblage of the UZ peridotites (Scambelluri et al., 2006). Such a process can produce refertilized peridotites with similar major element compositions compared to peridotites which experienced little or no depletion (Gudelius, 2015 and references therein). Refertilization is further indicated by the enrichment in SiO_2, as many of the samples plot above the experimental melting trends in the Al_2O_3 vs. SiO_2 diagram (Figure 2.2c), as observed also by Ionov et al. (2017). Gudelius (2015) observed positive correlations between whole-rock SiO_2 content with the abundances of ortho- and clinopyroxene, as well as a negative correlation between SiO_2 and the olivine abundance, whereby coarse-grained peridotites form the silica-rich end-member of the trend. In UZ peridotites, addition of SiO_2 and associated formation of orthopyroxene at the expense of olivine has previously been interpreted as a result of peridotite interaction with a silicic melt or Si-rich subduction fluids, although the exact mechanism of SiO_2 enrichment remains enigmatic (Malaspina et al., 2006; Ionov et al., 2017). This is in agreement with the highest SiO_2 contents displayed by three coarse-grained spinel peridotites of the new sample set in this study (Fig 2.2c), which are also rich in modal orthopyroxene and contain clinopyroxene (Figure 2.1a). Refertilization vs. melt depletion can be distinguished by plotting moderately incompatible elements, such as Al_2O_3 vs. TiO_2, where the former would result in a straight mixing line, whereas the latter would result in a concave trend (Niu, 1997). This shows that some UZ peridotites have Al_2O_3 vs. TiO_2-relationships more consistent with refertilization, whereas others (inclusive all coarse spinel peridotites) could reflect a primary melt depletion trend (Figure 2.2e). However, elevated Al_2O_3 concentrations may be also caused by addition of aluminous orthopyroxene from hot subduction-related melts, and the elevated SiO_2 contents of three coarse-grained peridotites preclude a primary melt depleted origin.

A corollary of the compositional trends displayed by the UZ peridotites, in part testifying to refertilization, is, that they cannot be indiscriminately used to estimate degrees or modes of melt depletion, and the melt extraction curves in Figure 2.2 can only be applied to samples that have not been modally metasomatized. Nevertheless, three samples of the new sample set (one coarse-grained peridotite PL1.1 and the two fine-grained spinel peridotites MBS6 and MOL1.3), which have the highest MgO and lowest Al_2O_3 of all samples studied so far (Figure 2.2a) in addition to low SiO_2 contents (Figure 2.2c), may record truly depleted compositions. According to the melt residue model of Herzberg (2004), these samples record minimum melt-depletion degrees of ca. 25-30 % at initial melting pressures of 3-5 GPa, that is, in the garnet stability field (Figure 2.2a). Consistent with their depleted major-element compositions, these three peridotites have also the lowest REE concentrations compared to the other peridotites in the respective petrographic groups (Figure 2.3). The lack of garnet and garnet pseudomorphs in the two fine-grained samples may imply that these samples derive from shallower depths in the mantle wedge and never entered garnet stability (Marocchi et al., 2007). The occurrence of peridotites derived from different depths of a mantle wedge is typical of a crust-mantle mélange formed in a subduction channel above submerging continental plates (Godard et al., 1996; Zheng, 2012). The coarse-grained spinel peridotite PL1.1 derives from the outcrop Malga Preghena were fine-grained garnet-amphibole peridotite is the dominant peridotite type. Although one coarse-grained orthopyroxene-rich sample (MBS2) with lower MgO and higher Al_2O_3 (40.87 wt. % and 2.79 wt. %, respectively) has similar low MREE to HREE concentrations as sample PL1.1, and LREE even below detection limit (Figure 2.3a), this discrepancy may indicate decoupling of major-element and trace-element systematic in this sample. This serves to highlight the consistent behavior of major and trace elements in the three “depleted” samples, implying that they were not subjected to re-enrichment that affected either major or trace elements.

Because of the decoupling of major and trace elements, it is possible that relatively fluid-immobile elements, such as Lu and Hf, retain their relatively melt-depleted characteristics (i.e. radiogenic Hf), from which age information can be obtained. Unfortunately, in particular the sample set of coarse-grained UZ peridotites is too Hf-poor to attempt analysis. Even though two fine-grained garnet-amphibole samples (U8 and U13) from the sample set reported in Ionov et al. (2017) show similar depleted major-element compositions, they yield implausible Depleted Mantle Hf model ages ($T_{DM,Hf}$) (Table 2.4). However, their Hf T_{CHUR} model ages of 1155 Ma (U8) and 1325 Ma (U13) are similar and broadly consistent with their Lu-Hf isochron age of ca. 1075 Ma, and with a $T_{CHUR,Nd}$ of 1444 Ma of depleted coarse-grained peridotite MOL1.5. If these ages are geologically meaningful, they may imply initial formation by depletion of primitive mantle, perhaps during assembly of the supercontinent Rodinia. An age array with ca. 550 Ma and radiogenic initial ε_{Hf} for a different sample set containing no coarse spinel peridotites was also interpreted to attest to a primitive mantle source which experienced depletion prior to Paleozoic isotopic re-equilibration, possibly related to an extensional event and partial melting in the mantle due to the break-up of the supercontinent Rodinia (Gudelius, 2015). The Lu-Hf model 3 isochron age defined by combined fine-grained garnet-amphibole peridotites (this study and Gudelius, 2015) which define a linear correlation (Figure 2.5a) is 786 ± 300 Ma. It must be noted, however, that the Lu-Hf system can be disturbed due to retrogression-related garnet breakdown as well as due to fluid-mediated addition of unradiogenic Hf (Gudelius, 2015), which is traditionally seen as fluid-immobile element (e.g. Kessel et al., 2005). In the UZ peridotites, fluid-mediated metasomatism caused (partial) breakdown of garnet and concomitant release of HREE, leading to redistribution of HREE between garnet and newly formed amphibole and HREE-incorporation in amphibole (Scambelluri et al., 2006; Sapienza et al., 2009; Gudelius, 2015). However, the loss of HREE due to garnet breakdown is larger than the HREE-gain of amphibole, which has been explained by fluid-mediated removal of HREE from the rock and/or by a dilution effect due to modal abundances of amphibole exceeding those of garnet (Gudelius, 2015). A regression through the three depleted samples U8, U13 and MBS6 in the Sm-Nd diagram does not yield any plausible age, indicating that the Sm-Nd system was disturbed during the evolution of the rocks by addition of crust-derived unradiogenic Nd (Gudelius, 2015; next section). Accordingly, these samples show, similarly to all other fine-grained peridotites, an offset to unradiogenic Nd compositions. This highlights that the radiogenic isotopic compositions do not necessarily mirror the apparently depleted character displayed by major and trace elements and reveals the calculated model ages to be geologically meaningless. The same is true for the Pb-Pb model ages (ca. 1.5 Ga) since the radiogenic Pb isotopic composition of the UZ peridotites (Figure 2.5d-f) and elevated concentrations of Pb, Th and U suggest subduction-related enrichment (e.g. Scambelluri et al., 2006).

The coarse-grained sample MOL1.5 contains radiogenic Hf (Figure 2.5a), similar to the two coarse-grained garnet-bearing peridotites (UN1, UN2) from Gudelius (2015). In contrast, this sample has unradiogenic Nd compositions, testifying to fluid ingress, which is mirrored by the high modal amphibole + dolomite abundance in this sample. Another coarse-grained sample (LP6) displays a similar Sm-Nd composition as sample MOL1.5 and contains even ca. 20 times less Hf, possibly testifying to its retaining relatively depleted compositions with regard to elements conventionally regarded as fluid-immobile, such as Lu and Hf. In contrast, while the Hf concentrations in the coarse-grained samples LP8 and MBS2 are similarly low or even below detection (Table 2.4), these two samples do retain also depleted Nd isotope signature (>DMM; Figure 2.5c), similar to the coarse-grained garnet-bearing peridotite ULT8 for which no elemental concentrations are available. Consistent with the depleted character, Sm and Nd concentrations in sample MBS2 are below detection, but the available data for sample LP8 permits calculation of the model ages $T_{CHUR,Nd}$ and $T_{DM,Nd}$, which are 544 Ma and 342 Ma, respectively (Table 2.4). These ages correspond to the suggested timing of isotopic re-equilibration at ca. 550 Ma (Gudelius, 2015) and to the ca. 330 Ma isotopic homogenization of all UZ rocks, which has been linked to migmatization at the high-pressure stage of the UZ peridotites (Tumiati et al., 2003). Given some evidence from Hf isotopes for formation from a Primitive Mantle source, discussed above, the DM age is considered minimum. Some coarse-grained garnet-bearing peridotites analyzed by Gudelius (2015) record depleted Hf and Nd compositions which were interpreted to be consistent with mantle residues after partial melting and largely unaffected by crustal metasomatism. These samples together with coarse-grained garnet-bearing peridotites from Tumiati et al. (2003) are linearly correlated, and sample LP8 conforms in this correlation as the most depleted end member (Figure 2.5b). Samples LP6 and MOL1.5 do not fit due to their less radiogenic Nd compositions. The age of 409 ± 38 Ma (Figure 2.6a) corresponds to the onset of the Variscan orogeny and the initial $^{143}Nd/^{144}Nd$ of the isochron is <DM but >CHUR at this time. If this age has significance, it may constrain the timing of isotopic re-equilibration after the Proterozoic partial melting event inferred from Hf isotopes. Similar ages were obtained from other coarse-grained peridotites from the UZ: a Sm-Nd garnet-whole-rock age of ca. 410 Ma (Thöni, 1999; Tumiati et al., 2003) and a Sm-Nd garnet-clinopyroxene age of 460 Ma (Tumiati et al., 2003). An age of ca. 470 Ma using the $^{207}Pb/^{206}Pb$ method on zircons in migmatized UZ gneisses was ascribed to an early crystallization of a magmatic protolith (Hauzenberger et al., 1993), whereas a younger zircon age (ca. 365 Ma) was ascribed to the Variscan high-grade metamorphism. These ages were interpreted to reflect incomplete isotope resetting of old protoliths during the subduction-related metamorphism (Tumiati et al., 2003). However, in view of the coincidence of this age with the onset of the Variscan orogeny, it may reflect the early interaction of the hot mantle wedge with metasomatic subduction-related hydrous melts, an event that has been recognized based on trace elements (Scambelluri et al., 2006) and which necessarily precedes the 330 Ma migmatization upon entrapment of the peridotites in the crustal portion of the subducting slab. In summary, the Lu-Hf and/or Sm-Nd isotope system can be argued to have remained largely undisturbed in some of the coarse-grained UZ peridotites. The combined sample sets from this study, Tumiati et al. (2003) and Gudelius (2015) can provide some - albeit imprecise - constraints on the timing of melt depletion (in the Proterozoic and potentially related to assembly of the Rodinian supercontinent) and imperfect isotopic re-homogenization at and after the onset of the Variscan orogeny.

2.5.2 Effects of fluid- and melt-mediated processes in continental subduction zones on multiple radiogenic isotope systematics

The trace-element compositions of the new UZ peridotite samples are consistent with previous studies (e.g. Rampone & Morten, 2001; Scambelluri et al., 2006; Ionov et al., 2017). All samples exhibit variable HREE-concentrations <DM (Figure 2.3), indicating variable degrees of partial melting. In contrast, the most incompatible trace elements distinguish the UZ peridotites with regard to the petrographic type. Trace element concentrations (Figures 2.3, 2.4) show that the majority of the fine-grained garnet-bearing and garnet-free peridotites are enriched in LREE (shown as example is La; Figure 2.4b) and LILE (Rb, Sr, Ba; Figure 2.4b,c) relatively to the coarse-grained samples. The lack of correlations of Al_2O_3 with these highly incompatible trace elements suggests that the addition of the incompatible elements was largely decoupled from the major elements. There is agreement that in the UZ, the input of LREE and LILE is owing to ingress of crust-derived aqueous fluid(s), leading to the crystallization of metasomatic phases, such as amphibole ± carbonates ± apatite (e.g. Rampone & Morten, 2001; Scambelluri et al., 2006; Marocchi et al., 2007; Sapienza et al., 2009; Förster et al., 2017). Fluid-assisted metasomatism is also depicted by the variable but low Th/U ratios (<DMM; Figure 2.4d), the variability of which has been interpreted to be caused by inhomogeneities in the fluid source (Gudelius, 2015). Some metasomatism may have already occurred during peridotite residence in the mantle wedge prior to insertion into the crustal host rocks (Scambelluri et al., 2006), but certainly accompanied peridotite emplacement in the crustal rocks and subsequent exhumation of the crust-peridotite association starting at ca. 330 Ma (Tumiati et al., 2003; Scambelluri et al., 2006; Braga & Sapienza, 2007; Marocchi et al., 2007; Sapienza et al., 2009). While the fine-grained recrystallized and hydrated UZ peridotites were strongly affected by this fluid-mediated metasomatism, the U-shaped REE patterns, with concentrations of the lightest REE >DM (Figure 2.3a), of the coarse-grained peridotites in this study, indicates partial enrichment in incompatible elements. This is in accordance to previous studies (e.g. Scambelluri et al., 2006; Gudelius, 2015; Ionov et al., 2017). Such U-shaped REE patterns have been interpreted to be the result of weak metasomatism of a relatively fertile peridotite by a LREE-enriched fluid or melt and chromatographic effects of porous melt flow at a farther distance from the melt source (Bodinier et al., 1990; Ionov et al., 2002; Gudelius, 2015) resulting in selective LREE-enrichment, as seen in some of the coarse-grained peridotites of this study (Figure 2.3a) and from Ionov et al. (2017; samples LP6 and LP8). However, variable HREE-concentrations <DM (Figure 2.3b,c) shown by the coarse-grained peridotites, but also by all fine-grained peridotites, indicate that these peridotites derive from an initially depleted mantle.

The strong enrichment of the fine-grained peridotites in LREE and LILE is also reflected by the striking offset to more unradiogenic Nd compositions at low ^{147}Sm/^{144}Nd ratios (<DM; Figure 2.5b) relative to the linear correlation of most of the coarse-grained peridotites with more radiogenic compositions (e.g. LP8). Selective LREE- and LILE-enrichment in some coarse-grained peridotites is evidenced by the similarly unradiogenic Nd compositions of some samples of this type (LP6 and MOL1.5). The absence of a correlation of present-day ^{143}Nd/^{144}Nd with ^{147}Sm/^{144}Nd testifies to disturbance of the Sm-Nd system due to introduction of unradiogenic crustal Nd (Tumiati et al., 2003; Gudelius, 2015). As discussed above, the fine-grained UZ peridotites analyzed in this study show a linear correlation of ^{167}Lu/^{177}Hf with ^{176}Hf/^{177}Hf, and their ^{176}Hf/^{177}Hf ratios are <DM, as observed also by Gudelius (2015) and interpreted to indicate metasomatic Hf addition. Thus, the Sm-Nd and Lu-Hf systems in the fine-grained peridotites (and some coarse-grained peridotites) were apparently disturbed. In this context, Gudelius (2015) observed that a decrease in ^{176}Lu/^{177}Hf is not only restricted to input of unradiogenic Hf, but can be also caused by progressive garnet breakdown and concomitant Lu- (HREE-) removal from the rock during retrogression. A ^{176}Hf/^{177}Hf vs. 1/Hf diagram (Figure 2.7a) shows that samples U15 and WG4, which contain garnet with kelyphite rims and/or pseudomorphs after garnet, have the highest Hf concentrations of the new sample set and low ^{176}Hf/^{177}Hf ratios as well as low ^{176}Lu/^{177}Hf ratios (Figure 2.5a). This may testify to addition of unradiogenic Hf concomitant with removal of both Lu and Hf through garnet breakdown during retrogression. In contrast, sample U8, which contains unaltered garnets, displays the lowest Hf concentrations and the highest isotopic ratios, whereas the strongly retrogressed sample U13 has similar low Hf concentrations but lower isotopic ratios, indicating the superposition of several processes (garnet break-down plus variable addition of unradiogenic Hf), which explains the lack of coherence in the isochron diagram. In summary, to obtain age data from Lu-Hf isotopes, a case-by-case study together with petrographic and elemental indicators, is required.

Interestingly, the ^{147}Sm/^{144}Nd and ^{143}Nd/^{144}Nd ratios (Figure 2.7b) of the fine-grained garnet-amphibole peridotites show some correlation with the modal abundance of amphibole and the degree of retrogression. The slightly retrogressed samples WG4 and SBA4 contain less amphibole and show higher Nd isotopic ratios than the similarly retrogressed sample U8 which has the highest amphibole mode (24.3 wt. %, Ionov et al., 2017). Although the retrogressed sample U13 contains less amphibole than U8, it shows a lower ^{143}Nd/^{144}Nd ratio but no decrease in the ^{147}Sm/^{144}Nd ratio, what may suggest that both Sm and Nd were introduced during retrogression. Sample U15 contains abundant amphibole and is very little retrogressed but the ^{143}Nd/^{144}Nd ratio is low similar to that of sample U13. Given the greater efficiency with which the metasomatic agent(s) are expected to overprint Sm-Nd isotopes in peridotites, retention of some coherence in the coarse-grained peridotites at depleted compositions (Figure 2.5b) is surprising, but consistent with their concave-upward trace element patterns.

In a εHf_i vs. εNd_i diagram (Figure 2.7c), two fine-grained garnet-amphibole peridotites U8 and WG4 plot in the first quadrant with both radiogenic Nd and Hf composition relatively to CHUR, consistent with the majority of the samples of Gudelius (2015). The samples U13 and U15 plot in the fourth quadrant with radiogenic Hf but unradiogenic Nd composition, the same is true for the coarse-grained sample MOL1.5 which deviates strongly from the mantle array. As discussed above, this decoupling can be interpreted as substantial input of unradiogenic Nd related to the high amphibole + dolomite abundance, whereas the Lu-Hf system remained largely undisturbed. However, all fine-grained garnet-amphibole peridotites analyzed in this study display slight derivation from the mantle array, which is stronger in εHf-εNd isotope space (Figure 2.7d), indicating decoupling of Hf and Nd isotopes from the main metasomatic stage at 330 Ma to present-day. The observation that sample U13 does not have the lowest εNd_i but evolved to the least radiogenic present-day Nd, indicates that the Sm-Nd ratio was lowered during retrogression, as observed also by Gudelius (2015).

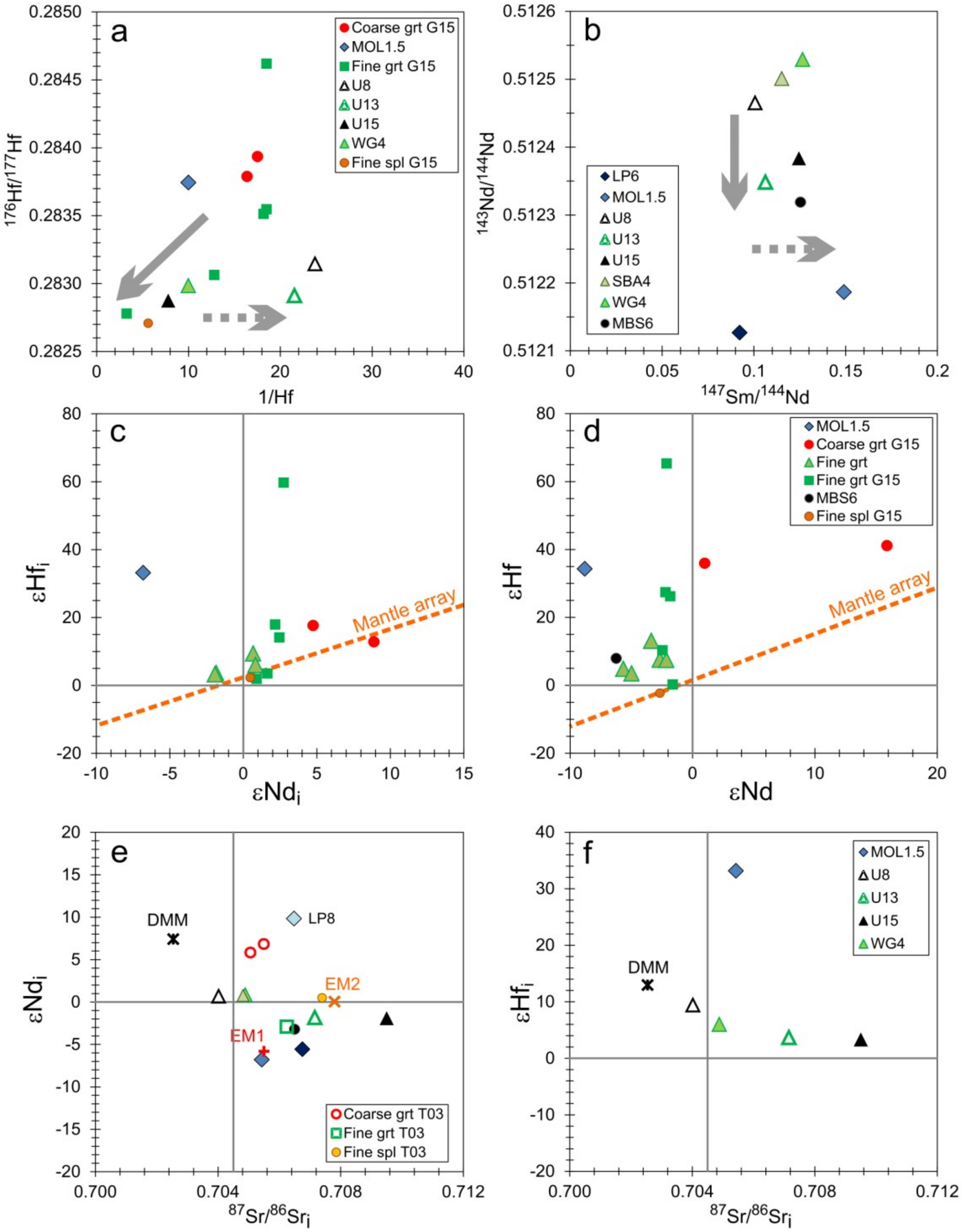

Figure 2.7. Covariation plots of present-day and initial (330 Ma) whole-rock isotope compositions from this study. (a) Present-day $^{176}Hf/^{177}Hf$ vs. 1/Hf, (b) present-day $^{143}Nd/^{144}Nd$ vs. $^{147}Sm/^{144}Nd$, (c) εHf_i vs. εNd_i, (d) εHf vs. εNd, (e) εNd_i vs. $^{87}Sr/^{86}Sr_i$, (f) εHf_i vs. $^{87}Sr/^{86}Sr_i$. Full arrows in (a) and (b) mark addition of unradiogenic Hf and Nd, dashed arrows mark addition of Lu and Sm, respectively. Other information as in Figure 2.5. The initial isotopic composition of DMM was back-calculated at 330 Ma, whereas the compositions of EM1 and EM2 are present-day ratios.

In pristine melt-depleted or ancient melt-refertilized mantle, an anticorrelation of the Sr-isotope compositions with Nd and with Hf would be expected. Overall, the majority of the UZ peridotites shows enriched Nd and Sr compositions similar to the isotopic compositions of the EM1 and EM2 reservoirs (Figure 2.7e) and may therefore indicate their provenance from a mantle portion with mixed recycled crustal components, or from different mantle sources. Enriched $^{87}Sr/^{86}Sr_i$ at depleted Nd isotopic composition observed for sample LP8 suggests interaction with a component having relatively low Nd abundances but radiogenic Sr (continental crust). Enriched compositions of both Sr and Nd, as shown by other coarse-grained peridotites and the majority of the fine-grained samples may suggest stronger interaction with the crustal component, such that Nd was also affected. This is in accordance with experimental demonstrations that aqueous fluids are less capable of influencing the Sm-Nd system than the Rb-Sr system (e.g. Kessel et al., 2005; Zheng & Hermann, 2014). Alternatively, the addition of a component with radiogenic Sr was decoupled from the main metasomatic fluid-related stage at high-pressure conditions at 330 Ma (Tumiati et al., 2003), and the Rb-Sr system was modified during subsequent - likewise fluid-mediated - retrogression (Gudelius, 2015). This is in agreement with the least radiogenic $^{87}Sr/^{86}Sr_i$ ratios displayed by the little retrogressed fine-grained garnet-amphibole peridotites (U8, WG4, SBA4; Figure 2.7e) but in contrast with the highest $^{87}Sr/^{86}Sr_i$ ratios of the little retrogressed fine-grained garnet-amphibole peridotite U15, suggesting multi-stage addition of crust-derived radiogenic Sr. Sample MOL1.5 strongly deviates from the mantle array in the εHf_i vs. εNd_i diagram (Figure 2.7c), presumably due to fluid-mediated strong overprint of its Nd- but not Hf-isotope composition, while the only moderately radiogenic Sr composition of this sample (Figure 2.7e) may be attributed to the lack of significant retrogression. Given that this sample and sample LP6 have the least radiogenic Nd measured, which is offset from the main array formed by fine-grained peridotites (Figure 2.5b), these samples may have interacted with recycled components, leading to lower Sm/Nd, during an older stage (possibly in the mantle wedge) of metasomatism involving aqueous fluids.

In a εHf_i vs. $^{87}Sr/^{86}Sr_i$ diagram (Figure 2.7f), fine-grained garnet-amphibole peridotites describe a correlation towards more enriched Sr and Hf compositions from sample U8 to sample U13 which is also reflected in the present-day ratios (not shown). This indicates a coupled Sr and Hf behavior during the main metasomatic event and also coupled addition of radiogenic Sr and unradiogenic Hf during subsequent retrogression. This suggests that fluids marked by radiogenic $^{87}Sr/^{86}Sr$ are capable of carrying HFSE. Thus, Gudelius (2015) related positive correlations of HFSE and LILE to enhanced mobility of HFSE in the presence of appropriate ligands, such as F^- and Cl^- in the fluid, promoting addition of some “crustal”, unradiogenic Hf to the peridotites. This is in agreement with the observations by Marocchi et al. (2009, 2010) who demonstrated at least moderate HFSE mobility during fluid-mediated crust-peridotite interaction and the formation of “hybrid” crust-peridotite contact rocks during exhumation. Indeed, elevated HFSE concentrations and the occurrence of zircon in fine-grained garnet-amphibole UZ peridotites appear to corroborate the capability of subduction-related aqueous fluids to transport HFSE (see thesis chapter 3).

Although sample LP8 has different Nd isotopic compositions compared to all other samples, it is interesting to note that both present-day and initial Pb isotopic compositions of LP8 are similar to those of the other coarse-grained samples and some fine-grained samples (Figure 2.5e,f; Figure 2.8). This may indicate mobilization of Pb in both melts and fluids and, thus, homogenization of Pb isotopes in samples with different pre-histories during both melt-mediated and fluid-mediated processes. Strontium and Pb isotopic compositions of subsets of peridotites co-vary positively but a general correlation of all samples is not present. For example, a subgroup of three fine-grained garnet-amphibole peridotites has significantly lower Pb isotopic ratios at given Sr isotopic ratios, indicating decoupling of the Sr and Pb systems during fluid-mediated metasomatism which mostly affected the fine-grained peridotites. The offset to lower Pb isotopic ratios cannot be explained by Pb addition during metasomatism because, for example, sample SBA4 with low Pb isotopic ratios contains less Pb than sample WG4 with higher Pb isotopic ratios. This suggests that these three samples record former depletion in highly incompatible U and Th compared to the other samples, or alternatively, that these samples did not experience pre-330 Ma enrichment through interaction with a subduction-related melt as proposed by Scambelluri et al. (2006). Importantly, UZ peridotites generally display radiogenic Pb isotopic compositions which are similar to or more radiogenic than other orogenic peridotites and mantle xenoliths (Figure 2.5e,f) and describe a mixing line between the compositions of EM2 and one similar to EM1. This is more pronounced in the coarse-grained peridotites but also includes some fine-grained peridotites. This suggests addition of mixed recycled crustal components, such as continental crust (EM2) and enriched (metasomatized) lithospheric mantle (EM1) (Hofmann, 1997). All coarse-grained peridotites and some of the fine-grained peridotites have Pb isotopic compositions closer to the EM2 reservoir, whereas the three fine-grained garnet-amphibole peridotites with lower Pb-isotope ratios nearly conform to the model EM1 reservoir. Subgroups of UZ peridotites show positive correlations of both measured and initial Pb isotopic ratios with U/Pb (Figure 2.8c) and Th/Pb (not shown): the three fine-grained samples with lower Pb isotopic ratios have similar U/Pb and Th/Pb ratios as all other samples, confirming that their lower Pb-isotope ratios are unrelated to the fluid-mediated main metasomatic event and retrogression. The correlations suggest that U and Th were not decoupled during 330 Ma metasomatism and afterwards, suggesting that U and Th were equally mobilized. Such a process is traditionally viewed as a signature of interaction with sediment-derived melt, whereas the involvement of aqueous fluids would result in decoupled U and Th (Taylor & McLennan, 1985; Keppler & Wyllie, 1990; Rudnick & Gao, 2003). However, the Pb isotopic compositions appear to reveal two different protoliths for the UZ peridotites with mixed recycled crustal components.

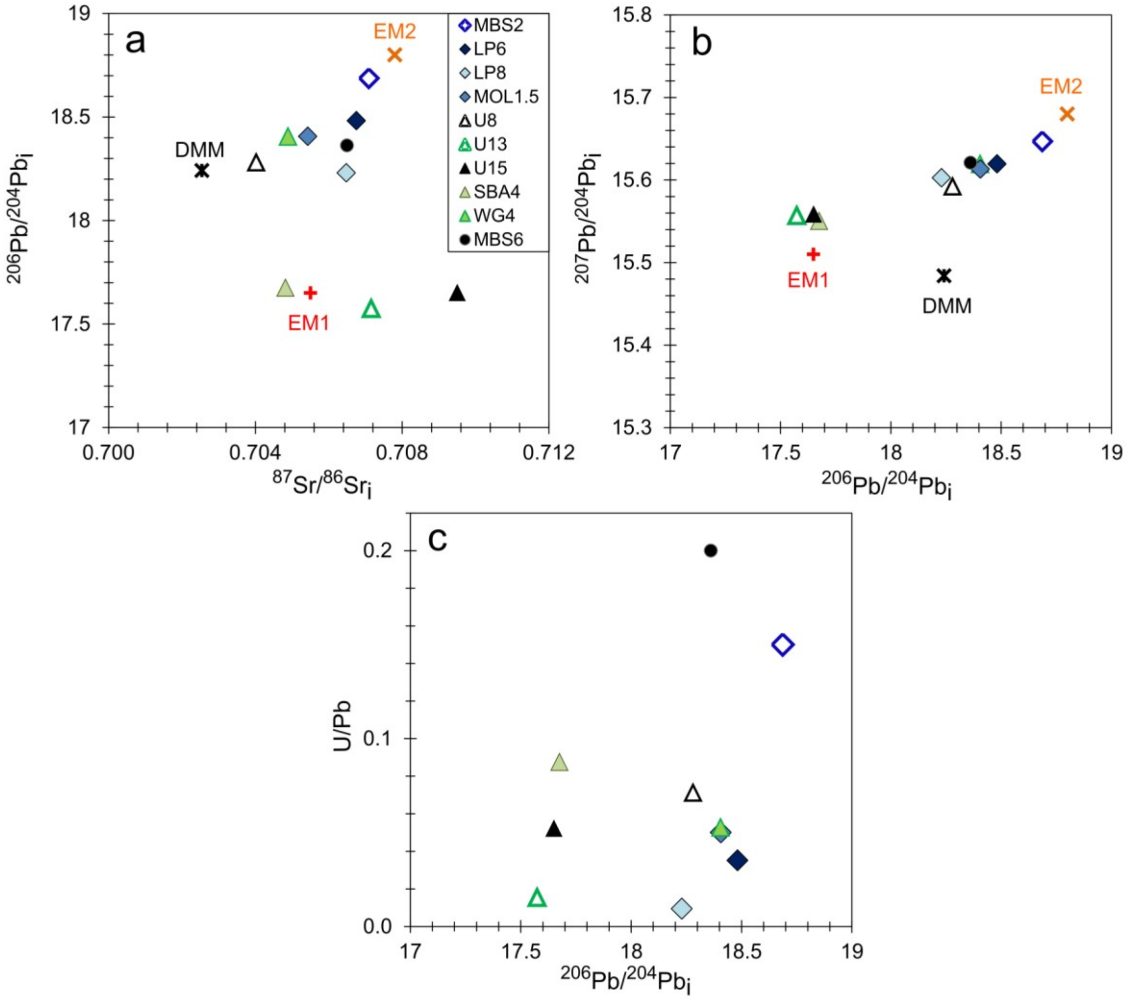

Figure 2.8. Initial (330 Ma) Pb-isotope ratios of Ulten Zone peridotites. (a) $^{206}Pb/^{204}Pb_i$ vs. $^{87}Sr/^{86}Sr_i$, (b) $^{207}Pb/^{204}Pb_i$ vs. $^{206}Pb/^{204}Pb_i$, (c) Whole-rock U/Pb vs. $^{206}Pb/^{204}Pb_i$. Values for DMM from Workman & Hart (2005), for EM1 and EM2 from Hart (1988). The initial isotopic composition of DMM was back-calculated at 330 Ma, whereas the compositions of EM1 and EM2 are present-day ratios.

In summary, combined petrographic, elemental and isotopic systematics clearly document the multi-stage evolution of the UZ mantle, with attendant disturbance of the radiogenic isotope systems. Nevertheless, careful sample-by-sample consideration provides some constraints on the effects of various processes in continental subduction channels – starting with metasomatism of the mantle wedge during onset of subduction, followed by entrapment in the subducting slab and finally exhumation and concomitant retrogression. Depending on these multi-stage pre-histories, samples with meaningful age information may be isolated.

2.6 Summary and conclusions

The combined results of petrography, whole-rock elemental and isotopic analyses of peridotites from the UZ were used to better constrain the conditions and timing of melt-assisted and fluid-assisted metasomatic events in the evolution of the peridotites from the mantle wedge towards involvement in the subducting crustal slab to exhumation in a crust-mantle mélange. In this context, the main findings of this study can be summarized as follows:

1) In the UZ peridotites, major elements and trace elements show a decoupled behavior indicating the multi-stage evolution of these peridotites. While all UZ peridotites have variable HREE compositions <DM, indicating variable degrees of partial melting, the compositional trends displayed by whole-rock major elements record refertilization in addition to a former partial melting event. Furthermore, the fine-grained peridotites are enriched in the most incompatible trace elements relatively to the coarse-grained peridotites, implying ingress of crust-derived aqueous fluid(s) enriched in these elements, during interaction of the wedge-derived peridotites with the crustal slab.
2) Hafnium T_{CHUR} and Nd T_{CHUR} model ages of fine-grained samples with depleted major-element compositions and of one coarse-grained sample with depleted Hf-isotope compositions yield broadly consistent ages > 1 Ga, which may indicate initial formation of these peridotites by depletion of a primitive mantle during the assembly of the supercontinent Rodinia.
3) One coarse-grained sample has depleted Nd-isotope compositions and combination of this sample with samples reported in previous studies (Tumiati et al., 2003; Gudelius, 2015) yields a Sm-Nd isochron age of 409 ± 38 Ma which corresponds to the onset of the Variscan orogeny. This age may constrain the timing of isotopic re-equilibration after the Proterozoic partial melting event, as the result of interaction of the hot mantle wedge with subduction-related metasomatic liquids.
4) Although some of the coarse-grained UZ peridotites retain largely undisturbed isotopic compositions, the generally highly variable isotopic compositions displayed by the UZ peridotites imply multi-stage disturbance of the radiogenic isotope systems. Thus, careful sample-by-sample consideration provides some constraints on the effects of various processes during the evolution of the peridotites. Fine-grained hydrated UZ peridotites show relatively low Hf and Nd isotopic ratios testifying to the fluid-mediated addition of unradiogenic Hf and Nd. While some coarse-grained samples have unradiogenic Nd compositions but retain depleted Hf compositions, other coarse-grained samples show both depleted Hf and Nd compositions. Decoupling of the Lu-Hf and Sm-Nd isotopic systems can be explained by substantial input of unradiogenic Nd and Hf during the fluid-assisted main metasomatic event at 330 Ma (Tumiati et al., 2003) and during subsequent fluid-mediated retrogression.
5) Addition of radiogenic Sr in the majority of the UZ peridotites is attributed to crustal input during and after the main metasomatic event. Coupled behavior of Sr and Hf suggests coupled addition of radiogenic Sr and unradiogenic Hf during retrogression, indicating that subduction-related crustal fluids marked by radiogenic Sr compositions are capable of mobilizing HFSE.
6) The UZ peridotites display radiogenic Pb isotopic compositions which describe a mixing line between the compositions of the model reservoirs EM1 and EM2, revealing that the UZ peridotites derive from

protoliths with mixed recycled crustal components. Fluid-mediated metasomatism and retrogression resulted in decoupling of the Pb isotopic compositions from the other isotopic systems, whereas U and Th remained coupled and the Pb isotope systems remained largely undisturbed.

2.7 References

1. Bargossi, G.M., Bondi, M., Mordenti, A., Morten, L. (2003). The abundances of 55 elements and petrovolumetric models of the crust in the Non and Ulten Valley (Site 3). In: F.P. Sassi (Ed.). The abundance of 55 elements and petrovolumetric models of the crust in 9 type areas from the crystalline basements of Italy, with some geophysical and petrophysical data, Accademia Nazionale delle Scienze detta dei XL, Scritti e Documenti, Roma, 163-196.
2. Beyer, E.E., Griffin, W.L., O'Reilly, S.Y. (2006). Transformation of Archaean lithospheric mantle by refertilization: Evidence from exposed peridotites in the Western Gneiss Region, Norway. Journal of Petrology 47, 1611-1636.
3. Blichert-Toft, J., Albarède, F. (1997). The Lu-Hf isotope geochemistry of chondrites and the evolution of the mantle-crust system. Earth and Planetary Science Letters 148, 243-258.
4. Blichert-Toft, J., Puchtel, I.S. (2010). Depleted mantle sources through time: evidence from Lu-Hf and Sm-Nd isotope systematics of Archean komatiites. Earth and Planetary Science Letters 297, 598-606.
5. Bodinier, J.L., Vasseur, G., Vernieres, J., Dupuy, C., Fabries, J. (1990). Mechanisms of mantle metasomatism: geochemical evidence from the Lherz orogenic peridotite. Journal of Petrology 31, 597-628.
6. Bodinier, J.-L., Godard, M. (2014). Orogenic, ophiolitic, and abyssal peridotites. In: R.W. Carlson (Ed.). The mantle and core, Treatise on Geochemistry (Second Edition) 3, 103-167.
7. Bondi, M., De Francesco, A.M., Morten, L. (1992). Major elements, 3d transition elements, Cu and Sr geochemistry of peridotitic rocks within the Austridic crystalline basement, Nonsberg area, Northern Italy. In: L. Carmignani, F.P. Sassi (Eds.). Contributions to the Geology of Italy with special regard to the Paleozoic basements, IGCP Newsletter 5, 229-235.
8. Bosch, D., Blichert-Toft, J., Moynier, F., Nelson, B.K., Telouk, P., Gillot, P.-Y., Albarède, F. (2008). Pb, Hf and Nd isotope compositions of the two Réunion volcanoes (Indian Ocean): A tale of two small-scale mantle "blobs"?. Earth and Planetary Science Letters 265, 748-765.
9. Chen, Y., Su, B., Guo, S. (2015). The Dabie-Sulu orogenic peridotites: progress and key issues. Science China-Earth Sciences 58, 1679-1699.
10. Chen, R.-X., Li, H.-Y., Zheng, Y.-F., Zhang, L., Gong, B., Hu, Z., Yang, Y. (2017). Crust-mantle interaction in a continental subduction channel: evidence from orogenic peridotites in North Qaidam, Northern Tibet. Journal of Petrology 58, 191-226.
11. Choi, S.H., Kwon, S.T., Mukasa, S.B., Sagong, H. (2005). Sr-Nd-Pb isotope and trace element systematics of mantle xenoliths from Late Cenozoic alkaline lavas, South Korea. Chemical Geology 221, 40-64.
12. Choi, S.H., Mukasa, S.B., Andronikov, A.V., Marcano, M.C. (2007). Extreme Sr-Nd-Pb-Hf isotopic compositions exhibited by the Tinaquillo peridotite massif, Northern Venezuela: implications for geodynamic setting. Contributions to Mineralogy and Petrology 153, 443-463.
13. Connelly, J.N., Ulfbeck, D.G., Thrane, K., Bizzarro, M., Housh, T. (2006). A method for purifying Lu and Hf for analyses by MC-ICP-MS using TODGA resin. Chemical Geology 233, 126-136.
14. DePaolo, D.J. (1988). Neodymium isotope geochemistry: an introduction. Springer, New York.
15. Förster, B., Braga, R., Aulbach, S., Lo Pò, D., Bargossi, G.M., Mair, V. (2017). A petrographic study of carbonate phases in the Ulten Zone ultramafic rocks: Insights into carbonation in the mantle wedge and exhumation-related decarbonation. Ofioliti 42, 105-127.

16. Gebauer, D., Grünenfelder M. (1978). U-Pb dating of alpine-type garnet-peridotites example: Val Ultimo (Eastern Alps, northern Italy). U.S. Geological Survey Open-File Report OF 78-0701, 135-137.
17. Godard, G., Martin, S., Prosser, G., Kiénast, J. R. & Morten, L. (1996). Variscan migmatites, eclogites and garnet-peridotites of the Ulten zone, Eastern Austroalpine system. Tectonophysics 259, 313-341.
18. Gudelius, D. (2015). Metasomatism in the mantle wedge: New insights from Eastern Alpine peridotites from the Ulten Zone (N Italy). Unpublished Master thesis, Goethe University Frankfurt
19. Hamelin, B., Allègre, C.J. (1988). Lead isotope study of orogenic lherzolite massifs. Earth and Planetary Science Letters 91, 117-131.
20. Hart, S.R. (1984). A large-scale isotope anomaly in the Southern Hemisphere mantle. Nature 309, 753-757.
21. Hart, S.R. (1988). Heterogeneous mantle domains – signatures, genesis and mixing chronologies. Earth and Planetary Science Letters 90, 273-296.
22. Hauzenberger, C.A., Höller, W., Hoinkes, G., Klötzli, U., Thöni, M. (1993). Metamorphic evolution of the Austroalpine basement in the Nonsberg area, Ultental (Val d'Ultimo), southern Tyrol, Terra Abstracts 5, 13.
23. Hermann, J., Spandler, C., Hack, A., Korsakov, A.V. (2006). Aqueous fluids and hydrous melts in high-pressure and ultra-high pressure rocks: implications for element transfer in subduction zones. Lithos 92, 399-417.
24. Herzberg, C., Riccio, L., Chiesa, S., Fornoni, A., Gatto, G.O., Gregnanin, A., Piccirillo, E.M., Scolari, A. (1977). Petrogenetic evolution of a spinel-garnet-lherzolite in the Austridic crystalline basement from Val Clapa (Alto Adige, northeastern Italy). Memorie degli Istituti di Geologia e Mineralogia dell'Università di Padova 30, 3-28.
25. Herzberg, C. (2004). Geodynamic information in peridotite petrology. Journal of Petrology 45, 2507-2530.
26. Hofmann, A.W. (1997). Mantle geochemistry: the message from oceanic volcanism. Nature 385, 219-229.
27. Holmes, A. (1946). An estimate of the age of the Earth. Nature 157, 680-684.
28. Houtermans, F.G. (1946). Die Isotopen-Häufigkeiten im natürlichen Blei und das Alter des Urans. Naturwissenschaften 33, 185-187.
29. Ionov, D.A., Bodinier, J.L., Mukasa, S.B., Zanetti, A. (2002). Mechanisms and sources of mantle metasomatism: Major and trace element compositions of peridotite xenoliths from Spitsbergen in the context of numerical modelling. Journal of Petrology 43, 2219-2259.
30. Ionov, D.A., Hofmann, A.W. (2007). Depth of formation of sub-continental off-craton peridotites. Earth and Planetary Science Letters 261, 620-634.
31. Ionov, D.A. (2010). Petrology of mantle wedge lithosphere: new data on supra-subduction zone peridotite xenoliths from the andesitic Avacha volcano, Kamchatka. Journal of Petrology 51, 327-361.
32. Ionov, D.A., Bigot, F., Braga, R. (2017). The provenance of the lithospheric mantle in continental collision zones: petrology and geochemistry of peridotites in the Ulten-Nonsberg Zone (Eastern Alps). Journal of Petrology 58, 1451-1472.
33. Jacobsen, S.B., Wasserburg, G.J. (1980). Sm-Nd evolution of chondrites. Earth and Planetary Science Letters 50, 139-155.
34. Keppler, H., Wyllie, P.J. (1990). Role of fluids in transport and fractionation of uranium and thorium in magmatic processes. Nature 348, 531-533.
35. Kessel, R., Schmidt, M.W., Ulmer, P., Pettke, T. (2005). Trace element signature of subduction-zone fluids, melts and supercritical fluids at 120-180 km depth. Nature 437, 724-727.
36. Le Roux, V., Bodinier, J.-L., Tommasi, A., Alard, O., Dautria, J.-M., Vauchez, A., Riches, A.J.V. (2007). The Lherz spinel lherzolite: refertilized rather than pristine mantle. Earth and Planetary Science Letters 259, 599-612.

37. Ludwig, K.R. (2008). User's Manual for Isoplot 3.70. A geochronological toolkit for Microsoft *Excel*. Berkeley Geochronology Center, Special Publication No. 4, 77 p.
38. Lugmair, G.W., Marti, K. (1978). Lunar initial ^{143}Nd/^{144}Nd: differential evolution of the lunar crust and mantle. Earth and Planetary Science Letters 39, 348-357.
39. Malaspina, N., Hermann, J., Scambelluri, M., Compagnoni, R. (2006). Polyphase inclusions in garnet-orthopyroxenite (Dabie Shan, China) as monitors for metasomatism and fluid-related trace element transfer in subduction zone peridotite. Earth and Planetary Science Letters 249, 173-187.
40. Malaviarachchi, S.P.K, Makishima, A., Tanimoto, M., Kuritani, T., Nakamura, E. (2008). Highly unradiogenic lead isotope ratios from the Horoman peridotite in Japan. Nature Geoscience 1, 859-863.
41. Marocchi, M., Hermann, J., Morten, L. (2007). Evidence for multi-stage metasomatism of chlorite-amphibole peridotites (Ulten Zone, Italy): constraints from trace element compositions of hydrous phases. Lithos 99, 85-104.
42. Marocchi, M., Mair, V., Tropper, P., Bargossi, G.M. (2009). Metasomatic reaction bands at the Mt. Hochwart gneiss-peridotite contact (Ulten Zone, Italy): insights into fluid-rock interaction in subduction zones. Mineralogy and Petrology 95, 251-272.
43. Marocchi, M., Hermann, J., Tropper, P., Bargossi, G.M., Mair, V. (2010). Amphibole and phlogopite in "hybrid" metasomatic bands monitor trace element transfer at the interface between felsic and ultramafic rocks (Eastern Alps, Italy). Lithos 117, 135-148.
44. McCulloch, M.T., Black, L.P. (1984). Sm-Nd isotope systematic of Enderby Land granulites and evidence for the redistribution of Sm and Nd during metamorphism. Earth and Planetary Science Letters 71, 46-58.
45. McDonough, W.F., Sun, S.-s. (1995). The composition of the Earth. Chemical Geology 120, 223-253.
46. Mukasa, S.B., Shervais, J.W. (1999). Growth of subcontinental lithosphere: evidence from repeated dike injections in the Balmuccia lherzolite massif, Italian Alps. Lithos 48, 287-316.
47. Nir-El, Y., Lavi, N. (1998). Measurement of the half-life of ^{176}Lu. Applied radiation and isotopes 49, 1653-1655.
48. Niu, Y. (1997). Mantle melting and melt extraction processes beneath ocean ridges: evidence from abyssal peridotites. Journal of Petrology 38, 1047-1074.
49. Obata, M., Morten, L. (1987). Transformation of spinel lherzolite to garnet lherzolite in ultramafic lenses of the Austridic Crystalline Complex, Northern Italy. Journal of Petrology 28, 599-623.
50. Pearson, D.G., Canil, D., Shirey, S.B. (2003). Mantle samples included in volcanic rocks: xenoliths and diamonds. In: R.W. Carlson (Ed.). The mantle and core, Treatise on Geochemistry (Second Edition) 3, 171-276.
51. Pin, C., Briot, D., Bassin, C., Poitrasson, F. (1994). Concomitant separation of strontium and samarium-neodymium for isotopic analysis in silicate samples, based on specific extraction chromatography. Analytica Chimica Acta 298, 209-217.
52. Rampone, E., Morten, L. (2001). Records of crustal metasomatism in the garnet peridotites of the Ulten Zone (Upper Austroalpine, Eastern Alps). Journal of Petrology 42, 207-219.
53. Rosenbaum, J.M., Wilson, M., Downes, H. (1997). Multiple enrichment of the Carpathian-Pannonian mantle: Pb-Sr-Nd isotope and trace element constraints. Journal of Geophysical Research – Solid Earth 102, 14947-14961.
54. Rost, F., Brenneis, P. (1978). Die Ultramafite im Bergzug südlich des Ultentales, Provinz Alto Adige (Oberitalien), Tschermaks Mineralogische und Petrographische Mitteilungen 25, 257-286.
55. Rudnick, R.L., Gao, S. (2003). Composition of the continental crust. In: H.D. Holland, K.K. Turekian, R.L. Rudnick (Eds.). Treatise on Geochemistry, Vol. 3 – The Crust. Elsevier, 1-64.
56. Salters, V.J.M., Stracke, A. (2004). Composition of the depleted mantle. Geochemistry Geophysics Geosystems 5

57. Sapienza, G.T., Scambelluri, M., Braga, R. (2009). Dolomite-bearing orogenic garnet peridotites witness fluid-mediated carbon recycling in a mantle wedge (Ulten Zone, Eastern Alps, Italy). Contributions to Mineralogy and Petrology 158, 401-420.
58. Scambelluri, M., Hermann, J., Morten, L., Rampone, E. (2006). Melt- versus fluid-induced metasomatism in spinel to garnet wedge peridotites (Ulten Zone, Eastern Italian Alps): clues from trace element and Li abundances. Contributions to Mineralogy and Petrology 151, 372-394.
59. Scambelluri, M., Pettke, T., Van Roermund, H.L.M. (2008). Majoritic garnets monitor deep subduction fluid flow and mantle dynamics. Geology 36, 59-62.
60. Scambelluri, M., Van Roermund, H.L.M., Pettke, T. (2010). Mantle wedge peridotites: fossil reservoirs of deep subduction zone processes Inferences from high and ultrahigh-pressure rocks from Bardane (Western Norway) and Ulten (Italian Alps). Lithos 120, 186-201.
61. Scambelluri, M., Pettke, T., Rampone, E., Godard, M., Reusser, E. (2014). Petrology and trace element budgets of high-pressure peridotites indicate subduction dehydration of serpentinized mantle (Cima di Gagnone, Central Alps, Switzerland). Journal of Petrology 55, 459-498.
62. Schmidberger, S.S., Simonetti, A., Francis, D. (2001). Sr-Nd-Pb isotope systematics of mantle xenoliths from Somerset Island kimberlites: Evidence for lithosphere stratification beneath Arctic Canada. Geochimica et Cosmochimica Acta 65, 4243-4255.
63. Shi, R.D., Griffin, W.L., O'Reilly, S.Y., Zhao, G.C., Huang, Q.S., Li, J., Xu, J.F. (2010). Evolution of the Luliangshan garnet peridotites in the North Qaidam UHP belt, Northern Tibetan Plateau: Constraints from Re-Os isotopes. Lithos 117, 307-321.
64. Steiger, R.H., Jäger, E. (1977). Subcommission on geochronology – convention on use of decay constants in geochronology and cosmochronology. Earth and Planetary Science Letters 36, 359-362.
65. Taylor, S.R., McLennan, S.M. (1985). The continental crust: its composition and evolution. Blackwell Scientific Publication, Oxford, 312 pp.
66. Thöni, M. (1999). A review of geochronological data from the Eastern Alps. Schweizer Mineralogische und Petrographische Mitteilungen 79, 209-230.
67. Tumiati, S., Thöni, M., Nimis, P., Martin, S., Mair, V. (2003). Mantle-crust interactions during Variscan subduction in the Eastern Alps (Nonsberg-Ulten zone): geochronology and new petrological constraints. Earth and Planetary Science Letters 210, 509-526.
68. Tumiati, S., Godard, G., Martin, S., Klötzli, U., Monticelli, D. (2007). Fluid-controlled crustal metasomatism within a high-pressure subducted mélange (Mt. Hochwart, Eastern Italian Alps). Lithos 94, 148-167.
69. Vervoort, J.D., Blichert-Toft, J. (1999). Evolution of the depleted mantle: Hf isotope evidence from juvenile rocks through time. Geochimica et Cosmochimica Acta 63, 533-556.
70. Vrijmoed, J.C., Austrheim, H., John, T., Hin, R.C., Corfu, F., Davies, G.R. (2013). Metasomatism in the ultrahigh-pressure Svartberget garnet-peridotite (Western Gneiss Region, Norway): implications for the transport of crust-derived fluids within the mantle. Journal of Petrology 54, 1815-1848.
71. White, W.M., Albarède, F., Télouk, P. (2000). High-precision analysis of Pb isotope ratios by multi-collector ICP-MS. Chemical Geology 167, 257-270.
72. Whitney, D.L., Evans, B.W. (2010). Abbreviations for names of rock-forming minerals. American Mineralogist 95, 185-187.
73. Workman, R.K., Hart, S.R. (2005). Major and trace element composition of the depleted MORB mantle (DMM). Earth and Planetary Science Letters 231, 53-72.
74. Xiong, Q., Griffin, W.L., Zheng, J.-P., O'Reilly, S.Y., Pearson, N.J. (2015). Episodic refertilization and metasomatism of Archean mantle: evidence from an orogenic peridotite in North Qaidam (NE Tibet, China). Contributions to Mineralogy and Petrology 169, 31.
75. Zangana, N.A., Downes, H., Thirlwall, M.F., Hegner, E. (1997). Relationship between deformation, equilibration temperatures, REE and radiogenic isotopes in mantle xenoliths (Ray Pic, Massif Central,

France): An example of plume-lithosphere interaction?. Contributions to Mineralogy and Petrology 127, 187-203.

76. Zhang, R.Y., Li, T., Rumble, D., Yui, T.-F., Li, L., Yang, J.S., Pan, Y., Liou, J.G. (2007). Multiple metasomatism in Sulu ultrahigh-P garnet peridotite constrained by petrological and geochemical investigations. Journal of Metamorphic Geology 25, 149-164.
77. Zhang, Z.M., Dong, X., Liou, J.G., Liu, F., Wang, W., Yui, F. (2011). Metasomatism of garnet peridotite from Jiangzhuang, southern Sulu UHP belt: constraints on the interactions between crust and mantle rocks during subduction of continental lithosphere. Journal of Metamorphic Geology 29, 917-937.
78. Zheng, Y.-F. (2012). Metamorphic chemical geodynamics in continental subduction zones. Chemical Geology 328, 5-48.
79. Zheng, Y.-F., Hermann, J. (2014). Geochemistry of continental subduction-zone fluids. Earth, Planets and Space 66, 93.

3 Zircons in mantle wedge peridotites from the orogenic Ulten Zone (Eastern Alps, Italy): Indicators for metasomatic processes in a crust-mantle subduction mélange

3.1 Introduction

Active convergent margins are key geologic settings where fluid- and melt-assisted processes promote mass transfer and element cycling among Earth's reservoirs. Thus, subduction-related crust-mantle interaction and the capability of mantle wedge lithologies to store and/or release elements are of particular interest to understand the global mass transfer. Mantle wedge-derived peridotites, now exposed in eroded orogens, are generally metasomatized by melts/fluids derived from descending slabs or from upwelling asthenospheric mantle. Metasomatic phases, e.g. hydrous minerals such as amphiboles and micas, are valuable tracers to fingerprint the composition and evolution of lithospheric mantle and the involvement of fluids and melts in subduction zone environments. Among metasomatic phases, zircon is of particular interest. Zircon normally does not form in a primary peridotite mineral assemblage because the activity of Zr and Si in ultramafic rocks is too low (Palme & O'Neill, 2003). Nevertheless, zircon-bearing orogenic peridotite is occasionally reported, typically from continental collision settings, linking their origin to mantle metasomatism by fluids and/or melts that originated from the associated crustal slab and/or deeper levels of the subduction zone (e.g. Zhang et al., 2005; Liati & Gebauer, 2009; Chen et al., 2017). One such occurrence are peridotites from the Ulten Zone (UZ) in the Eastern Italian Alps, which originated as a portion of a mantle wedge that was brought to garnet-facies depths during continental subduction related to the Variscan orogeny, and subsequently exhumed together with host gneisses (e. g. Scambelluri et al., 2006). In this geological setting the wedge-derived peridotite underwent diverse melt/fluid-mediated metasomatic events during the tectono-metamorphic history of the UZ, which is recorded by various metasomatic phases in peridotite (Rampone & Morten, 2001; Scambelluri et al., 2006). Previous studies reported the occurrence of discrete zircon crystals in UZ peridotites (Gebauer & Grünenfelder, 1979; Marocchi et al., 2009) and pyroxenites (Gebauer & Grünenfelder, 1979), in (migmatized) gneisses (Hauzenberger et al., 1993; Tumiati et al., 2003, 2007; Braga & Massonne, 2008) and in phlogopitites and amphibolites which derived from hybrid metasomatic reaction bands at the peridotite-gneiss contact (Tumiati et al., 2003, 2007; Marocchi et al., 2009, 2010, 2011).

The only age determination using U-Pb geochronology on zircons in UZ garnet-bearing ultramafic rocks performed so far yielded concordant ages of 336 and 332 Ma, interpreted as the time of formation of primary magmatic zircons that were subsequently recrystallized during metamorphic transformation of the host rock (Gebauer & Grünenfelder, 1979). Later work ascribed the presence of zircons in ultramafic UZ lithologies to metamorphism and local metasomatism of the host peridotite (Tumiati et al., 2007; Marocchi et al., 2009). Here, we present an integrated study of geochronology and chemistry on zircons from the UZ orogenic peridotites and a phlogopitite. Using new U-Th-Pb age dating and trace element compositions for zircons in UZ peridotites and metasomatic reaction bands, we will discuss the processes leading to zircon growth in the ultramafic rocks as well as the nature, timing and effects of metasomatism during subduction-related crust-mantle interactions and fluid/melt-mediated processes in the UZ crust-peridotite mélange, with implications for the dynamics in a collision zone setting.

3.2 Geologic background and previous work

The UZ tectonic unit (Figure 3.1; e.g. Morten et al., 1976; Martin et al., 1993; Martin et al., 1998) is a fragment of the Variscan belt (Godard et al., 1996) and is composed of a mélange of orogenic rocks deriving from a Paleozoic subduction zone that was exposed at the surface due to Variscan exhumation (Godard et al., 1996; Scambelluri et al., 2006). Lenses of ultramafic rocks (peridotite ± pyroxenite; Morten & Obata, 1983; Obata & Morten, 1987), often up to hundreds of meters in length, are embedded in foliated high-grade metamorphic crustal basement consisting of gneisses and migmatites (Obata & Morten, 1987; Godard et al., 1996). The "hybrid" gneiss-peridotite and migmatite-peridotite contact zones consist of metasomatic reaction bands rich in hydrous mineral assemblages (Tumiati et al., 2003; Marocchi et al., 2009, 2010) and are usually sharp but rarely exposed at the surface (Obata & Morten, 1987).

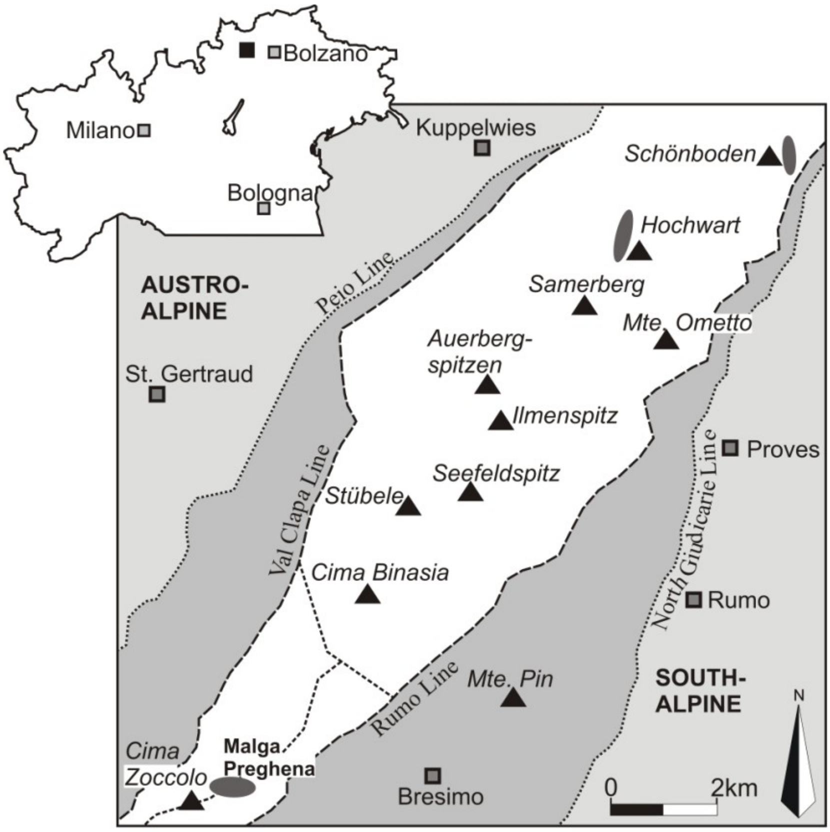

Figure 3.1. Simplified geological map of the Ulten Zone (UZ) tectonic unit with (a) its location in the Eastern Italian Alps and (b) a detailed structural map of the UZ (white field) as fragment of the Variscan belt belonging to the Austroalpine. The UZ consisting of crustal rocks (mainly gneisses and migmatites) with enclosed lenses of ultramafic rocks (peridotites ± pyroxenites) is delineated by the Val Clapa Line in the north-west and the Rumo Line in the south-east. The dark ovals mark the ultramafic bodies of which zircon-bearing peridotites and crust-mantle contact rocks were taken for this study. Sketch modified after Marocchi et al. (2007).

The peridotites display a wide range of textures, from coarse-grained (up to few cm) spinel-peridotites, via a transitional porphyroclastic garnet-bearing peridotite with large orthopyroxene and olivine in a granoblastic-polygonal matrix, to highly deformed fine-grained (0.2 mm to 1 mm) amphibole-garnet peridotites and amphibole-chlorite peridotites (Obata & Morten, 1987; Nimis & Morten, 2000). This variable petrographic appearance has been attributed to the complex tectono-metamorphic history of the UZ peridotites. In an early stage, the upwelling of subduction-related melts from deeper levels of the mantle wedge, which comprise a component of recycled crustal material, metasomatized the primary coarse-grained protogranular spinel lherzolite (Nimis & Morten, 2000; Scambelluri et al., 2006). During the subsequent subduction-related metamorphic evolution, the UZ peridotites were transformed and recrystallized into garnet-amphibole peridotites due to the infiltration of crust-derived carbon-bearing aqueous fluids (Rampone & Morten, 2001; Scambelluri et al., 2006; Marocchi et al., 2007; Tumiati et al., 2007). The wedge-derived peridotites were eventually transported to greater depths, close to the slab-wedge interface due to corner flow (Nimis & Morten, 2000), where they were ultimately incorporated as mantle slivers in country rock gneisses from a subducting crustal slab (Godard et al., 1996; Nimis & Morten, 2000).

Furthermore, recent studies demonstrate that carbonated hydrous peridotite, as applies to the UZ peridotites, did commonly not exceed 1.9 GPa during garnet-facies metamorphism (Braga & Sapienza, 2007; Malaspina & Tumiati, 2012; Tumiati et al., 2013). It has been debated, however, whether hydration and recrystallization (and pressure peak metamorphism) of the peridotites occurred while they were still residing in the mantle wedge before entrapment in the host gneisses (Scambelluri et al., 2006) or whether, conversely, peridotites and gneisses jointly reached the metamorphic peak during subduction and after tectonic peridotite incorporation in crustal rocks (Tumiati et al., 2007). The latter is supported by isotopic data showing that common isotopic homogenization of crustal and ultramafic rocks occurred at ca. 330 Ma, most likely when the wedge-derived peridotites were already incorporated in the crustal host rocks (Tumiati et al., 2003, 2007). Although the dynamics and timing of this metamorphic subduction-related scenario are not fully constrained yet, it is evident that both peridotites and subducted crustal rocks have a common exhumation history beginning at ca. 330 Ma (Tumiati et al., 2003, 2007), with the exception of some chlorite-amphibole peridotites, which did not have garnet-bearing precursors but were incorporated in the crustal rocks during exhumation (Marocchi et al., 2007). Ongoing infiltration of crust-related aqueous fluids during exhumation led to retrogression and the formation of chlorite-amphibole peridotite (Obata & Morten, 1987; Scambelluri et al., 2006; Braga & Sapienza, 2007; Marocchi et al., 2007, 2009) as well as to the formation of “hybrid” metasomatic reaction bands at the peridotite-gneiss contact (Tumiati et al., 2007; Marocchi et al., 2009, 2010).

The COH-fluids that prompted partial melting of the gneisses and concomitant crustal metasomatism of the peridotite slivers were suggested to have been introduced via dehydration of seawater-altered subducted sediments (Tumiati et al., 2007). While the composition of the crust-derived aqueous fluids was approximately constant during exhumation (Scambelluri et al., 2006), thermodynamic modeling indicates that its CO_2-content increased, at least locally (Braga & Sapienza, 2007). Migmatization and crustal peridotite metasomatism possibly continued along the whole late- or post-Variscan retrograde exhumation cycle of the UZ (Godard et al., 1996). The metamorphic signatures and mineral assemblages of the UZ lithologies have been preserved because the Alpine orogeny affected the UZ only weakly (Godard et al., 1996; Hauzenberger et al., 1996).

3.3 Sample material and description

Three zircon-bearing peridotites and one zircon-bearing phlogopitite sample deriving from different peridotite-bearing localities in the UZ tectonic unit (Figure 3.1, Table 3.1) were selected for this study.

3.3.1 Peridotites

In accordance with the observations by Tumiati et al. (2003) and Marocchi et al. (2009), zircons occur usually in fine-grained peridotites of the UZ (Figure 3.2). The term “fine-grained peridotite” used in this work refers to the “fine-type peridotite” described by Obata & Morten (1987). Sample PL1.6 is a fine-grained mylonitic peridotite with granoblastic-porphyroblastic texture crosscut by highly abundant serpentine veins associated with Fe oxide (Figure 3.2a). The mineral assemblage is composed of olivine + orthopyroxene + amphibole + garnet + spinel + minor clinopyroxene.

Table 3.1 Summary of salient petrographic features of zircon-bearing peridotite and phlogopitite from the Ulten Zone (Italy), summary of zircon characterization, zircon U-Pb age data and Ti-in-zircon temperatures.

Sample/type	Locality	Texture[1]	Zircon description[1]	Zrn U-Pb age (Ma)	Error (±Ma)	Type of age	T_{zircon}[2] (°C)	average T_{zircon}[2] (°C)	rsd[3] (%)
Fine-grained garnet-bearing peridotite									
PL1.6	Malga Preghena	Granoblastic-porphyroclastic mylonitic, serpentinized, with grt porphyroclasts	Elongated zrn grain (~1.5 mm) with curvilinear, sharp grain boundaries, crosscut by fine fractures, contains µm-sized inclusions	333	2	Weighted mean age	698 - 751	718 (n = 9)	3
				236	8	Weighted mean age			
Fine-grained (garnet-free) peridotite									
VM25P10A	Mount Hochwart	Granoblastic-porphyroclastic mylonitic, with post-garnet pseudomorph consisting of amp, spl, dol	Coarse euhedral zrn (~1 cm) with sharp grain boundaries, crosscut by abundant fractures, inclusions are mm-sized lobate dol and ap	333.7	2.8	Weighted mean age	680 - 728	704 (n = 13)	2
SBB2F	Mount Schönboden	Granoblastic-porphyroclastic mylonitic, highly amphibolized and serpentinized, displaying several petrographic domains, with opx porphyroclasts	Zrn grain (~100 µm) included in amp, contains mineral inclusions, one probably phl	2299	1100	Upper intercept	626 - 716	679 (n = 4)	6
				320	6.9	Lower intercept			
Phlogopitite ("hybrid" peridotite-crust contact)									
NB103	Mount Hochwart	Phl-rich domain (fibrous phl + green amp) and amp-rich domain (amp, qz, phl, ap, rt)	Euhedral µm-sized zrn grains in amp, rounded to ovoid µm-sized grains in qz	332.9	3.1	Weighted mean age	622 -664, spot G2-1: 483	646 (n = 4, exclusive G2-1)	3

[1] Zrn = zircon, grt = garnet, amp = amphibole, spl = spinel, dol = dolomite, ap = apatite, opx = orthopyroxene, phl = phlogopite, qz = quartz, rt = rutile.

[2] calculated using the Ti-in-zircon thermometer after Ferry & Watson (2007) using Ti concentrations of all analyzed zircon spots.

[3] relative standard deviation.

Garnet porphyroblasts partly have kelyphitic coronas and accessory minerals are sulfides and carbonates. This sample derives from a peridotite block from a debris fan of an ultramafic lens of several hundred meters extent. In contrast, sample VM25P10A is a fine-grained, weakly serpentinized mylonitic garnet-free peridotite (Figure 3.2b). The main mineral assemblage consists of olivine, orthopyroxene, amphibole and spinel, while sulfides occur as accessory minerals. Matrix olivine may contain amphibole inclusions and occasionally amphibole is zoned and contains orthopyroxene inclusions. Porphyroclasts of Cr-rich spinel also occur in the matrix. Pseudomorphs, probably after garnet, comprise amphibole, spinel and dolomite (Figure 3.2b).

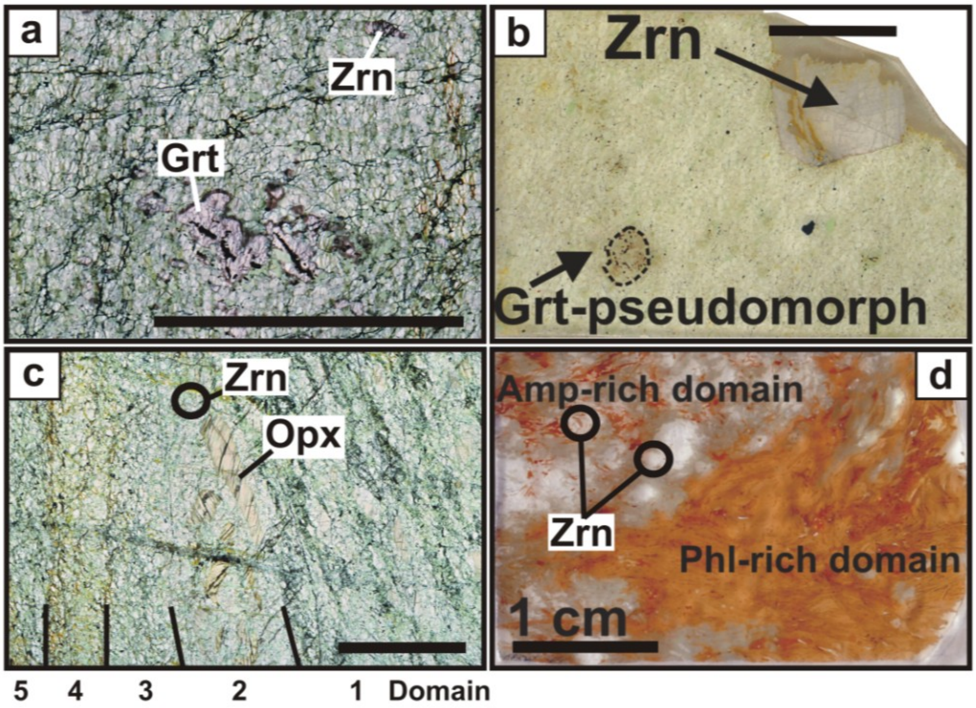

Figure 3.2. Thin section scans of the zircon-bearing rocks of the Ulten Zone selected for this study; (a) sample PL1.6 from Malga Preghena, a fine-grained mylonitic grt-amp peridotite crosscut by srp veins. The main mineral assemblage is ol + opx + amp + grt + spl + minor cpx; (b) sample VM25P10A from Hochwart, a fine-grained, weakly serpentinized mylonitic peridotite with pseudomorphs after grt. The main mineral assemblage is ol + opx + amp + spl; (c) sample SBB2F from Schönboden is a fine-grained mylonitic, partly porphyroclastic and highly amphibolized peridotite. It comes from a peridotite block where coarse-grained porphyroclastic peridotite grades into fine-grained mylonitic peridotite. The sample displays several textural domains (1-5) which are amphibolized and deformed in different degrees. All domains contain opx porphyroclasts of variable sizes. Domain 2 hosts the largest opx crystals (up to 1 cm in length) and the zircon; (d) sample NB103 from Hochwart (previously reported in Marocchi et al., 2009, 2010) is a fragment of a metasomatic reaction band between peridotites and crustal rocks. It consists of a phl-rich domain, containing fibrous phl and green amp, and a green amp-rich domain which contains green amp, qz, phl, pl, Cl-ap and rt. Scale bars denote 1 cm. Mineral abbreviations after Whitney & Evans (2010).

This sample derives from the mount Hochwart peridotite locality. Sample SBB2F derives from the fine-grained, partly porphyroclastic part of a peridotite block where a coarse porphyroclastic zone grades via a fine-grained porphyroclastic transitional zone into a fine-grained mylonitic rock. The porphyroclasts in this rock are coarse orthopyroxenes with frayed grain boundaries and kink band texture set in a highly deformed amphibole-rich peridotite matrix with large extent of replacement of major phases by secondary minerals (chlorite/serpentine). Sample SBB2F is a highly mylonitic fine-grained granoblastic-porphyroblastic peridotite displaying different textural domains (Figure 3.2c) and is generally intensively crosscut by serpentine veins associated with Fe oxide. Domain 1 is highly amphibolized with substantially recrystallized olivine. In this domain the orthopyroxene porphyroclasts are small (up to 2 mm in length) and elongated conforming to the orientation of the mylonitic foliation. Embedded within the serpentine veins of this domain veins and an aggregate of retrograde magnesite occur (Förster et al., 2017). In the adjacent domain 2 olivine is still present and the partly elongated orthopyroxene porphyroclasts are up to 1 cm in length. It is in this domain that a zircon inclusion in amphibole is observed (section 3.5.2.3). Domain 3 is characterized by elevated olivine content and more serpentine/chlorite veins, while domain 4 is the amphibole-richest domain. Domain 5 is similar to domain 3. Although sample SBB2F is garnet-free, it derives from an outcrop where mainly fine-grained garnet-amphibole peridotites occur.

3.3.2 Phlogopitite

Petrographic features and mineral compositions (major and trace elements) of sample NB103 were previously reported in Marocchi et al. (2009, 2010). This sample derives from a metasomatic reaction band between peridotites and crustal rocks at Mount Hochwart (Figure 3.1). The metasomatic reaction zone contains phlogopite-rich to tremolite-anthophyllite-rich cm wide bands from the gneisses towards the peridotite. The thin section NB103 consists of a phlogopite-rich domain, containing fibrous phlogopite and green amphibole, and a pale-green amphibole-rich domain (Figure 3.2d). This domain also bears green amphibole, quartz, phlogopite, plagioclase, Cl-apatite and rutile, with amphibole partly containing rutile and graphite inclusions while quartz bears amphibole and phlogopite inclusions.

3.4 Analytical techniques

3.4.1 Petrography

Petrographic observations of zircons in the UZ peridotites were carried out on polished thick sections (~100 µm) using conventional optical microscopy and scanning electron microscopy (SEM, Philips 515B with energy-dispersive system EDS; 5 µm spot size, 15 kV voltage) at the Dipartimento di Scienze Biologiche, Geologiche e Ambientali of the University of Bologna (Italy) as well as optical microscopy at Géosciences Montpellier at the University of Montpellier (France).

3.4.2 Bulk rock analysis

Analyses of bulk-rock compositions (major and trace element contents) of samples PL1.6 and VM25P10A were carried out by inductively coupled (ICP) atomic emission spectroscopy (major elements) and ICP mass spectrometry (trace elements) at Activation Laboratories (Ontario, Canada). The concentration of FeO was determined by titration. Detailed information of analytical techniques and detection limits is reported in Table A3 in the Appendix. Precision and accuracy for trace element analyses are within 10%.

3.4.2 Mineral major element and trace element analyses and zircon U-Pb age dating

Major element compositions of garnets in sample PL1.6 were analyzed using an electron microprobe CAMECA SX100 (Géosciences Montpellier) with an accelerating voltage and beam current of 20 kV and 10 nA respectively. *In-situ* analyses of trace element compositions in zircon and garnet and U-Pb age determinations on zircons were performed on thick sections of the four samples. Analyses were performed by LA-ICP-MS using a LambdaPhysik Compex 102 excimer laser coupled to a ThermoFinnigan Element XR ICP-MS (AETE-ISO regional facility of the OSU OREME, University of Montpellier). The instrument was tuned for maximum sensitivity and low oxide production (ThO/Th < 1%). Analytical conditions are identical to those reported in previous studies (e.g. Bosch et al., 2011; Bruguier et al., 2017) where ablation experiments were performed under helium in order to increase sensitivity and to reduce inter-element fractionation (Günther & Heinrich, 1999). The helium stream and particles ablated from the sample were subsequently mixed with Ar before entering the plasma. Laser spot size for age determinations varied between 26 µm (PL1.6, SBB2F, NB103) and 51 µm (VM25P10A). The laser was operated at a repetition rate of 3 Hz using a 12 J/cm^2 energy density. Total analysis time was 60 s with the first 15 s used for background measurement which was subtracted from the sample signal. Before each analysis, the surface of the targeted zone was cleaned with 10 pulses using a spot size larger than the size used for U-Pb analysis. Pb/U and Pb/Pb ratios were calibrated against the zircon standards G91500 (Wiedenbeck et al., 1995) and GJ1 (Jackson et al., 2004), which were used to correct the measured ratios for mass discrimination and inter-element fractionation. In the course of this study the zircon standards were measured twice each five unknowns. U-Th-Pb isotopic data were reduced using the *Glitter* software (van Achterberg et al., 2001) and ages were calculated using *Isoplot* (Ludwig, 2003) and are quoted in the text at the 2σ confidence level.

Trace element analyses were performed using the same laser ablation equipment described above. For zircon, the spot size varied between 26 µm (SBB2F, NB103) and 51 µm (PL1.6, VM25P10A), depending on the size of the zircon grain. The spot size for garnet analyses was 77 µm. Synthetic glass NIST612 was used for external standardization (values after Pearce et al., 1997), whereas the matrix matching zircon standard G91500 (Wiedenbeck et al., 1995) and the BIR1-G basaltic glass (values taken from GEOREM preferred values) were used to check the results for accuracy on unknown zircon and garnet, respectively. Internal standardization used SiO_2 for zircon (32.97 wt. % stoichiometric value) and CaO for garnet (4.55 to 5.25 wt. % from electron microprobe analyses). Data evaluation was done using the software package *Glitter* (van Achterberg et al., 2001).

3.5 Results

3.5.1 Whole-rock trace element compositions

Results of whole-rock major and trace element analyses of the two peridotite samples PL1.6 and VM25P10A and of the phlogopitite sample NB103 are given in Table A3 (Appendix). The chemical composition of NB103 was previously reported in Marocchi et al. (2009) (see their Table 3, NB101B_03, Zone C). In order to compare individual peridotite types (coarse-grained garnet-free/garnet bearing, fine-grained garnet-amphibole peridotite, fine-grained amphibole(-chlorite) peridotite) regarding their trace element budget, trace element compositions of the studied samples are shown together with literature data and unpublished data on other UZ peridotite samples (Figure 3.3).

The Ce_N/Yb_N ratio (Figure 3.3a) as well as the ΣLREE (not shown) increase from coarse-grained to fine-grained peridotites. In addition, Ce_N/Yb_N and Zr contents show a positive correlation (Figure 3.3a), as do the LILE Sr, Ba (Figure 3.3b,c), Rb as well as Hf, Nb, U (not shown) and Th (Figure 3.3d). The geochemical heterogeneity of the different types of peridotites is highlighted by Zr concentrations, which are generally higher in fine-grained peridotites, especially the garnet-bearing ones, relative to the coarse-grained both garnet-free and garnet-bearing peridotites. Peridotites with low abundance of amphibole show the lowest concentrations in Zr and all other studied trace elements. Although UZ peridotites show enrichment in LILE over HFSE (e.g. Rampone & Morten, 2001; Scambelluri et al., 2006), fine-grained peridotites are clearly enriched in HFSE compared to coarse-grained peridotites.

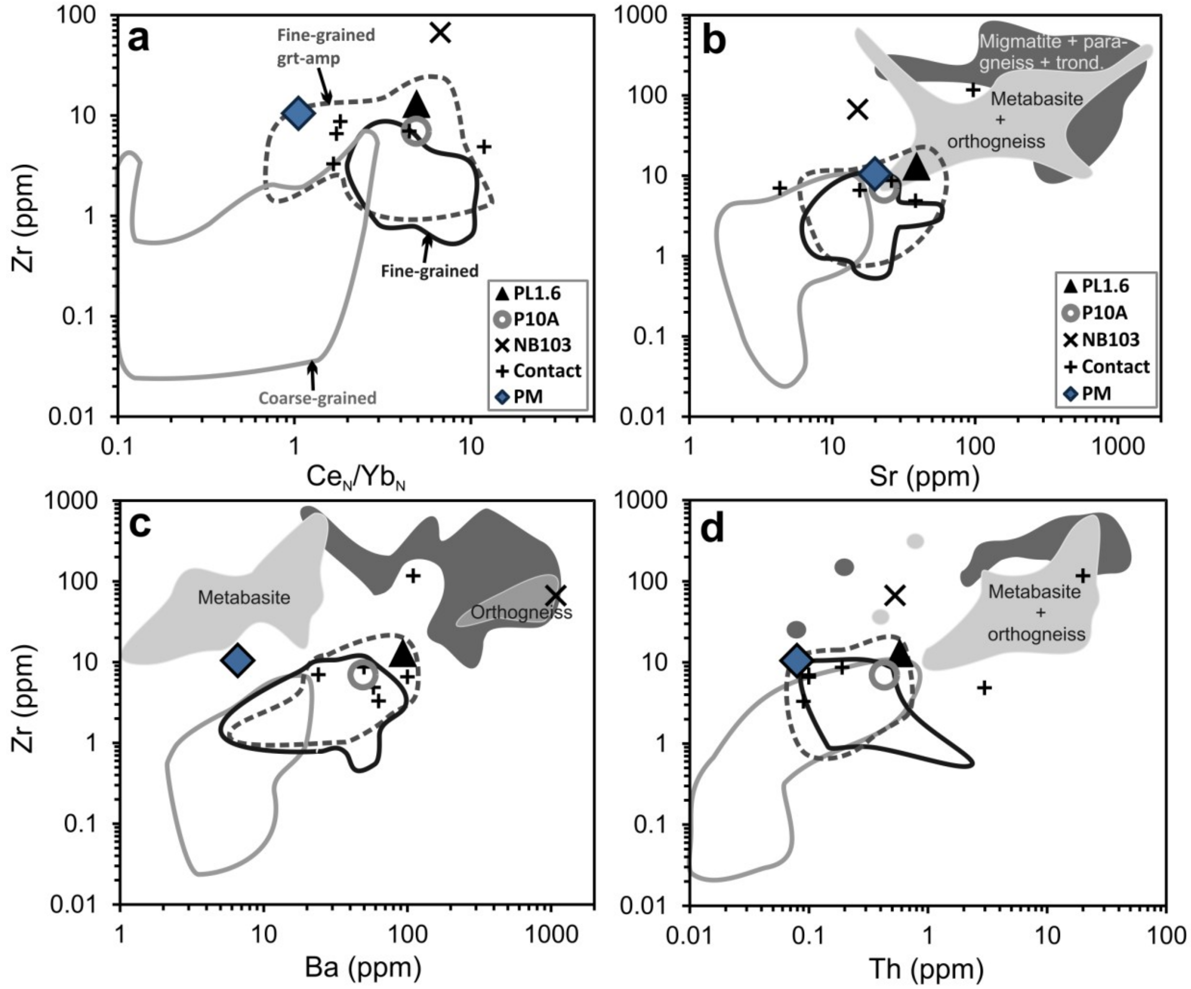

Figure 3.3. Bulk-rock trace element compositions showing Zr vs. (a) Ce_N/Yb_N, (b) Sr, (c) Ba, (d) Th, of zircon-bearing Ulten Zone (UZ) peridotites PL1.6 and VM25P10A and phlogopitite sample NB103, compared to literature data and new data (not published) for zircon-free coarse-grained, fine-grained grt-free and garnet-bearing UZ peridotite, rocks from the crust-peridotite contact zone, crustal rocks (gray shaded fields) and primitive mantle (PM; McDonough & Sun, 1995). Literature data for NB103 from Marocchi et al. (2009), for crust-mantle contact zones from Tumiati et al. (2007) and Marocchi et al. (2009), for coarse-grained peridotites from Morten & Obata (1990), Scambelluri et al. (2006), Tumiati et al. (2006), Ionov et al., (2017), for fine-grained garnet-free peridotites from Morten & Obata (1990), Bargossi et al. (2003), Scambelluri et al. (2006), Tumiati et al. (2006), Marocchi et al. (2007, 2009), Ionov et al., (2017), for fine-grained garnet-bearing peridotites from Morten & Obata (1990), Bargossi et al. (2003), Scambelluri et al. (2006), Tumiati et al. (2006), Marocchi et al. (2009), Sapienza et al. (2009), Ionov et al., (2017) and for crustal rocks from Del Moro et al. (1999), Bondi & Morten (2000), Bargossi et al. (2003), Tumiati et al. (2007), Marocchi et al. (2009).). CeN and YbN chondrite-normalized, chondrite values from Sun & McDonough (1989). Mineral abbreviations after Whitney & Evans (2010).

3.5.2 Zircon petrography, geochronology and trace element compositions

3.5.2.1 Sample PL1.6

One elongated zircon grain of ~1.5 mm length with curvilinear but sharp grain boundaries against the ultramafic matrix was observed in sample PL1.6 (Figure 3.4). The zircon contains small inclusions, is crosscut by thin fractures and is in contact with the surrounding matrix olivine, amphibole and serpentine veins (Figure 3.4a,b). Results of zircon age determination are listed in Table 3.1.

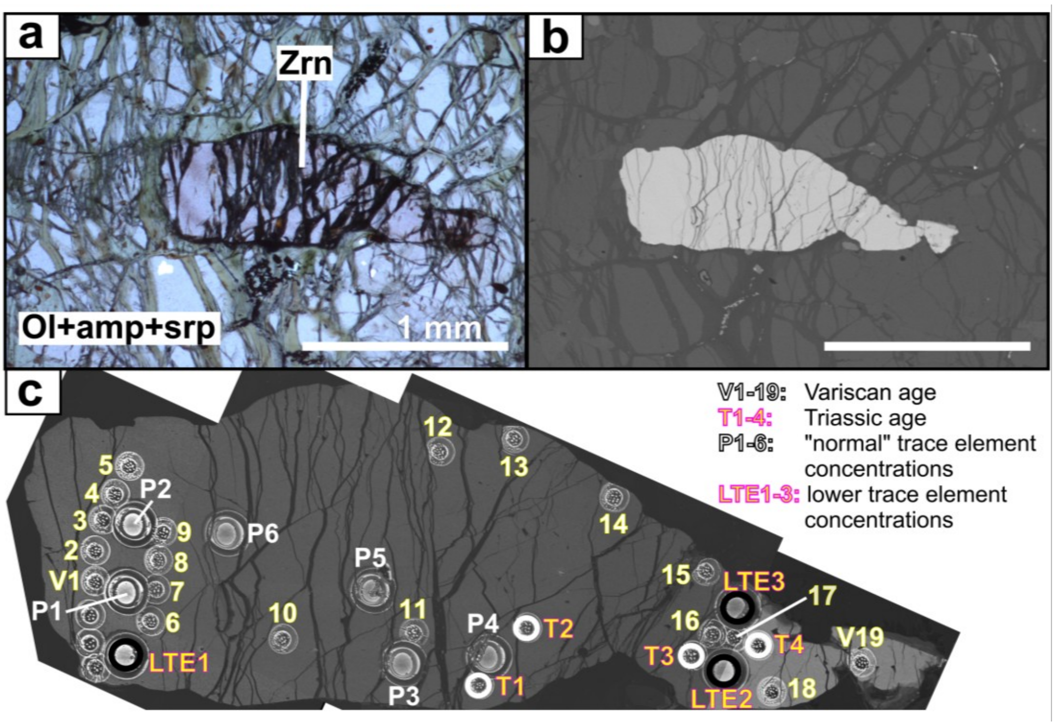

Figure 3.4. (a) Photomicrograph of the zircon (~1.5 mm) in the fine-grained garnet-bearing peridotite PL1.6 in association to the matrix mineral assemblage (olivine, amphibole and serpentine veins). (b) Back-scattered electron (BSE) image of the zircon crystal set in the peridotite matrix and (c) BSE image composed of four individual images (note that slightly different gray shades across images do not relate to composition) with spots from LA-ICP-MS for U-Pb geochronology (small pits) and for trace element analyses (large pits). The four spots labeled T1, T2, T3 and T4 display Triassic ages (ca. 236 Ma) while the other spots (V1-V19) exhibit Variscan ages (ca. 333 Ma). The three marked spots labeled LTE1, LTE2 and LTE3 have lower trace element concentrations than all other spots (P1-P6). Different gray shading is due to different brightness in the individual BSE images. Mineral abbreviations after Whitney & Evans (2010).

Analyses for U-Pb dating comprise 23 spots both at the rim and in the core of the grain (Table 3.2; Figure 3.5a). Of these, 19 spot analyses (V1 – V19; Figure 3.4c) performed in both core and rim, yield concordant data points which can be combined to provide a ^{206}Pb/^{238}U weighted mean age of 333.0 ± 2.0 Ma (MSWD = 0.47). Four spot analyses, located close to the rim (T1, T2, T3, T4; Figure 3.4c), yield a younger age of 236.0 ± 8.0 Ma (MSWD = 0.22). A total of 9 spots, likewise distributed in core and rim of the grain (Figure 3.4c), were measured for trace element compositions (Table 3.3).

Table 3.2 U-Th-Pb LA-ICP-MS zircon data from three peridotites and one phlogopitite from the Ulten Zone (Italy)

Spot name	Domain	Pb* (ppm)	Th (ppm)	U (ppm)	Th/U	^{207}Pb/206Pb (uncorrected)	±Error (1σ)	^{207}Pb/^{235}U	±Error (1σ)	^{206}Pb/^{238}U	±Error (1σ)	^{206}Pb/^{238}U age (Ma)	±Error (1σ)
Peridotite PL1.6													
V1	Core	55	311	885	0.352	0.0535	0.0015	0.3905	0.0095	0.0531	0.0006	334	4
V2	Core	30	134	500	0.268	0.0549	0.0016	0.3971	0.0104	0.0526	0.0006	330	4
V3	Core	17	64	323	0.199	0.0533	0.0021	0.3835	0.0137	0.0523	0.0008	329	5
V4	Core	48	266	795	0.335	0.0538	0.0014	0.3911	0.0091	0.0528	0.0006	332	3
V5	Core	57	316	876	0.360	0.0538	0.0014	0.3916	0.0089	0.0529	0.0006	332	3
V6	Core	27	112	481	0.233	0.0543	0.0025	0.3938	0.0168	0.0527	0.0009	331	5
V7	Core	19	67	340	0.196	0.0540	0.0020	0.3952	0.0137	0.0532	0.0008	334	5
V8	Core	37	172	608	0.283	0.0545	0.0016	0.3985	0.0105	0.0531	0.0006	334	4
V9	Core	67	414	1051	0.394	0.0538	0.0013	0.3978	0.0089	0.0538	0.0006	338	3
V10	Core	39	202	680	0.297	0.0540	0.0017	0.3882	0.0108	0.0522	0.0007	328	4
V11	Core/fracture	14	54	255	0.211	0.0535	0.0024	0.3940	0.0164	0.0535	0.0009	336	5
V12	Rim	57	330	960	0.344	0.0533	0.0017	0.3900	0.0110	0.0532	0.0007	334	4
V13	Rim	23	83	427	0.196	0.0534	0.0021	0.3837	0.0138	0.0522	0.0008	328	5
V14	Rim	11	25	219	0.112	0.0533	0.0029	0.3913	0.0201	0.0533	0.0011	335	6
V15	Rim	19	70	334	0.211	0.0529	0.0024	0.3862	0.0163	0.0531	0.0009	333	5
V16	Core	23	118	420	0.282	0.0525	0.0030	0.3772	0.0204	0.0522	0.0011	328	7
V17	Core	24	96	408	0.236	0.0524	0.0023	0.3881	0.0160	0.0538	0.0009	338	6
V18	Rim	28	136	487	0.279	0.0529	0.0024	0.3881	0.0160	0.0533	0.0009	335	6
V19	Rim	51	174	870	0.200	0.0542	0.0022	0.3992	0.0148	0.0534	0.0009	336	5
T1	*Rim*	*4*	*23*	*105*	*0.214*	*0.0546*	*0.0071*	*0.2738*	*0.0342*	*0.0364*	*0.0013*	*231*	*8*
T2	*Core*	*4*	*20*	*97*	*0.203*	*0.0536*	*0.0108*	*0.2798*	*0.0540*	*0.0379*	*0.0023*	*240*	*14*
T3	*Rim*	*7*	*48*	*179*	*0.270*	*0.0612*	*0.0049*	*0.3177*	*0.0242*	*0.0377*	*0.0010*	*239*	*6*
T4	*Rim*	*6*	*25*	*155*	*0.165*	*0.0520*	*0.0059*	*0.2671*	*0.0292*	*0.0373*	*0.0013*	*236*	*8*
Peridotite VM25P10A													
10A-1	Core	2	8	39	0.204	0.0511	0.0041	0.3780	0.0289	0.0537	0.0013	337	8
10A-2	Core/fracture	4	22	74	0.301	0.0541	0.0026	0.3927	0.0180	0.0527	0.0009	331	6
10A-3	Core/fracture	3	20	62	0.317	0.0539	0.0028	0.3988	0.0200	0.0537	0.0010	337	6
10A-4	Close to rim	1	6	28	0.219	0.0524	0.0050	0.3859	0.0358	0.0534	0.0014	335	9
10A-5	Rim	3	34	52	0.651	0.0529	0.0032	0.3903	0.0223	0.0536	0.0011	336	6
10A-6	Close to rim	5	50	85	0.586	0.0523	0.0025	0.3844	0.0177	0.0533	0.0009	335	6
10A-7	"Fine-grained" domain/fracture	4	26	75	0.341	0.0549	0.0028	0.3940	0.0190	0.0520	0.0010	327	6
10A-8	Core/fracture	4	23	69	0.334	0.0524	0.0028	0.3795	0.0192	0.0525	0.0010	330	6
10A-9	Core	3	16	53	0.302	0.0545	0.0034	0.3974	0.0237	0.0529	0.0011	332	7
10A-10	Core	3	17	56	0.307	0.0532	0.0035	0.3923	0.0247	0.0535	0.0012	336	7
10A-11	Core/fracture	3	21	67	0.313	0.0516	0.0035	0.3717	0.0242	0.0523	0.0012	328	7

Spot name	Domain	Pb* (ppm)	Th (ppm)	U (ppm)	Th/U	^{207}Pb/206Pb (uncorrected)	±Error (1σ)	^{207}Pb/^{235}U	±Error (1σ)	^{206}Pb/^{238}U	±Error (1σ)	^{206}Pb/^{238}U age (Ma)	±Error (1σ)
10A-12	Core	3	17	62	0.275	0.0544	0.0033	0.3969	0.0227	0.0530	0.0011	333	7
10A-13	Core/close to rim	4	27	70	0.389	0.0558	0.0030	0.4048	0.0206	0.0527	0.0010	331	6
10A-14	Core	2	6	30	0.212	0.0512	0.0072	0.3720	0.0504	0.0527	0.0020	331	12
10A-15	Core	2	10	46	0.227	0.0530	0.0043	0.3857	0.0300	0.0528	0.0013	332	8
10A-16	Core	3	11	53	0.210	0.0599	0.0040	0.4364	0.0279	0.0528	0.0012	332	7
10A-17	Core	3	8	39	0.202	0.0550	0.0118	0.4115	0.0843	0.0543	0.0039	341	24
10A-18	Core	2	6	31	0.182	0.0525	0.0076	0.3898	0.0547	0.0538	0.0022	338	14
10A-19	Core	3	18	55	0.332	0.0536	0.0047	0.4016	0.0340	0.0544	0.0015	341	9
10A-20	Close to rim	3	18	54	0.334	0.0583	0.0039	0.4329	0.0274	0.0539	0.0012	338	7
10A-21	Core	2	11	47	0.229	0.0564	0.0046	0.4094	0.0320	0.0527	0.0013	331	8
10A-22	Close to rim	2	8	42	0.197	0.0552	0.0070	0.4022	0.0499	0.0529	0.0014	332	9
10A-23	Rim	27	488	436	1.119	0.0538	0.0015	0.3980	0.0101	0.0537	0.0007	337	4
10A-24	"Fine-grained" domain	3	21	61	0.353	0.0544	0.0047	0.4106	0.0343	0.0547	0.0014	343	9
10A-25	"Fine-grained" domain	4	16	73	0.225	0.0543	0.0034	0.3949	0.0240	0.0527	0.0011	331	7
Peridotite SBB2F													
S1		46	111	931	0.120	0.0528	0.0015	0.3770	0.0094	0.0518	0.0006	326	4
S2		39	137	736	0.186	0.0571	0.0016	0.4200	0.0109	0.0534	0.0007	335	4
S3		77	292	1544	0.189	0.0536	0.0014	0.3731	0.0088	0.0506	0.0006	318	4
S4		91	437	1720	0.254	0.0560	0.0015	0.3977	0.0095	0.0516	0.0006	324	4
S5		82	457	1520	0.301	0.0531	0.0015	0.3770	0.0098	0.0516	0.0006	324	4
S6		61	319	976	0.327	0.0559	0.0022	0.4024	0.0144	0.0522	0.0009	328	5
Phlogopitite NB103													
NB1-1	Grain 1	113	192	2240	0.086	0.0534	0.0015	0.3983	0.0101	0.0541	0.0007	340	4
NB1-2	Grain 1	125	259	2549	0.102	0.0533	0.0015	0.3896	0.0100	0.0531	0.0007	333	4
NB1-3	Grain 1	81	156	1678	0.093	0.0530	0.0016	0.3828	0.0109	0.0525	0.0007	330	4
NB2-1	Grain 2	111	130	2262	0.057	0.0541	0.0016	0.4003	0.0111	0.0537	0.0007	337	4
NB2-2	Grain 2	121	194	2543	0.076	0.0532	0.0016	0.3821	0.0109	0.0521	0.0007	327	4
NB2-3	Grain 2	129	191	2694	0.071	0.0525	0.0018	0.3857	0.0122	0.0533	0.0008	335	5
NB3-1	Grain 3	199	381	4403	0.087	0.0527	0.0020	0.3792	0.0133	0.0522	0.0009	328	5
NB3-2	Grain 3	75	117	1609	0.073	0.0521	0.0022	0.3768	0.0153	0.0525	0.0010	330	6

* Pb* denotes radiogenic lead.

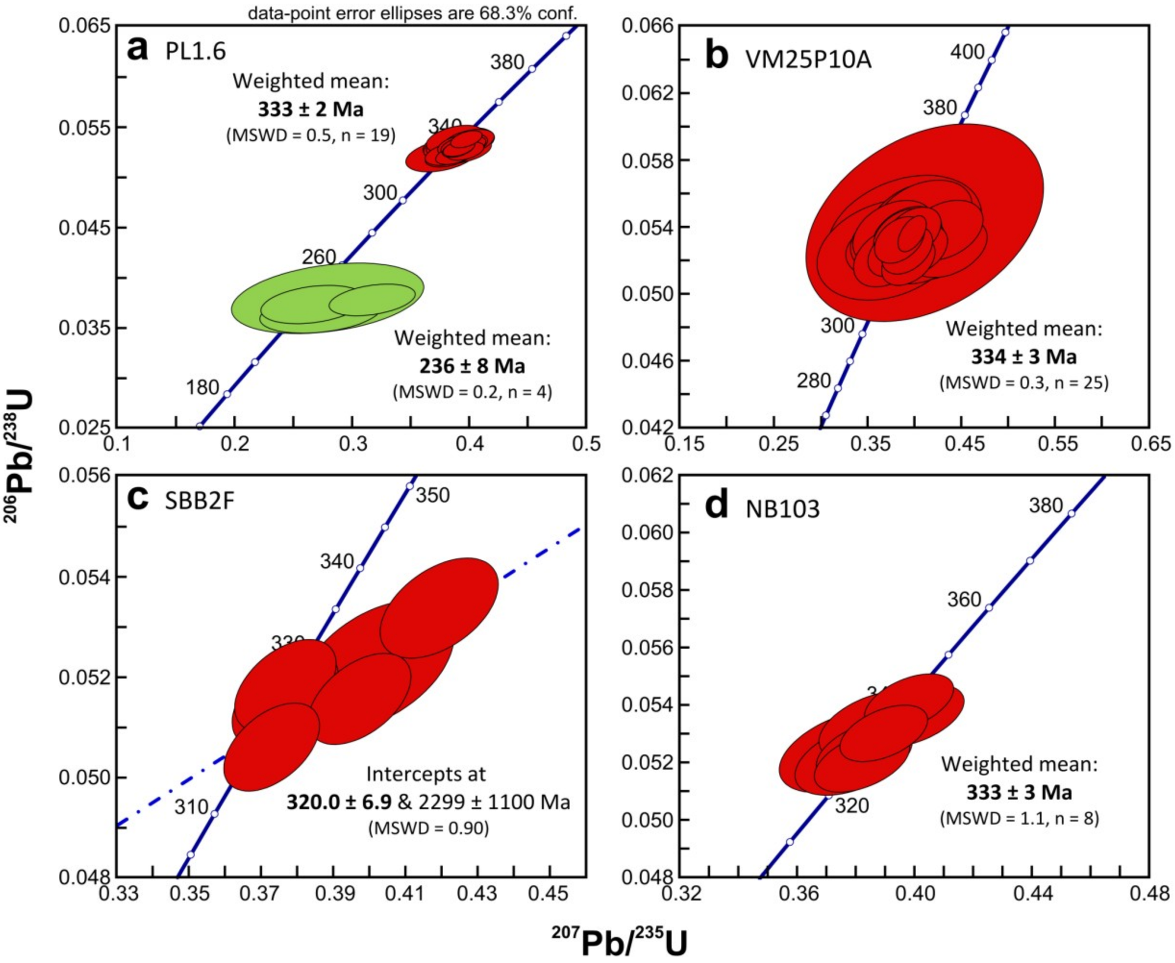

Figure 3.5. Zircon U-Pb concordia diagrams for peridotites and a crust-peridotite contact rock (phlogopitite) from the Ulten Zone using LA-ICP-MS. (a) the zircon in the garnet-bearing peridotite PL1.6 exhibits a domain with Variscan age (333 ± 2 Ma) and four spots show a younger Triassic age (236 ± 8 Ma); (b) the large zircon (~1 cm) in the peridotite with garnet-pseudomorphs VM25P10A yields 334 ± 3 Ma; (c) the U-Pb system in the zircon in the highly amphibolized peridotite SBB2F provides a lower intercept age of 320.0 ± 6.9 Ma; (d) the three zircons in the phlogopitite NB103 exhibit a consistent age of 333 ± 3 Ma.

All analyses show chondrite-normalized REE patterns with a positive Ce anomaly and no Eu anomaly (Figure 3.6a). Based on REE concentrations and MREE/HREE fractionation, the trace element analyses can be subdivided into two groups.

The first group, composed of three analyses (LTE1 – LTE3), has normalized REE concentrations lower than the second group (P1 – P6; Figures 3.4c, 3.7a). The slope of MREE to HREE of the first group is steeper (Sm/Yb = 0.06 - 0.13) than that of the second group (Sm/Yb = 0.18 - 0.27). Two of those spots (LTE2 and LTE3) are spatially close to two spots with the younger U-Pb age (T3 and T4; Figure 3.4c), but also close to two spots with the older age (V16 and V17; Figure 3.4c). The other spot with low trace element contents (LTE1) cannot be related to a particular zircon age. The Th/U ratio ranges from 0.55 to 0.82 (Table 3.3; Figure 3.7c) and shows no correlations with locations in the zircon grain. Ti concentrations range from 4.3 to 10.6 ppm (Table 3.3).

Table 3.3 Trace element concentrations (ppm) of zircons in peridotites and a phlogopitite from the Ulten Zone (Italy).

	Peridotite																										Phlogopitite						Standard	
Sample:	PL1.6									VM25P10A													SBB2F				NB103						G91500	
Spot name:	P1	P2	P3	P4	P5	LTE1	LTE2	LTE3	P6	A1	A2	A3	A4	A5	A6	A7	A8	A9	A10	A11	A12	A13	S1	S2	S3	S4	G1-1	G1-2	G1-3	G2-1	G2-2	G2-3	Mean value	stdev (%)
Domain :							Close to "Triassic" age			Highly fractured part				Close to dol								Rim					Grain 1			Grain 2				
P	264	373	308	369	486	151	130	94	338	119	110	98	92	70	75	161	99	100	111	98	80	68	64	103	109	263	142	150	169	146	134	132	23	13
Ca	23	237	28	484	226	<dl	24	<dl	80	<dl	<dl	<dl	11	<dl	<dl	233	16	<dl	26	<dl	16	<dl	<dl	<dl	<dl	<dl	<dl	<dl	<dl	<dl	<dl	<dl	13	96
Ti	7.83	10.56	8.75	5.84	8.63	6.97	5.95	4.26	9.34	8.25	7.80	7.83	7.39	6.38	5.99	5.32	5.85	6.88	5.62	5.88	4.74	4.85	2.34	4.05	6.60	7.22	2.59	<dl	2.23	0.23	3.89	3.85	5.21	7
Rb	0.08	0.09	0.12	0.10	0.21	0.08	0.02	0.05	0.10	0.07	0.00	0.03	<dl	<dl	<dl	<dl	<dl	0.01	<dl	<dl	<dl	0.01	0.07	0.06	0.01	0.86	0.082	0.039	0.304	0.157	0.167	0.074	0.058	48
Sr	0.21	0.94	0.41	1.19	0.93	0.35	0.13	0.16	0.58	0.12	0.16	0.43	0.11	0.55	0.13	3.23	1.01	0.14	0.14	0.20	0.07	0.14	<dl	<dl	0.09	<dl	0.27	<dl	<dl	<dl	<dl	<dl	0.13	11
Y	409.94	484.33	524.59	646.08	676.59	223.71	195.42	79.80	442.05	51.63	44.49	26.06	15.74	22.69	14.93	22.21	22.77	20.90	21.10	22.89	18.78	23.84	48.27	200.24	161.74	429.99	384.96	363.21	644.2	241.91	504.94	391.65	119.80	11
Nb	7.57	12.44	4.05	5.59	8.99	1.84	1.67	1.11	11.19	1.10	1.23	1.55	1.71	1.92	1.58	1.81	1.87	1.15	0.85	1.09	1.15	1.82	1.44	2.93	2.90	5.91	1.50	1.45	2.49	1.78	2.17	1.63	1.01	7
Sn	0.92	1.30	0.76	1.08	1.53	0.24	0.17	0.20	1.33	0.19	0.10	0.20	0.15	0.19	0.09	0.23	0.03	0.13	<dl	0.29	0.23	0.25	0.05	0.41	0.52	0.57	0.96	0.61	0.88	0.15	0.75	0.17	0.23	83
Cs	<dl	0.00	0.00	<dl	<dl	<dl	<dl	0.00	0.02	<dl	<dl	<dl	<dl	<dl	<dl	0.03	<dl	<dl	<dl	0.01	<dl	0.00	0.03	0.01	0.02	0.11	0.013	<dl	0.046	<dl	<dl	<dl	0.018	45
Ba	0.09	0.12	0.09	1.06	0.23	0.49	0.02	0.08	0.49	0.02	0.00	0.26	<dl	1.29	0.07	0.19	1.00	0.02	<dl	0.07	0.02	0.05	0.28	0.44	0.13	0.92	0.05	<dl	0.08	<dl	0.31	0.39	0.002	2125
La	0.046	0.264	0.082	0.116	0.450	0.024	0.035	0.021	0.171	0.012	0.043	0.049	0.024	0.045	0.043	1.597	0.286	0.058	0.052	0.033	0.005	0.006	0.051	0.039	0.256	0.590	0.049	0.028	0.067	0.035	<dl	0.108	0.016	98
Ce	21.17	31.97	18.30	27.13	30.60	5.45	6.61	3.18	25.76	1.83	2.84	6.80	8.10	7.15	8.33	9.61	9.93	4.22	1.68	1.77	2.29	4.38	4.61	11.50	16.00	34.16	3.04	2.44	1.87	1.36	1.68	3.59	2.31	7
Pr	0.42	0.71	0.81	0.98	1.74	0.12	0.22	0.06	0.60	0.02	0.04	0.07	0.06	0.04	0.05	0.21	0.10	0.06	0.02	0.01	0.02	0.02	0.05	0.09	0.23	0.66	0.05	0.01	0.03	0.04	<dl	0.08	0.010	53
Nd	7.95	13.03	14.15	19.24	23.73	2.35	3.39	0.86	11.46	0.25	0.43	0.58	0.81	0.43	0.65	1.00	0.60	0.57	0.29	0.11	0.17	0.40	0.44	1.28	2.86	7.65	0.98	1.37	0.78	0.18	0.33	1.17	0.20	23
Sm	11.61	17.96	18.33	26.54	29.69	3.21	4.52	1.23	15.09	0.45	0.49	0.44	0.56	0.29	0.45	0.64	0.48	0.34	0.30	0.26	0.32	0.38	0.52	1.68	3.52	9.71	3.92	3.71	2.06	0.72	1.96	2.06	0.38	22
Eu	5.54	8.13	8.95	12.28	14.07	1.81	2.08	0.64	7.32	0.30	0.20	0.18	0.18	0.16	0.18	0.18	0.21	0.15	0.12	0.13	0.11	0.10	0.38	1.22	2.04	4.94	1.30	1.48	0.89	0.18	0.88	0.88	0.18	16
Gd	28.48	40.33	42.90	54.69	59.97	9.61	10.52	3.49	34.87	1.70	1.31	0.85	0.69	0.86	0.83	1.10	1.06	0.51	0.76	0.70	0.51	0.65	1.29	5.94	8.44	19.53	11.59	12.77	10.06	2.93	10.69	8.78	1.57	22
Tb	6.55	8.57	8.81	12.42	12.90	2.67	2.70	0.91	7.56	0.47	0.43	0.25	0.18	0.17	0.12	0.25	0.23	0.16	0.17	0.20	0.13	0.18	0.48	1.96	2.06	6.60	4.80	5.24	5.29	1.65	4.72	3.75	0.71	8
Dy	54.14	73.25	72.33	98.65	104.51	26.00	24.03	8.36	62.85	5.86	4.83	2.46	1.59	2.28	1.60	2.44	2.07	1.86	2.02	1.70	1.65	2.57	5.66	21.17	22.11	54.91	45.34	43.91	63.15	22.45	54.16	41.98	10.44	7
Ho	13.98	17.54	18.43	24.28	25.51	7.70	6.44	2.70	15.73	1.84	1.52	0.84	0.51	0.71	0.47	0.74	0.73	0.65	0.61	0.75	0.60	0.80	1.62	6.64	5.45	14.94	12.29	11.75	22.06	7.94	17.09	12.90	4.23	7
Er	45.67	54.17	57.37	77.25	78.18	26.41	22.50	10.10	49.54	7.96	6.58	3.77	2.26	3.12	2.14	3.08	3.32	3.27	3.09	3.17	2.85	3.45	6.46	25.49	20.66	52.51	46.28	44.56	94.68	37.68	66.72	53.57	21.91	8
Tm	8.22	9.28	10.18	13.18	13.62	4.95	4.07	2.07	8.82	1.76	1.63	0.93	0.62	0.87	0.47	0.84	0.79	0.80	0.86	0.91	0.64	0.88	1.68	5.96	4.38	9.09	10.10	9.03	21.42	9.09	14.23	11.12	6.40	6
Yb	66.16	77.04	83.67	108.19	111.04	43.79	35.84	19.41	70.11	19.87	17.03	10.49	5.74	8.20	5.01	8.15	8.54	8.41	9.08	8.96	7.37	8.75	15.21	53.07	35.62	81.92	95.06	86.21	210.84	95.13	117.60	97.65	73.50	4
Lu	9.97	10.99	12.93	16.10	15.88	7.43	5.82	3.18	10.27	3.38	3.03	1.75	1.20	1.63	0.97	1.51	1.62	1.73	1.60	1.78	1.51	1.79	3.03	9.08	6.05	11.87	15.13	13.00	33.19	16.31	20.24	15.32	10.07	11
Hf	11765	12167	12086	12066	12168	12134	11719	12578	13555	7016	7235	6907	7443	7402	7846	7734	7870	7719	7336	7188	7836	7871	11364	14115	12144	11956	13584	14546	13997	13229	13413	13561	5436	13
Ta	3.32	5.62	1.92	2.44	3.98	1.16	0.88	0.71	5.00	0.37	0.32	0.48	0.39	0.74	0.33	0.48	0.45	0.33	0.34	0.38	0.34	0.82	1.03	2.12	1.23	2.25	2.74	2.75	2.9	3.04	2.89	2.23	0.54	6
Pb*	24.4	35.3	17.2	24.5	26.1	14.5	18.1	14.9	27.8	4.4	3.5	3.1	2.3	4.7	2.0	3.1	3.1	2.9	2.9	2.8	2.7	16.9	25.2	67.3	40.8	91.3	240.9	197.0	89.5	129.9	127.6	133.5	13.78	6
Th	290.8	493.8	176.2	285.3	338.4	169.7	205.0	135.2	321.8	23.4	19.2	14.4	9.4	62.2	12.4	24.0	18.4	10.9	9.2	12.5	12.5	252.1	120.9	196.9	283.6	785.3	57.2	66.6	33.2	23.3	30.5	31.8	23.54	9
U	424.4	601.3	296.1	422.6	454.3	265.8	327.5	245.4	492.9	72.3	60.0	53.3	37.0	79.2	33.6	51.1	50.8	49.8	49.3	47.4	44.5	295.1	386.9	1075.6	695.5	1457.4	3041.8	2681.7	1241.9	1997.4	1922.0	1812.9	68.60	7
Nb/Ta	2.28	2.21	2.11	2.29	2.26	1.58	1.89	1.56	2.24	2.98	3.89	3.23	4.37	2.58	4.79	3.76	4.14	3.52	2.50	2.86	3.35	2.23	1.41	1.38	2.35	2.63	0.55	0.53	0.86	0.59	0.75	0.73	1.87	7
Y/Ho	29.3	27.6	28.5	26.6	26.5	29.1	30.3	29.6	28.1	28.1	29.2	31.1	30.9	32.2	31.5	30.2	31.0	32.0	34.7	30.7	31.1	30.0	29.7	30.2	29.7	28.8	31.3	30.9	29.2	30.5	29.5	30.4	28.24	4
Th/U	0.69	0.82	0.59	0.68	0.74	0.64	0.63	0.55	0.65	0.32	0.32	0.27	0.25	0.79	0.37	0.47	0.36	0.22	0.19	0.26	0.28	0.85	0.31	0.18	0.41	0.54	0.02	0.02	0.03	0.01	0.02	0.02	0.34	4
Sm/Yb	0.18	0.23	0.22	0.25	0.27	0.07	0.13	0.06	0.22	0.02	0.03	0.04	0.10	0.04	0.09	0.08	0.06	0.04	0.03	0.03	0.04	0.04	0.03	0.03	0.10	0.12	0.04	0.04	0.01	0.01	0.02	0.02		
Yb/Sm	5.70	4.29	4.56	4.08	3.74	13.64	7.93	15.78	4.65	44.06	34.68	23.95	10.31	28.47	11.04	12.79	17.90	24.96	30.78	33.94	23.10	23.33	29.25	31.59	10.12	8.44	24.25	23.24	102.35	132.13	60.00	47.40		
Ce/Ce*	37.48	18.17	17.39	19.69	8.48	25.43	18.34	21.80	19.75	26.99	17.85	28.78	51.90	41.06	45.10	4.11	14.40	18.32	11.92	26.56	50.73	100.05	23.09	46.82	16.24	13.43	15.37	30.22	10.37	9.39	<dl	9.35		
Eu/Eu*	0.93	0.92	0.98	0.99	1.02	0.98	0.99	0.92	0.94	1.05	0.75	0.92	0.87	0.96	0.87	0.66	0.90	1.09	0.74	0.94	0.79	0.59	1.43	1.18	1.14	1.10	0.59	0.66	0.60	0.39	0.59	0.63		

Internal standardization was done stoichiometrically by assuming SiO_2 = 32,97%.

* Pb* denotes radiogenic lead.

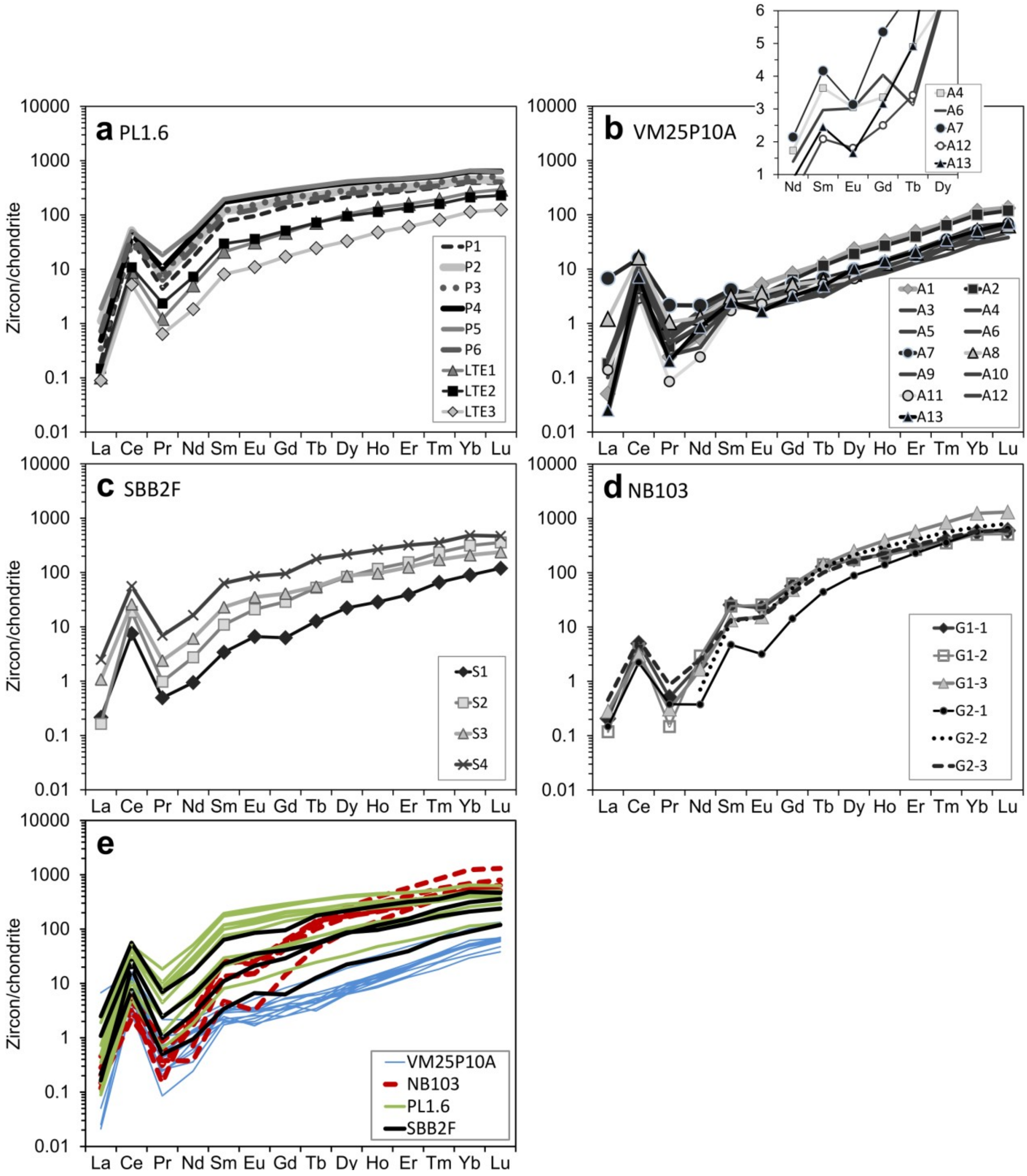

Figure 3.6. Chondrite-normalized REE patterns for zircon in peridotites. (a) PL1.6, (b) VM25P10A, (c) SBB2F, and (d) phlogopitite (from the crust-peridotite contact zone) NB103, from the Ulten Zone. In (a) spots P1 to P6 are linked to the Variscan age, while the spots with lower trace element contents (LTE1 to LTE3) are partly linked to the Triassic age. (e) Comparison of all zircons. The REE patterns of the zircons in peridotites are similar, whereas the REE concentrations exhibit high inter-grain variabilities. See text for information. Chondrite values are from Sun & McDonough (1989).

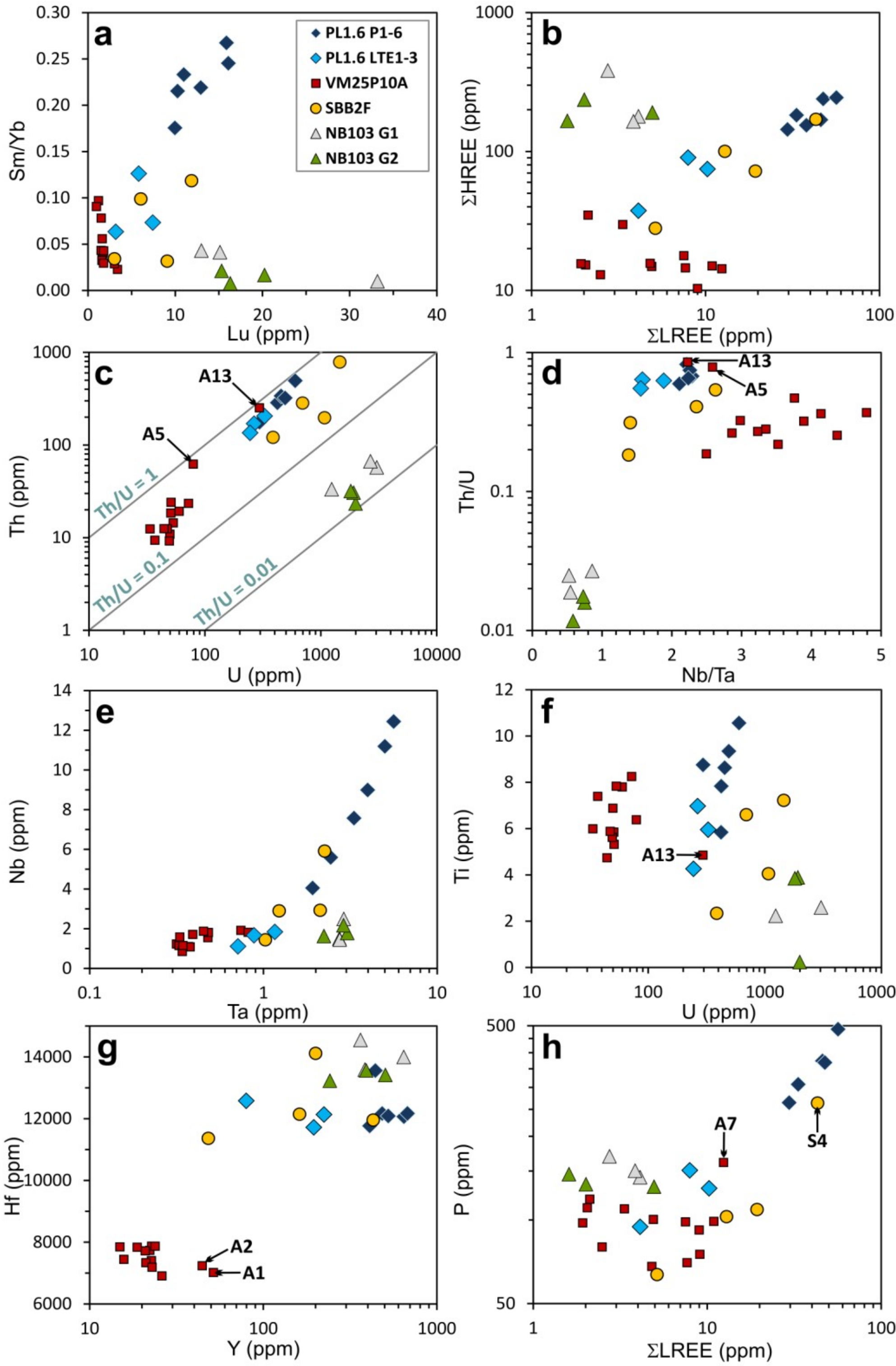

Figure 3.7. Concentrations and correlations of trace elements in zircons from peridotites and phlogopite (from the crust-peridotite contact zone) from the Ulten Zone. PL1.6 P1-6 denotes the zircon spots P1 to P6 with higher trace element contents and linked to the Variscan U-Pb age in the peridotite sample PL1.6, while PL1.6 LTE1-3 denotes the three spots LTE1 to LTE3 with lower trace element contents and partly linked to the Triassic U-Pb age. NB103 G1 and NB103 G2 denote grain 1 and grain 2, respectively, in the phlogopitite sample NB103. A5 delineates a spot spatially related to the dolomite inclusion in the zircon in peridotite VM25P10A and A13 delineates the spot located at the grain rim. S4 denotes the spot in the zircon included in amphibole in the peridotite sample SBB2F with higher trace element concentrations.

3.5.2.2. Sample VM25P10A

Sample VM25P10A contains a coarse euhedral zircon that was cut perpendicular to the *c* axis. It is ~1 cm (Figures 3.2b, 3.8a,b) in size, with sharp grain boundaries to the peridotite matrix minerals along two crystal faces. The other faces are exposed to the weathered sample surface. The zircon is crosscut by many cracks that are much more abundant close to the sample surface (Figure 3.8a) and generally follow the cleavage property of the tetragonal crystal structure. Inclusions in this zircon are mm-sized lobate dolomite and apatite (Förster et al., 2017). The zircon is set in the peridotite matrix and its linear and sharp grain boundaries crosscut the matrix minerals (Figure 3.8b), which do not exhibit any flowing around the grain. A total of 25 spots, randomly distributed over the whole grain in both core and rim, were measured for U-Pb geochronology. The analyses yield uniform U-Pb ages (Tables 3.1, 3.3; Figure 3.5b), and plot concordantly with a $^{206}Pb/^{238}U$ weighted mean age of 333.7 ± 2.8 Ma (MSWD = 0.30).

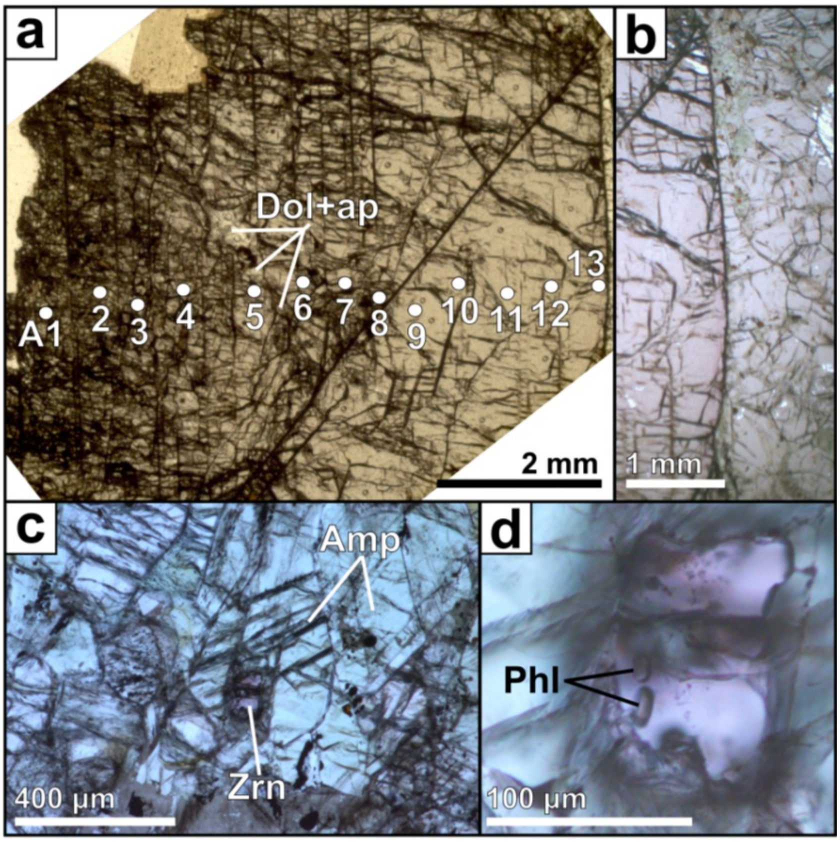

Figure 3.8. Photomicrographs of (a) zircon (~1 cm) in the fine-grained peridotite VM25P10A containing garnet pseudomorphs; spots A1 to A13 were analyzed for trace element compositions; (b) textural occurrence of the zircon in the peridotite matrix; the zircon displays sharp grain boundaries; (c) zircon included in amphibole in the amphibolized peridotite SBB2F and (d) zircon with phlogopite inclusions. Mineral abbreviations after Whitney & Evans (2010).

Trace elements were measured on a rim-core-rim line of 13 spots (A1-A13) across the zircon grain (Figure 3.8a). Although the U-Pb ages are homogeneous in all parts of the grain, the trace element compositions measured at different locations are distinct. In general, the chondrite-normalized REE pattern shows a strong positive Ce anomaly, absent or slightly negative Eu anomaly (Eu/Eu* = 0.59 to 0.87, Table 3.3, Figure 3.6b) with the lowest value displayed by the rim spot A13 and a strong MREE/HREE fractionation (Figure 3.6b, with Sm/Yb and Y/Ho ratios ranging from 0.02 to 0.10 and 28.1 to 34.7, respectively; Table 3.3, Figure 3.7a). Concentrations of LREE are highly variable, showing much higher scatter than the MREE and HREE (Figure 3.6b). Two spots that are located close to the surface rim and in the strongly fractured part of the zircon grain (A1, A2; Figure 3.8a) have higher MREE and HREE values with respect to all other spots. Interestingly, one spot that is located on the grain rim and in contact with the peridotite matrix minerals (A13) does not exhibit distinct REE values but is clearly enriched in other trace elements such as U, Th, Pb, Ta, Hf, and depleted in P (Table 3.3; Figure 3.7). This spot and one spot close to a dolomite+apatite multi-phase inclusion in the zircon (A5; Figure 3.8a) show the highest Th/U ratios (0.85 and 0.79, respectively) and low Nb/Ta ratios (2.23 and 2.58, respectively) of all measured spots (Table 3.3, Figure 3.7d). The spot close to the dolomite inclusion is slightly enriched in Sr, U, Th, Pb, Ta and depleted in P with respect to the other spots. In addition, it exhibits the highest Ba and Nb concentrations (1.29 and 1.92 ppm, respectively; Table 3.3). The highest P, Ca, Sr and LREE concentrations are displayed by a spot in the grain core (A7). Excluding the aforementioned high-Th/U spots, zircon Th/U ratios range from 0.19 to 0.47 and Ti concentrations range from 4.74 to 8.25 ppm (Table 3.3).

3.5.2.3 Sample SBB2F

The single zircon grain observed in sample SBB2F occurs as an inclusion (~100 µm length) within amphibole (Figure 3.8c) in the serpentine-poor, amphibole-rich domain 2. It contains mineral inclusions (Figure 3.8d), among which a K-rich mineral grain that is exposed on the section surface. According to its EDS spectrum (Figure A1 in Appendix), this mineral was identified as a phlogopite. The size of the grain allowed measurements of only six spots for U-Pb dating. In the concordia diagram, the six data points are concordant to slightly discordant and yield intercepts at 320.0 ± 6.9 Ma and at 2299 ± 1100 Ma (MSWD = 0.90) (Table 3.2; Figure 3.5c). The high value of the upper intercept (ca. 2.3 Ga) is indicative of the incorporation of common Pb in the analyses rather than reflecting inheritance. This is in agreement with the occurrence of inclusions visible under microscopic examination (Figure 3.8d), which can have contributed to a small but significant amount of common Pb. The upper intercept is thus not regarded as geologically meaningful and will not be discussed further. Due to the small size of the grain, trace element analyses were subsequently carried out on four of these spots. The chondrite-normalized REE pattern (Figure 3.6c) shows a positive Ce anomaly and MREE/HREE fractionation (Sm/Yb = 0.03 – 0.12, Y/Ho = 28.8 – 30.2, Table 3.3). The zircon grain has highly variable intra-grain trace element and REE concentrations, but all spots yield strong positive Ce anomalies (Figure 3.6c). A high variability is also displayed by all other trace elements (Table 3.3; Figure 3.7). The variable Th/U ratios range from 0.18 to 0.54 and Ti concentrations vary between 2.34 and 7.22 ppm (Table 3.3).

3.5.2.4 Sample NB103

Four µm-sized euhedral to subhedral zircon grains were observed in phlogopitite sample NB103 (Figure 3.9). Zircon 1 is 100 µm (Figure 3.9a,b), zircon 2 ~150 µm (Figure 3.9c,d), zircon 3 ~30 µm (Figure 3.9e) and zircon 4 ~40 µm in size (Figure 3.9f). These grains exhibit the tetragonal crystal faces, and grains 3 and 4 are rounded to ovoid (Figure 3.9e,f). These morphological features are typical for metamorphic zircon (Corfu et al., 2003). Zircons 1 and 2 are located within amphibole (Figure 3.9a-d), while the smaller zircons 3 and 4 are located in quartz (Figure 3.9e,f). Three zircon grains (1, 2 and 3) were analyzed for geochronology, three spots in grain 1 and 2, respectively, and two spots in grain 3. In the concordia diagram, all analyses plot concordantly and provide a ^{206}Pb/^{238}U weighted mean age (Tables 3.1, 3.3; Figure 3.5d) of 332.9 ± 3.1 Ma (MSWD=1.11). Trace element concentrations were measured in the same spots of zircon 1 and zircon 2. All spots show similar REE patterns with a strong positive Ce anomaly and a slightly negative Eu anomaly with a stronger Eu anomaly in spot G2-1 (Figure 3.6d). The MREE are depleted relative to HREE (Sm/Yb ranging from 0.01 to 0.04 and Y/Ho ranging from 29.2 to 31.3; Table 3.3). The REE concentrations are in general only slightly variable (Figure 3.6d). One spot (G2-1) in zircon grain 2 is located close to the grain rim and shows lower MREE and HREE values than all other spots. Th/U show homogeneous values ranging between 0.01 and 0.03 and Ti concentrations vary between 0.23 and 3.89 ppm (Table 3.3). Spot G2-1 differs from the other spots by displaying the lowest concentrations of Ti, Y, Sn, Hf and Th and the highest concentration of Ta (Table 3.3). The two other spots in zircon 2 differ from this spot in having much higher Ti concentrations and containing Ba, while Ba in G2-1 is below detection. Also the spots in zircon 1 show intra-grain trace element variations, especially spot G1-2 displays lower concentrations of U, Th, and Pb but higher concentrations of HREE, P, Rb, Y, Nb, and Ta with respect to the two other spots (Table 3.3).

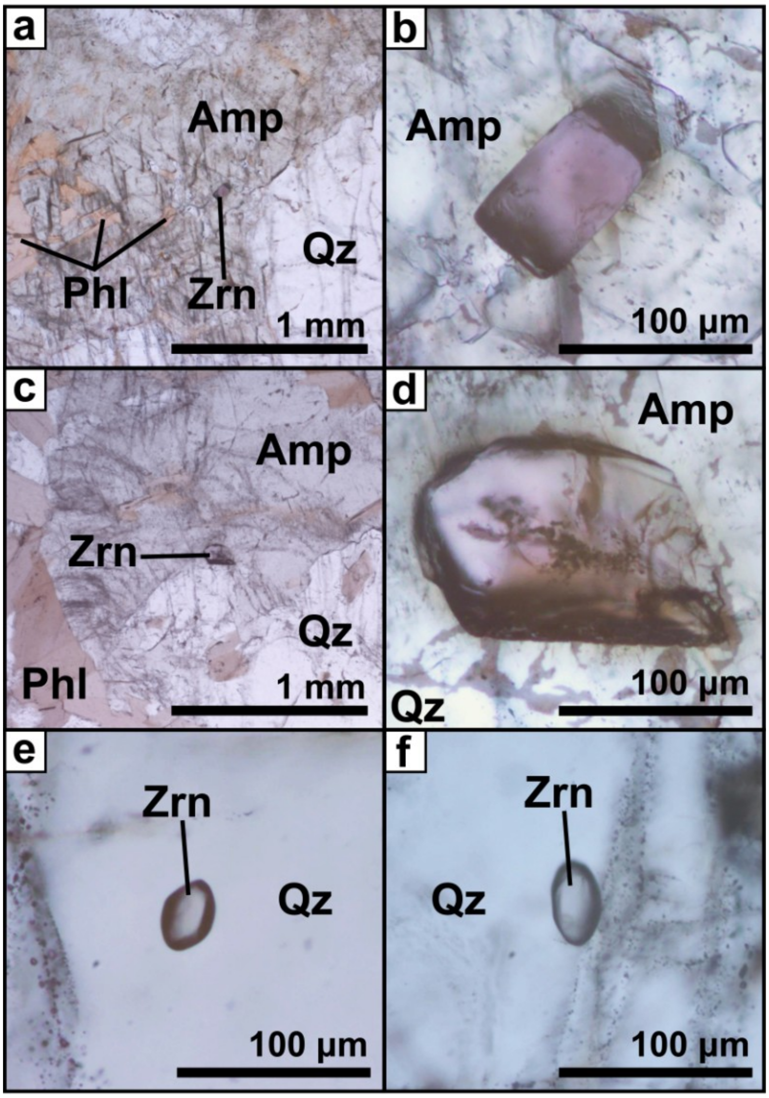

Figure 3.9. Photomicrographs of zircons in phlogopitite sample NB103 from a crust-peridotite contact zone. (a) Location of zircon 1 (100 µm in length) in the sample; (b) close-up view of zircon 1 in amphibole; (c) location of zircon 2 (~150 µm in length) in the sample; (d) close-up view in zircon 2 in amphibole; (e) zircon 3 (~30 µm in length) and (f) zircon 4 (~40 µm in length) in quartz. All zircons exhibit the tetragonal crystal faces and the two zircons, which are rounded to ovoid in shape, are typical of metamorphic zircons (Corfu et al., 2003). The scale bar in (d), (e) and (f) denotes 100 µm, as in (b). Mineral abbreviations after Whitney & Evans (2010).

3.5.3 Trace element composition of garnet

Only one of the studied zircon-bearing peridotites, sample PL1.6, contains garnet (Table 3.1, Figure 3.2a). Garnet crystals occur as porphyroclasts of variable size (up to ~600 µm), within the fine-grained peridotite matrix. All garnets have thin kelyphite coronas (Figure A2, Appendix), which formed as a result of decompression during exhumation (Godard & Martin, 2000). The large anhedral garnet porphyroclast (Figure A2, Appendix) contains spinel with a vermicular shape, while the smaller garnets are spinel-free (Figure A2, Appendix). Trace element compositions for the different garnets in sample PL1.6 are shown in Table A4 (Appendix). The garnet spot analyses can be grouped according to their location in the different garnets (grain size, grain core vs. grain rim) and the linked trace element compositions (Figure 3.10a).

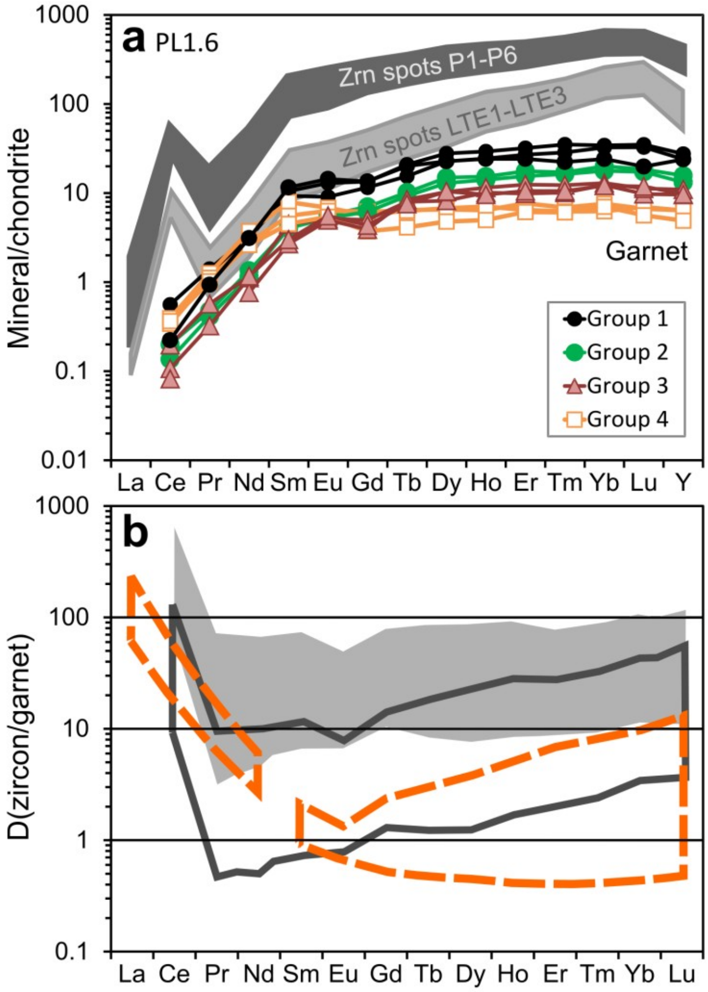

Figure 3.10. (a) Chondrite-normalized REE pattern and Y concentrations for zircon and garnet in the fine-grained garnet-bearing peridotite PL1.6. Chondrite values from Sun & McDonough (1989). The zircon spots with high REE concentrations (P1 to P6) are those related to the Variscan U-Pb age of ca. 333 Ma, the spots with low REE concentrations (LTE1 to LTE3) are partly related to the Triassic U-Pb age of ca. 236 Ma. The garnet groups (Group 1 to Group 4) can be distinguished in terms of their trace element concentrations, correlating to the locations of the analyzed spots in the garnets (see text for explanation); (b) distribution coefficients (D) of REE and Y between zircon and coexisting garnet in the garnet-bearing peridotite PL1.6. Light shaded field: coefficients calculated using the zircon spots P1 to P6 which are related to the Variscan U-Pb age (ca. 333 Ma), dark full line: coefficients calculated using the zircon spots LTE1 to LTE3 which are partly related to the Triassic U-Pb age (ca. 236 Ma). For calculations all garnet analyses as shown in (a) were used. Stippled line encompasses experimentally determined (800°C to 1000°C, Rubatto & Hermann, 2007a) and modeled equilibrium distribution coefficients (900°C to 1000°C, Taylor et al., 2015).

The spots of group 1, which are located at core and rim of medium-sized garnets, have the highest REE and Y values of all analyzed garnets (Table A4, Appendix). Group 2 spots are located in a small grain and at the rim of the large garnet porphyroclast (Table A4, Appendix) and have lower REE and Y values with respect to group 1. Group 3 comprises spots in the core of a small garnet and spots located near the grain rim of the large garnet. They contain less MREE to HREE and Y compared to group 2 and exhibit the lowest LREE values of all analyzed garnets (Figure 3.10a). Group 4 garnets display high LREE values but the lowest MREE to HREE and Y values (Figure 3.10a). These spots are located in the large garnet porphyroclast at the grain rim or close to it.

Calculated REE distribution coefficients between zircon and garnet show that MREE and HREE favorably partition into zircon (Figure 3.10b). Zircon/garnet equilibrium distribution coefficients were determined in several studies at high temperatures (800-1000°C) and it was shown that $D_{MREE-HREE}$ are close to unity and/or about one magnitude higher in this temperature range (Rubatto, 2002; Rubatto & Hermann, 2007a; Taylor et al., 2015 and references therein). The calculated D(zircon/garnet) for MREE and HREE in sample PL1.6 are similar and much larger than unity for spots P1 to P6 (Figure 3.10b). The distribution coefficients for the spots LTE1 to LTE3 are generally lower than those for the spots P1 to P6 and partly overlap experimentally derived D(zircon/garnet) (Figure 3.10b). However, the distribution of LREE for the PL1.6 zircon and garnet shows significant differences compared to the experimental values.

3.5.4 Ti-in-zircon thermometry

Ti-in-zircon temperatures for the zircons in this study were calculated using the calibration of Ferry & Watson (2007) and are reported in Table 3.1. This calibration considers the activities of TiO_2 and SiO_2 in the equilibrium controlling the Ti content in zircon ($ZrSiO_4 + TiO_2 = ZrTiO_4 + SiO_2$ or $TiO_2 + SiO_2 = TiSiO_4$, Ferry & Watson, 2007; Page et al., 2007). Because of Ti substitution in the Si site of zircon, the Ti content increases with decreasing SiO_2 activity and thus, the effects of the activities of TiO_2 and SiO_2 in the temperature calculation are compensated, which makes this calibration applicable also on rocks where rutile and quartz are absent (Ferry & Watson, 2007). Due to the unconstrained activities of TiO_2 and SiO_2 in the zircons of the present study, definite temperature estimates for zircon growth are difficult, but activities of TiO_2 and SiO_2 below unity are likely. For temperature calculation we assumed the same value for both TiO_2 and SiO_2 activities, thus, they are compensated in the temperature calibration. The Ti-in-zircon thermometer gives 672°C to 751°C (average 718°C) for the zircon in sample PL1.6, 680°C to 728°C (average 704°C) for the zircon in sample VM25P10A and 626°C to 716°C (average 679°C) for the zircon in sample SBB2F. In the phlogopitite NB103, the temperatures of two spots in zircon 1 and two spots in zircon 2 range from 622°C to 664°C (average 646°C), while one spot in zircon 2 yields 483°C. Although rutile is present in the amphibolitic part of the rock, it is absent in the zircon-bearing phlogopite-rich domain and thus, a rutile-zircon interaction in terms of element transfer during zircon crystallization cannot be ensured.

3.6 Discussion

3.6.1 Implications for crust-mantle interaction in a continental collisional setting

The identical age (~333 Ma) revealed by two of the three peridotite-hosted zircons (samples PL1.6 and VM25P10A) and by the zircons in the hybrid contact rock (NB103) in this study conforms to the age of zircons in an amphibolite sample (333 Ma) from the crust-mantle contact previously studied by Tumiati et al. (2007; Table A5, Appendix) and the age of zircons in a foliated garnet-peridotite and two pyroxenitic UZ samples (one unfolded garnet-amphibole websterite and one folded garnet-amphibole clinopyroxenite; Gebauer & Grünenfelder, 1979; Morten & Obata, 1983; Table A5, Appendix). The more strongly foliated rocks give ages of 336 Ma while the less deformed pyroxenite yields a younger age of 332 Ma (analytical errors are not given for these ages, Gebauer & Grünenfelder, 1979). We, thus, infer that the consistent zircon ages of peridotites, pyroxenites and crust-peridotite contact rocks reflect the time of a single-stage crustal metasomatism due to crust-peridotite interaction. The younger age (~320 Ma) of the zircon in the highly amphibolized peridotite (sample SBB2F) implies that the metasomatic process occurred, at least locally, over a long time span, or that a second pulse of zircon-forming metasomatism occurred. Interestingly, the 333 Ma age of zircons in UZ peridotites agrees with that of zircons in garnet peridotite from the Variscan basement of the Erzgebirge, ascribed to fluid/melt infiltration during exhumation of the gneiss-peridotite mélange (~332 Ma; Liati & Gebauer, 2009). Within the analytical errors (Table A5, Appendix) the zircon ages further overlap the Sm-Nd ages of ca. 330 ± 6 Ma for different UZ lithologies, interpreted to reflect the time of isotopic homogenization of ultramafic and crustal rocks after the entrainment of ultramafic rocks in the host gneisses and subsequent migmatization at garnet-facies conditions (Tumiati et al., 2003, 2007). Pre-Variscan zircon ages in UZ migmatites from orthogneisses (~470 Ma, Hauzenberger et al., 1993) were related to intrusion and crystallization of the orthogneiss (Hauzenberger et al., 1993) and those in felsic leucosomes (733 +150/-180 Ma, Tumiati et al., 2007; Table A5, Appendix) were inherited from the sedimentary protolith of the migmatites (Tumiati et al., 2007). Combining the age data by Tumiati et al. (2003) and the zircon ages from this and earlier studies (Gebauer & Grünenfelder, 1979; Tumiati et al., 2007), it is evident that the metasomatic event involving zircon-forming fluids in peridotites and hybrid contact zones occurred during or after peridotite incorporation in the crustal host rocks at ca. 333 Ma. It has been suggested that 330 Ma marks the beginning of the common exhumation of the crust-peridotite mélange at ca. 850°C and ca. 2.7 GPa, as isotopic homogenization and the identical age are recorded by all UZ lithologies (Nimis & Morten, 2001; Tumiati et al., 2003). In contrast, crustal slab-related metasomatism of the peridotites involved an aqueous fluid, probably released after leucosome crystallization (Rampone & Morten, 2001), which is in agreement with the suggested *P-T* conditions for the formation of the hybrid contact zones during exhumation of the crust-peridotite mélange below the wet solidus for metapelites (ca. 660-700°C and <1.2 GPa; Marocchi et al., 2009, 2010). In this context, it seems paradoxal that identical ages within error are recorded by UZ lithologies ascribed to high-*P-T* conditions as well as by the low-*P-T* hybrid contact zones. This is true also for the zircons which occur in garnet-amphibole peridotites and contact rocks. Accordingly, Marocchi et al. (2010) argued that the contact metasomatism related to the incorporation of the peridotite slices in the crustal rocks must be attributed to a low-pressure stage. In this case, the 330 Ma age would record low-*P-T* contact metasomatism after leucosome crystallization and would not describe isotopic homogenization at garnet-stage conditions. In this context, our new results on zircon geochemistry and geochronology may contribute to unravel the sequence and timing of events during the UZ geodynamic evolution.

The observation that zircons occur in garnet-bearing UZ peridotites, would support zircon growth at garnet-facies conditions. However, the calculated REE partitioning between zircon and garnet in sample PL1.6 exhibit Dzrn/grt of MREE and HREE much larger than expected in case of contemporaneous zircon and garnet growth at equilibrium conditions (Rubatto, 2002). Such non-equilibrium trace element partitioning was also observed in orogenic garnet peridotites from the Erzgebirge. It was suggested that zircon formed in these peridotites during post-peak metamorphism on an exhumation path, with zircon ages that postdate peak metamorphism (Liati & Gebauer, 2009). Additionally, the textural occurrence of the large zircon in the peridotite matrix (sample VM25P10A) indicates late zircon growth. Thus, zircon and garnet appear to have formed independently, what would be possible in the garnet-stability field if the volume of the metasomatic agent responsible for zircon growth was too low to equilibrate with garnet. However, we rather suggest that zircon in UZ peridotites formed as retrograde phase during exhumation, concomitantly with zircon formation in the hybrid contact rocks. Accordingly, Hermann et al. (2006) observed that zircon in garnet peridotites did not necessarily form during peak metamorphic conditions but on a retrograde path. As described above, Ti-in-zircon temperatures must be treated with caution since peridotites do not represent adequate mineral assemblages to buffer the Ti concentration in zircon, and the activities of TiO_2 and SiO_2 are largely unconstrained. However, if the temperatures are realistic, they conform with the temperatures suggested for the formation of the crust-peridotite contact zones (around or below 700°C, Marocchi et al., 2009, 2010) but exhibit a striking discrepancy to the suggested temperatures for the metamorphic garnet-facies stage (>800°C, e.g. Nimis & Morten, 2001; Braga & Sapienza, 2007; Sapienza et al., 2007; Malaspina & Tumiati, 2012). Low pressure and low temperature conditions were calculated only for garnet-free peridotites (1.5-1.7 GPa and 730°C by Braga & Sapienza, 2007; 1.2-1.4 GPa and ca. 670°C by Sapienza et al., 2007; ca. 1.6 GPa and 750°C by Malaspina & Tumiati, 2012), which partly represent the retrograde transformation of former garnet peridotites (Braga & Sapienza, 2007). Considering the relatively low-*P*-*T* conditions for peak metamorphic conditions of UZ crustal rocks (600-650°C at 1.1-1.2 GPa) and for subsequent decompressional heating (up to 720°C at 0.9-1.0 GPa) calculated by Braga et al. (2007), leucosome crystallization and the formation of the contact zones occur shortly after crustal peak metamorphism. Thus, we follow the suggestion of Marocchi et al. (2009, 2010) that peridotites were captured by the crustal host rocks during exhumation and that the identical age of UZ rocks (peridotites and contact rocks) and zircons reflects the low-*P*-*T* contact zone metasomatism. This implies that the garnet peridotites experienced pressure and temperature decrease from garnet-facies conditions when they still resided in the mantle wedge and were subsequently incorporated in the crustal rocks in the course of exhumation. In this scenario, it is possible that migration of slab-derived aqueous fluids released from the partial melt of the crustal rocks into the overlying mantle wedge (Scambelluri et al., 2006) marks a first stage of crustal metasomatism (> 333 Ma). If so, the formation of the hybrid contact zones due to crust-peridotite interaction by aqueous fluids released after leucosome crystallization (at ca. 333 Ma) would represent an additional metasomatic overprint, leading to local enrichment in HFSE and zircon growth. This would be in agreement with the conclusions by Hauzenberger et al. (1996) and Marocchi et al. (2007), who demonstrated multi-stage exhumation-related overprint of peridotites by fluids of different chemical compositions. However, Marocchi et al. (2007) suggested that spinel peridotites from the UZ, that do not contain garnet or garnet pseudomorphs, derive from a mantle wedge portion associated to shallow levels of the continental subduction zone, but never equilibrated in the garnet-stability field. So far, zircon has not been observed in such spinel peridotites and in chlorite peridotites that were suggested to be the products of spinel-peridotite retrogression (Marocchi et al., 2007). Thus, further investigations of possible zircon occurrences in these peridotite types may enhance the understanding of the sequence of events recorded by the UZ rocks. The model of a two-stage exhumation starting at 330 Ma from ca. 100 km depth (Ranalli et al., 2005) is not in agreement with our suggestion that the crust-peridotite association developed at low-pressure and low-temperature conditions at 330 Ma. However, according to the *P*-*T*-*t*-conditions suggested for the second slow exhumation stage ($T < 600$°C and $P < 1$ GPa at 205 to 300 Ma, Figure 4 in Ranalli et al., 2005), this model is not in conflict with a Triassic zircon age (236 ± 8 Ma) related to a late serpentinization event at crustal levels in the course of the second slow exhumation stage.

3.6.2 Origin of zircon in Ulten Zone peridotites: implications on crust-peridotite interaction

Exhumation-related zircon formation in peridotites of subduction-related origin was observed also in other orogenic (U)HP terranes and has been attributed to different origins: (1) Infiltration of peridotites by crust-derived fluids/melts (e.g. in the Erzgebirge, Liati & Gebauer, 2009 and in the Luliangshan massif of the North Qaidam belt, Chen et al., 2017), whereby the fluids derived from continental and/or oceanic crust (Chen et al., 2017); (2) Subsolidus zircon formation after the breakdown of a Zr-bearing phase during subduction and concomitant Zr addition into peridotites by crustal fluids (e.g. Monte Duria, Hermann et al., 2006); (3) physical transportation of crustal zircons into peridotite by metasomatic fluids (Sulu terrane, Li et al., 2016). Given that zircon formation in peridotites and crust-peridotite contact zones is related to leucosome crystallization and the formation of the contacts, two possible parental metasomatic agents may be considered: (1) the hydrous felsic melt that was generated during migmatization of the gneisses (Godard et al., 1996; Hauzenberger et al., 1996; Del Moro et al., 1999); (2) the residual hydrous H_2O-CO_2-mixed fluid released after the *in-situ* crystallization of the host migmatite leucosomes (Hauzenberger et al., 1993; Rampone & Morten, 2001) or by silica-consuming reactions with the peridotites (Scambelluri et al., 2006). On the other hand, the *P-T* path of the UZ peridotites does not allow for the presence of critical fluids (e.g. Scambelluri et al., 2006). The zircons are spatially closely associated to metasomatic amphibole and the lack of flowing of the secondary hydrous minerals around the large zircon in sample VM25P10A argues for zircon formation through fluid-assisted metasomatism leading to the formation of abundant hydrous minerals. Furthermore, in contrast to zircons in other orogenic peridotites which experienced (deep) subduction (Zhang et al., 2005; Song et al., 2005; Hermann et al., 2006; Liati & Gebauer, 2009; Li et al., 2016; Chen et al., 2017, the zircons in UZ peridotites do not contain felsic inclusions that can be related to zircon growth from Si-rich melts. Inclusions in zircons from UZ crustal rocks were suggested to be the products of former Si-rich melt produced by partial melting of metapelites (Braga & Massonne, 2008). The absence of migmatite-related inclusions in the zircons may indicate that Si-rich melts were unable to infiltrate the peridotite, possibly due to local *in-situ* crystallization in the crust and/or they were “stopped” by the formation of hydrous metasomatic crust-peridotite reaction zones. Additionally, it was proposed that a siliceous melt is inconsistent with the lack of extensive orthopyroxene growth (Scambelluri et al., 2006), but such a melt may produce a orthopyroxene-rich layer at the slab-mantle interface that can act as a filter for slab agents by enhancing precipitation of the most compatible elements (e.g. Si and Al), producing a residual aqueous fluid enriched in the incompatible LILE, LREE and light elements (Scambelluri et al., 2006). However, orthopyroxenites have not been observed in the UZ, and the occasionally occurring orthopyroxene porphyroclasts in some fine-grained peridotites are interpreted as relics of a former coarse-grained mantle assemblage. Phlogopite can precipitate from migmatite-related melts together with orthopyroxene and garnet (Scambelluri et al., 2006) but it has been observed in UZ peridotites as hydrous fluid-derived metasomatic phase (Rampone & Morten, 2001; Scambelluri et al., 2006). Thus, the origin of the phlogopite inclusion in the zircon (in sample SBB2F) cannot be clearly resolved. In terms of the trace-element budget, the zircon HREE concentrations are lower than expected for magmatic zircons (Rubatto & Hermann, 2007b). In summary, these observations indicate that magmatic zircon growth in the UZ peridotites is unlikely and we therefore suggest that the aqueous fluid, released from the crustal slab after leucosome crystallization was the metasomatic agent responsible for zircon formation in UZ peridotites and hybrid contact rocks. Moreover, the occurrence of inclusions of dolomite ± apatite in zircon (Figure 3.8a) testifies to the presence of a carbon species in the fluid in accordance to previous studies (Rampone & Morten, 2001; Sapienza et al., 2009; Förster et al., 2017). It was demonstrated that fluid metasomatism in UZ peridotites resulted in enrichment in LILE and LREE over HFSE (Rampone & Morten, 2001; Scambelluri et al., 2006). However, whole-rock trace element data of different UZ lithologies (Figure 3.3) show a more detailed picture of the trace element concentrations in the different peridotite types. The higher average concentrations of Zr, LREE (Ce_N/Yb_N), Sr, Nb and Th displayed by fine-grained garnet-bearing peridotites compared to the coarse-grained ones (Figure 3.3) overlap with the PM values, while the Sr and Zr concentrations of the coarse-grained peridotites are < PM. On the other hand, the Ba and U concentrations of the coarse-grained peridotites are similar to PM, while the fine-grained ones have much higher U concentrations. If the coarse-grained peridotites represent the pre-metasomatic spinel-facies mantle peridotite that was depleted in some elements (in variable amounts LREE, Th, Sr, Zr), the average higher concentrations of not only the LILE (LREE, Sr, Ba) and U, but also of Zr and Nb show that the fine-grained garnet-bearing peridotites were also re-enriched in HFSE. Enrichment in HFSE by hydrous fluids released after migmatization apparently contradicts previous studies that demonstrate that Si-rich anatectic melts of crustal protoliths in a continental subduction zone are generally HFSE-depleted (Zheng & Herrmann, 2014). For example, a LILE-enriched but HFSE-depleted signature of amphiboles in Finero peridotites was interpreted as the result of peridotite interaction with crust-derived Si-rich hydrous melts (Zanetti et al., 1999). However, the solubility of HFSE in subduction-related aqueous fluids is dependent on several factors, such as *P-T* conditions, pH and the presence of ligands like F and Cl in the fluid (Jiang et al., 2005; Wilke et al., 2012). Thus, zircon solubility increases with presence of alkalis in Si-bearing fluids, whereby the formation of alkali zirconosilicate complexes may be responsible for enhanced zircon solubility and HFSE mobilization in aqueous fluids (Wilke et al., 2012; Louvel et al., 2013; Mysen, 2015). Zircon solubility in subduction fluids is further enhanced by increasing hydroxyl concentration in the fluid (Ayers et al., 2012). The moderate mobility of HFSE during crust-peridotite interaction is also demonstrated by the hybrid contact zones (Figure 3.3; Marocchi et al., 2009, 2010) and may favor the transport of HFSE into the adjacent peridotite and ultimately zircon formation therein. In summary, the presence of a HFSE-enriched aqueous fluid seems likely, since the activity of Si and Zr in the residual fluid must have been high enough to allow crystallization of zircon upon interaction with peridotite without inducing orthopyroxene growth at the expense of olivine, as evidenced by the inconspicuous orthopyroxene modes in the zircon-bearing samples.

Local variability in the trace element budget of the fluid, resulting from variable initial compositions of the putative hydrous Si-rich melt from which the fluid formed, and variations in the wall rock mineral assemblage (Rubatto, 2002; Zheng & Hermann, 2014), can explain the distinct zircon trace element compositions of the different zircons in the UZ peridotites and the phlogopitite. For example, whereas the low Th/U ratio of the zircons in the phlogopitite conform with the commonly low Th/U ratios (<0.1) of zircons in UHP garnet peridotites which formed from aqueous fluids (Chen et al., 2017 and references therein), elevated Th/U ratios such as those in the zircons in the UZ peridotites (Th/U > 0.1 and zircon in sample PL1.6 has Th/U > 0.5, Table 3.3) have been observed in zircons that form during peritectic reactions with contemporaneously generated hydrous melts (Chen et al., 2017 and references therein). We therefore suggest that the aqueous fluid responsible for zircon growth in UZ peridotites inherited its elevated Th/U ratio from the putative parental hydrous melt. However, it may be also possible that zircons in the crust-peridotite contact zone formed first and incorporated U over Th due to favored U partitioning compared to Th (e.g. Rubatto, 2002). The residual fluid migrating into the peridotites had an elevated Th/U ratio, recorded in the zircons in the peridotites. It may be that zircon and amphibole formed from the same fluid and amphibole incorporated the LREE, LILE and HFSE (shown in Scambelluri et al., 2006). The high modal abundance of amphibole in sample VM25P10A may be, therefore, responsible for the bulk-rock enrichment in these elements. Since amphibole incorporates less Zr and Hf relative to other HFSE (Scambelluri et al., 2006), a residual fluid after amphibole formation would be relatively enriched in Zr and Hf. Such a fluid could then be the source of zircon. The rim (spot A13) of the large zircon in sample VM25P10A displays higher contents of U, Th, Hf and Ta than the other spots in this zircon and U and Th concentrations are similar to those of the zircon in the garnet-bearing peridotite (PL1.6), while the REE concentrations of A13 are lower. Due to the location of this spot close to the zircon rim, element diffusion between zircon and adjacent minerals, possibly fluid-mediated, seems likely. Spots that are located close to the dolomite inclusions also demonstrate reaction of the zircon with the dolomite ± apatite (elevated LREE, Ba, Sr, Th, U). Due to the anhedral texture of the dolomite it may be speculated that zircon and dolomite formed contemporaneously from the same fluid. This would be consistent with the findings that the crust-derived aqueous fluid carried a carbon-component responsible for the formation of dolomite (Rampone & Morten, 2001; Scambelluri et al., 2006; Sapienza et al., 2009; Förster et al., 2017). The relative depletion in HFSE as well as in REE of the three spots located closer to the grain rim and partly related to the younger U-Pb age (236 ± 8 Ma) is noteworthy. Given that this zircon is in spatial relationship to the serpentine mesh texture, which is not the case for the other studied zircons, it appears likely that interaction with the serpentinizing fluid caused resetting of the U-Pb system in the zircon rims. A fluid-mediated Pb loss and disturbance of the U-Pb system in zircon can be enhanced by the occurrence of a carbon component in the fluid as demonstrated by Rizanova et al. (2000). Since dolomite precipitated in UZ peridotites in the course of metasomatism (Sapienza et al., 2009; Förster et al., 2017) and since the serpentinizing fluid likely carried a carbon species (Förster et al., 2017), carbon-rich aqueous fluids percolating the UZ peridotites (Rampone &

Morten, 2001; Scambelluri et al., 2006; Sapienza et al., 2009; Förster et al., 2017) may be responsible for resetting of the U-Pb zircon age close to the edge of the grain.

Importantly, the Ca content of the zircon in sample PL1.6 and in some zircon spots in sample VM25P10A is elevated. Incorporation of "non-stoichiometric" elements, such as Ca, is typical for metamict and fluid-altered zircon (re)crystallized during hydrothermal events (e.g. Geisler & Schleicher, 2000; Geisler et al., 2003, 2007). In addition to elevated Ca concentrations, such zircons are also enriched in LREE, but retain their HREE budget as well as their U-Th-Pb systematics (Geisler & Schleicher, 2000; Geisler et al., 2003). In contrast, the two UZ zircons do not display elevated LREE concentration, thus, their elevated Ca concentrations may be related to the formation of fractures but remains largely enigmatic.

3.7 Summary and conclusions

We studied zircons in orogenic (garnet-)amphibole peridotites and in a phlogopitite rock from a crust-peridotite contact zone from the UZ. The main findings are summarized as follows:

1) Zircon U-Pb geochronology yields an age of ca. 333 Ma, with analytical errors consistent with previously determined ages for zircons in UZ peridotites (332 and 336 Ma; Gebauer & Grünenfelder, 1979), contact rocks (ca. 333 Ma; Tumiati et al., 2007) and UZ rocks (ca. 330 Ma; Tumiati et al., 2003). This age reflects the time of the formation of the hybrid crust-peridotite contact zones in the course of exhumation. One zircon in a highly amphibolized peridotite reveals a significantly younger age of ca. 320 Ma, indicating zircon growth, at least locally, over a long time span, or during a second pulse of zircon-forming metasomatism. Distribution of REE between zircon and garnet reflects disequilibrium formation and is taken as evidence that zircon grew independently of garnet. These results indicate that the peridotites remained in the mantle wedge until entrainment into the crustal rocks and leucosome crystallization under low-*P*-*T* conditions at ca. 333 Ma.
2) Calculated Ti-in-zircon temperatures reflect temperatures (ca. 600-700°C), which are in agreement with conditions prevailing during late-stage exhumation. We thus propose that zircon grew from aqueous fluid/s released after leucosome crystallization during emplacement of the peridotites into the crustal host rocks and formation of the crust-peridotite contact zones.
3) The occurrence of zircon and the elevated average Zr concentrations in fine-grained (garnet-)amphibole-bearing peridotites relatively to the coarse-grained peridotites indicate zircon formation induced by addition of Zr during crustal metasomatism and imply that slab-derived aqueous fluids were able to mobilize HFSE.
4) Younger rims on zircon display a Triassic age of 236 ± 8.0 Ma. This age is heretofore the first geochronological evidence for a post-Variscan event in the UZ. It testifies to resetting of the U-Pb system, possibly due to fluid-rock interaction during the late serpentinization stage accompanying exhumation.
5) Future geochemical investigations of the zircons must be carried out in order to enhance the understanding of the origin and nature of the zircon-forming fluids that interacted with the UZ peridotites. For example, analyses of Hf- and O-isotope compositions of zircons in both peridotites and contact rocks combined with the zircon age data may shed light on the geodynamic link between those lithologies and ultimately the timing and conditions of their amalgamation in the collisional setting.

3.8 References

1. Ayers, J.C., Zhang, L., Luo, Y., Peters, T.J. (2012). Zircon solubility in alkaline aqueous fluids at upper crustal conditions. Geochimica et Cosmochimica Acta 96, 18-28.

2. Bargossi, G.M., Bondi, M., Mordenti, A., Morten, L. (2003). The abundances of 55 elements and petrovolumetric models of the crust in the Non and Ulten Valley (Site 3). In: F.P. Sassi (Ed.). The abundance of 55 elements and petrovolumetric models of the crust in 9 type areas from the crystalline basements of Italy, with some geophysical and petrophysical data, Accademia Nazionale delle Scienze detta dei XL, Scritti e Documenti, Roma, 163-196.
3. Bondi, M., Morten. L. (2000). Geochemistry of metabasites of the austridic crystalline basement from Monte Pin (Val di Non) central eastern Alps. Mineralogica et Petrographica Acta 43, 75-86.
4. Bosch, D., Garrido, C.J., Bruguier, O., Dhuime, B., Bodinier, J.L., Padron-Navarta, J.A., Galland, B. (2011). Building an island-arc crustal section: Time constraints from a LA-ICP-MS zircon study. Earth and Planetary Science Letters 309, 268-279.
5. Braga, R., Sapienza, G.T. (2007). The retrograde evolution of a dolomite-bearing hydrous peridotite from the Ulten Zone (Italian Alps). GeoActa 6, 37-45.
6. Braga, R., Massonne, H.-J., Morten, L. (2007). An early metamorphic stage for the Variscan Ulten Zone gneiss (NE Italy): evidence from mineral inclusions in kyanite. Mineralogical Magazine 71, 691-702.
7. Braga, R., Massonne, H.-J. (2008). Mineralogy of inclusions in zircon from high-pressure crustal rocks from the Ulten Zone, Italian Alps. Periodico di Mineralogia 77, 43-64.
8. Bruguier O., Bosch D., Caby R., Vitale-Brovarone A., Fernandez L., Hammor D., Laouar R., Ouabadi A., Abdallah N., Mechati M. (2017). Age of UHP metamorphism in the Western Mediterranean: Insight from rutile and minute zircon inclusions in a diamond-bearing garnet megacryst (Edough Massif, NE Algeria). Earth and Planetary Science Letters 474, 215-225.
9. Chen, R.-X., Li, H.-Y., Zheng Y.-F., Zhang, L., Gong, B., Hu, Z., Yang, Y. (2017). Crust-mantle interaction in a continental subduction channel: evidence from orogenic peridotites in North Qaidam, Northern Tibet. Journal of Petrology 58, 191-226.
10. Corfu, F., Hanchar, J.M., Hoskin, P.W.O., Kinny, P. (2003). Atlas of zircon textures. Reviews in Mineralogy and Geochemistry 53, 469-500.
11. Del Moro, A., Martin, S., Prosser, G. (1999). Migmatites of the Ulten Zone (NE Italy), a record of melt transfer in deep crust. Journal of Petrology 40, 1803-1826.
12. Ferry, J.M., Watson, E.B. (2007). New thermodynamic models and revised calibrations for the Ti-in-zircon and Zr-in-rutile thermometers. Contributions to Mineralogy and Petrology 154, 429-437.
13. Förster, B., Braga, R., Aulbach, S., Lo Pò, D., Bargossi, G.M., Mair, V. (2017). A petrographic study of carbonate phases in the Ulten Zone ultramafic rocks: Insights into carbonation in the mantle wedge and exhumation-related decarbonation. Ofioliti 42, 105-127.
14. Gebauer, D., Grünenfelder, M. (1979). U-Pb zircon dating of mafic and ultramafic rocks, in: Panayiotou, A. (Ed.), Ophiolites: Proceedings International Ophiolite Symposium Cyprus, Ministry of Agriculture and Natural Resources, Geological Survey Department, Nicosia, 215-218.
15. Geisler, T., Schleicher, H. (2000). Improved U-Th-total Pb dating of zircons by electron microprobe using a simple new background modeling procedure and Ca as a chemical criterion of fluid-induced U-Th-Pb discordance in zircon. Chemical Geology 163, 269-285.
16. Geisler, T., Rashwan, A.A., Rahn, M.K.W., Poller, U., Zwingmann, H., Pidgeon, R.T., Schleicher, H., Tomaschek, F. (2003). Low-temperature hydrothermal alteration of natural metamict zircons from the Eastern Desert, Egypt. Mineralogical Magazine 67, 485-508.
17. Geisler, T., Schaltegger, U., Tomaschek, F. (2007). Re-equilibration of zircon in aqueous fluids and melts. Elements 3, 43-50.
18. Godard, G., Martin, S., Prosser, G., Kiénast, J.R., Morten, L. (1996). Variscan migmatites, eclogites and garnet-peridotites of the Ulten zone, Eastern Austroalpine system. Tectonophysics 259, 313-341.
19. Godard, G., Martin, S. (2000). Petrogenesis of kelyphites in garnet peridotites: a case study from the Ulten zone, Italian Alps. Journal of Geodynamics 30, 117-145.
20. Günther, D., Heinrich, C.A. (1999). Enhanced sensitivity in LA-ICP-MS using helium-argon mixture as aerosol carrier. Journal of Analytical Atomic Spectrometry 14, 1369-1374.

21. Hauzenberger, C.A., Höller, W., Hoinkes, G., Klötzli, U., Thöni, M. (1993). Metamorphic evolution of the Austroalpine basement in the Nonsberg Area, Ultental (Val d'ultimo), Southern Tyrol. Terra Nova Abstract Supplement 4, Terra Nova 5, 13.
22. Hauzenberger, C.A., Höller, W., Hoinkes, G. (1996). Transition from eclogite to amphibolite-facies metamorphism in the Austroalpine Ulten Zone. Mineralogy and Petrology 58, 111-130.
23. Hermann, J., Rubatto, D., Trommsdorff, V. (2006). Sub-solidus Oligocene zircon formation in garnet peridotite during fast decompression and fluid infiltration (Duria, Central Alps). Mineralogy and Petrology 88, 181-206.
24. Ionov, D.A., Bigot, F., Braga, R. (2017). The provenance of the lithospheric mantle in continental collision zones: petrology and geochemistry of peridotites in the Ulten-Nonsberg Zone (Eastern Alps). Journal of Petrology 58, 1451-1472.
25. Jackson, S.E., Pearson, N.J., Griffin, W.L., Belousova, E.A. (2004). The application of laser ablation-inductively coupled plasma-mass spectrometry to in situ U-Pb zircon geochronology. Chemical Geology 211, 47-69.
26. Jiang, S.-Y., Wang, R.-C., Xu, X.-S., Zhao, K.-D. (2005). Mobility of high field strength elements (HFSE) in magmatic-, metamorphic-, and submarine-hydrothermal systems. Physics and Chemistry of the Earth 30, 1020-1029.
27. Li, H.-Y., Chen, R.-X., Zheng, Y.-F., Hu, Z. (2016). The crust-mantle interaction in continental subduction channels: Zircon evidence from orogenic peridotite in the Sulu orogen. Journal of Geophysical Research: Solid Earth 121, 687-712.
28. Liati, A., Gebauer, D. (2009). Crustal origin of zircon in a garnet peridotite: a study of U-Pb SHRIMP dating, mineral inclusions and REE geochemistry (Erzgebirge, Bohemian Massif). European Journal of Mineralogy 21, 737-750.
29. Louvel, M., Sanchez-Valle, C., Malfait, W.J., Testemale, D., Hazemann, J.-L. (2013). Zr complexation in high pressure fluids and silicate melts and implications for the mobilization of HFSE in subduction zones. Geochimica et Cosmochimica Acta 104, 281-299.
30. Ludwig, K.R. (2003). Isoplot/Ex. A Geochronological Toolkit for Microsoft Excel. Berkeley Geochronological Centre, Special Publication 4, 71 p.
31. Malaspina, N., Tumiati, S. (2012). The role of C-O-H and oxygen fugacity in subduction-zone garnet peridotites. European Journal of Mineralogy 24, 607-618.
32. Marocchi, M., Hermann, J., Morten, L. (2007). Evidence for multi-stage metasomatism of chlorite-amphibole peridotites (Ulten Zone, Italy): Constraints from trace element compositions of hydrous phases. Lithos 99, 85-104.
33. Marocchi, M., Mair, V., Tropper, P., Bargossi G.M. (2009). Metasomatic reaction bands at the Mt. Hochwart gneiss-peridotite contact (Ulten Zone, Italy): insights into fluid-rock interaction in subduction zones. Mineralogy and Petrology 95, 251-272.
34. Marocchi, M., Hermann, J., Tropper, P., Bargossi, G.M., Mair, V. (2010). Amphibole and phlogopite in "hybrid" metasomatic bands monitor trace element transfer at the interface between felsic and ultramafic rocks (Eastern Alps, Italy). Lithos 117, 135-148.
35. Marocchi, M., Marschall, H.R., Konzett J., Tropper P., Ludwig, T., Mair, V., Bargossi, G.M. (2011). Metasomatic tourmaline in hybrid contact-bands between gneiss and peridotite in the Ulten Zone of the Eastern Italian Alps: Chemistry and boron isotopic composition. The Canadian Mineralogist 49, 245-261.
36. Martin S., Morten L., Prosser G. (1993). Metamorphic and structural evolution of the Spl- to Grt-peridotites and surrounding basement rocks from the Nonsberg area. In: L. Morten (Ed.). Italian Eclogites and Related Rocks, Rendiconti dell'Accademia Nazionale Quaranta, XIII, 237-251.
37. Martin S., Godard G., Prosser G., Schiavo A., Bernoulli D., Ranalli, G. (1998). Evolution of the deep crust at the junction Austroalpine/Southalpine: the Tonale Nappe. Memorie di Scienze Geologiche (Padova) 50, 3-50.
38. McDonough, W.F., Sun, S.-S. (1995). The composition of the Earth. Chemical Geology 120, 223-253.

39. Morten L., Bargossi G.M., Bargossi F. (1976). Notizie preliminari sulle metamorfiti della Val di Rumo, Val di Non, Trento. Mineralogica et Petrographica Acta 21, 137-144.
40. Morten, L., Obata, M. (1983). Possible high-temperature origin of pyroxenite lenses within garnet peridotite, northern Italy. Bulletin de Minéralogie 106, 775-780.
41. Morten, L., Obata, M. (1990). Rare earth abundances in the eastern Alpine peridotites, Nonsberg area, Northern Italy. European Journal of Mineralogy 2, 643-653.
42. Mysen, B. (2015). An in situ experimental study of Zr4+ transport capacity of water-rich fluids in the temperature and pressure range of the deep crust and upper mantle. Progress in Earth and Planetary Science 2, 38.
43. Nimis, P., Morten, L. (2000). P-T evolution of “crustal” garnet peridotites and included pyroxenites from Nonsberg area (upper Austroalpine), NE Italy: from the wedge to the slab. Journal of Geodynamics 30, 93-115.
44. Obata, M., Morten, L. (1987). Transformation of spinel lherzolite to garnet lherzolite in ultramafic lenses of the Austridic Crystalline Complex, Northern Italy. Journal of Petrology 28, 599-623.
45. Page, F.Z., Fu, B., Kita, N.T., Fournelle, J., Spicuzza, M.J., Schulze, D.J., Viljoen, F., Basei, M.A.S., Valley, J.W. (2007). Zircons from kimberlite: New insights from oxygen isotopes, trace elements, and Ti in zircon thermometry. Geochimica et Cosmochimica Acta 71, 3887-3903.
46. Palme, H., O’Neill, H.St.C. (2003). Cosmochemical constraints of mantle composition. In: H.D. Holland, K.K. Turekian (Eds.). Treatise on Geochemistry, Volume 2, Elsevier, 1-38.
47. Pearce, N.J.G., Perkins, W.T., Westgate, J.A., Gorton, M.P., Jackson, S.E., Neal, C.R., Chenery, S.P. (1997). A compilation of new and published major and trace data from NIST SRM 610 and NIST SRM 612 glass reference material. Geostandards Newsletter 20, 247-261.
48. Rampone, E., Morten, L. (2001). Records of crustal metasomatism in the garnet peridotites of the Ulten Zone (Upper Austroalpine, Eastern Alps). Journal of Petrology 42, 207-219.
49. Ranalli, G., Martin, S., Mahatsente, R. (2005). Continental subduction and exhumation: an example from the Ulten Unit, Tonale Nappe, Eastern Austroalpine. In: D. Gapais, J.P. Brun, P.R. Cobbold (Eds.). Deformation mechanisms, rheology and tectonics: from minerals to the lithosphere, Geological Society of London, Special Publications 243, 159-174.
50. Rizanova, N.G., Levchenkov, O.A., Belous, A.E., Bezmen, N.I., Maslenikov, A.V., Komarov, A.N., Makeev, A.F., Levskiy, L.K. (2000). Zircon reaction and stability of the U-Pb isotope system during interaction with carbonate fluid: experimental hydrothermal study. Contributions to Mineralogy and Petrology 139, 101-114.
51. Rubatto, D. (2002). Zircon trace element geochemistry: partitioning with garnet and the link between U-Pb ages and metamorphism. Chemical Geology 184, 123-138.
52. Rubatto, D., Hermann, J. (2007a). Experimental zircon/melt and zircon/garnet trace element partitioning and implications for the geochronology of crustal rocks. Chemical Geology 241, 38-61.
53. Rubatto, D., Hermann, J. (2007b). Zircon behaviour in deeply subducted rocks. Elements 3, 31-35.
54. Sapienza, G.T., Braga, R., Marocchi, M., Bargossi, G.M., Bondi, M. (2007). P-T and density constraints on a chlorite-amphibole-peridotite (Ulten Zone, Italy). Ofioliti 32, 83-84.
55. Sapienza, G.T., Scambelluri, M., Braga, R. (2009). Dolomite-bearing orogenic garnet peridotites witness fluid-mediated carbon recycling in a mantle wedge (Ulten Zone, Eastern Alps, Italy). Contributions to Mineralogy and Petrology 158, 401-420.
56. Scambelluri, M., Hermann, J., Morten, L., Rampone, E. (2006). Melt- versus fluid-induced metasomatism in spinel to garnet wedge peridotites (Ulten Zone, Eastern Italian Alps): clues from trace element and Li abundances. Contributions to Mineralogy and Petrology 151, 372-394.
57. Song, S., Zhang, L., Niu, Y., Su, L., Jian, P., Liu, D. (2005). Geochronology of diamond-bearing zircons from garnet peridotite in the North Qaidam UHPM belt, Northern Tibetan Plateau: A record of complex histories from oceanic lithosphere subduction to continental collision. Earth and Planetary Science Letters 234, 99-118.

58. Sun, S.-s., McDonough, W.F. (1989). Chemical and isotopic systematic of oceanic basalts: implications for mantle composition and processes. In: A.D. Saunders, M.J. Norry (Eds.). Magmatism in the ocean basins, Geological Society of London, London, 313-345.
59. Taylor, R.J.M., Harley, S.L., Hinton, R.W., Elphick, S., Clark, C., Kelly, N.M. (2015). Experimental determination of REE partition coefficients between zircon, garnet and melt: a key to understanding high-T crustal processes. Journal of Metamorphic Geology 33, 231-248.
60. Tumiati, S., Thöni, M., Nimis, P., Martin, S., Mair, V. (2003). Mantle-crust interactions during Variscan subduction in the Eastern Alps (Nonsberg-Ulten Zone): geochronology and new petrological constraints. Earth and Planetary Science Letters 210, 509-526.
61. Tumiati, S., Godard, G., Martin, S., Klötzli, U., Monticelli, D. (2007). Fluid-controlled crustal metasomatism within a high-pressure subducted mélange (Mt. Hochwart, Eastern Italian Alps). Lithos 94, 148-167.
62. Tumiati, S., Fumagalli, P., Tiraboschi, C., Poli, S. (2013). An experimental study on COH-bearing peridotite up to 3.2 GPa and implications for crust-mantle recycling. Journal of Petrology 54, 453-479.
63. Van Achterberg, E., Ryan, C.G., Jackson, S.E., Griffin, W.L. (2001). Data reduction software for LA-ICP-MS: appendix. In: P.J. Sylvester (Ed.). Laser Ablation-ICP-Mass Spectrometry in the Earth Sciences: Principles and Applications, Short Course Series 29, Mineralogical Association of Canada, Ottawa, Ontario, Canada, 239-243.
64. Wiedenbeck, M., Allé, P., Corfu, F., Griffin, W.L., Meier, M. (1995). Three natural zircon standards for U-Th-Pb, Lu-Hf, trace element and REE analyses. Geostandards Newsletter 19, 1-23.
65. Wilke, M., Schmidt, C., Dubrail, J., Appel, K., Borchert, M., Kvashnina, K., Manning, C.E. (2012). Zircon solubility and zirconium complexation in $H_2O+Na_2O+SiO_2±Al_2O_3$ fluids at high pressure and temperature. Earth and Planetary Science Letters 349-350, 15-25.
66. Zanetti, A., Mazzucchelli, M., Rivalenti, G., Vannucci, R. (1999). The Finero phlogopite-peridotite massif: an example of subduction-related metasomatism. Contributions to Mineralogy and Petrology 134, 107-122.
67. Zhang, R.Y., Yang, J.S., Wooden, J.L., Liou, J.G., Li, T.F. (2005). U-Pb SHRIMP geochronology of zircon in garnet peridotite from the Sulu UHP terrane, China: Implications for mantle metasomatism and subduction-zone UHP metamorphism. Earth and Planetary Science Letters 237, 729-743.
68. Zheng, Y.-F., Hermann, J. (2014). Geochemistry of continental subduction-zone fluids. Earth, Planets and Space 66, 93.

4 A petrographic study of carbonate phases in the Ulten Zone ultramafic rocks: Insights into carbonation in the mantle wedge and exhumation-related decarbonation

4.1 Introduction

In the debate of carbon (C) transfer between Earth's reservoirs, the cycling of carbon between crust and mantle during subduction is of particular interest because carbon is effectively mobilized and recycled at active convergent margins (Poli, 2015 and references therein). Being largely incompatible in mantle silicate minerals (Shcheka et al., 2006), carbon in the mantle is commonly hosted by carbonate minerals, graphite and/or diamond as well as occurring in volatile carbon species, such as COH-fluids. Carbon may be introduced into peridotite mantle via (1) the release of crust-derived C-bearing fluids at the slab-mantle interface during subduction (e.g. Bebout, 1996; Kerrick & Connolly, 1998; Molina & Poli, 2000; Scambelluri & Philippot, 2001; Poli et al., 2009) and/or (2) the reaction of mantle peridotite with carbonated melts (e.g. Green & Wallace, 1988; Green et al., 1992; Ionov et al., 1993, 1996). Nevertheless, due to sparse natural record of carbonated peridotite samples, the nature of carbon transfer between crust and mantle remains little understood. Experimental studies reveal that carbonates in both hydrous and anhydrous mantle peridotite are stable in a broad temperature and pressure range (e.g. Wyllie & Huang, 1975; Eggler, 1978, Eggler et al., 1979; Tumiati et al., 2013), and several studies report the occurrence of carbonate minerals in mantle-derived ultramafic rocks (e.g. Ionov et al., 1993, 1996, 1998 and references therein; Zanetti et al., 1999; Lee et al., 2000; Laurora et al., 2001; Braga & Sapienza, 2007; Sapienza et al., 2009). However, for example, although mantle xenoliths have provided invaluable insights into the composition and evolution of the mantle, carbonate minerals can be destabilized during decompression upon entrainment in the host lava (Canil, 1990), largely excluding this sample type as a direct source of information on the deep carbon cycle. Experimental studies dealing with the stability of carbonate minerals at mantle conditions under appropriate oxygen fugacities revealed that carbonation of peridotite starts with the formation of dolomite + orthopyroxene at the expense of forsterite + clinopyroxene + CO_2 (Wyllie & Huang, 1975). In mantle peridotite, dolomite is stable at $P < 1.9$ GPa and at 900°C, followed by coexistent dolomite and magnesite up to 2.4 GPa and ultimately stability of magnesite at $P > 2.4$ GPa (Wyllie & Huang, 1975; Eggler et al., 1979; Tumiati et al., 2013). It has been shown that carbonate minerals are robust even at subduction zone conditions involving fluids and/or melts (Molina & Poli, 2000; Kerrick & Connolly, 2001). Decarbonation of peridotite occurs only at conditions of low pressures and high temperatures that are virtually not achieved along subduction geotherms (Tumiati et al., 2013), but exhumation on a clockwise retrograde *P*-*T* path is considered to prompt decarbonation and CO_2-degassing of formerly subducted carbonate-bearing rocks (Kerrick & Connolly, 1998). It is becoming increasingly clear, however, that mantle carbonates are soluble as ionic species in aqueous fluids and in carbonatitic liquids under *P*-*T* conditions applicable to subduction zones, thus helping to redress the discrepancy between observed carbon inputs and outputs in subduction zones that arises if only decarbonation reactions are considered (Frezzotti et al., 2011; Manning et al., 2013; Ague & Nicolescu, 2014; Facq et al., 2014; Poli, 2015; Ferrando et al., 2017). Orogenic carbonate-bearing mantle peridotite can provide important constraints on the nature and effects of subduction-related fluids and melts on the trapping and remobilization of carbon during collisional tectonics.

In this paper we present a comprehensive petrographic study on the occurrence of diverse carbonate minerals in orogenic peridotites and pyroxenites from the Ulten Zone (UZ) tectonic unit in the Eastern

Italian Alps (Figure 4.1). These peridotites derive from a supra-subduction zone mantle wedge being affected by various petrologic processes involving metasomatic agents during subduction and exhumation (Scambelluri et al., 2006; Tumiati et al., 2007). Several previous studies (Obata & Morten, 1987; Godard et al., 1996; Marocchi et al., 2009; Braga & Sapienza, 2007; Sapienza et al., 2009; Malaspina & Tumiati, 2012) reported the occurrence of dolomite in different textural sites in the UZ peridotites, the precipitation of which has been suggested to be prompted by infiltration of C-bearing metasomatic aqueous fluids at different depths along the interface between the subducting continental slab and the overlying mantle wedge (Rampone & Morten, 2001; Sapienza et al., 2009).

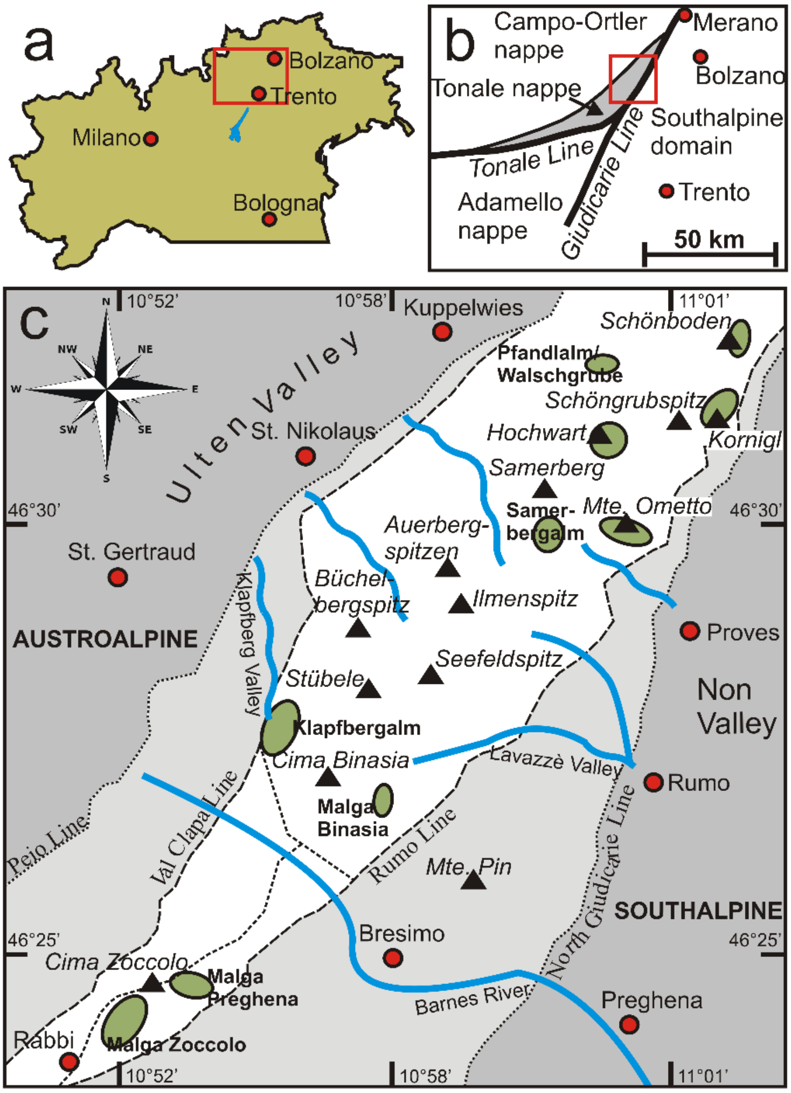

Figure 4.1. Map of the Ulten Zone tectonic unit. (a) Rectangle marks the location of the Ulten Zone in the Alps in North Italy; (b) Rectangle marks the location of the Ulten Zone in the Tonale nappe as a fragment of the Paleozoic Variscan belt; (c) White field encompasses the Ulten Zone located between the Val Clapa Line and the Rumo Line. Ellipses mark the locations of the ultramafic bodies from which peridotite samples were selected for this study.

Here, we present new and extended petrographic evidence of carbonate minerals and especially the occurrence of dedolomitization products in wedge-derived peridotite mantle, which have not been described previously. As we will show, different carbonate minerals in these rocks were precipitated during different stages of the subduction-exhumation cycle. In addition, their occurrence in a variety of textural settings, from discrete grains to veins, attests to the mobilization and "fixation" of carbon. Hence, the UZ peridotites are a promising natural laboratory to study carbon cycling in orogenic settings. We will discuss the presence of carbonate minerals and dolomite-breakdown products in the context of the complex tectono-metamorphic evolution of the UZ and we will link our petrographic observations to known carbonate stability at conditions occurring in crust and mantle in collisional subduction zone settings.

4.2 Geologic background and previous work

The Ulten Zone (UZ) tectonic unit (e.g. Morten et al., 1976; Martin et al., 1993; Martin et al., 1998) outcrops in the Nonsberg mountain range located between the Ulten Valley and Non Valley in the Eastern Alps in Italy (Figure 4.1). The orogenic UZ represents a fragment of the Late Paleozoic Variscan belt (Figure 4.1b; Godard et al., 1996) and consists of foliated high-grade metamorphic crustal basement (garnet-kyanite paragneiss, migmatite and granitic to tonalitic orthogneiss; Obata & Morten, 1987; Godard et al., 1996; Martin et al., 1998) and bodies of ultramafic rocks (peridotite ± pyroxenites; Morten & Obata, 1983; Obata & Morten, 1987; Godard et al., 1996 and references therein). These numerous peridotite bodies are exposed at the surface as lenses of variable sizes (usually a few meters thick and up to hundreds of meters length) included within the crustal metamorphic basement. The contact zones between the crustal rocks and the peridotite lenses are usually sharp but rarely exposed at the surface (Obata & Morten, 1987). The UZ peridotites have been interpreted to represent slices of a Late Paleozoic supra-subduction zone mantle wedge that were incorporated in a subducting continental slab (Godard et al., 1996; Nimis & Morten, 2000) and subsequently exhumed during the Variscan orogeny (Godard et al., 1996). Ulten Zone peridotites display a transition from coarse-grained (up to a few cm) spinel-peridotites via a transitional type to highly deformed fine-grained (0.2 mm to 1 mm) garnet-amphibole peridotites and amphibole-chlorite peridotites (Obata & Morten, 1987). The transitional type is a porphyroclastic garnet-bearing peridotite with large orthopyroxene and olivine in a granoblastic-polygonal matrix. The highly variable petrographic occurrences have been interpreted to record several processes during the complex tectono-metamorphic UZ history. Recent studies suggest the following evolutionary stages: (1) Coarse-grained protogranular spinel-lherzolite predominantly constituted the initial lithotype in the mantle wedge (Obata & Morten, 1987), residing at high temperatures (>1100°C) and moderate pressure (~1.5 GPa; Nimis & Morten, 2000). At this early, pre-Variscan stage, the peridotites were infiltrated by hot (>1400°C) melts derived from deeper levels of the mantle wedge (Nimis & Morten, 2000; Scambelluri et al., 2006; Marocchi et al., 2007), enabling the crystallization of pyroxenitic segregates (Nimis & Morten, 2000). (2) While flowing towards the continental subducting slab via corner flow, the peridotites underwent isobaric cooling (down to ~850°C), followed by transport to greater depths (corresponding to pressures of 2.0 to 2.5 GPa) close to the slab-wedge interface (Obata & Morten, 1987; Nimis & Morten, 2000). Due to the high-pressure eclogite-facies conditions and the infiltration of slab-derived aqueous fluids at this stage, coarse spinel peridotites were re-crystallized into amphibole ± garnet-bearing assemblages (Rampone & Morten, 2001; Scambelluri et al., 2006; Marocchi et al., 2007; Tumiati et al., 2007). Two hypotheses have been suggested for the subsequent metamorphic path: (a) incorporation of peridotites into the continental slab and subduction on a common prograde *P-T* path to peak metamorphic conditions (~2.7 GPa and ~850°C; Nimis & Morten, 2000), accompanied by the transformation into garnet-amphibole peridotite; (b) the peridotites reside in the mantle wedge and are infiltrated by crust-derived aqueous fluids while the slab reaches peak metamorphic conditions, followed by emplacement of peridotites during exhumation of crustal rocks. (3) In both cases peridotites and crustal rocks would start a common exhumation path at ca. 330 Ma (Tumiati et al., 2003). The Late Paleozoic exhumation, mylonitic deformation and retrograde overprint into fine-grained porphyroclastic garnet-amphibole peridotite (Obata & Morten, 1987; Scambelluri et al., 2006) is evidenced by the occurrence of kelyphites overgrowing the deformed textures (Godard & Martin, 2000) and this marks the latest Variscan stage of the UZ evolution.

Since the UZ was only slightly overprinted by Alpine metamorphism, the UZ lithologies preserve pre-Alpine metamorphic signatures and assemblages (Godard et al., 1996; Hauzenberger et al., 1996).

4.3 Sample materials and petrographic analytical methods

The Ulten Zone peridotites described in this study largely derive from a new sample set including samples from localities widespread across the whole UZ tectonic unit, including localities that were not previously studied (Table A6, Appendix; Figure 4.1c). The sampled ultramafic bodies consist of peridotites ± pyroxenitic rocks and allowed targeted sampling of, in general, well-preserved outcrops without visible weathering. The chosen specimens are representative of all macroscopically detectable petrographic characteristics in each sample locality.

Polished thick sections (~100 µm) of samples of the new sample set were analyzed using an optical transmitted light microscope and an energy dispersive (EDS) scanning electron microscope (SEM; Philips 515B, 5 µm spot size, 15 kV voltage) at the University of Bologna (Italy) as well as a Phenom XL SEM (15 kV voltage) at Lehigh University (USA). The latter allows detection of the volatile elements carbon and oxygen and was, therefore, used to distinguish carbonate and oxide phases and for the generation of element maps. The petrographic observations of the Hochwart sample set were also carried out with polarizing optical microscopy and electron imaging at the University of Bologna as well as with a JEOL SuperProbe 8100 at the Institute of Mineralogy and Petrography, University of Innsbruck (Austria).

Table A6 (Appendix) summarizes the provenance and petrographic characteristics of the studied peridotite samples as well as the occurrences of different carbonate phases in theses samples. For the petrographic description of the Ulten Zone peridotites we use the petrographic terms “coarse-grained” and “fine-grained” peridotites corresponding to the terms “coarse-type” and “fine-type” introduced by Obata & Morten (1987). The coarse-grained type is mostly relatively undeformed spinel lherzolite and composed of (in decreasing modal abundance order) olivine + orthopyroxene + clinopyroxene + spinel ± garnet with texture ranging from protogranular to porphyroclastic. If garnet is present, spinel is rimmed by garnet, which in turn is rimmed by a kelyphitic corona (Godard & Martin, 2000). The fine-grained type reveals various metamorphic textures, from porphyroclastic to tabular or mosaic equigranular. The main mineral assemblage is composed of olivine + orthopyroxene + pale-green amphibole + garnet + spinel ± clinopyroxene. In this fine-type peridotite, garnet is locally completely transformed into aggregates consisting of kelyphites (amphibole + pyroxenes ± spinel). The serpentinization degree of the fine-grained peridotite ranges from virtually absent to strongly serpentinized. According to Obata & Morten (1987), peridotites of the fine-grained type are much more abundant than the coarse-grained peridotites of the Ulten Zone. Indeed, while fine-grained spinel-peridotites occur in all newly studied localities (n = 9, exclusive Hochwart), coarse-grained spinel-peridotite was found in only six of the sampled peridotite bodies. In those exposures coarse-grained undeformed peridotite often occurs as “lenses” within the fine-grained peridotite that reveals mylonitic deformation (Figure 4.2).

4.4 Carbonates in Ulten Zone peridotites

4.4.1 Dolomite

Previous studies report consistently the occurrence of dolomite in diverse structural sites of fine-grained garnet-amphibole peridotite of the UZ: as inclusions in garnet (Obata & Morten, 1987; Godard et al., 1996); in the peridotite matrix, as large cm-sized grains (Obata & Morten, 1987; Marocchi et al., 2009) or porphyroclasts (Sapienza et al., 2009); and as interstitial µm-sized grains disseminated within the recrystallized foliated peridotite matrix (Godard et al., 1996; Braga & Sapienza, 2007; Sapienza et al., 2009). The observed dolomites commonly coexist and/or are in contact with apatite grains, regardless their microstructural site. These reports are consistent with our observation that interstitial disseminated matrix dolomite grains occur only in fine-grained porphyroclastic mylonitic garnet-amphibole peridotites (Figure 4.3) and in similar samples containing garnet pseudomorphs (Table A7, Appendix).

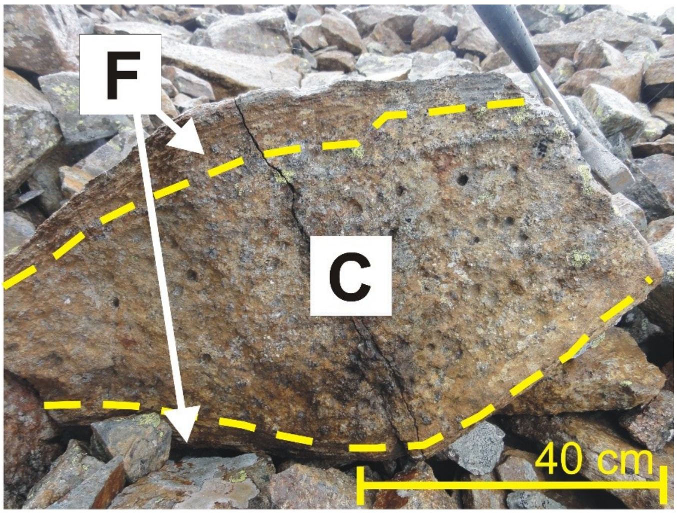

Figure 4.2. Photograph of an Ulten Zone peridotite block from Malga Binasia consisting of a coarse-grained peridotite lens (C) embedded in fine-grained mylonitic deformed peridotite (F). The coarse lens was largely excluded from hydration and shearing.

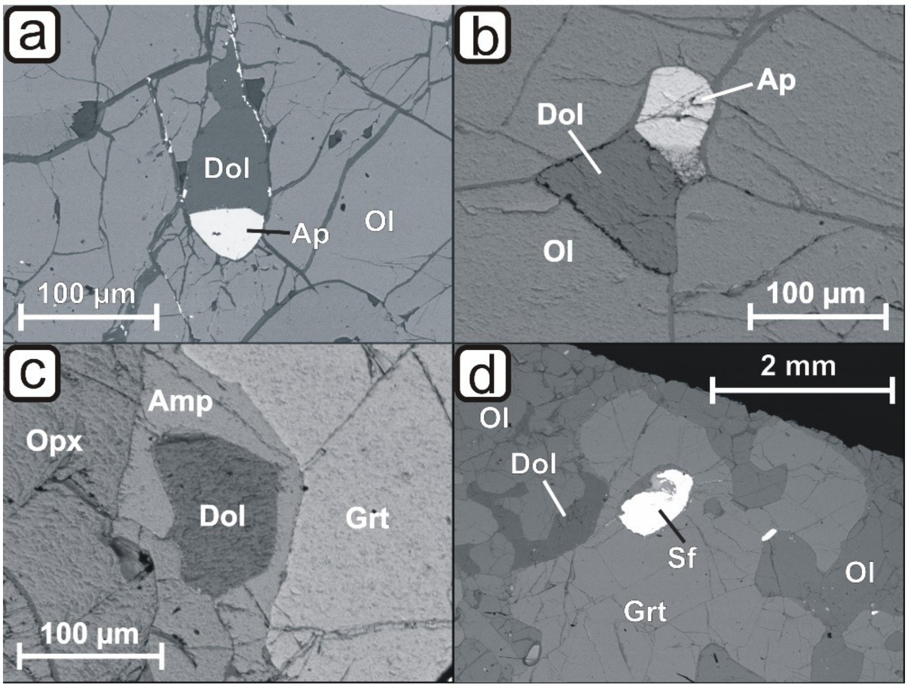

Figure 4.3. Back-scattered electron images of sections showing discrete dolomite grains in the matrix of non-serpentinized fine-grained garnet-amphibole peridotites associated with (a,b) apatite (samples KL1.2-3 and SBA4), (c,d) amphibole and garnet (SBA7). Mineral abbreviations after Whitney & Evans (2010), sf: sulfide.

These peridotites are largely non-serpentinized and garnets occasionally have kelyphite coronas. Dolomite grains are often in contact with apatite (Figure 4.3a,b) and amphibole (Figure 4.3c), as well as with garnet (kelyphite-free; Figure 4.3c,d). In some of these samples and in other fine-grained garnet-amphibole peridotites, dolomite occurs also as inclusions in matrix apatite (Figure 4.4a), amphibole (Figure 4.4b) and olivine (Figure 4.4c). In one sample, dolomite is associated with apatite as lobate inclusions in a coarse zircon crystal (~1 cm length; Figure 4.4d). Also, dolomite occurs as part of multi-phase solid inclusions (Figure 4.4e) in coarse garnet (~2 cm length) with a kelyphitic corona consisting of amphibole-pyroxene symplectites. Observed dolomite-bearing mineral associations in these multi-phase solid inclusions are dolomite ± spinel ± chlorite and amphibole + dolomite + sulfide ± calcite ± dissakisite ± apatite ± spinel ± chlorite ± sapphirine, whereas dolomite-free mineral associations comprise amphibole + apatite + phlogopite + spinel + sulfide. Such multi-phase solid inclusions represent former entrapped fluid inclusions, as described by Frezzotti & Ferrando (2015).

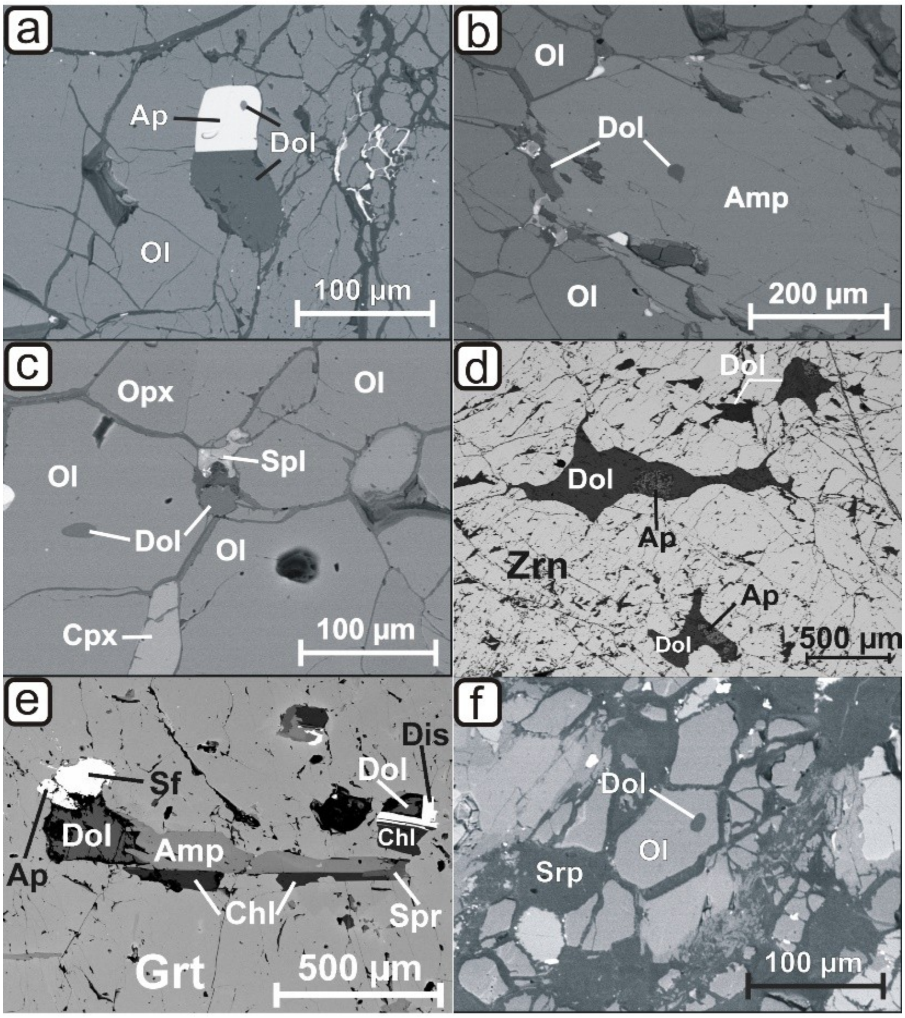

Figure 4.4. Back-scattered electron images of dolomite inclusions in (a) apatite (KL1.2-3), (b) amphibole (SBA5), (c) olivine (SBA5) in the matrix of non-serpentinized fine-grained garnet-amphibole peridotites; (d) lobate inclusions of anhedral dolomite with curvilinear grain boundaries in zircon crystal (~1 cm length) in a fine-grained garnet-amphibole peridotite (VM25P10A); (e) dolomite as part of a multi-phase solid inclusion in a coarse garnet (~2 cm length) surrounded by a kelyphitic corona (VM25P10B); (f) dolomite inclusion in olivine located in the serpentine mesh texture in a serpentinized fine-grained garnet-amphibole peridotite (SB3.4). Mineral abbreviations after Whitney & Evans (2010), sf: sulfide, dis: dissakisite.

In samples with retrogressed garnet, dolomite occurs in a garnet pseudomorph together with amphibole and spinel (Figure 4.5a), in contact with kelyphite around garnet, as part of pseudomorphs after garnet together with kelyphite, calcite and chlorite and in spinel-free amphibole coronas together with orthopyroxene around garnet. Occasionally, aggregates of dolomite form bands (vein-like?) and occur in contact with amphibole with curvilinear to embayed contacts to the matrix minerals (Figure 4.5b-d). It rarely appears that dolomite veins contain patches of calcite-brucite intergrowths (next section).

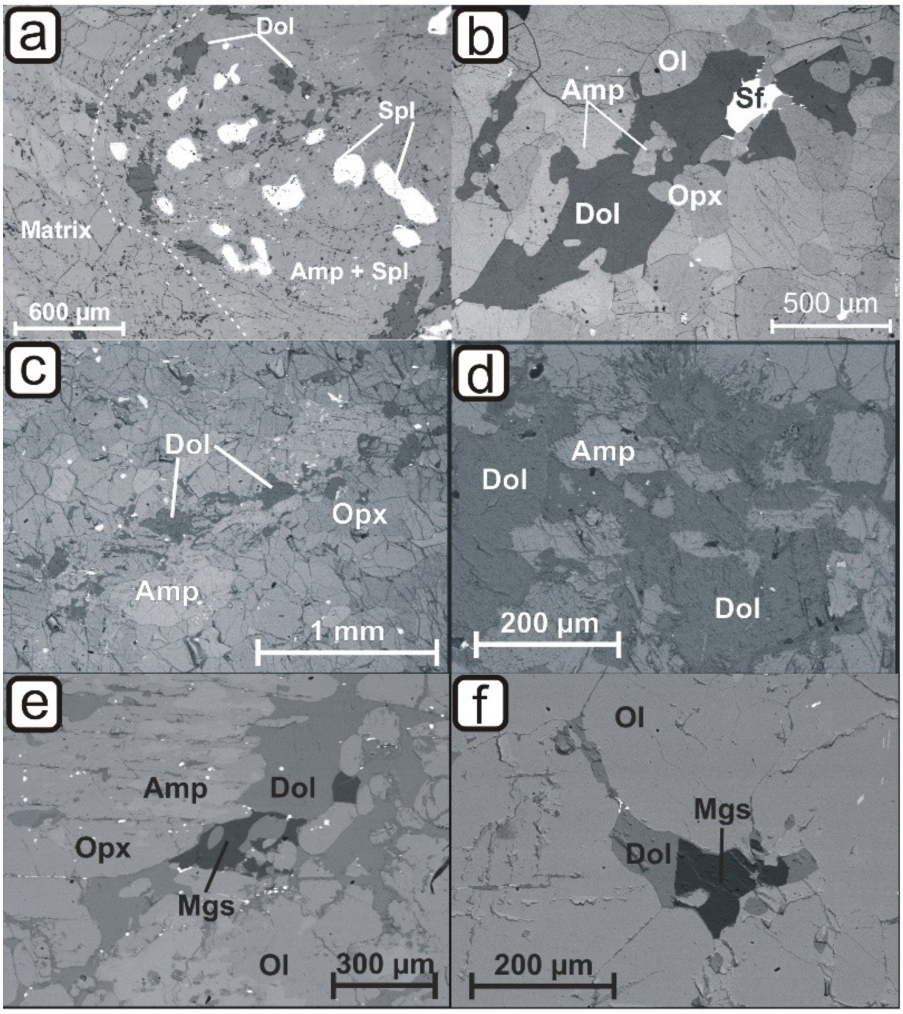

Figure 4.5. Back-scattered electron images of (a) dolomite in retrogressed garnet associated with spinel and amphibole in a fine-grained garnet-amphibole peridotite (VM25P10A); (b-d) bands/veins of dolomite associated with amphibole in fine-grained garnet-amphibole peridotites, dolomite has curvilinear contacts to the matrix minerals, in (b) sample VM25P10B and (c,d) sample KL1.6; (e,f) interstitial anhedral dolomite grains associated with magnesite with curvilinear contacts to matrix minerals in coarse-grained protogranular peridotite MOL1.5. Mineral abbreviations after Whitney & Evans (2010), sf: sulfide.

A lenticular polycrystalline aggregate of dolomite (~5 cm in length; Figure 4.6a) in one sample is composed of randomly oriented crystals with an average grain size of 500 μm which decreases towards the aggregate rim. Apatite is commonly located between the dolomite and the matrix (Figure 4.6b,c); the dolomite aggregate hosts coarse amphibole enclosing spinel, sulfides and fracture-filling dolomite. Dolomite in the little-serpentinized garnet-amphibole peridotites may also occur as grains with frayed boundaries located within rare serpentine veins crosscutting the matrix.

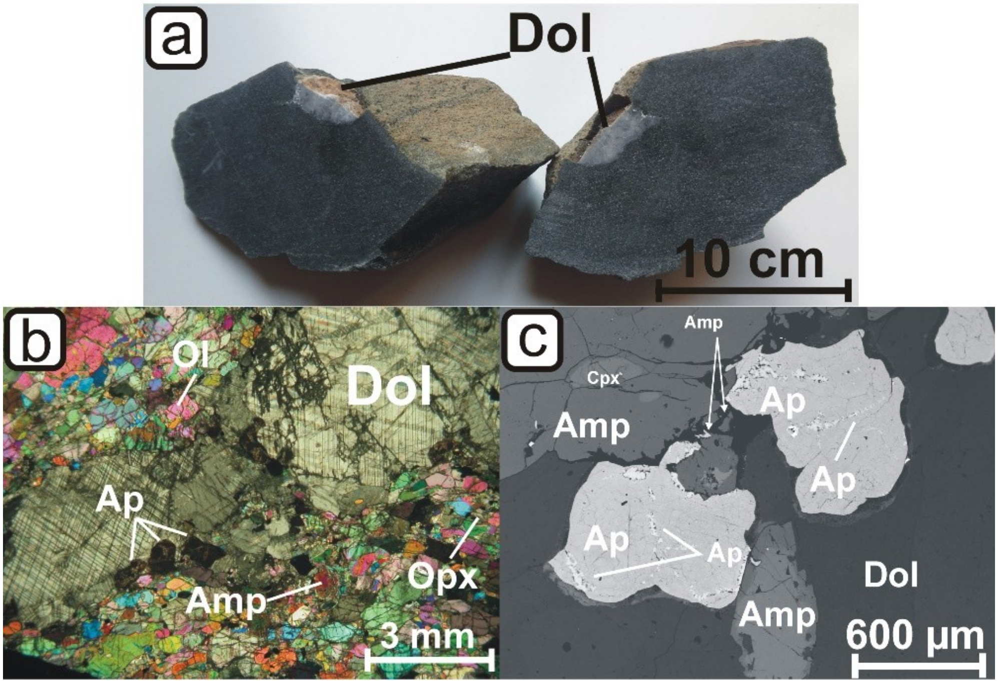

Figure 4.6. (a) Photograph of the hand specimen of sample VM25P11 with a lenticular polycrystalline aggregate of dolomite (~5 cm length); (b) polarized transmitted light photograph of a part of the polycrystalline aggregate of dolomite (thick section ~100 µm), (c) back-scattered electron image of the contact between the dolomite polycrystalline aggregate and matrix apatite and amphibole. Mineral abbreviations after Whitney & Evans (2010).

In (highly-)serpentinized fine-grained garnet-bearing samples, fine veinlets (~10 µm) consisting of dolomite associated with magnetite ± calcite ± (secondary?) serpentine(/chlorite?) crosscut the pre-existing serpentine mesh texture (Figure 4.7a). Future chemical analyses will resolve the presence of serpentine vs. chlorite. A highly-serpentinized fine-grained garnet-free peridotite contains a distinct secondary serpentine vein (~3 mm thickness) containing dolomite grains with frayed grain boundaries (Figure 4.7b). In other samples, rare dolomite grains occur within the serpentine mesh texture (Figure 4.7c) that replaces the primary ultramafic mineral assemblage. In one fine-grained porphyroclastic mylonitic sample, a well-preserved idiomorphic dolomite crystal (~150 µm length) and a magnesite aggregate with rippled grain boundaries are in textural equilibrium, residing within the serpentine mesh that replaces the primary ultramafic mineral assemblage (Figure 4.7d-f). The magnesite aggregate is crosscut by thin (~10 µm) dolomite veinlets which do not occur in the surrounding serpentine (Figure 4.7d-f). The different shades of the dolomite crystal (black) and the dolomite veins (gray) in Figure 4.7d indicate two different dolomite generations with different chemical compositions. In other serpentinized fine-grained garnet-amphibole peridotites, dolomite occurs as an inclusion in matrix olivine (Figure 4.4f) and as a euhedral inclusion in spinel hosted in garnet (Figure 4.8a).

In one coarse-grained protogranular sample, which also contains a distinct magnesite vein, interstitial anhedral dolomite with curvilinear grain boundaries in contact with the silicate minerals is highly abundant (Figure 4.5e,f) and spatially associated with amphibole. So far, this is the first example of dolomite + magnesite in coarse-grained protogranular UZ peridotites. The interstitial dolomite grains are partly associated with magnesite (Figure 4.5e,f). This sample also bears a vein of amphibole aggregates containing a 3-mm-large dolomite crystal. Fine veinlets consisting of dolomite associated with magnetite ± calcite ± (secondary?) serpentine(/chlorite?) crosscutting the pre-existing serpentine mesh texture were also rarely observed in one coarse-grained protogranular sample.

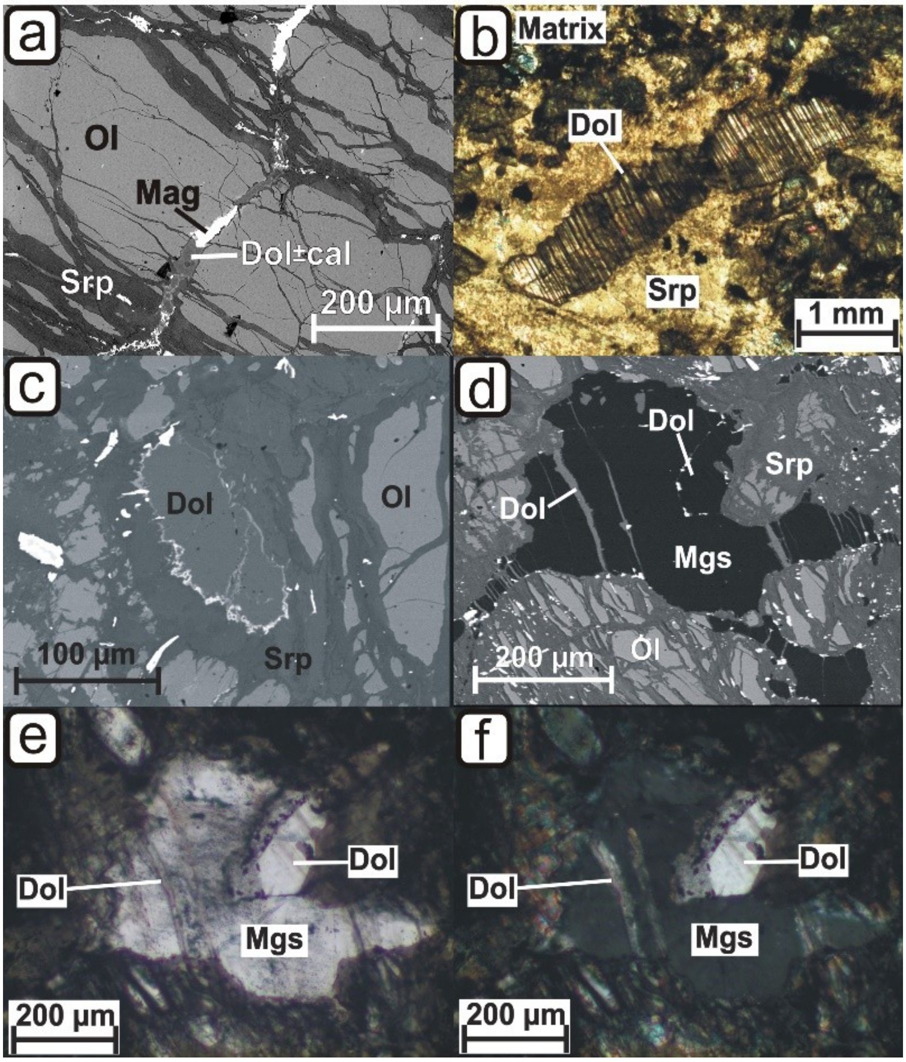

Figure 4.7. (a) Back-scattered electron (BSE) image of fine veinlets consisting of dolomite ± magnetite ± calcite ± serpentine crosscutting the pre-existing serpentine mesh texture in serpentinized fine-grained garnet-amphibole peridotites (WG1); (b) transmitted light photomicrograph of a distinct secondary serpentine vein (~3 mm thickness) containing discrete dolomite grains with frayed grain boundaries in a serpentinized fine-grained peridotite (MR141B, thick section ~100 µm); (c) back-scattered electron images of a dolomite grain with frayed grain boundary and associated with magnetite, located within the serpentine mesh texture of a serpentinized fine-grained garnet-amphibole peridotite (WG1); (d-f) back-scattered electron image (d), transmitted light photograph (e) and polarized transmitted light photograph (f) of a euhedral dolomite crystal (~150 µm length) associated with a magnesite aggregate located in the serpentine mesh texture of a serpentinized, highly mylonitic peridotite (SBB2F, thick section ~100 µm). The magnesite aggregate is interspersed with fine dolomite veinlets ("gray" in the BSE image), which are of different origin than the dolomite crystal ("black" in the BSE image). Mineral abbreviations after Whitney & Evans (2010).

4.4.2 Calcite-brucite intergrowths

In the UZ peridotites, acicular calcite and brucite are finely intergrown (µm-scale; Figures 4.8-4.10) and are found mostly in serpentinized fine-grained garnet-bearing samples, but are also observed in fine- and medium-grained garnet-free samples (Table A7, Appendix). The texture of these calcite-brucite intergrowths indicates that they are pseudomorphs after dolomite and the conditions of dolomite retrogression will be discussed in section 4.5.6. Under the optical microscope, the different phases of the intergrowths are not distinguishable nor is the acicular shape visible (Figure 4.9a,b). The intergrowths are noticeable as gray-black patches in both bright field view and cross-polarized view (Figure 4.9a,b). The different phases of which the intergrowths are composed are distinguishable only with electron microscopy (Figure 4.9c). The calcite-brucite intergrowths appear as grains with frayed grain boundaries and are commonly located within serpentinized parts of the peridotites, often contoured by Fe-oxide (magnetite; Figure 4.9a-d), and in the peridotite matrix crosscut by serpentine veins (Figure 4.9e). A textural relation to calcite veinlets within the serpentine phases is observed in some samples (Figure 4.9d,f).

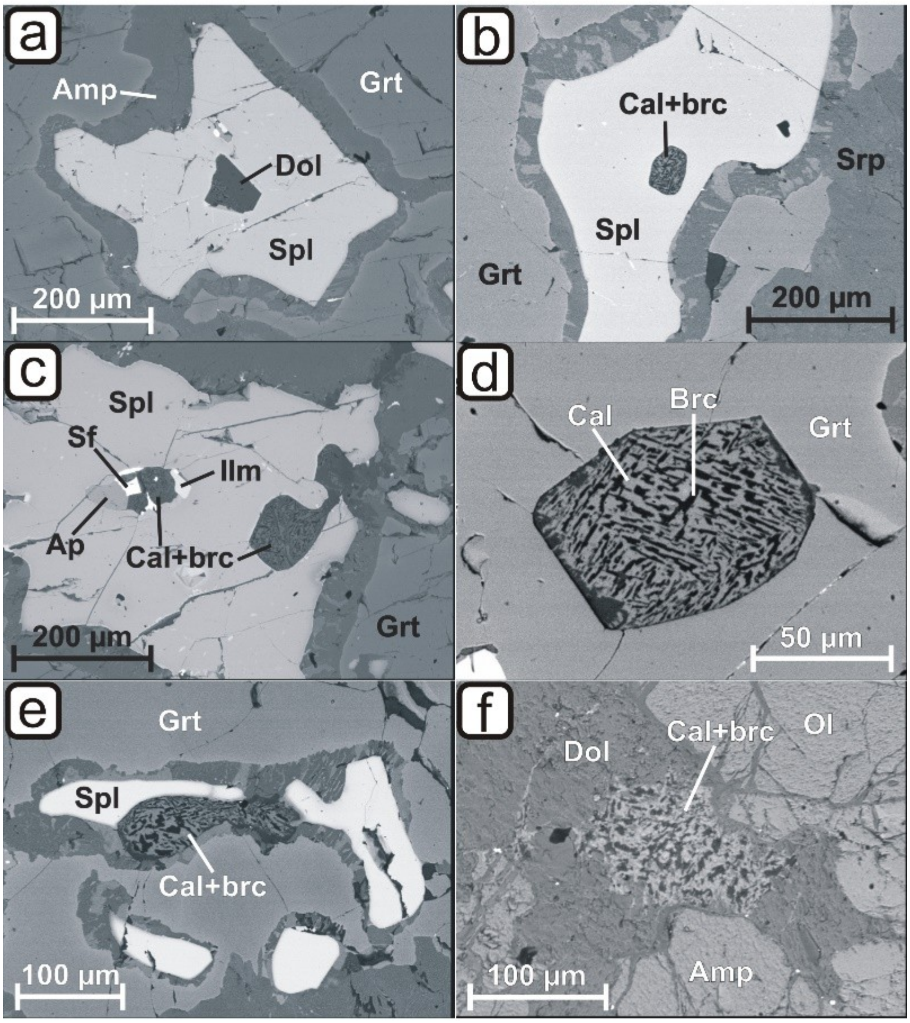

Figure 4.8. Back-scattered electron images of (a) an inclusion of euhedral dolomite in spinel surrounded by garnet in serpentinized fine-grained garnet-amphibole peridotite KL2.4-2b; (b) inclusion of calcite-brucite intergrowth in spinel surrounded by garnet in serpentinized fine-grained garnet-amphibole peridotite WG7; (c) calcite-brucite intergrowths as part of multi-phase solid inclusions in spinel in serpentinized fine-grained garnet-amphibole peridotite KL2.4-2b; (d,e) partly euhedral grains of calcite-brucite intergrowths as inclusion in garnet in serpentinized fine-grained garnet-amphibole peridotite (KBA8), (e) occasionally related to spinel hosted in garnet (WG7); (f) patch of calcite-brucite intergrowth with frayed grain boundary situated within a vein of associated anhedral dolomite and amphibole (KL1.6). Mineral abbreviations after Whitney & Evans (2010), sf: sulfide.

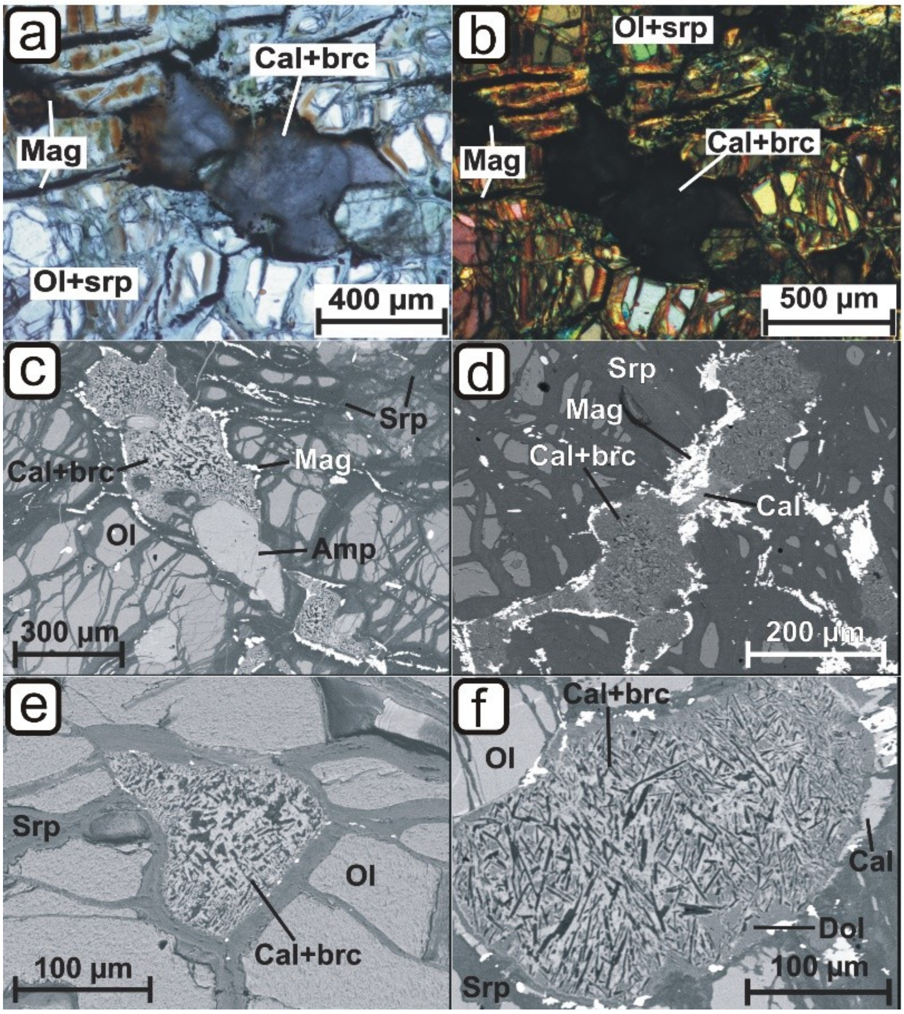

Figure 4.9. (a) Transmitted light photograph, (b) polarized transmitted light photograph and (c) back-scattered electron image of an intergrowth of acicular calcite and brucite located within the serpentine mesh texture in serpentinized fine-grained garnet-amphibole peridotite PL1.6, associated with amphibole and magnetite (thick section ~100 µm); (d-f) back-scattered electron images of calcite-brucite intergrowths in serpentinized fine-grained garnet-amphibole peridotites, (d) contoured by magnetite and associated with calcite patches, located within serpentinized parts (SB2.2), (e) located in the peridotite matrix crosscut by serpentine veins (KL1.3c), (f) with interspersed dolomite patches, located within the serpentine mesh texture, associated with magnetite, contoured by calcite veinlets (WG1). Mineral abbreviations after Whitney & Evans (2010).

In order to verify the mineralogical composition of these intergrowths, the relative abundance of elements (Ca, C, Mg, O, Fe) of selected areas of intergrowths was qualitatively measured. The relative element contents of all phases occurring in one intergrowth (sample WG1; Figure 4.10) are shown as "false-color" element maps (Figure 4.10b-f). The light gray part in the back-scattered-electron image (Figure 4.10a) is clearly richer in Ca and C and poorer in Mg, O and Fe than the black part in the electron image.

The key point regarding the element maps is that the black part is C-free, as the small C-content visible in the C-element map presumably derives from the carbon coating of the thin section. Comparison of the element abundances in the intergrowths confirmed the presence of brucite, a magnesium hydroxide ($Mg(OH)_2$). In the electron image (Figure 4.10a), a darker gray phase occurring as patches between calcite and brucite is clearly visible and was identified as dolomite. According to this observation, in some samples some calcite-brucite intergrowths contain relics of dolomite (dolomite patches and/or dolomitic rims; Figure 4.9f) indicating that dolomite was only partly replaced by calcite-brucite intergrowths.

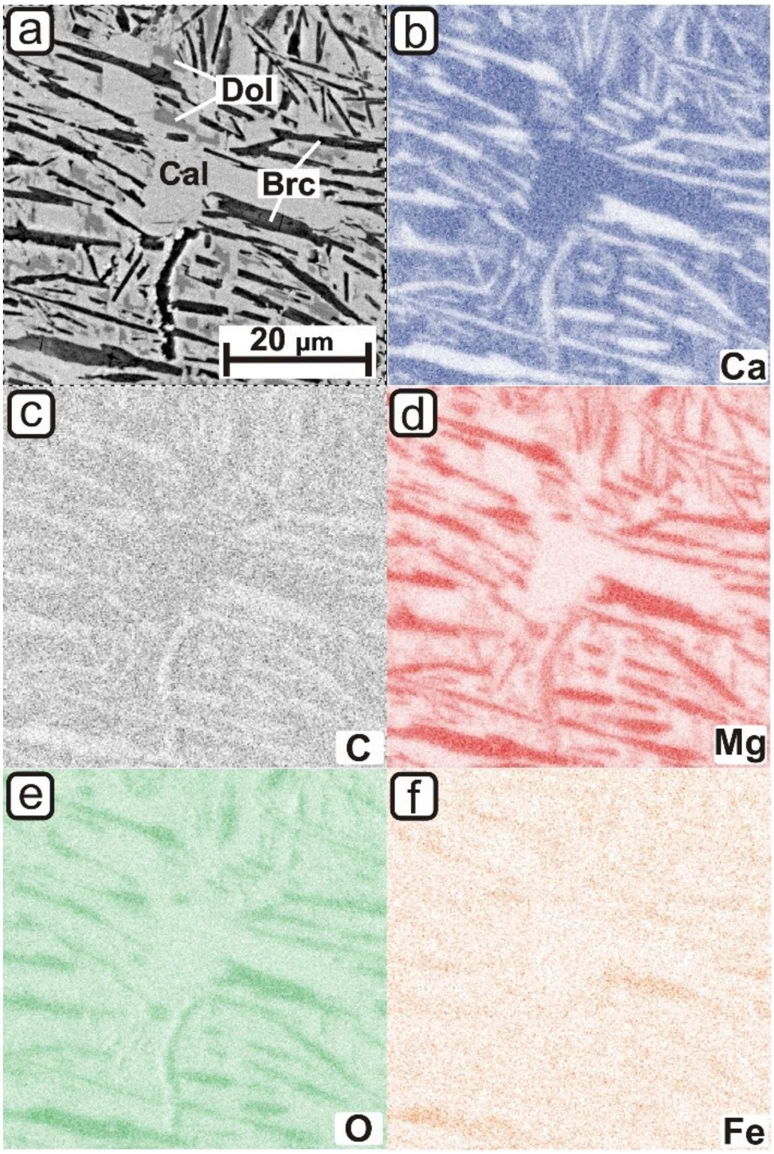

Figure 4.10. (a) Back-scattered electron image of an intergrowth of calcite (light gray phase) and acicular brucite (black phase) with interspersed dolomite patches (dark gray phase); (b-f) “false-color” element maps of the calcite-brucite intergrowths showing the distribution of (b) calcium, (c) carbon, (d) magnesium, (e) oxygen and (f) iron between the mineral phases. In the element maps (b-f) dark areas denote high element abundances and light areas denote low element abundances. Mineral abbreviations after Whitney & Evans (2010).

Occasionally, distinct euhedral calcite-brucite intergrowths occur as inclusions in spinel, also in spinel which is itself enclosed in garnet, and as part of multi-phase solid inclusions (Figure 4.8c). These inclusions are composed of calcite-brucite intergrowths + apatite ± serpentine ± sulfide ± ilmenite (Figure 4.8c). The contact zones between spinel and garnet commonly consist of kelyphite.

Also, grains of calcite-brucite intergrowths that are partly euhedral occur as inclusions in garnet (Figure 4.8d), occasionally touching spinel (Figure 4.8e) and/or related to serpentine. Finally, calcite + serpentine intergrowths as part of a multi-phase solid inclusion in spinel and in garnet related to a serpentine vein were observed. Patches of calcite-brucite intergrowths occur also situated within a vein of anhedral dolomite referred to earlier (section 4.4.1, Figure 4.5c,d). Also, veins consisting of calcite + brucite occur in serpentine veins and are there interlaced with serpentine and magnetite (Figure 4.11a,b). With one exception of a serpentinized coarse-grained sample, neither coarse-grained garnet-free nor garnet-bearing samples contain calcite-brucite intergrowths. This is in agreement with the lack of precursor dolomite in these samples.

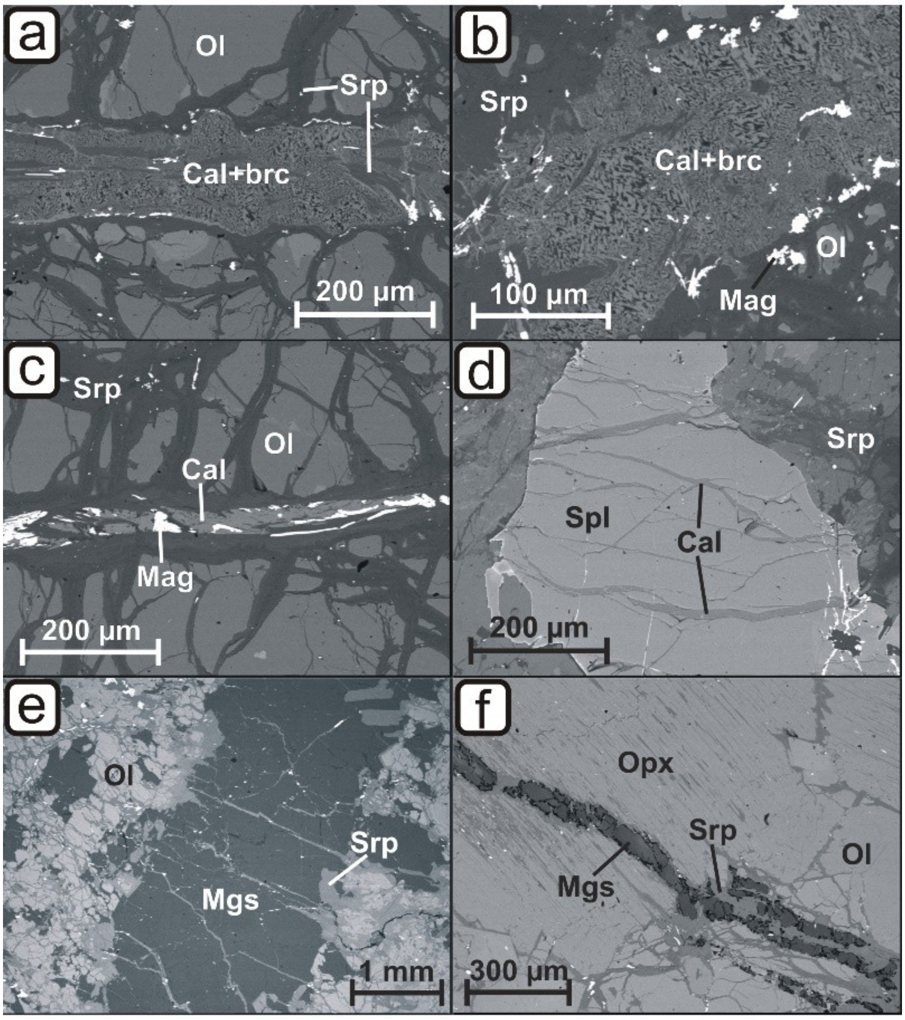

Figure 4.11. Back-scattered electron images of (a,b) a vein (~150 µm thickness) consisting of calcite-brucite intergrowths situated within a serpentine vein in serpentinized medium-grained peridotite KoDb2. The intergrown acicular calcite and brucite are interlaced with serpentine and magnetite; (c) calcite veinlet related to magnetite situated in the serpentine mesh texture of serpentinized medium-grained peridotite KoDb2; (d) calcite veinlets in spinel in serpentinized medium-grained peridotite KoDb2; (e) distinct magnesite vein with frayed boundaries in the mineral assemblage of serpentinized fine-grained garnet-free sample KoD9; (f) magnesite grains embedded in distinct serpentine vein with sharp boundary occurring within the ultramafic mineral assemblage of coarse-grained protogranular peridotite KoD4 as well as intersecting orthopyroxene and olivine in this sample. Mineral abbreviations after Whitney & Evans (2010).

4.4.3 Calcite veinlets

Fine veinlets (a few µm thick) and patches consisting of calcite occur in both fine- and medium-grained garnet-free peridotites and in garnet-bearing peridotites, as well as in coarse-grained garnet-free peridotites (Table A7, Appendix; Figure 4.11c,d). These calcite veinlets and patches are often situated within the serpentinized mesh texture in both fine-grained and coarse-grained peridotites where they are often associated with magnetite (Figure 4.11c). In this textural context, calcite veinlets are occasionally spatially closely related to the calcite-brucite intergrowths, often contouring the calcite-brucite grain boundaries (fine-grained garnet-bearing peridotites; Figure 4.9f). As mentioned in section 4.4.1, veinlets of calcite + dolomite + magnetite occur occasionally in serpentinized fine-grained garnet-bearing samples (Figure 4.7a). Calcite veinlets also crosscut mineral grains such as amphibole, clinopyroxene, garnet and spinel (Figure 4.11d).

4.4.4 Magnesite

In the studied sample set, magnesite occurs as anhedral grains in textural equilibrium with dolomite, as veins on a µm-to-mm scale (Table A7, Appendix), commonly situated within serpentine veins or the serpentine mesh texture in both coarse-grained and fine-grained garnet-free peridotites. In one coarse-grained protogranular sample, interstitial anhedral dolomite and magnesite are in textural equilibrium (Figure 4.5e,f) and are spatially closely related to a ~500 µm thick distinct magnesite vein (not shown) with frayed boundaries. This vein crosscuts the ultramafic mineral assemblage perpendicularly to the rock fabric. This is true also for a ~2 mm thick magnesite vein in a fine-grained garnet-free sample (Figure 4.11e). Another fine-grained garnet-free sample contains an anhedral magnesite aggregate in textural equilibrium with a euhedral dolomite crystal, situated in the serpentine mesh texture (Figure 4.7d-f). In this sample, magnesite also occurs as irregularly aligned grains embedded in a fine serpentine vein with sharp boundaries crosscutting the ultramafic mineral assemblage. A similar vein consisting of serpentine + magnesite occurs also in another coarse-grained protogranular peridotite (Figure 4.11f).

4.5 Discussion

The occurrences of different carbonates in the mantle wedge-derived ultramafic rocks from the UZ will be discussed in the following in the context of the regional tectono-metamorphic evolution. The various mineralogical and microstructural peridotite types (Table A7, Appendix) record different petrologic processes in the Ulten Zone and can be linked to particular carbonate minerals, associations and textures. Thus, this relationship may reflect different stages of carbonate formation and carbonate breakdown/replacement (stages 1-6, Figures 4.12, 4.13) accompanying the evolution of the UZ tectonic unit (Figure 4.12b) during continental collision.

4.5.1 Carbonate inclusions in primary spinel: Indicators for the mobilization of carbonated silicate melt in the hot mantle wedge

The dolomite inclusions, the calcite-brucite intergrowths after former dolomite (see section 4.5.6.) and the carbonate-bearing multi-phase solid inclusions (calcite-brucite + apatite ± ilmenite ± sulfide ± serpentine) entrapped in garnet-hosted coarse spinel (Figure 4.8a-c) indicate early carbonate formation in the UZ mantle wedge in the high-temperature spinel stage (stage 1, Figures 4.12, 4.13). Recent studies report the occurrence of multi-phase solid inclusions containing a carbon component in spinel in both orogenic peridotites (Zaccarini et al., 2004; Carswell & Van Roermund, 2005; Naemura et al., 2009) and peridotite xenoliths (Timina et al., 2012). For the first case, two hypotheses of carbon introduction into the mantle have been postulated: (1) The origin of such multi-phase inclusions in high-*T* Cr-spinel has been attributed to the reaction of protolith-peridotite with alkaline-carbonatite fluids formed from an original carbonatitic melt and a hydrous fluid, presumably generated during the emplacement of a mantle plume and mantle uplifting (Zaccarini et al., 2004). (2) Carbonate-bearing multi-phase inclusions (together with microdiamonds) originate from a supercritical COH-fluid that was generated during UH*P*-prograde dehydration and decarbonation reactions in a subducting continental slab (Carswell & Van Roermund, 2005). For peridotite xenoliths, it has been assumed that carbonate-water-chloride-rich fluids caused metasomatism accompanied by the formation of carbon-bearing solid inclusions in spinel (Timina et al., 2012).

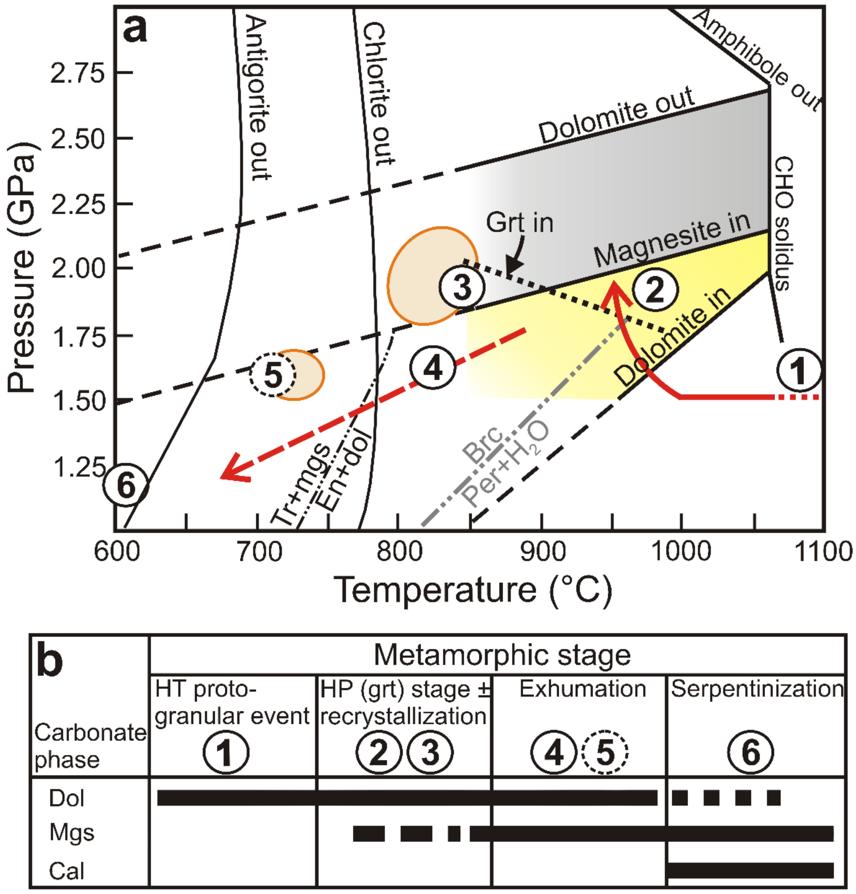

Figure 4.12. (a) Pressure-temperature (*P*-*T*) diagram with stages of carbonate formation in the tectono-metamorphic evolution of the Ulten Zone peridotites (1-6). The circle in stage 5 is dashed because the position of this stage in the diagram is only a possibility and may be shifted to lower pressures and temperatures in the antigorite stability field. Stability of dolomite (yellow shaded field) and dolomite + magnesite (gray shaded field) ≥1.5 GPa and ≥850°C (full lines) in the peridotite-COH system is taken from Tumiati et al. (2013) and extrapolated to lower pressures and temperatures (dashed lines). Dolomite-in, magnesite-in and dolomite-out curves from Tumiati et al. (2013) refer to carbonate formation from COH-fluids. Univariant reaction tremolite (tr) + magnesite (mgs) = enstatite (en) + dolomite (dol) taken from Malaspina & Tumiati (2012) for X_{CO2} = 0.5. Garnet-in curve based on experimental results of Tumiati et al. (2013). *P*-*T* curve for the brucite (brc) = periclase (per) + water (H_2O) equilibrium from Schramke et al. (1982). Antigorite-out curve and chlorite-out curve from Fumagalli & Poli (2005). Ovals overlapping with stage 3 and stage 5 mark *P*-*T* estimates for dolomite-bearing garnet-amphibole and chlorite-amphibole assemblages, respectively, from Braga & Sapienza (2007). Dotted red arrow marks cooling and pressure decrease from magmatic conditions due to corner flow, full red arrow marks isobaric cooling and subduction path of the Ulten Zone peridotites, dashed red arrow marks direction of exhumation path. (b) Table showing the stages of carbonate formation (stages 1 to 6) and carbonate stability linked to metamorphic stages of the Ulten Zone peridotites. H*T*: high temperature, H*P*: high pressure. Mineral abbreviations after Whitney & Evans (2010).

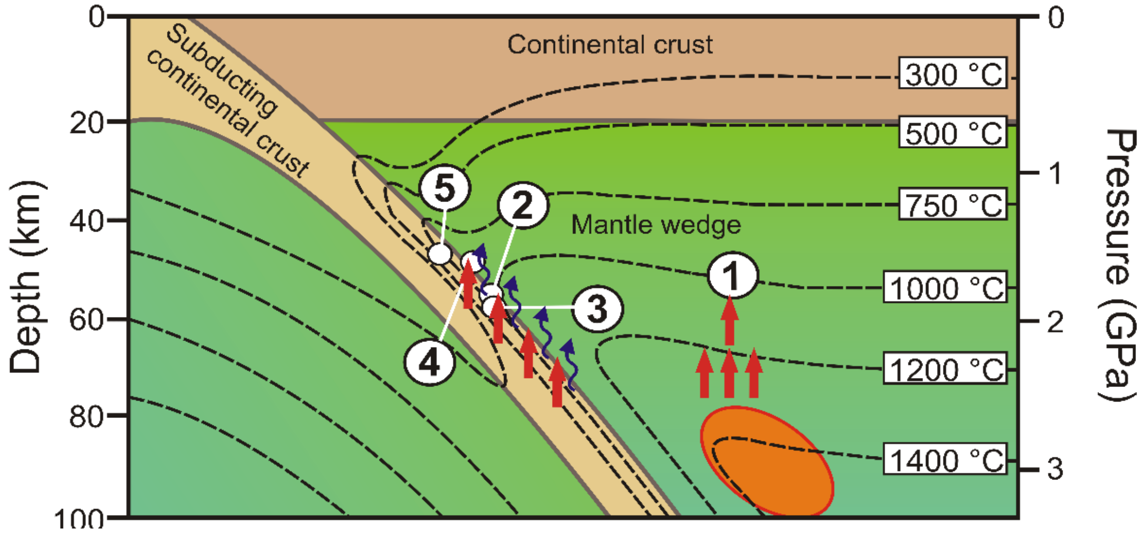

Figure 4.13. Schematic illustration of continental subduction and a possible scenario of the Ulten Zone evolution with different stages of carbonate formation. Infiltration of carbonated silicate melts or COH-fluids (red oval and arrows, stage 1) derived from an oceanic slab prompting dolomite formation during the high-temperature spinel stage. This is followed by isobaric cooling of peridotite as corner flow drags the mantle towards the cooler slab and infiltration of slab-derived aqueous COH-fluids (thin blue arrows), again leading to dolomite formation (stage 2). The COH-fluids are residual from reaction of slab-derived hydrous silicate melt (small red arrows in slab) with the mantle wedge (Rampone & Morten, 2001). During this event, at slightly higher pressure but lower temperature in the subduction mélange, these fluids led to the formation of associated dolomite and magnesite in the peridotite (stage 3). Exhumation starting at ca. 330 Ma (Tumiati et al., 2003) was accompanied by several stages of carbonate formation in the Ulten Zone peridotites, i.e. formation of interstitial vein-associated dolomite, again from continental slab-derived aqueous fluids, at lower pressure and temperature (stage 4) and formation of retrograde magnesite (±dolomite) from C-rich aqueous fluids (stage 5).

Supercritical fluids (which can vary from pure H_2O to hydrous melt) are restricted to ultrahigh-pressure conditions (e.g. Manning, 2004) in subduction zones and may not play a role during continental subduction. Oceanic subduction prior to continental subduction may have been associated with carbonate dissolution and silico-carbonatite formation in the supra-subduction mantle wedge as modeled by Tumiati et al. (2013). Evidence for carbonate dissolution in both oceanic and continental ultra-high pressure rocks have been reported recently (e.g. Frezzotti et al., 2011; Ferrando et al., 2017) and hydrous carbonatitic liquids were recently shown to form at temperatures down to 870°C to 900°C (Poli, 2015). Such liquids may have been liberated from a former oceanic slab and migrated upward into the hot portion of the wedge. In this case, dolomite and/or dedolomitization products would be expected also in spinel peridotites that never equilibrated in the garnet-stability field.

However, matrix dolomite and/or calcite-brucite intergrowths have not been observed in coarse-grained spinel peridotites or in the few fine-grained (post-)garnet-free peridotites available for study. On the other hand, Scambelluri et al. (2006) suggested that primary spinel lherzolites in the mantle wedge were infiltrated by subduction-related mafic melts which derived from deeper magma sources and carried recycled crustal components. We infer that these subduction-related mafic melts carried a carbon component responsible for the formation of carbonate in the multi-phase solid inclusions in spinel. The mineral assemblage in the multi-phase solid inclusions is not indicative of the pressure and temperature conditions at the time of entrapment of the melts. This assemblage precipitates during the subsequent evolution of the rock and may be, therefore, used to constrain the chemical composition of the melt (Frezzotti & Ferrando, 2015). Stage 1 in Figure 4.12 may, however, depict the conditions for the entrapment of the carbon-bearing melts in spinel. Considering their high-temperature mantle wedge origin, dolomite formation in the spinel peridotites likely predated entrainment in the subducting slab and associated metasomatic reactions.

4.5.2 Dolomite formation from crust-derived aqueous fluids at high pressures

In previous studies based on porphyroclastic and fine-grained garnet peridotites it has been consistently suggested that matrix dolomite and the coexisting hydrous phases (pargasitic amphibole ± phlogopite) plus apatite are of metasomatic origin and crystallized in equilibrium with garnet from aqueous COH-fluids in the garnet-stability field (Obata & Morten, 1987; Godard et al., 1996; Rampone & Morten, 2001; Tumiati et al., 2003; Marocchi et al., 2009; Sapienza et al., 2009). Such fluids have been interpreted to derive from a hydrous silicate melt released from the continental slab during migmatization of the host gneiss (Rampone & Morten, 2001; Tumiati et al., 2003; Sapienza et al., 2009) ca. 330 Ma ago (Tumiati et al., 2003). The low dolomite/amphibole proportion in the peridotites has been interpreted to reflect a low CO_2/H_2O ratio of the metasomatic fluid (Rampone & Morten, 2001).

In the present study, the fine-grained garnet-amphibole peridotites contain dolomite disseminated within the peridotite matrix (Figure 4.3), dolomite in a multi-phase solid inclusion in garnet (Figure 4.4e) as well as calcite-brucite intergrowths, which are interpreted to be dedolomitization products (section 4.5.6.), as inclusions in garnet (Figure 4.8d,e). The occurrences of dolomite in the multi-phase solid inclusion and of inclusions of calcite-brucite intergrowths in garnet lends strong support to the inference that the formation of dolomite occurred during garnet formation (stage 2, Figures 4.12, 4.13). Dolomite inclusions in matrix apatite and amphibole (Figure 4.4a,b) in these garnet-amphibole peridotites and the occasional close spatial relation between dolomite and these phases in the peridotite matrix (Figure 4.3) further support the assumption that they co-precipitated from a phosphorus-bearing COH-fluid. The rare observations of dolomite inclusions in matrix olivine (Figure 4.4c,f) in fine-grained garnet-amphibole peridotites indicate that the interaction of wedge peridotite with crust-derived fluids may have accompanied the formation of garnet + olivine at the expense of spinel + orthopyroxene + clinopyroxene (e.g. Jenkins & Newton, 1979; Obata & Morten, 1987; Klemme & O'Neil, 2000). Overall, based on P-T estimates for anhydrous peridotites (Nimis & Morten, 2000), Sapienza et al. (2009) suggested high-pressure dolomite formation (~2.5 GPa and 850-900°C, <100 km depth) and an additional dolomite formation episode at low-pressure retrograde metamorphic conditions (1.5-1.8 GPa and <850°C, shallow depths) in the UZ peridotites. The latter is consistent with the absence of primary discrete magnesite in the samples studied here, in accord with previous observations in UZ peridotites (Malaspina & Tumiati, 2012) and experimental results (magnesite stability >1.9 GPa at 900°C, Tumiati et al., 2013). Additionally, based on experimentally determined garnet stability in COH-bearing peridotites (Tumiati et al., 2013), it can be inferred that $T \geq 900°C$ at 1.9 GPa is required for dolomite formation when garnet is stable (stage 2, Figures 4.12, 4.13). Nevertheless, the association of dolomite, chlorite and dissakisite in the multi-phase solid inclusion in garnet (Figure 4.4e) may have crystallized at lower temperatures from a fluid inclusion entrapped in garnet. Tumiati et al. (2005; 2007) suggested that the mineral dissakisite-(La) ($CaLaAl_2MgSi_3O_{12}(OH)$), which is enriched in large ion lithophile elements (LILE), crystallized from crust-derived aqueous fluids at $P \leq 2.7$ GPa and $T \leq 850°C$. In this case the mineral association of the multi-phase solid inclusion would reflect the chemical composition of the carbon-bearing LILE-rich aqueous fluid which infiltrated the peridotites during the garnet-forming stage. The occurrence of dolomite + apatite as inclusion in zircon may be, as well, related to this stage. However, future geochronological and chemical analyses of the zircon will address the formation conditions of zircon in the UZ peridotites and the occurrence of dolomite inclusions in zircon.

In contrast to the fine-grained garnet-bearing peridotites, coarse garnet- and spinel peridotites commonly contain amphibole but generally neither apatite nor dolomite nor calcite-brucite intergrowths (except sample

MOL1.5; Table A7, Appendix). Tumiati et al. (2003) report that peridotite portions in the mantle wedge can escape hydration while other portions undergo infiltration of aqueous fluids and partial dolomite (re)crystallization. Accordingly, the absence of dolomite, calcite-brucite intergrowths as well as apatite in both coarse-grained spinel- and garnet peridotites suggests their preservation as lenses within the fine-grained host peridotites. This is in agreement with our field observation of the occurrence of coarse-grained peridotite as relics embedded within deformed fine-grained peridotite (Figure 4.2). In one locality (Samerbergalm), coarse-grained garnet-peridotites that are free of carbonate and apatite are spatially closely related, at meter scale, to the dolomite-bearing fine-grained garnet-amphibole peridotites. This structural occurrence may be attributed to the entrapment of fine-grained garnet-peridotites by the continental slab and attendant shearing, deformation and hydration/carbonation while the coarse peridotite was embedded and shielded from these processes.

4.5.3 Local formation of dolomite + magnesite from continental crust-derived aqueous fluids

Stability of magnesite + dolomite outside garnet stability can be achieved in a small *P-T* window (at ~1.8-2.0 GPa and at 850-900°C; stage 3, Figure 4.12) in the pressure and temperature range covered by the experiments by Tumiati et al. (2013). The only garnet-free sample containing associated anhedral magnesite and dolomite is a coarse-grained non-serpentinized peridotite (MOL1.5; Figure 4.5e,f) that probably never equilibrated in the garnet-stability field. The coexistence of interstitial anhedral dolomite and a magnesite vein in this sample indicates local injection of a crust-derived C-rich aqueous fluid with high CO_2/H_2O ratio. The absence of antigorite and chlorite in this sample shows that this peridotite-fluid interaction occurred indeed in the *P-T* window between the chlorite-out and garnet-in curves (stage 3, Figure 4.12). Interestingly, the location of stage 3 (magnesite + dolomite in garnet-free peridotite) in the *P-T* diagram (Figure 4.12) overlaps the *P-T* estimates for equilibration of dolomite-bearing hydrous garnet-amphibole peridotite at ~1.8-2.2 GPa and >800°C from Braga & Sapienza (2007). These *P-T* conditions were calculated considering a COH-fluid with $X_{CO2} = 0.1$ (Braga & Sapienza, 2007) and are in agreement with *P-T* estimates of 1.96 GPa and minimum temperature of 841°C by Malaspina & Tumiati (2012) for a dolomite + orthopyroxene inclusion in garnet. The discrepancy between these *P-T* estimates and those of Tumiati et al. (2013) may be explained by different X_{CO2} and/or other conditions for the calculations. Considering the experimentally determined phase relations by Tumiati et al. (2013), the temperature estimates for dolomite formation in garnet-amphibole peridotite by Braga & Sapienza (2007) and Malaspina & Tumiati (2012) are underestimated.

4.5.4 Dolomite in retrogression textures and dolomite veins: Indicators for low-pressure carbonation?

The occurrence of interstitial band-like dolomite and distinct dolomite veins (Figure 4.5b-d) related to amphibole in weakly serpentinized fine-grained peridotites leads to the assumption that at a certain stage on the exhumation path (stage 4, Figure 4.12) C-rich fluids prompted dolomite precipitation. This is in agreement with the occurrence of anhedral dolomite grains in amphibole-rich domains that were interpreted to derive from a COH-fluid during low-pressure retrograde conditions (Sapienza et al., 2009). Considering the low abundance of these dolomite veins and their limited extent, such fluids probably occurred only locally (similar to the carbonate occurrence in sample MOL1.5, discussed in section 4.5.3.). The veins consisting of calcite-brucite intergrowths observed in two serpentinized fine-grained samples (Figure 4.11a,b) crosscut the peridotite embedded in the serpentine mesh texture. This may indicate that the local formation of dolomite veins from a C-rich aqueous fluid occurred at a time after high-pressure dolomite formation (stage 2) and prior to low-temperature serpentinization during exhumation. The occurrence of dolomitic veinlets crosscutting the serpentine mesh texture (Figure 4.7a) and dolomite grains within a distinct serpentine vein (sample MR141B, Figure 4.7b) show that additional pulses of probably C-rich, aqueous fluids percolated the peridotites syn- and/or post-serpentinization during exhumation. It has been suggested that during exhumation a dolomite-magnesiohornblende-bearing garnet-free assemblage develops at ~1.8 GPa and ≥790°C (Malaspina & Tumiati, 2012). At these retrograde metamorphic conditions, dolomite occurs as part of a kelyphitic assemblage (orthopyroxene + magnesiohornblende + spinel + minor dolomite) around garnet, while larger dolomite neoblasts, orthopyroxene, magnesiohornblende and olivine constitute the stable matrix assemblage (Malaspina & Tumiati, 2012). These observations may be in agreement with the dolomite in garnet pseudomorphs (Figure 4.5a) and kelyphitic coronas in some fine-grained peridotites that once equilibrated in the garnet-stability field. However, the question arises if low-pressure formation of dolomite + magnesiohornblende by crust-derived aqueous fluids (Sapienza et al., 2009) during exhumation overprinted or recrystallized a pre-existing dolomite-bearing assemblage, which originally formed at higher pressure conditions while garnet was stable. If dolomite neoblasts that are ascribed to crystallization at equilibrium with garnet (Sapienza et al., 2009) coexist with retrograde dolomite in kelyphites, low-pressure retrograde ingress of COH-fluids would form new dolomite but not destabilize the pre-existing matrix dolomite. Chemical analyses of dolomites and associated amphiboles will help distinguish between different stages of dolomite formation. In this context, it must be noted that it remains subject of debate whether the polycrystalline dolomite aggregate (Figure 4.6) can be attributed to high-pressure dolomite formation during garnet stability (stage 2) or to low-pressure formation of vein-like dolomite (stage 4).

4.5.5 Formation of retrograde magnesite

In contrast to magnesite + dolomite in sample MOL1.5 (section 4.5.3.), the anhedral magnesite aggregate touching a euhedral dolomite crystal (Figure 4.7d-f) in a garnet-free serpentinized fine-grained peridotite (sample SBB2F) is set in the serpentine mesh and presumably of different origin than the dolomite + magnesite in sample MOL1.5. The stability of magnesite + dolomite may be achieved at lower pressures and temperatures during retrograde metamorphic stages (Malaspina & Tumiati, 2012). These authors report the formation of magnesite coronas around dolomite attributed to the transition from magnesiohornblende-dolomite peridotite to chlorite-tremolite-magnesite peridotite with decreasing pressure and temperature in the UZ (Malaspina & Tumiati, 2012). Retrograde magnesite formation in this mineral assemblage is consistent with the *P-T* estimates of Braga & Sapienza (2007) of ~730°C at ~1.6 GPa (Malaspina & Tumiati, 2012) for $X_{CO2} = 0.5$ for garnet-free, carbonate-bearing peridotite. Stage 5 in Figure 4.12 marks a possible location of retrograde magnesite formation as observed in sample SBB2F according to the *P-T* estimates of Braga & Sapienza (2007) and the univariant reaction tremolite + magnesite = enstatite + dolomite + H_2O + CO_2 modeled by Malaspina & Tumiati (2012), also considering $X_{CO2} = 0.5$. Interestingly, the *P-T* estimates of dolomite-bearing chlorite-amphibole peridotite of Braga & Sapienza (2007) plot in the magnesite-stability field estimated by Malaspina & Tumiati (2012). Those for the dolomite-bearing assemblage depend on the X_{CO2} in the fluid (Braga & Sapienza, 2007) and a lower X_{CO2} would shift magnesite stability to higher *P-T* conditions. This may explain the absence of magnesite in this assemblage and the discrepancy of the different *P-T* estimates. For the magnesite + dolomite-bearing sample SBB2F, pre-existing dolomite may have decomposed leading to the formation of magnesite. Alternatively, sample SBB2F never contained dolomite (as e.g. from stage 2, since further dolomite has not been observed in this sample). In this case, dolomite + magnesite may have formed from a COH-fluid at high X_{CO2}, which shifts the COH-fluid magnesite-in curve to lower pressures (Tumiati et al., 2013). The coexistence of magnesite + dolomite with serpentine in this sample may indicate that the carbonate phases were stable at even lower temperatures (<730°C) in the antigorite stability field during exhumation. In this case, magnesite may coexist with antigorite at exhumation *P-T* conditions. Common stability of carbonate phases and serpentine may, thus, indicate elevated X_{CO2} (>0.5?) in the metasomatizing fluid. Alternatively, they formed at higher temperatures and persisted metastably because fluid flow subsequently was insufficient to catalyze their breakdown. This may also apply to the magnesite vein in serpentinized sample KoD9 (Figure 4.11e).

4.5.6 Dedolomitization in Ulten Zone peridotites

Intergrowths of calcite and the magnesium hydroxide brucite ($Mg(OH)_2$) in natural ultramafic rocks have been rarely observed to date. Berg (1986) first reported the presence of finely intergrown calcite and brucite in mantle-derived xenoliths in diamond-bearing volcanic kimberlite of the Kimberly pipe, South Africa. These calcite-brucite intergrowths were observed in coarse garnet lherzolite, porphyroclastic lherzolite and porphyroclastic wehrlite and were interpreted to reflect the breakdown products of dolomite (Berg, 1986). We here present a new observation of calcite-brucite intergrowths as dedolomitization products in wedge-derived peridotite. This interpretation is supported by the occurrence of dolomite patches within the intergrown calcite and brucite (Figure 4.9a), which may represent relict dolomite from incomplete dolomite breakdown. Also, located in the ultramafic matrix, the calcite-brucite intergrowths often inherit the grain shape of former discrete dolomite. Since the occurrence of calcite-brucite intergrowths is commonly associated with serpentinization, we suggest that the breakdown of dolomite in the UZ peridotites is linked to the reaction with serpentinizing aqueous fluids at low *P-T* conditions (stage 6, Figure 4.12). Consistent with dolomite formation at the time of garnet formation (section 4.5.2.), calcite-brucite intergrowths after dolomite predominate in serpentinized fine-grained mylonitic peridotites that once equilibrated in the garnet stability field. This is in agreement with the suggested clockwise exhumation path of the UZ rocks (Nimis & Morten, 2000; Tumiati et al., 2003), where coexisting hornblende + dolomite become instable at pressures < 1.5 GPa and temperatures ≤ 700°C (Nimis & Morten, 2000) while antigorite stabilizes (Figure 4.12). In contrast, the preservation of interstitial discrete dolomite in some garnet-bearing fine-grained peridotites is attributed to the lack of serpentinization of these samples and the rapid *P-T* decrease during exhumation. This would be consistent with the late-Carboniferous fast exhumation of the UZ mélange (Ranalli et al., 2005) and the assumption that rapid exhumation may have hampered slow dolomite-consuming silicate-carbonate reactions (Berg, 1986), in particular in the absence of catalyzing fluids. This also explains the occasional preservation of dolomite inclusions in crack-free host minerals, even in highly-serpentinized samples that contain calcite-brucite intergrowths related to serpentinization. The breakdown of dolomite into periclase + calcite symplectites, according to the reaction dolomite = calcite + periclase + CO_2, was observed in high-pressure garnet-peridotites (Yang et al., 1993), in mantle-derived xenoliths (Berg, 1986) and in marbles (Goldsmith, 1980). In the latter case, subsequent hydration of periclase led to formation of brucite (Berg, 1986). This reaction sequence has been also suggested for other dolomite marbles where brucite has a spherical shape that has been interpreted to record the primary cubic periclase structure (Müller et al., 2009). The acicular habit of brucite within the calcite-brucite intergrowths in UZ peridotites reflects its trigonal crystal structure, and thus, brucite cannot be interpreted to be pseudomorphic after periclase. This is in agreement with the overlap of the UZ exhumation path (Nimis & Morten, 2000; Tumiati et al., 2003) with the brucite stability field given by the *P-T* curve for brucite-periclase equilibrium (Figure 4.12) experimentally determined by Schramke et al. (1982). In the temperature range for UZ exhumation (decreasing from ~900°C), brucite forms even at decreasing water fugacities (Schramke et al., 1982) in a low-pressure range (0.1 to 2.0 GPa). This supports the inference that dedolomitization and carbon release in the UZ peridotites are caused by late low-*P-T* fluid infiltration inducing serpentinization (stage 6, Figure 4.12) and direct formation of calcite-brucite intergrowths according to the reaction $CaMg(CO_3)_2 + H_2O \rightarrow CaCO_3 + Mg(OH)_2 + CO_2$. The occasional occurrence of dolomite grains embedded in the serpentine mesh texture (Figure 4.7c) in samples containing calcite-brucite intergrowths may indicate infiltration by serpentinizing aqueous fluids while the mantle was still in the dolomite stability field and/or that dolomite which formed at high-pressure conditions (stage 2) persists metastably. Extrapolation of dolomite stability from experimentally determined conditions (Tumiati et al., 2013) to lower pressure and temperature (Figure 4.12; area below 850°C) shows that dolomite may be stable at *P-T* conditions of antigorite stability, probably below 700°C during the UZ exhumation path.

4.5.7 Fate of carbon during dedolomitization and carbon recycling in collisional settings

The fine magnesite + serpentine veinlets with sharp boundaries crosscutting the ultramafic mineral assemblage (Figure 4.11f) are interpreted as fracture fillings. Magnesite in these veinlets probably precipitated from a near-surface COH-fluid. This process has been previously suggested also for hydrothermal magnesite veins in serpentinites (e.g. Ghoneim et al., 2003) and is similar to the reaction path leading to listwanite formation in peridotites and serpentinites (e.g. Hansen et al., 2005; Power et al., 2013; Zhang et al., 2015): magnesite precipitates as fracture filling from fluids at the expense of serpentine minerals at a time after the serpentinization process, as discussed earlier for magnesite veins in samples SBB2F and KoD9 (section 5.5.5.). Calcite veinlets in some coarse-grained samples cutting the ultramafic minerals may also be fracture fillings. In contrast, the fine calcite veinlets and patches in serpentinized fine-grained peridotites, rather than representing late fracture fillings, are suggested to be related to serpentinization as they are embedded within the serpentine mesh texture and therein often related to the calcite-brucite intergrowths. The close spatial relationship between calcite veinlets and magnetite within the serpentine veins reveals that the serpentinizing fluid was carbon-bearing. Although the source of carbon in this fluid is presently unconstrained, it may be speculated that dedolomitization, which was likely caused by fluid ingress, led to release of a mobile carbon species into the fluid (i.e. $CaMg(CO_3)_2 + H_2O \rightarrow CaCO_3 + Mg(OH)_2 + CO_2$). This would have enabled *in-situ* formation of secondary carbonate generations, now observed as veins (Figure 4.11c,d). The lack of dedolomitization products in the majority of the coarse-grained peridotites, yet presence of calcite veinlets in some of these samples, is here taken to reflect local variations in the volume and carbon content (e.g. CO_2/H_2O) of the fluid. While the ultimate fate of the carbon released by dedolomitization remains unclear, multiple pieces of evidence suggest that the supra-subduction zone peridotitic mantle from the UZ largely acted as an efficient carbon trap: (1) Preservation of an early generation of discrete dolomite grains dating from the high-temperature mantle wedge stage, (2) additional generation of dolomite during interaction of supra-subduction zone mantle with fluids derived from the subducting continental crust, (3) and breakdown of dolomite into calcite-brucite intergrowths, with attendant release of a carbon species that may have precipitated secondary carbonate minerals in veins and veinlets elsewhere as a function of *P-T-X*. Carbon fixation at the slab-wedge interface has been documented also in subduction zones involving oceanic slabs (Piccoli et al., 2016; Scambelluri et al., 2016).

4.6 Summary and conclusions

The occurrences of different carbonate phases in various textural settings in the peridotites of the UZ indicate multi-stage carbonation and carbonate breakdown and may be linked to particular petrologic processes affecting the mantle wedge peridotite during the UZ tectono-metamorphic evolution. At each stage of carbonate formation from COH-fluids, the composition of the fluid (e.g. X_{CO2}) controls the precipitation of particular carbonate phases making it difficult to estimate *P-T* conditions from a petrographical point of view only. Nevertheless, for the UZ peridotites, different stages of carbonate formation and breakdown can be identified and related to changing *P-T* conditions, depending on the presence or absence of fluids that are able to catalyze prograde or retrograde reactions:

1) An early generation of dolomite formed in the high-temperature spinel-stability field (stage 1). This is evidenced by euhedral grains of dolomite and calcite-brucite intergrowths in primary coarse spinel

surrounded by garnet. The liquids responsible for dolomite formation may have been mafic carbonated melts produced in deeper parts of the subduction zone.

2) Dolomite and hydrous phases, such as pargasitic amphibole and apatite, are suggested to have formed from a H_2O-CO_2-mixed aqueous fluid released by the subducting continental slab in the garnet-stability field (~1.9 GPa, ≥900°C) during migmatization of host crustal rocks at 330 Ma (stage 2). Petrographic evidence for this includes euhedral discrete dolomite grains, often associated with and occasionally included in garnet, amphibole, apatite and olivine, exclusively in fine-grained non-serpentinized garnet-amphibole peridotites.
3) Local injection of a CO_2-rich aqueous fluid may have caused the formation of coexisting dolomite + magnesite outside garnet stability at ~2.0 GPa and ~850°C (stage 3), as suggested by associated interstitial anhedral dolomite and magnesite associated with amphibole in non-serpentinized coarse-grained garnet-free peridotite.
4) After high-pressure dolomite formation (stage 2) and prior to low-temperature serpentinization, CO_2-rich aqueous fluids locally caused the formation of veins and anhedral interstitial dolomite + amphibole (stage 4). This event is similar to stage 3 but takes place outside magnesite stability and is inferred from the observation of distinct veins consisting of anhedral dolomite grains associated with amphibole ± serpentine, crosscutting the peridotite matrix.
5) Retrograde magnesite formed in the antigorite stability field (≤730°C and ≤1.6 GPa) together with serpentine from an aqueous COH-fluid (stage 5), as indicated by an anhedral magnesite aggregate related to magnesite veinlets in garnet-free serpentinized fine-grained peridotite and therein texturally associated with serpentine.
6) During low-pressure/temperature serpentinization, dolomite decomposed into finely intergrown calcite + brucite due to interaction with H_2O-rich fluids (stage 6). This is evidenced by pseudomorphs after dolomite and the close spatial relationship of the intergrowths to serpentinization products. A carbon species was likely released during the process, which may have precipitated carbonates in veins and veinlets at appropriate *P-T-X* conditions, as observed ubiquitously in both fine-grained garnet-free and garnet-bearing peridotites, as well as in coarse-grained garnet-free peridotites.
7) Carbon-bearing aqueous near-surface fluids triggered syn- or post-serpentinization formation of veins in pre-existing pathways (e.g. cracks), consisting of further serpentine + magnesite and/or calcite.

Considering the stability of the various carbonates and coexisting silicate minerals, we suggest that the *P-T* conditions for carbonate formation in the UZ peridotites from aqueous COH-fluids could only be achieved in the supra-subduction zone mantle wedge close to the continental slab (Figure 4.13). In contrast, carbonate formation in peridotite in the hot wedge, farther from the slab, could occur only from rising fluids and/or melts possibly originating from deeper parts of the subduction zone. A portion of the carbon released to the serpentinizing fluid causing dolomite breakdown may have escaped the system. However, overall, the ubiquity of carbonates in a variety of textural settings in the UZ peridotites, from discrete dolomite grains to vein-associated carbonates, and likely formed from a variety of liquids during several tectono-metamorphic stages in the rocks' evolution, suggests that the supra-subduction zone mantle in continental settings represents an efficient carbon trap.

4.7. References

1. Ague, J.J., Nicolescu, S. (2014). Carbon dioxide released from subduction zones by fluid-mediated reactions. Nature Geoscience 7, 355-360.
2. Bebout, G.E. (1996). Volatile transfer and recycling at convergent margins: mass-balance and insights from high-P/T metamorphic rocks. In: G.E. Bebout, D.W. Scholl, S.H. Kirby, J.P. Platt (Eds.). Subduction top to bottom, American Geophysical Union, Washington, D.C., 179-193.

3. Berg, G.W. (1986). Evidence for carbonate in the mantle. Nature 324, 50-51.
4. Braga, R., Sapienza, G.T. (2007). The retrograde evolution of a dolomite-bearing hydrous peridotite from the Ulten Zone (Italian Alps). GeoActa 6, 37-45.
5. Canil, D. (1990). Experimental study bearing on the absence of carbonate in mantle-derived xenoliths. Geology 18, 1011-1013.
6. Carswell, D.A., Van Roermund, H.L.M. (2005). On multi-phase mineral inclusions associated with microdiamond formation in mantle-derived peridotite lens at Bardane on Fjørtoft, west Norway. European Journal of Mineralogy 17, 31-42.
7. Eggler, D.H. (1978). Stability of dolomite in a hydrous mantle, with implications for the mantle solidus. Geology 6, 397-400.
8. Eggler, D.H., Kushiro, I., Holloway, J.R. (1979). Free energies of decarbonation reactions at mantle pressures: I. Stability of the assemblage forsterite-enstatite-magnesite in the system MgO-SiO_2-CO_Z-H_2O to 60 kbar. American Mineralogist 64, 288-293.
9. Facq, S., Daniel, I., Montagnac, G., Cardon, H., Sverjensky, D. (2014). *In situ* Raman study and thermodynamic model of aqueous carbonate speciation in equilibrium with aragonite under subduction zone conditions. Geochimica et Cosmochimica Acta 132, 375-390.
10. Ferrando, S., Groppo, C., Frezzotti, M.L., Castelli, D., Proyer, A. (2017). Dissolving dolomite in a stable UHP mineral assemblage: Evidence from Cal-Dol marbles of the Dora-Maira Massif (Italian Western Alps). American Mineralogist 102, 42-60.
11. Frezzotti, M.L., Selverstone, J., Sharp, Z.D., Compagnoni, R. (2011). Carbonate dissolution during subduction revealed by diamond-bearing rocks from the Alps. Nature Geoscience 4, 703-706.
12. Frezzotti, M.L., Ferrando, S. (2015). The chemical behaviour of fluids released during deep subduction based on fluid inclusions. American Mineralogist 100, 352-377.
13. Fumagalli, P., Poli, S. (2005). Experimentally determined phase relations in hydrous peridotites to 6.5 GPa and their consequences on the dynamics of subduction zones. Journal of Petrology 46, 555-578.
14. Ghoneim, M.F., Salem, L.A., Hamdy, M.M. (2003). Origin of magnesite veins in serpentinites from Mount El-Rubshi and Mount El-Maiyit, Eastern desert, Egypt. Archiwum Mineralogiczne 54, 41-63.
15. Godard, G., Martin, S., Prosser, G., Kienast, J.R., Morten, L. (1996). Variscan migmatites, eclogites and garnet-peridotites of the Ulten zone, Eastern Austroalpine system. Tectonophysics 259, 313-341.
16. Godard, G., Martin, S. (2000). Petrogenesis of kelyphites in garnet peridotites: a case study from the Ulten zone peridotites, Italian Alps. Journal of Geodynamics 30, 117-145.
17. Goldsmith, J.R. (1980). Thermal Stability of Dolomite at High Temperatures and Pressures. Journal of Geophysical Research 85, 6949-6954.
18. Green, D.H., Wallace, M.E. (1988). Mantle metasomatism by ephemeral carbonatite melts. Nature 336, 459-462.
19. Green, T.H., Adam, J., Sie, S.H. (1992). Trace element partitioning between silicate minerals and carbonatite at 25 kbar and application to mantle metasomatism. Mineralogy and Petrology 46, 179-184.
20. Hansen, L.D., Dipple, G.M., Gordon, T.M., Kellet, D.A. (2005). Carbonated serpentinite (listwanite) at Atlin, British Columbia: a geological analogue to carbon dioxide sequestration. Canadian Mineralogist 43, 225-239.
21. Hauzenberger, C.A., Höller, W., Hoinkes, G. (1996). Transition from eclogite to amphibolite-facies metamorphism in the Austroalpine Ulten Zone. Mineralogy and Petrology 58, 111-130.
22. Ionov, D.A., Dupuy, C., O'Reilly, S.Y., Kopylova, M.G., Genshaft, Y.S. (1993). Carbonated peridotite xenoliths from Spitsbergen: implications for trace element signature of mantle carbonate metasomatism. Earth and Planetary Science Letters 119, 283-297.
23. Ionov, D.A., O'Reilly, S.Y., Genshaft, Y.S., Kopylova, M.G. (1996). Carbonate-bearing mantle peridotite xenoliths from Spitsbergen: phase relationships, mineral compositions and trace-element residence. Contrib. Mineralogy and Petrology 125, 375-392.
24. Ionov, D.A. (1998). Trace element composition of mantle-derived carbonates and coexisting phases in peridotite xenoliths from alkali basalts. Journal of Petrology 39, 1931-1941.

25. Jenkins, D.M., Newton, R.C. (1979). Experimental determination of the spinel peridotite to garnet peridotite inversion at 900° C and 1,000° C in the system CaO-MgO-Al_2O_3-SiO_2, and at 900° C with natural garnet and olivine. Contributions to Mineralogy and Petrology 68, 407-419.
26. Kerrick, D.M., Connolly, J.A.D. (1998). Subduction of ophicarbonates and recycling of CO_2 and H_2O. Geology 26, 375-378.
27. Kerrick, D.M., Connolly, J.A.D. (2001). Metamorphic devolatilization of subducted marine sediments and the transport of volatiles into the Earth's mantle. Nature 411, 293-296.
28. Klemme, S., O'Neill, H.St.C. (2000). The near-solidus transition from garnet lherzolite to spinel lherzolite. Contributions to Mineralogy and Petrology 138, 237-248.
29. Laurora, A., Mazzucchelli, M., Rivalenti, G., Vannucci, R., Zanetti, A., Barbieri, M.A., Cingolani, C.A. (2001). Metasomatism and melting in carbonated peridotite xenoliths from the mantle wedge: the Gobernador Gregores case (Southern Patagonia). Journal of Petrology 42, 69-87.
30. Lee, C.-T., Rudnick, R.L., McDonough, W.F., Horn, I. (2000). Petrologic and geochemical investigation of carbonates in peridotite xenoliths from northeastern Tanzania. Contributions to Mineralogy and Petrology 139, 470-484.
31. Malaspina, N., Tumiati, S. (2012). The role of C-O-H and oxygen fugacity in subduction-zone garnet peridotites. European Journal of Mineralogy 24, 607-618.
32. Manning, C.E. (2004). The chemistry of subduction-zone fluids. Earth and Planetary Science Letters 223, 1-16.
33. Manning, C.E., Shock, E.L., Sverjensky, D.A. (2013). The chemistry of carbon in aqueous fluids at crustal and upper-mantle conditions: experimental and theoretical constraints. Reviews in Mineralogy and Geochemistry 75, 109-148.
34. Marocchi, M., Hermann, J., Morten, L. (2007). Evidence for multi-stage metasomatism of chlorite-amphibole peridotites (Ulten Zone, Italy): Constraints from trace element compositions of hydrous phases. Lithos 99, 85-104.
35. Marocchi, M., Mair, V., Tropper, P., Bargossi, G.M. (2009). Metasomatic reaction bands at the Mt. Hochwart gneiss-peridotite contact (Ulten Zone, Italy): insights into fluid-rock interaction in subduction zones. Mineralogy and Petrology 95, 251-272.
36. Martin, S., Morten, L., Prosser, G. (1993). Metamorphic and structural evolution of the Spl- to Grt-peridotites and surrounding basement rocks from the Nonsberg area. In: L. Morten (Ed.). Italian Eclogites and Related Rocks, Rendiconti della Accademia Nazionale Quaranta, XIII, 237-251.
37. Martin, S., Godard, G., Prosser, G., Schiavo, A., Bernoulli, D., Ranalli, G. (1998). Evolution of the deep crust at the junction Austroalpine/Southalpine: the Tonale Nappe. Memorie di Scienze Geologiche (Padova) 50, 3-50.
38. Molina, J.F., Poli, S. (2000). Carbonate stability and fluid compositions in subducted oceanic crust: an experimental study on H_2O-CO_2-bearing basalts. Earth and Planetary Science Letters 176, 295-310.
39. Morten, L., Bargossi, G.M., Bargossi, F. (1976). Notizie preliminari sulle metamorfiti della Val di Rumo, Val di Non, Trento. Mineralogica et Petrographica Acta 21, 137-144.
40. Morten, L., Obata, M. (1983). Possible high-temperature origin of pyroxenite lenses within garnet peridotite, northern Italy. Bulletin de Minéralogie 106, 775-780.
41. Müller, T., Baumgartner, L.P., Foster Jr., C.T., Bowman, J.R. (2009). Crystal size distribution of periclase in contact metamorphic dolomite marbles from Southern Adamello Massif, Italy. Journal of Petrology 50, 451-465.
42. Naemura, K., Hirajima, T., Svojtka, M. (2009). The pressure-temperature path and the origin of phlogopite in spinel-garnet peridotites from the Blanský Les Massif of the Moldanubian Zone, Czech Republic. Journal of Petrology 50, 1795-1827.
43. Nimis, P., Morten, L. (2000). P-T evolution of "crustal" garnet peridotites and included pyroxenites from Nonsberg area (Upper Austroalpine), NE Italy: from the wedge to the slab. Journal of Geodynamics 30, 93-115.

44. Obata, M., Morten, L. (1987). Transformation of spinel lherzolite to garnet lherzolite in ultramafic lenses of the Austridic Crystalline Complex, Northern Italy. Journal of Petrology 28, 599-623.
45. Piccoli, F., Vitale-Brovarone, A, Beyssac, O., Martinez, I., Ague, J.J., Chaduteau, C. (2016). Carbonation by fluid-rock interactions at high-pressure conditions: Implications for carbon cycling in subduction zones. Earth and Planetary Science Letters 445, 146-159.
46. Poli, S., Franzolin, E., Fumagalli, P., Crottini, A. (2009). The transport of carbon and hydrogen in subducted oceanic crust: An experimental study to 5 GPa. Earth and Planetary Science Letters 278, 350-360.
47. Poli, S. (2015). Carbon mobilized at shallow depths in subduction zones by carbonatitic liquids. Nature Geoscience 8, 633-636.
48. Power, I.M., Wilson, S.A., Dipple, G.M. (2013). Serpentinite carbonation for CO_2 sequestration. Elements 9, 115-121.
49. Rampone, E., Morten, L. (2001). Records of crustal metasomatism in the garnet peridotites of the Ulten Zone (Upper Austroalpine, Eastern Alps). Journal of Petrology 42, 207-219.
50. Ranalli, G., Martin, S., Mahatsente, R. (2005). Continental subduction and exhumation: an example from the Ulten Unit, Tonale Nappe, Eastern Austroalpine. In: D. Gapais, J.P. Brun, P.R. Cobbold (Eds.). Deformation Mechanisms, Rheology and Tectonics: from Minerals to the Lithosphere, Geological Society, London, Special Publications 243, 159-174.
51. Sapienza, G.T., Scambelluri, M., Braga, R. (2009). Dolomite-bearing orogenic garnet peridotites witness fluid-mediated carbon recycling in a mantle wedge (Ulten Zone, Eastern Alps, Italy). Contributions to Mineralogy and Petrology 158, 401-420.
52. Scambelluri, M., Philippot, P. (2001). Deep fluids in subduction zones. Lithos 55, 213-227.
53. Scambelluri, M., Hermann, J., Morten, L., Rampone, E. (2006). Melt- versus fluid-induced metasomatism in spinel to garnet wedge peridotites (Ulten Zone, Eastern Italian Alps): clues from trace element and Li abundances. Contributions to Mineralogy and Petrology 151, 372-394.
54. Scambelluri, M., Bebout, G.E., Belmonte, D., Gilio, M., Campomenosi, N., Collins, N., Crispini, L. (2016). Carbonation of subduction-zone serpentinite (high-pressure ophicarbonate; Ligurian Western Alps) and implications for the deep carbon cycling. Earth and Planetary Science Letters 441, 155-166.
55. Schramke, J.A., Kerrick, D.M., Blencoe, J.G. (1982). Experimental determination of the brucite = periclase + water equilibrium with a new volumetric technique. American Mineralogist 67, 269-276.
56. Shcheka, S.S., Wiedenbeck, M., Frost, D.J., Keppler, H. (2006). Carbon solubility in mantle minerals. Earth and Planetary Science Letters 245, 730-742.
57. Timina, T.Y., Kovyazin, S.V., Tomilenko, A.A. (2012). The composition of melt and fluid inclusions in spinel of peridotite xenoliths from Avacha volcano (Kamchatka). Doklady Earth Sciences 442, 115-119.
58. Tumiati, S., Thöni, M., Nimis, P., Martin, S., Mair, V. (2003). Mantle-crust interactions during Variscan subduction in the Eastern Alps (Nonsberg-Ulten zone): geochronology and new petrological constraints. Earth and Planetary Science Letters 210, 509-526.
59. Tumiati, S., Godard, G., Martin, S., Nimis, P., Mair, V., Boyer, B. (2005). Dissakisite-(La) from the Ulten zone peridotite (Italian Eastern Alps): A new end-member of the epidote group. American Mineralogist 90, 1177-1185.
60. Tumiati, S., Godard, G., Martin, S., Klötzli, U., Monticelli, D. (2007). Fluid-controlled crustal metasomatism within a high-pressure subducted mélange (Mt. Hochwart, Eastern Italian Alps). Lithos, 94, 148-167.
61. Tumiati, S., Fumagalli, P., Tiraboschi, C., Poli, S. (2013). An experimental study on COH-bearing peridotite up to 3.2 GPa and implications for crust-mantle recycling. Journal of Petrology 54, 453-479.
62. Whitney, D.L., Evans, B.W. (2010). Abbreviations for names of rock-forming minerals. American Mineralogist 95, 185-187.
63. Wyllie, P.J., Huang, W.L. (1975). Peridotite, kimberlite, and carbonatite explained in the system CaO-MgO-SiO2-CO2. Geology 3, 621-624.

64. Yang, J., Godard, G., Kiénast, J.R., Lu, Y., Sun, J. (1993). Ultrahigh-pressure (60 kbar) magnesite-bearing garnet peridotites from Northeastern Jiangsu, China. Journal of Geology 101, 541-554.
65. Zaccarini, F., Stumpel, E.F., Garuti, G. (2004). Zirconolite and Zr-Th-U minerals in chromitites of the Finero complex, Western Alps, Italy: evidence for carbonatite-type metasomatism in a subcontinental mantle plume. Canadian Mineralogist 42, 1825-1845.
66. Zanetti, A., Mazzucchelli, M., Rivalenti, G., Vannucci, R. (1999). The Finero phlogopite-peridotite massif: an example of subduction-related metasomatism. Contributions to Mineralogy and Petrology 134, 107-122.
67. Zhang, L., Yang, J., Robinson, P.T., Xiong, F., Chen, Y., Lai, S., Chen, M. (2015). Origin of listwanite in the Luobusa Ophiolite, Tibet, implications for chromite stability in hydrothermal systems. Acta Geologica Sinica – English Edition 89, 402-417.

5 Carbon cycling in a continental collisional setting: Insights from carbon concentrations and stable-isotope geochemistry on peridotites from the Ulten Zone (Italian Eastern Alps)

5.1 Introduction

The cycling of carbon (C) between the Earth's reservoirs is of crucial importance in the context of the global C budget and how it relates to past and modern climate change. Of particular interest are the transport of C from the atmosphere to the mantle via subduction and the long-term storage of C in mantle lithologies. The imbalance between the subducting C budget and that return in volcanic arcs could in part be explained by storage of C in the mantle wedge or overlying oceanic and continental crust. However, C concentrations in the mantle are poorly known (Sapienza et al., 2009; Kelemen & Manning, 2015; Collins et al., 2015). Numerous studies of natural suites and experimental approaches have been carried out to unravel the mechanisms of C transfer from crust to mantle during the subduction of oceanic lithosphere. The release of C-bearing hydrous fluids and partial melting of subducted oceanic rocks enable C-bearing melts (e.g. Green & Wallace, 1988; Green et al., 1992; Ionov et al., 1993, 1996) and fluids (Bebout, 1996; Kerrick & Connolly, 1998; Molina & Poli, 2000; Scambelluri & Philippot, 2001; Poli et al., 2009) to migrate into the overlying mantle wedge, resulting in the storage of C in carbonates, graphite/diamond, and volatile C species, such as COH-fluids (Molina & Poli, 2000; Ducea et al., 2005; Poli et al., 2009; Stachel & Harris, 2009; Alt et al., 2012; Tumiati et al., 2013; Cook-Kollars et al., 2014; Collins et al., 2015; Poli, 2015) in mantle peridotite. Carbonates form in mantle lithologies due to the very low solubility of C in mantle silicate minerals (e.g. Keppler et al., 2003; Shcheka et al., 2006) and can maintain stability at pressure and temperature conditions of the upper to the lowermost mantle (e.g. Kushiro, 1975; Wyllie & Huang, 1975; Eggler et al., 1979; Isshiki et al., 2004; Dasgupta & Hirschmann, 2006; Ghosh et al., 2009; Tumiati et al., 2013). However, carbonates may break down during the ascent of mantle xenoliths in the volcanic host rock (Wyllie et al., 1983; Canil, 1990; Ionov et al., 1996) and in general, xenoliths do not allow a large-scale interpretation in the context of the geodynamic history of the peridotite. However, studies on carbonates and the systematics of C transfer in wedge-derived peridotites from orogenic settings are more uncommon (Sapienza et al., 2009; Malaspina & Tumiati, 2012 and references therein). For this reason, the orogenic carbonate-bearing peridotites from the Ulten Zone (Eastern Alps, Italy) provide the unique opportunity to combine petrographic and chemical information on the occurrence and nature of carbonates in mantle wedge-derived rocks in the context of geodynamic setting and petrologic evolution of the Ulten Zone. The Ulten Zone peridotites contain various carbonate phases displaying a wide range of microstructures (Förster et al., 2017), which largely can be linked to individual evolutionary stages of the Ulten Zone. For the origin of dolomite in the Ulten Zone peridotites it has been suggested that a H_2O-CO_2-mixed fluid released by the crustal slab migrated into the peridotite and promoted dolomite precipitation (e.g. Rampone & Morten, 2001; Sapienza et al., 2009; Malaspina & Tumiati, 2012). Such fluid-mediated carbonate growth in supra-subduction zone mantle peridotites, at various *P*-*T*-conditions, has been reported also for wedge-derived peridotites in other orogenic settings, such as the Jiangsu metamorphic belt (Yang et al., 1993), the Sulu terrane (Zhang et al., 2007 and references therein; Malaspina & Tumiati, 2012), Bardane (Carswell & Van Roermund, 2005; Scambelluri et al., 2008; Malaspina et al., 2010) and the Finero peridotite massif (Zanetti et al., 1999). Moreover, the high variety of carbonate phases present in the Ulten Zone peridotites indicates multi-stage carbonate formation in the peridotites during both their residence in the mantle wedge and their ascent as mantle-wedge slivers in crustal host rocks on their retrograde exhumation path (Förster et al., 2017).

In this paper we first review the petrographic occurrences of various carbonate phases in Ulten Zone peridotites, then present a novel integrated study on the C concentration and C-isotope composition in whole-rock Ulten Zone peridotites and the stable-isotope (C and O) geochemistry on the carbonates. Our goal in this work was to shed light on the origin and nature of the metasomatic agents that introduced C in wedge-derived ultramafic rocks during the tectono-metamorphic evolution of the Ulten Zone. More broadly, this work aimed to elucidate the means of input, storage, and recycling of C at convergent continental margins.

5.2 Geological background

The orogenic Ulten Zone (UZ) tectonic unit (e.g. Morten et al., 1976; Martin et al., 1993) in the Eastern Italian Alps (Figure 5.1a) is a part of the Austroalpine Tonale nappe (Figure 5.1b), delineated by the Val Clapa Line in the northwest and the Rumo Line in the southeast (Figure 5.1c). It is composed of high-grade metamorphic basement rocks (garnet-kyanite paragneiss and migmatites + orthogneiss; Obata & Morten, 1987; Godard et al., 1996; Martin et al., 1998; Del Moro et al., 1999) containing lenses (up to several hundred meters in length) of ultramafic rocks.

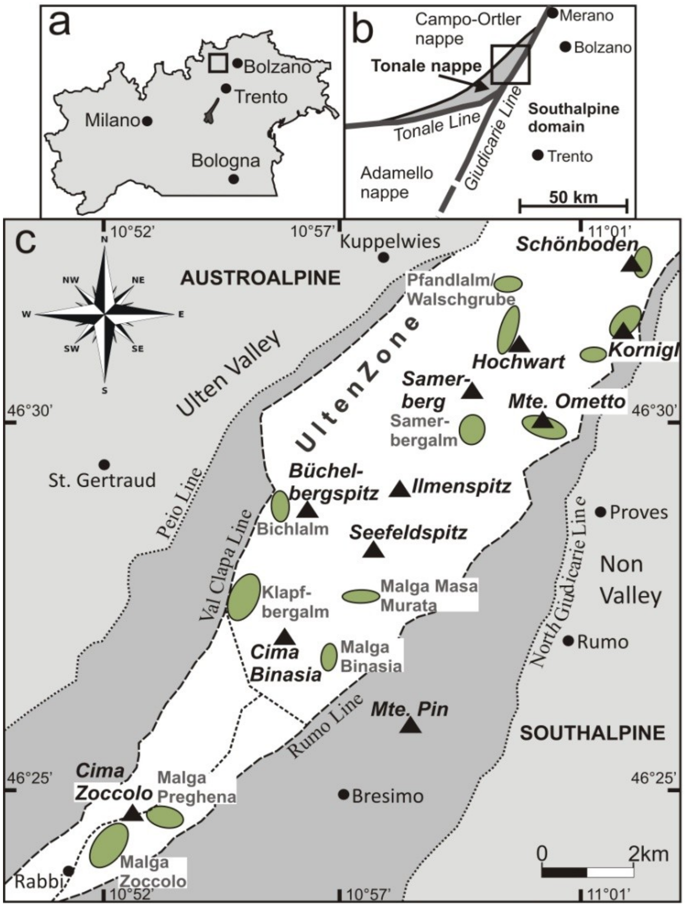

Figure 5.1. Map of the Ulten Zone tectonic unit. (a) Location of the Ulten Zone in the Italian Eastern Alps in North Italy; (b) Location of the Ulten Zone, a part of the Tonale nappe, as a fragment of the Paleozoic Variscan belt; (c) White field marks the Ulten Zone located between the Val Clapa Line and the Rumo Line. Ellipses mark the locations of the ultramafic bodies from which the majority of peridotite samples were selected for this study.

These rocks are composed of mainly peridotite and minor pyroxenite, displaying a variety of petrographical and mineralogical occurrences (Morten & Obata, 1983; Obata & Morten, 1987; Godard et al., 1996 and references therein): the dominant occurrence is mylonitic deformed fine-grained peridotite (0.2 mm to 1 mm grain size), often with a garnet- and amphibole-bearing mineral assemblage and occasionally with a garnet-free amphibole-chlorite-bearing assemblage. The minor occurrence are coarse-grained (up to few cm) both garnet-bearing and garnet-free peridotites (Obata & Morten, 1987). The tectonic evolution of the UZ has been ascribed to continental subduction and subsequent continent-continent collision during the Variscan orogeny, thus the UZ represents a fragment of the Late Paleozoic Variscan belt (Godard et al., 1996). The peridotites are thought to derive from the supra-subduction zone mantle wedge, parts of which were flaked off and entrained by the crustal slab (Godard et al., 1996; Nimis & Morten, 2000). The peridotites were partly infiltrated by crust-derived aqueous fluids released by the slab during migmatization of the crustal rocks (Obata & Morten, 1987; Nimis & Morten, 2000; Rampone & Morten, 2001; Scambelluri et al., 2006; Marocchi et al., 2007) and it is matter of debate whether the peridotites still resided in the mantle wedge (Tumiati et al., 2003; Scambelluri et al., 2006) or had already been encased by the crustal host rocks (Tumiati et al., 2003) at that stage. So far, it has been suggested that migmatization of the gneisses, garnet-facies metamorphic conditions and intense metasomatism of the peridotites, evidenced by high amphibole modal abundance and LILE- and LREE-enrichment (Obata & Morten, 1987; Morten & Obata, 1990; Rampone & Morten, 2001; Tumiati et al., 2003, 2005, 2007; Scambelluri et al., 2006; Marocchi et al., 2007, 2009, 2010), occurred contemporaneously at ca. 330 Ma (Tumiati et al., 2003). The nature of the metasomatic agent has been thought to be a hydrous fluid with a low CO_2/H_2O ratio (Rampone & Morten, 2001). However, U-Pb geochronology on zircons in UZ peridotites and "hybrid" gneiss/migmatite-peridotite contact rocks which formed at low-*P*-*T* conditions during exhumation (Marocchi et al., 2009, 2010) yield an age of ca. 333 Ma (thesis chapter 3). This implies that peridotite insertion into the crustal host rocks occurred at a late exhumation stage and that fluid ingress during garnet stability occurred in the mantle wedge before 333 Ma (see thesis chapter 3). Nevertheless, the peridotites and their crustal host rocks share a common exhumation history starting at 330 Ma (Tumiati et al., 2003; Ranalli et al., 2005). In any case, some of the coarse-grained peridotites could largely escape the crustal metasomatism (Rampone & Morten, 2001; Tumiati et al., 2007) and deformation by being preserved as pockets within highly deformed fine-grained peridotites (Obata & Morten, 1987). A two-stage exhumation path (first fast exhumation, followed by slow exhumation) brought the Ulten mélange (ultramafic rocks + crustal host rocks) to lower crustal levels (Ranalli et al., 2005) and was potentially continuously accompanied by ongoing migmatization and peridotite metasomatism (Godard et al., 1996; Nimis & Morten, 2000; Tumiati et al., 2003). The general composition of the metasomatic agent remained approximately constant during exhumation (Scambelluri et al., 2006) but the CO_2-content of the fluid phase increased, although potentially only locally (Braga & Sapienza, 2007). Due to the weak overprint by Alpine metamorphism, the pre-Alpine evolution of the Ulten Zone is still recorded in the mineral assemblages, textures and chemical signatures (Godard et al., 1996; Hauzenberger et al., 1996; Martin et al., 1998).

5.3 Carbonates in Ulten Zone ultramafic rocks

Various recent studies reported the presence of dolomite (Obata & Morten, 1987; Godard et al., 1996; Morten & Trommsdorff, 2003; Tumiati et al., 2005; Braga & Sapienza, 2007; Marocchi et al., 2009; Sapienza et al., 2009; Malaspina & Tumiati, 2012; Förster et al., 2017), magnesite (Malaspina & Tumiati, 2012; Förster et al., 2017) and calcite (Förster et al., 2017) in UZ peridotites. The microstructure of the carbonates in a selection of the samples we used for the analyses in the present paper were previously detailed described in Förster et al. (2017). Here we summarize the evidence of various types of carbonates (dolomite, magnesite, calcite) that occur in different microtextural domains in the UZ peridotites (Figure

5.2) and the, to date, suggested chronology of carbonate-formation stages in the petrologic evolution of these rocks (Förster et al., 2017).

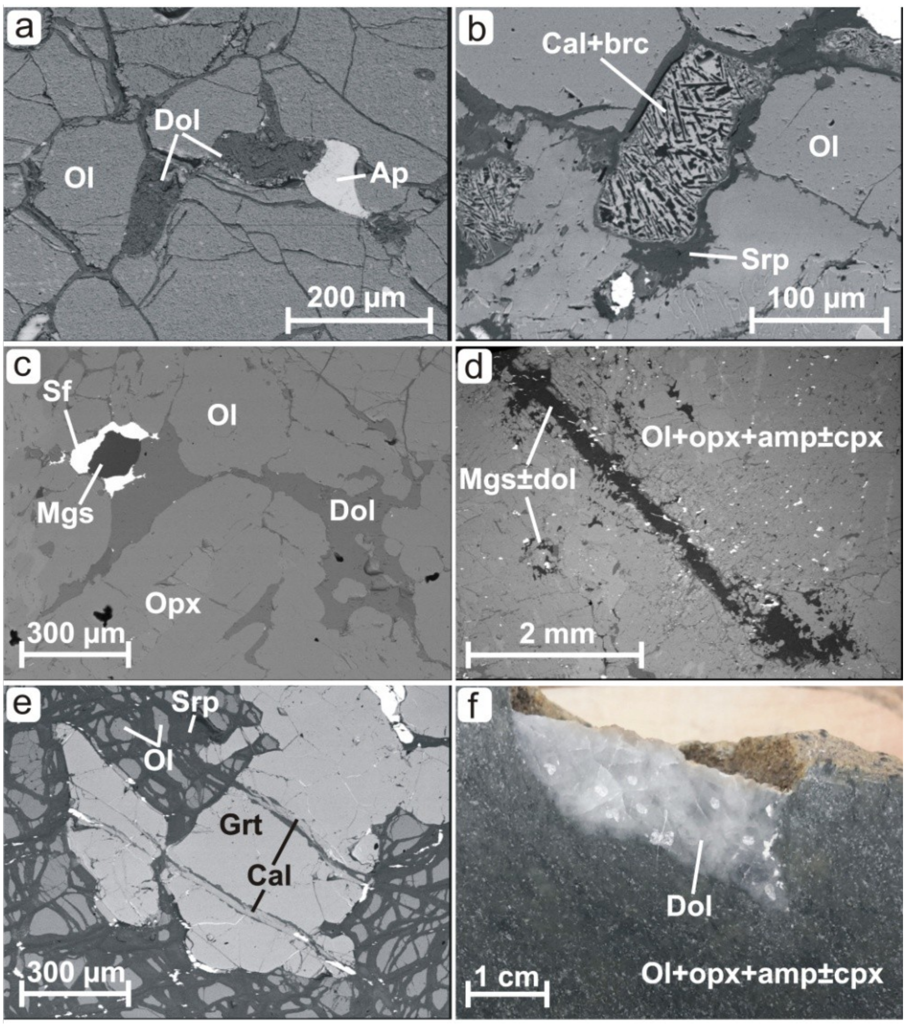

Figure 5.2. (a-e) Back-scattered electron images of sections showing (a) discrete dolomite grains in the matrix of non-serpentinized fine-grained garnet-amphibole peridotites associated with apatite (sample SBA7), (b) calcite-brucite intergrowths, which are dolomite-breakdown products, situated in the serpentine mesh texture of serpentinized fine-grained garnet-amphibole peridotite (sample WG2), (c) interstitial anhedral dolomite and magnesite with curvilinear contacts to matrix minerals and (d) a vein of magnesite crosscutting the matrix of coarse-grained protogranular peridotite MOL1.5, (e) calcite veinlets related to magnetite situated in the serpentine mesh texture and crosscutting garnet (sample SB3.2, serpentinized fine-grained garnet-amphibole peridotite), (f) photograph of polycrystalline aggregate of dolomite (~5 cm length) in fine-grained garnet-amphibole peridotite VM25P11; the drill pits after micro-drilling for stable-isotope analyses are visible. Mineral abbreviations after Whitney & Evans (2010), sf: sulfide.

The type of carbonate can be linked to the peridotite petrographic type, and the following stages for carbonate formation and breakdown in the UZ peridotites have been suggested by Förster et al. (2017): (1) Carbon-bearing fluids or silicate melts may have infiltrated the peridotites when they still resided in the mantle wedge. This event may be recorded by grains of dolomite and calcite-brucite symplectites, the latter a product of dolomite breakdown that occur as inclusions in primary spinel. However, coarse-grained protogranular peridotites believed to represent the initial wedge peridotites do not contain interstitial carbonates; (2) A metasomatic agent, presumably a C-bearing hydrous fluid (low CO_2/H_2O) released by the subducting continental slab (e.g., Rampone & Morten, 2001), infiltrated the peridotites either a short time before or after their entrainment into the crustal host rocks and lead to the formation of interstitial dolomite grains, often spatially associated with other metasomatic phases, such as amphibole and apatite. This event is thought to have occurred when garnet was stable, as this interstitial dolomite occurs only in recrystallized fine-grained garnet-amphibole peridotites; (3) Probably during the retrograde path of the peridotites, local injection of C-rich hydrous fluids (high CO_2/H_2O) caused the formation of (a) coexisting dolomite + magnesite outside garnet stability, as observed in a coarse-grained garnet-free peridotite, (b) anhedral dolomite and distinct dolomite veins that crosscut the matrix of fine-grained peridotites and (c) retrograde magnesite associated with dolomite in a strongly serpentinized fine-grained peridotite; (4) Peridotite interaction with serpentinizing fluids (low CO_2/H_2O) led to dolomite breakdown in the garnet-amphibole peridotites from stage 2, resulting in the transformation of dolomite into symplectites of calcite + brucite and the liberation of a C-species in the fluid, according to the reaction $CaMg(CO_3)_2 + H_2O = CaCO_3 + Mg(OH)_2 + CO_2$; (5) the infiltration of C-bearing near-surface fluids lead to local formation of carbonate, mainly calcite, veins in pre-existing pathways and/or co-crystallizing with serpentine, as demonstrated by calcite veinlets in the serpentine mesh textures in coarse- and fine-grained peridotites as well as in pyroxenitic rocks associated with the peridotites.

5.4 Analytical methods

For the analyses of whole-rock C concentrations and C-isotope compositions we chose those samples for which the carbonate phases were previously studied (Förster et al., 2017) and further samples from the same localities as well as additional samples from another sample set. Analysis of the O- and C-isotope compositions of carbonates in whole rocks of the UZ peridotites ± pyroxenites were carried out partly for these same whole-rock samples.

5.4.1 Bulk-rock oxidized carbon and reduced carbon

Analyses of the concentrations of oxidized and reduced C in whole-rocks were carried out at the Goethe University Frankfurt (Germany) using a LECO RC-412 Multiphase Carbon Determinator. A calcite standard is used for calibration of the instrument. For each analysis 0.3 g of whole-rock powder of 51 selected samples of UZ ultramafic rocks were used and inserted into the furnace inside a quartz container. The total C concentration in a sample was determined from the analysis of the emitted CO_2 via infrared spectrometry after combustion of a powder sample. The heating was ramped up first to 550°C and then up to 1000°C. The concentration of reduced C was calculated as the difference between the concentration of total C and oxidized C (in weight percent).

5.4.2 Bulk-rock total carbon concentrations and carbon-isotope compositions

Analyses of total elemental C concentration and bulk-rock C isotopic ratios in UZ peridotites were performed at the University of Ferrara (Italy) using a Continuous Flow Isoprime100 Isotope Mass Spectrometer coupled to a Micro Cube Elemental Analyzer (EA-CF-IRMS). The low concentration of C in peridotites required detailed testing of the reliability of the analytical results. The application of this technique to study the C concentration in low-C matrices such as peridotites was previously described in Bianchini & Natali (2017). Reproducibility of three standards (Carrara marble, Jacupiranga carbonatite, and sulfanilamide) with progressively reduced sample mass allowed defining a reliability threshold of the signal at 0.9 nA for UZ peridotites (Figure 5.3a). Analyses with a slightly lower signal were not excluded from the dataset but treated with caution. The reproducibility of the technique was tested by analyzing duplicates

(Figure 5.3b) and the maximum variation Δ^{13}C for duplicates is 0.54‰. This difference is smaller than the used symbols in the δ^{13}C diagrams. The relationship between the measured isotopic ratio (δ^{13}C$_m$) and the expected theoretical ratio (δ^{13}C$_t$) for the three standards defines an interpolation curve (Figure 5.3c). The data for the UZ peridotites plot ideally on this curve, showing that the analytical technique is applicable for these rocks. The C elemental concentration is reported in wt. % and the C isotopic composition is expressed in δ^{13}C relative to VPDB.

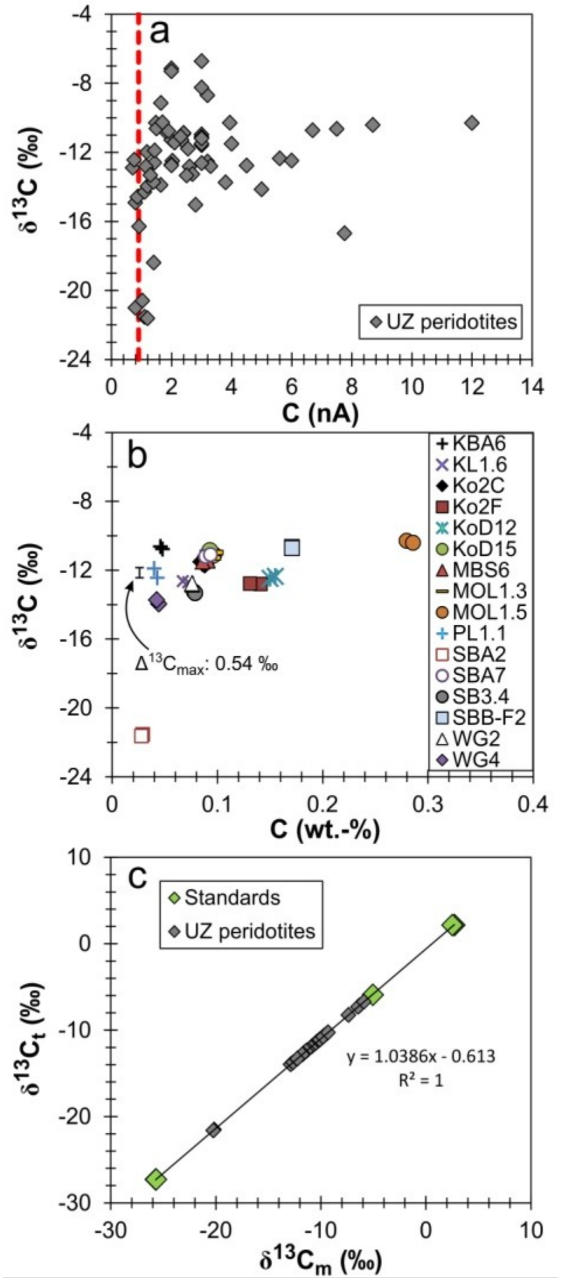

Figure 5.3. Results of testing the reliability of the analyses for the total carbon content (C) and the carbon isotopic composition (δ^{13}C) in whole-rock peridotites from the Ulten Zone. (a) Relationship between the obtained signal (nA) and δ^{13}C. The reliability threshold of the signal (stippled line) is 0.9 nA for the peridotites. (b) Reproducibility of carbon content and δ^{13}C for duplicated analyses of the peridotite samples. The maximum variation Δ^{13}C for duplicates is 0.54‰. (c) Relationship between the measured isotopic ratio (δ^{13}C$_m$) and the expected theoretic ratio (δ^{13}C$_t$) for the three standards defines an interpolation curve. The obtained carbon isotopic ratio for UZ peridotites plots ideally on this curve, showing that the analytical technique is applicable for these rocks that are low-carbon matrices.

5.4.3 Carbon and oxygen isotope analyses on carbonates

Analyses of the O and C isotopic compositions of bulk carbonate in peridotites, and micro-drilled carbonate phases, were performed at Lehigh University (USA) using a Finnigan MAT 252 interfaced with a GasBench II system (see the more detailed description of this method by Collins et al., 2015).

For a part of this work, peridotite whole-rock powder was reacted with phosphoric acid at 72°C resulting in the dissolution of the carbonates in the samples. Due to the low and highly variable modal abundance of carbonates in the peridotites (based on petrographic observations), tests were essential to determine the appropriate amount of bulk-rock powder required for carbonate dissolution to produce as much as CO_2 as needed to yield reliable signals (>0.5 mV). We conducted the testing on three representative peridotite samples (PRE-A, SBA4, WG2) with known carbonate contents based on the petrographic observations presented in Förster et al. (2017). During the testing we increased stepwise the weight of bulk-rock powder of each sample and compared the results of the yield (amplitude divided by the weight of the powder) and the C and O isotopic composition. Based on previously reported reaction times for carbonate dissolution in phosphoric acid (Das Sharma et al., 2002; Collins et al., 2015) sample PRE-A which contains calcite veins reacted for 1 hour, whereas samples SBA4 containing dolomite and sample WG2 containing calcite and dolomite reacted for 3 hours. The testing aimed to obtain a stable yield and stable isotopic ratios over a range of various sample weights. When yield and isotopic ratios remain unaffected by any increase of the sample weight, the sample amount in this range is applicable to produce reliable results of the carbonate stable isotopic composition. For sample PRE-A, in the weight range from 5 mg to 35 mg, the yield and the C-isotope ratio increase (Figure 5.4a), whereas both reach stability in the range from 40 to 60 mg (standard deviation for stable-isotope ratios <0.2‰; Figure 5.4b). This means that, in the range from 40 mg to 60 mg, the stable isotope analyses are the most reliable. The test results for sample SBA4 show that yield and stable-isotope ratios are stable in the sample-weight range between 80 mg and 110 mg (standard deviation for $\delta^{13}C$ and $\delta^{18}O$ ≤0.2‰; Figure 5.4c,d). An additional test using 223 mg of powder shows that the yield decreases (Figure 5.4c), whereas the stable isotopic ratios display the highest values (Figure 5.4d). This may be attributed to insufficient carbonate dissolution in the acid due to incomplete reaction of the bulk-rock powder with the phosphoric acid. Although the amount of phosphoric acid added to the bulk-rock powder was adjusted (0.3 to 0.5 ml) to the increasing sample amount, we observed incomplete mixture of bulk-rock powder in the phosphoric acid, even after shaking the vials in order to obtain full mixing of powder and acid. The mixing becomes more difficult with increasing amounts of powder because the powder sticks and forms clusters, preventing the infiltration of the acid. These results showed that attention must be paid especially when higher amounts of bulk-rock powder are required to obtain a feasible signal. Slightly increasing yields and isotopic ratios over the entire range of sample weights (15 mg to 85 mg) were observed also during the testing using sample WG2 (standard deviation for $\delta^{13}C$ and $\delta^{18}O$ ~0.3‰; Figure 5.4e,f). Based on the test results, ~80 mg whole-rock powder was chosen for the analyses of the UZ peridotites. Analyses were repeated using more or less powder when the signal was too low or too high, respectively. Thus, the used sample weights for the measurements range from 16 mg to 122 mg.

For sample WG2, one test run was additionally carried out with 52 mg of sample and a reaction time of 30 hours in order to test possible variations of the yield and isotopic ratios after a longer reaction time. Interestingly, this run resulted in an elevated yield relatively to those after 3 hours reaction time and a slightly elevated O-isotope ratio. This may indicate that the sample contains more Mg-rich dolomite for which the reaction time with the acid is longer. In order to define the reaction time for the variable carbonate contents in the UZ peridotites with phosphoric acid, we conducted further testing (Figure 5.5). The tests were carried out on samples with unknown (Figure 5.5a,c,e) and multiple carbonate contents (samples containing calcite-brucite intergrowths, Figure 5.5b,d,f) and reaction times were 1 hour, 3, 6 and 30 hours. For most of the tested samples the test results show the highest absolute yield (amplitude of signal per amount of whole-rock powder, mV/mg) after 30 hours reaction (Figure 5.5a,b). For some samples the C-isotope values change significantly after 30 hours reaction time (up to 3‰, sample MZS1-6, Figure 5.5c) and, in other cases, it does not differ significantly for the different reaction times. Instead, the O isotopic ratio largely shows significant variation (Figure 5.5e,f). Thus, for whole-rock samples containing multiple carbonate phases and for samples with unknown carbonate content reaction time of 30 hours was set as the most reliable.

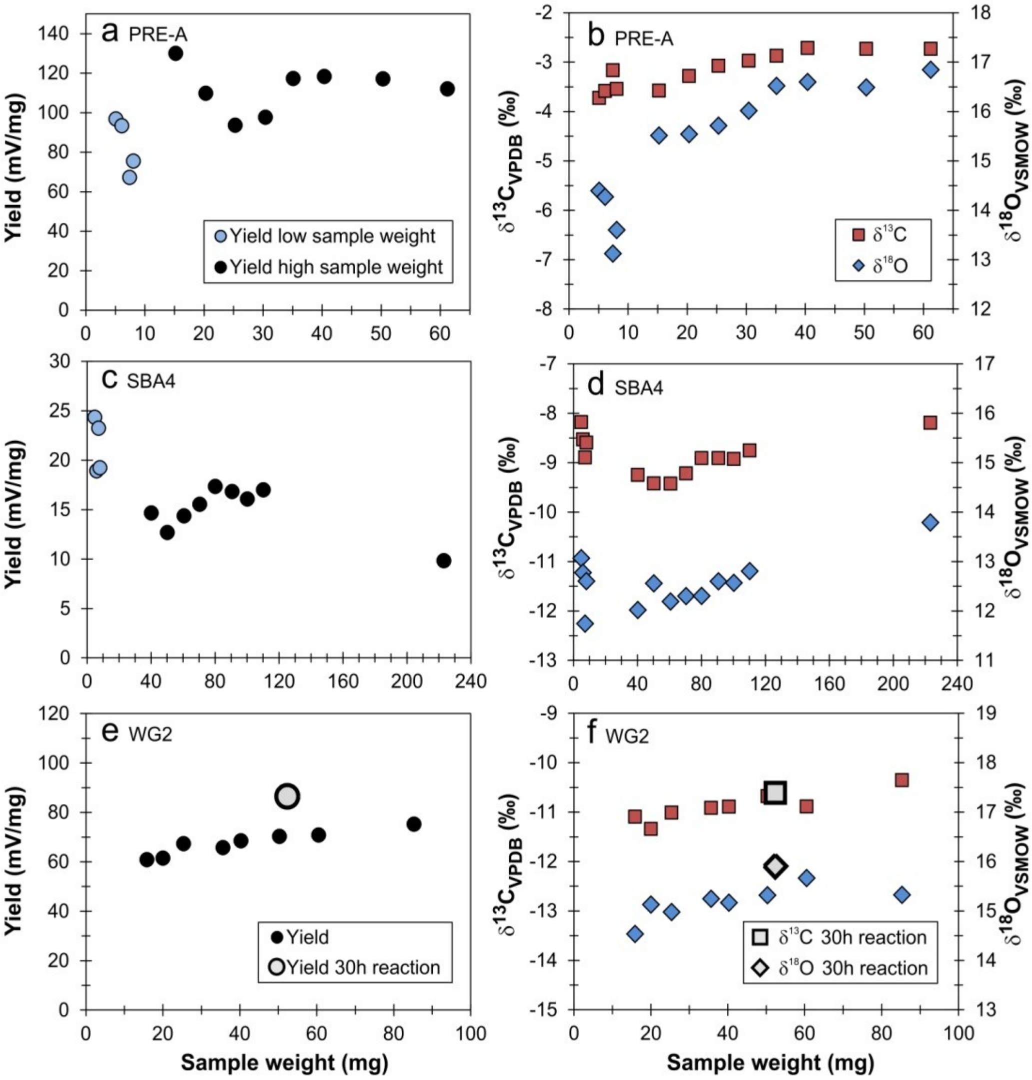

Figure 5.4. Results of testing the required sample amount of Ulten Zone peridotites, which are low-carbonate rocks, for carbonate stable-isotope analyses to obtain reliable results. Tests were carried out on peridotite samples, the carbonate contents of which are known. Variations of (a) the obtained absolute yield and (b) $\delta^{13}C$ and $\delta^{18}O$ as a function of the sample weight for sample PRE-A containing calcite veinlets. Tests were carried out using different sample amounts to check when yield and isotopic compositions remain stable. The same procedure was carried out for samples (c,d) SBA4 containing dolomite and (e,f) WG2 containing calcite and dolomite. See text for detailed explanation of the testing.

Carbonate in macroscopically visible textural sites (magnesite in samples MOL1.5 (Figure 5.2d), KoD4 and KoD9 and dolomite in samples MR141B, MOL1.5 and VM25P11 (Figure 5.2f)) was sampled by micro-drilling using 1 mm and 2 mm tungsten carbide bits. These pure carbonate phases were reacted with 0.2 ml phosphoric acid with reaction times adjusted for complete CO_2 release accepted for pure calcite, pure dolomite and pure magnesite were ≥ 0.5, 3 and 30 hours, respectively.

Analyses of a calcite house standard and the international calcite standard NBS-19 were obtained to monitor and correct the isotopic data revealing standard deviation (1σ) of ≤ 0.2‰ for both $\delta^{13}C$ and $\delta^{18}O$, which are reported relative to VPDB and VSMOW, respectively.

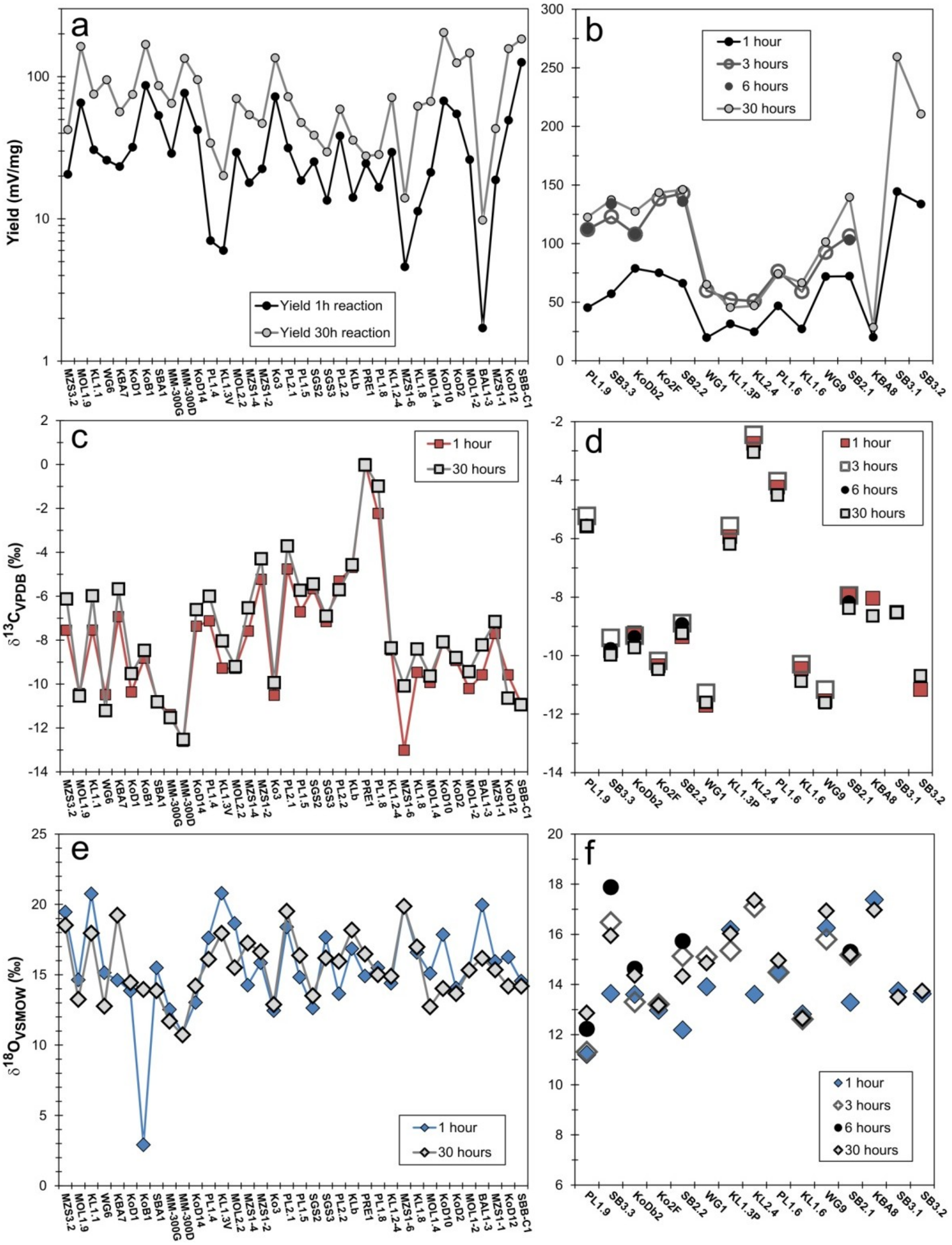

Figure 5.5. Results of testing the required reaction time of carbonates in Ulten Zone peridotites with phosphoric acid in order to obtain reliable results from the carbonate stable-isotope analyses. The absolute yield obtained for samples with (a) unknown carbonate content and (b) multiple carbonate content, i.e. containing calcite-brucite intergrowths ± dolomite, is always higher relative to the yield obtained after 1 hour reaction time. (c,d) The C-isotope ratio ($\delta^{13}C$) for the same samples partly changes significantly after the different reaction times, whereas (e,f) the O-isotope ratio ($\delta^{18}O$) displays greater variations. Reaction time of 30 hours was accepted as the required reaction time for the carbonate stable-isotope analyses.

5.5 Results

5.5.1 Oxidized and reduced carbon in UZ peridotites

The concentrations of both oxidized C (in carbonate), and reduced C in all petrographical types of the UZ peridotites are generally low (Table 5.1; Figure 5.6). In peridotites of the coarse type (15 analyzed samples) the amount of oxidized C ranges from 0.007 to 0.181 wt. %, in one coarse-grained garnet-bearing peridotite it is 0.002 wt. %, in fine-grained peridotites (20 samples) it ranges from 0.015 to 0.092 wt. %, in fine-grained garnet-bearing peridotites (13 samples) it ranges from 0.012 to 0.113 wt. % and in pyroxenitic-amphibolized samples from 0.001 to 0.003 wt. %. The coarse-grained peridotites contain 0.022 to 0.124 wt. % reduced C, the coarse-grained garnet-bearing peridotite contains 0.026 wt. %. In the fine-grained peridotites reduced C ranges from 0.019 to 0.103 wt. %, in the fine-grained garnet-bearing samples from 0.020 to 0.052 wt. % and the pyroxenitic-amphibolized samples contain 0.016 and 0.022 wt. % reduced C. The variability of oxidized and reduced C is largely independent on the petrographic peridotite type (coarse vs. fine, garnet-bearing vs. garnet-free) with exceptions of the coarse-grained garnet-bearing peridotite and the pyroxenitic-amphibolized samples which exhibit the lowest C concentrations (Figure 5.6a). However, these samples exhibit a high $C_{red.}/C_{oxi.}$ ratio of ~10, whereas the other peridotite types show largely much lower $C_{red.}/C_{oxi.}$ (Figure 5.6a). In contrast, Figure 5.6b reveals that peridotites from localities in the northeastern (NE) UZ contain generally more oxidized (0.020 to 0.181 wt. %, one exception 0.002 wt. %) and reduced C (0.019 to 0.124 wt. %) compared to the peridotites from the southwestern (SW) UZ (0.001 to 0.063 wt. % and from 0.016 to 0.103 wt. %, respectively). However, the relatively low $C_{oxi.}$ concentrations but elevated $C_{red.}$ concentrations of the coarse-grained garnet-bearing peridotite (Samerbergalm, NE domain) and the pyroxenitic samples (Malga Zoccolo, SW domain) seem to be unrelated to the provenance of the samples but rather controlled by the petrographic/mineralogic rock type.

5.5.2 Total carbon concentration and carbon isotopic composition in bulk-rock UZ peridotites

The total C concentration in UZ ultramafic rocks was measured in 54 samples of different petrographic types and ranges from 0.013 to 0.280 wt. %, with the majority of all samples (80%) containing total C in the range of 0.030 to 0.100 wt. % (Table 5.2, Figure 5.7). Carbon-isotope compositions of the bulk-rock ultramafic rocks range from $\delta^{13}C$ of -22‰ to -7‰, the majority of which (72%) displays $\delta^{13}C$ between -15‰ to -10‰ (Table 5.2, Figure 5.7). Thus, the C isotopic composition of UZ peridotites is generally lower relatively to the notional main mantle range ($\delta^{13}C \sim -8‰$ to -2.5‰, Shirey et al., 2013). Peridotites from the UZ contain by majority more total C (70% of the samples ≥0.05 wt. % total C) than the average mantle inferred from mantle xenoliths (95% of mantle xenoliths contain <0.05 wt. % total C; Deines, 2002; Figure 5.7a). The concentration of total C as well as the C-isotope composition do not show any correlation to the individual petrographic types of peridotite (Figure 5.7a). Exceptions are displayed by one coarse-grained garnet-bearing peridotite and the pyroxenitic-amphibolized samples which exhibit very low total C concentrations and $\delta^{13}C$ (Figure 5.7a). For comparison, the total C concentration and $\delta^{13}C$ of UZ crustal rocks (gneisses and migmatites) are shown in Figure 5.7a. The crustal rocks' total C content (0.050 to 0.220 wt. %) is similar to that of the UZ peridotites, whereas the $\delta^{13}C$ is more negative (-33‰ to -25‰). The variabilities of the total C content and $\delta^{13}C$ in UZ ultramafic rocks are related to the localities in the UZ (Figure 5.7b): samples from SW localities in the UZ show stronger variability of $\delta^{13}C$ (-21‰ to -7‰) and relatively lower C concentrations (0.013 to 0.097 wt. %) compared to samples from the NE of the UZ exhibiting a narrower range in $\delta^{13}C$ but increasing total C concentrations ($\delta^{13}C$ from -16‰ to -10‰, one exception -21‰ and from 0.029 to 0.280 wt. % total C). Among the latter, two samples containing magnesite veins display the highest C concentration (0.171 and 0.280 wt. %). This relationship between the whole-rock δ^{13}C and the sample provenance in the UZ is probably dictated by the carbonates, the δ^{13}C of which is strictly coupled to the sample locality in the UZ (see next section). However, although the pyroxenitic-amphibolized samples derive from one sample locality (Malga Preghena, SW domain), it seems that in case of these samples the distinct C content and δ^{13}C is rather related to the specific rock type.

Table 5.1 Localities, summary of petrographic characteristics and whole-rock concentration of oxidized and reduced carbon of ultramafic rocks from the Ulten Zone.

Sample	Locality	Type	$C_{oxi.}$ (wt. %)	$C_{red.}$ (wt. %)	$C_{oxi.+red.}$ (wt. %)	$C_{red.}/C_{oxi.}$
BAL1.2	Bichlalm	Fine spl	0.0407	0.0358	0.0765	0.88
KBA6	Klapfbergalm	Fine grt-amp	0.0184	0.0261	0.0445	1.42
KBA8	Klapfbergalm	Fine grt-amp	0.0120	0.0236	0.0356	1.97
KL1.5	Klapfbergalm	Fine spl	0.0456	0.0324	0.0780	0.71
KL1.6	Klapfbergalm	Fine grt-amp	0.0486	0.0204	0.0690	0.42
KL1.7	Klapfbergalm	Fine spl	0.0215	0.0352	0.0567	1.64
KL2.3	Klapfbergalm	Fine spl	0.0425	0.0282	0.0707	0.66
Ko2C	Kornigl	Coarse spl	0.0537	0.0401	0.0938	0.75
Ko2F	Kornigl	Fine spl	0.0833	0.0470	0.1303	0.56
Ko3	Kornigl	Fine spl	0.0656	0.0447	0.1103	0.68
KoB1	Kornigl	Fine spl	0.0848	0.0461	0.1309	0.54
KoD12	Kornigl	Coarse spl	0.0521	0.1210	0.1731	2.32
KoD15	Kornigl	Fine spl	0.0328	0.0605	0.0933	1.84
KoD4	Kornigl	Coarse spl	0.0203	0.0536	0.0739	2.64
KoDb2	Kornigl	Fine spl	0.0530	0.0527	0.1057	0.99
MBS1	Malga Binasia	Coarse spl	0.0175	0.0322	0.0497	1.84
MBS2	Malga Binasia	Coarse spl	0.0409	0.0307	0.0716	0.75
MBS3F	Malga Binasia	Fine spl	0.0193	0.1030	0.1223	5.34
MBS6	Malga Binasia	Fine spl	0.0455	0.0545	0.1000	1.20
MBS8	Malga Binasia	Coarse spl	0.0235	0.0220	0.0455	0.94
MOL1.1C	Monte Ometto	Coarse spl	0.0371	0.0491	0.0862	1.32
MOL1.1F	Monte Ometto	Fine spl	0.0374	0.0522	0.0896	1.40
MOL1.5	Monte Ometto	Coarse spl	0.1810	0.1070	0.2880	0.59
MOL1.3	Monte Ometto	Fine spl	0.0401	0.0562	0.0963	1.40
MZS1.1	Malga Zoccolo	Fine spl	0.0277	0.0226	0.0503	0.82
MZS1.2	Malga Zoccolo	Coarse spl	0.0255	0.0260	0.0515	1.02
MZS1.3	Malga Zoccolo	Pyroxenitic-amphibolized	0.0030	0.0217	0.0247	7.23
MZS1.5	Malga Zoccolo		0.0014	0.0164	0.0178	11.71
MZS3.1	Malga Zoccolo	Coarse spl	0.0272	0.0396	0.0668	1.46
PL1.1	Malga Preghena	Coarse spl	0.0069	0.0306	0.0375	4.43
PL1.3	Malga Preghena	Fine grt-amp	0.0552	0.0522	0.1074	0.95
PL1.4	Malga Preghena	Coarse spl	0.0166	0.0235	0.0401	1.42
PL1.5	Malga Preghena	Fine spl	0.0225	0.0284	0.0509	1.26
PL1.6	Malga Preghena	Fine grt-amp	0.0508	0.0300	0.0808	0.59
PL2.3	Malga Preghena	Coarse spl	0.0219	0.0657	0.0876	3.00
PRE2	Malga Preghena	Fine spl	0.0151	0.0292	0.0443	1.93
PRE-A	Malga Preghena	Coarse spl	0.0633	0.0683	0.1316	1.08
SBA1	Samerbergalm	Fine spl	0.0568	0.0188	0.0756	0.33
SBA2	Samerbergalm	Coarse grt	0.0022	0.0256	0.0278	11.64
SBA4	Samerbergalm	Fine grt-amp	0.0199	0.0232	0.0431	1.17
SBA5	Samerbergalm	Fine grt-amp	0.0375	0.0425	0.0800	1.13
SBA7	Samerbergalm	Fine grt-amp	0.0677	0.0238	0.0915	0.35
SB3.2	Schönboden	Fine grt-amp	0.1130	0.0467	0.1597	0.41
SB3.4	Schönboden	Fine grt-amp	0.0438	0.0369	0.0807	0.84
SBB-C2	Schönboden	Coarse spl	0.1280	0.1240	0.2520	0.97
SBB-F2	Schönboden	Fine spl	0.0920	0.0941	0.1861	1.02
SGS1	Schöngrubspitz	Fine spl	0.017	0.0336	0.0506	1.98
WG1	Walschgrube	Fine grt-amp	0.0341	0.0374	0.0715	1.10
WG2	Walschgrube	Fine grt-amp	0.0386	0.0391	0.0777	1.01
WG4	Walschgrube	Fine grt-amp	0.0206	0.0234	0.0440	1.14
WG6	Walschgrube	Fine spl	0.0776	0.0564	0.1340	0.73

Mineral abbreviations after Whitney & Evans (2010)

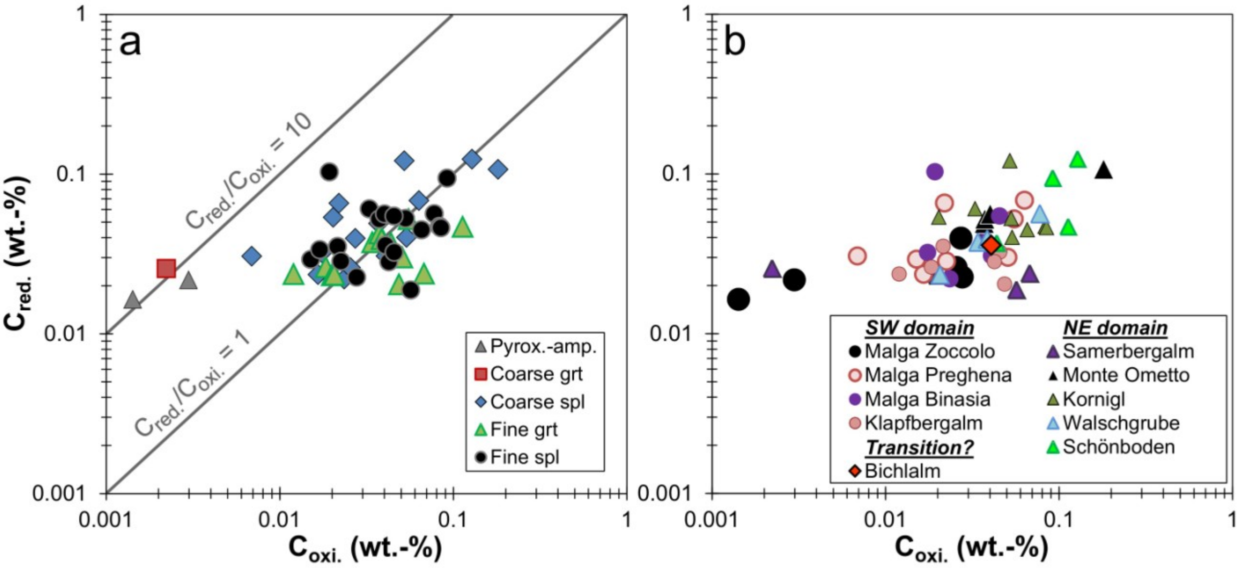

Figure 5.6. Comparison of the concentrations of oxidized ($C_{oxi.}$) and reduced ($C_{red.}$) C in Ulten Zone ultramafic whole rocks grouped in (a) regarding the petrographic type as illustrated in Figure 5.7; (b) regarding the sample locality in the Ulten Zone as also illustrated in Figure 5.7. Ulten Zone ultramafic rocks contain oxidized C, i.e. carbonate C, and reduced C in similar amounts and the range of concentrations is largely independent on the petrographic type (a) and the provenance of the samples (b). However, it is interesting to note that the one coarse-grained garnet-bearing peridotite and the two pyroxenitic-amphibolized samples exhibit a $C_{red.}/C_{oxi.}$ ratio ten times higher ($C_{red.}/C_{oxi.}$ ~10) compared to the other peridotite types ($C_{red.}/C_{oxi.}$ varying around 1). The sample locality Bichlalm is located in the center of the Ulten Zone between the SW domain and the NE domain and may represent a transition between the two domains.

5.5.3 Carbon and oxygen isotopic compositions of carbonates in UZ peridotites

The stable-isotope compositions (C and O isotopic ratios) of carbonates in 128 UZ peridotite samples and of drilled carbonates are reported in Table 5.3 and in Figure 5.8. Carbonate δ^{13}C ranges from -17‰ to -0.0‰ and δ^{18}O ranges from +7‰ to +21‰. The stable isotopic compositions of the carbonates are highly variable, regardless of the carbonate type in the samples (Figure 5.8a). Many of the δ^{13}C values are lower than the values for upper mantle (mantle range of -8‰ to -2.5‰; Shirey et al., 2013), whereas all δ^{18}O values are higher than the range for the upper mantle (δ^{18}O ~ +5.5‰ ± 0.4‰; Mattey et al., 1994). The isotopic compositions of carbonates in whole-rock samples with unknown carbonate content and containing calcite-brucite intergrowths and calcite veins are highly variable and plot in the same range (Figure 5.8a). The majority of these samples show less negative δ^{13}C and more positive δ^{18}O than the whole-rock samples containing discrete dolomite and dolomite + magnesite as well as relative to the drilled dolomites and magnesites (Figure 5.8a).

Comparison of the stable isotopic compositions of carbonates and the petrographic type of the host peridotite shows that there is no control of the petrographic type on the carbonate isotopic compositions, also regardless of the carbonate type. Instead, the isotopic compositions (δ^{13}C vs. δ^{18}O of the carbonates depend on the provenance of the samples in the UZ (Figure 5.8b). Carbonates from localities in the SW of the UZ have less negative δ^{13}C and more positive δ^{18}O (from -11.1‰ to -0.03‰ and from +12‰ to +21‰, respectively) compared to the carbonates from localities in the NE (from -16.8‰ to -5.7‰ and from +6.4‰ to +17.8‰, respectively; Figure 5.8b).

Table 5.2 Localities, summary of petrographic characteristics, total carbon concentration and whole-rock carbon isotopic composition of ultramafic rocks from the Ulten Zone.

Sample	Locality	Type	C_{tot} (wt. %)	$\delta^{13}C_{tot}$ (‰)
MR132A	Buca di Cloz	Fine spl	0.1030	-12.55
P10a	Hochwart	Fine amp + grt pseudo	0.0500	-15.16
P10b	Hochwart	Fine grt-amp	0.1600	-16.82
P10c	Hochwart	Fine grt-amp	0.0900	-14.10
P11b	Hochwart	Fine grt-amp	0.1100	-12.69
P11a	Hochwart	Fine grt-amp	0.0600	-12.32
P11c	Hochwart	Fine grt-amp	0.1200	-13.20
KBA6	Klapfbergalm	Fine grt-amp	0.0458	-10.63
KBA8	Klapfbergalm	Fine grt-amp	0.0364	-12.82
KL1.5	Klapfbergalm	Fine spl	0.0834	-7.16
KL1.6	Klapfbergalm	Fine grt-amp	0.0723	-12.71
Ko2C	Kornigl	Coarse spl	0.0880	-11.59
Ko2F	Kornigl	Fine spl	0.1410	-12.81
KoD12	Kornigl	Coarse spl	0.1550	-12.36
KoD15	Kornigl	Fine spl	0.0965	-11.12
300	Lavazzee valley	Fine spl	0.0335	-16.30
300/1	Lavazzee valley	Fine spl	0.0441	-12.60
300b/2005	Lavazzee valley	Fine spl	0.0323	-12.00
NB35	Lavazzee valley	Fine spl	0.0261	-12.90
NB 36/2	Lavazzee valley?	Fine spl	0.0275	-14.92
MBS2	Malga Binasia	Coarse spl	0.0630	-8.26
MBS6	Malga Binasia	Fine spl	0.0910	-11.45
MK5C/93	Monte Ometto	Fine grt-amp	0.0526	-12.50
MK5DVL	Monte Ometto	Coarse grt	0.0367	-14.30
MOL1.5	Monte Ometto	Coarse spl	0.2800	-10.30
MOL1.3	Monte Ometto	Fine spl	0.0921	-11.29
MZS1.1	Malga Zoccolo	Fine spl	0.0440	-10.27
MZS3.1	Malga Zoccolo	Coarse spl	0.0620	-7.31
MPS_1	Malga Preghena	Pyroxenitic-amphibolized	0.0156	-18.40
MPS_2d	Malga Preghena	Pyroxenitic-amphibolized	0.0469	-16.70
MPS_2p	Malga Preghena	Pyroxenitic-amphibolized	0.0295	-21.02
NB46	Malga Preghena	Coarse spl	0.0658	-10.90
NB47	Malga Preghena	Coarse spl	0.0594	-10.60
NB48	Malga Preghena	Fine spl	0.0550	-9.15
NB49/1	Malga Preghena	Fine spl	0.0840	-10.30
NB49/2	Malga Preghena	Fine spl	0.0967	-8.70
NB49/3	Malga Preghena	Fine spl	0.0461	-10.30
NB49/7	Malga Preghena	Coarse spl	0.0600	-10.80
NB49/8	Malga Preghena	Pyroxenitic-amphibolized	0.0130	-20.60
PL1.1	Malga Preghena	Coarse spl	0.0400	-11.9
PL1.6	Malga Preghena	Fine grt-amp	0.0775	-6.73
SBA2	Samerbergalm	Coarse grt	0.0290	-21.54
SBA4	Samerbergalm	Fine grt-amp	0.0391	-13.33
SBA7	Samerbergalm	Fine grt-amp	0.0888	-11.21
N5/1	Samerbergalm	Fine grt-amp	0.0461	-11.80
N5/2	Samerbergalm	Coarse grt	0.0381	-13.90
SB3.4	Schönboden	Fine grt-amp	0.0780	-13.27
SBB-F2	Schönboden	Fine spl	0.1710	-10.66
MO11	Seefeldalm	Fine grt-amp	0.0506	-11.30
ULT05/1	Strada provinciale	Fine spl	0.1727	-14.15
ULT05/1B	Strada provinciale	Fine spl	0.1263	-13.75
ULT05/2	Strada provinciale	Fine spl	0.0963	-15.05
WG2	Walschgrube	Fine grt-amp	0.0765	-12.84
WG4	Walschgrube	Fine grt-amp	0.0444	-13.97
UZ crustal rocks				
NB11W		Stromatic migmatite	0.0820	-32.96
NB14		Grt-ky gneiss	0.0500	-31.38
NB2W		Stromatic migmatite	0.2200	-29.17
TUN3		Grt-st gneiss	0.1600	-25.41
Mineral abbreviations after Whitney & Evans (2010)				

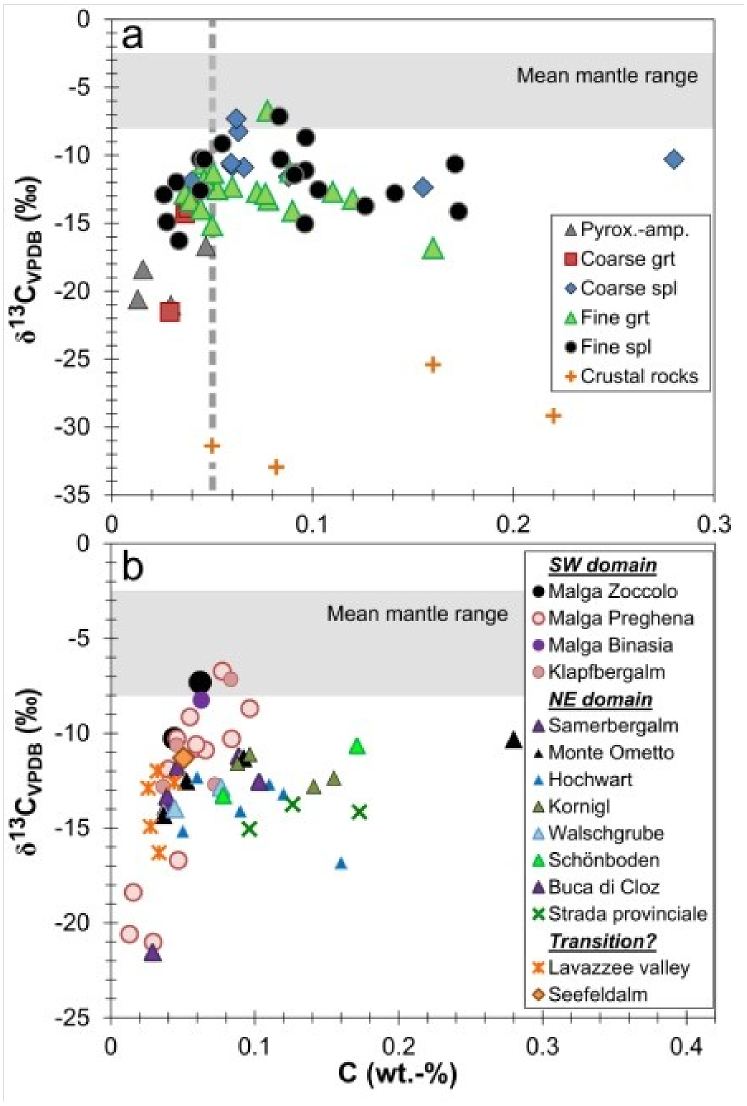

Figure 5.7. $\delta^{13}C$ and the total C concentration in Ulten Zone ultramafic whole rocks (a) classified by the petrographic type of peridotite regarding the texture (coarse-grained vs. fine-grained) and facies (garnet (grt) vs. spinel (spl)). Pyroxenitic amphibolized samples are not classified as peridotites and shown separately (pyrox.-amp.). The Ulten Zone peridotites partly contain total C up to 0.280 wt. % and show a high variability of $\delta^{13}C$. The total C concentration and the C isotopic composition of the Ulten Zone samples is largely independent on the peridotite type. The C isotopic composition and the total C concentration in Ulten Zone crustal rocks (gneisses and migmatites) is shown for comparison. The notional mean mantle range for $\delta^{13}C$ is shown for comparison ($\delta^{13}C$ from -8‰ to ~2.5‰, Shirey et al., 2013). The stippled line marks the reported threshold of the C concentration for general mantle samples, revealing that 95% of mantle xenoliths contain <0.05 wt. % C (Deines, 2002). (b) The same plot as in (a). The samples are grouped regarding their provenance in the Ulten Zone (SW domain and NE domain) as illustrated in Figure 5.6. The samples from the SW domain show a larger range in $\delta^{13}C$, compared to the samples from the NE domain. Samples from two other localities (Lavazzee valley and Seefeldalm) are spatially located in the center of the Ulten Zone and may represent a transitional type between the two domains.

The stable isotopic ratios of the drilled carbonates can be directly linked to the individual carbonate phases (Figure 5.8c). The drilled dolomite aggregate in sample VM25P11 (Figure 5.2f) has a narrow range of $\delta^{13}C$ (-10.1‰ to -9.6‰) but a larger range in $\delta^{18}O$ (+6.4‰ to +8.0‰ with one outlier with +10.4‰), regardless of the drilled surface (fresh cut surface vs. weathered surface). These values match those of the drilled dolomite grain in an amphibole vein in sample MOL1.5 (δ^{13}C of -10.1‰ and -9.4‰; δ^{18}O of +7.9‰ to +8.0‰), but do not match those of the drilled dolomite grain in a serpentine vein in sample MR141B (δ^{13}C -15.7‰; δ^{18}O +9.9‰). This dolomite rather conforms with the isotopic compositions for the drilled magnesite vein in sample KoD9 displaying δ^{13}C from -16.8‰ to -13.8‰ and δ^{18}O from +9.8‰ to +11.0‰. The drilled magnesite vein in sample MOL1.5 has less negative δ^{13}C (-10.8‰ to -10.7‰) but similar δ^{18}O (+9.6‰ to +9.7‰). The δ^{13}C of dolomite + magnesite in the whole-rock powder of sample MOL1.5 (-10.3‰) is similar to that of the drilled dolomite and magnesite in this sample, whereas δ^{18}O is more similar to that of the magnesite vein (+9.9‰). Interstitial discrete dolomite in the whole-rock samples SBA4, SBA5 and SBA7 displays δ^{13}C similar to that of the drilled dolomites in samples VM25P11 and MOL1.5 (-9.4‰ to -8.6‰) but more positive δ^{18}O (+11.5‰ to +13.2‰).

The petrographic observation that virtually no carbonates occur in the coarse-grained garnet-bearing samples from the Samerbergalm region (Förster et al., 2017) is confirmed by the very low CO_2 yields for sample SBA2 obtained during the stable isotope analyses.

Table 5.3 Locality of peridotites from the Ulten Zone, carbonate contents and carbon and oxygen isotopic composition of carbonates.

Sample	Locality	Carbonate phases	Method	δ^{13}C (‰)$_{VPDB}$	stdev	δ^{18}O (‰)$_{VSMOW}$	stdev
BAL1.2	Bichlalm	Unknown	Carbonate in WR	-8.07	0.02	16.15	0.02
BAL1.3	Bichlalm	Unknown	Carbonate in WR	-8.28	0.09	16.19	0.07
KBA1	Klapfbergalm	Unknown	Carbonate in WR	-4.93	0.03	17.77	0.06
KBA2	Klapfbergalm	Unknown	Carbonate in WR	-5.60	0.05	16.58	0.06
KBA5	Klapfbergalm	Unknown	Carbonate in WR	-8.81	0.09	18.20	0.19
KBA6	Klapfbergalm	Not observed	Carbonate in WR	-6.24	0.10	17.52	0.11
KBA7	Klapfbergalm	Unknown	Carbonate in WR	-5.67	0.04	19.22	0.13
KBA8	Klapfbergalm	Cal-brc intergrowths	Carbonate in WR	-8.64	0.17	16.97	0.09
KBA9	Klapfbergalm	Cal veins	Carbonate in WR	-5.16	0.09	16.02	0.09
KL1.1	Klapfbergalm	Unknown	Carbonate in WR	-5.99	0.04	17.95	0.11
KL1.2-1	Klapfbergalm	Unknown	Carbonate in WR	-8.71	0.01	14.31	0.07
KL1.2-2	Klapfbergalm	Unknown	Carbonate in WR	-7.43	0.12	17.68	0.08
KL1.2-3	Klapfbergalm	Cal-brc intergrowths	Carbonate in WR	-8.98	0.05	13.01	0.05
KL1.2-3	Klapfbergalm	Unknown	Carbonate in WR	-8.25	0.03	13.08	0.04
KL1.2-4	Klapfbergalm	Unknown	Carbonate in WR	-8.36	0.04	14.88	0.08
KL1.3P	Klapfbergalm	Cal-brc intergrowths	Carbonate in WR	-6.19	0.05	16.03	0.08
KL1.3V	Klapfbergalm	Unknown	Carbonate in WR	-8.04	0.07	17.94	0.09
KL1.4-1	Klapfbergalm	Unknown	Carbonate in WR	-7.42	0.03	16.19	0.05
KL1.4-2	Klapfbergalm	Unknown	Carbonate in WR	-7.67	0.04	16.18	0.04
KL1.5	Klapfbergalm	Unknown	Carbonate in WR	-4.52	0.02	16.79	0.12
KL1.6	Klapfbergalm	Cal-brc intergrowths	Carbonate in WR	-10.88	0.03	12.65	0.04
KL1.7-1	Klapfbergalm	Cal veins	Carbonate in WR	-9.53	0.02	18.34	0.09
KL1.7-2	Klapfbergalm	Cal veins	Carbonate in WR	-10.08	0.06	17.86	0.04
KL1.8	Klapfbergalm	Unknown	Carbonate in WR	-8.41	0.05	16.98	0.09
KL1.9	Klapfbergalm	Unknown	Carbonate in WR	-6.68	0.05	16.10	0.04
KL1b-2	Klapfbergalm	Unknown	Carbonate in WR	-5.05	0.02	16.92	0.06
KL2.3	Klapfbergalm	Unknown	Carbonate in WR	-8.92	0.04	16.72	0.11
KL2.4	Klapfbergalm	Cal-brc intergrowths	Carbonate in WR	-3.05	0.04	17.36	0.05
KL2.4-1	Klapfbergalm	Unknown	Carbonate in WR	-3.79	0.05	17.86	0.07
KL2.4-2	Klapfbergalm	Unknown	Carbonate in WR	-5.02	0.04	19.20	0.15
KL2.4-3	Klapfbergalm	Unknown	Carbonate in WR	-8.97	0.04	17.04	0.04
KLb	Klapfbergalm	Unknown	Carbonate in WR	-4.57	0.07	18.17	0.07
Ko1	Kornigl	Unknown	Carbonate in WR	-6.94	0.05	14.39	0.05
Ko2C	Kornigl	Cal veins	Carbonate in WR	-9.44	0.07	14.05	0.04
Ko2F	Kornigl	Cal-brc intergrowths	Carbonate in WR	-10.47	0.08	13.17	0.03
Ko3	Kornigl	Unknown	Carbonate in WR	-9.94	0.06	12.88	0.10
Ko4	Kornigl	Unknown	Carbonate in WR	-5.70	0.05	15.25	0.05
KoB1	Kornigl	Unknown	Carbonate in WR	-8.47	0.06	13.95	0.05

Sample	Locality	Carbonate phases	Method	$\delta^{13}C$ (‰)$_{VPDB}$	stdev	$\delta^{18}O$ (‰)$_{VSMOW}$	stdev
KoB2	Kornigl	Unknown	Carbonate in WR	-7.08	0.04	13.74	0.03
KoD1	Kornigl	Unknown	Carbonate in WR	-9.53	0.05	14.43	0.03
KoD10	Kornigl	Unknown	Carbonate in WR	-8.09	0.05	14.02	0.04
KoD11	Kornigl	Unknown	Carbonate in WR	-8.07	0.04	14.07	0.15
KoD12	Kornigl	Unknown	Carbonate in WR	-10.65	0.03	14.19	0.04
KoD14	Kornigl	Unknown	Carbonate in WR	-6.62	0.07	14.20	0.03
KoD15	Kornigl	Unknown	Carbonate in WR	-7.04	0.05	15.52	0.05
KoD2	Kornigl	Unknown	Carbonate in WR	-8.80	0.05	13.66	0.06
KoD3	Kornigl	Unknown	Carbonate in WR	-13.74	0.03	12.91	0.06
KoD4	Kornigl	Dol (±mgs)	Carbonate in WR	-8.50	0.03	13.96	0.16
KoD6	Kornigl	Unknown	Carbonate in WR	-10.74	0.04	13.78	0.07
KoD8	Kornigl	Unknown	Carbonate in WR	-6.91	0.08	15.11	0.10
KoD9-1	Kornigl	Mgs vein	Micro-drilled	-16.83	0.07	9.82	0.17
KoD9-2	Kornigl	Mgs vein	Micro-drilled	-15.48	0.05	9.84	0.11
KoD9-3	Kornigl	Mgs vein	Micro-drilled	-13.82	0.11	11.02	0.12
KoDb2	Kornigl	Cal-brc intergrowths	Carbonate in WR	-9.73	0.05	14.36	0.07
MBS1	Malga Binasia	Cal veins	Carbonate in WR	-6.77	0.11	18.76	0.14
MBS2	Malga Binasia	Cal veins	Carbonate in WR	-5.39	0.05	16.33	0.09
MBS3C	Malga Binasia	Unknown	Carbonate in WR	-6.68	0.05	16.61	0.05
MBS3F	Malga Binasia	Unknown	Carbonate in WR	-6.88	0.07	17.14	0.08
MBS5F	Malga Binasia	Unknown	Carbonate in WR	-5.52	0.12	15.99	0.12
MBS6	Malga Binasia	Unknown	Carbonate in WR	-5.62	0.05	13.90	0.05
MBS7	Malga Binasia	Unknown	Carbonate in WR	-5.05	0.07	16.76	0.06
MBS8	Malga Binasia	Not observed	Carbonate in WR	-3.66	0.15	15.99	0.14
MM-300D	Malga Masa Murada	Unknown	Carbonate in WR	-12.53	0.03	10.72	0.05
MM-300G	Malga Masa Murada	Unknown	Carbonate in WR	-11.54	0.05	11.70	0.02
MOL1.1C	Monte Ometto	Unknown	Carbonate in WR	-10.46	0.04	16.60	0.05
MOL1.1F	Monte Ometto	Unknown	Carbonate in WR	-10.88	0.03	16.42	0.03
MOL1.2	Monte Ometto	Unknown	Carbonate in WR	-9.44	0.04	15.32	0.04
MOL1.3	Monte Ometto	Unknown	Carbonate in WR	-9.68	0.06	16.41	0.05
MOL1.4	Monte Ometto	Unknown	Carbonate in WR	-9.64	0.05	12.72	0.04
MOL1.5	Monte Ometto	Dol + mgs	Carbonate in WR	-10.31	0.04	9.94	0.03
MOL1.5_M1	Monte Ometto	Mgs vein	Micro-drilled	-10.71	0.07	9.67	0.15
MOL1.5_M2	Monte Ometto	Mgs vein	Micro-drilled	-10.85	0.09	9.58	0.08
MOL1.5-Dol1	Monte Ometto	Dol grain in amp vein	Micro-drilled	-9.41	0.12	8.03	0.07
MOL1.5-Dol2	Monte Ometto	Dol grain in amp vein	Micro-drilled	-10.06	0.07	7.95	0.14
MOL1.7	Monte Ometto	Unknown	Carbonate in WR	-10.17	0.04	13.59	0.03
MOL1.8	Monte Ometto	Unknown	Carbonate in WR	-11.33	0.04	12.50	0.07
MOL1.9	Monte Ometto	Unknown	Carbonate in WR	-10.55	0.05	13.25	0.06
MOL2.1	Monte Ometto	Unknown	Carbonate in WR	-9.12	0.03	12.96	0.05
MOL2.2	Monte Ometto	Unknown	Carbonate in WR	-9.21	0.03	15.50	0.06
MOL2.3	Monte Ometto	Unknown	Carbonate in WR	-9.69	0.00	15.00	0.01
MOL2.4	Monte Ometto	Unknown	Carbonate in WR	-12.11	0.03	13.47	0.02
MZS1.1	Malga Zoccolo	Unknown	Carbonate in WR	-7.16	0.07	15.34	0.08
MZS1.2	Malga Zoccolo	Unknown	Carbonate in WR	-4.30	0.05	16.63	0.06
MZS1.3	Malga Zoccolo	Unknown	Carbonate in WR	-11.16	0.11	20.69	0.14
MZS1.4	Malga Zoccolo	Unknown	Carbonate in WR	-6.54	0.06	17.24	0.08
MZS1.5	Malga Zoccolo	Unknown	Carbonate in WR	-9.67	0.13	18.53	0.19
MZS3.1	Malga Zoccolo	Unknown	Carbonate in WR	-4.34	0.04	18.00	0.06
MZS3.2	Malga Zoccolo	Unknown	Carbonate in WR	-6.63	0.04	18.50	0.06
P11_CS_1	Mt. Hochwart	Dol aggregate	Micro-drilled	-10.09	0.06	6.90	0.07
P11_CS_2	Mt. Hochwart	Dol aggregate	Micro-drilled	-9.84	0.04	7.43	0.09
P11_CS_3	Mt. Hochwart	Dol aggregate	Micro-drilled	-10.08	0.09	6.40	0.04
P11_CS_4	Mt. Hochwart	Dol aggregate	Micro-drilled	-9.84	0.07	7.28	0.17
P11_CS_5	Mt. Hochwart	Dol aggregate	Micro-drilled	-9.61	0.04	10.42	0.07
P11_CS_6	Mt. Hochwart	Dol aggregate	Micro-drilled	-9.85	0.01	6.61	0.17
P11_CS_7	Mt. Hochwart	Dol aggregate	Micro-drilled	-9.96	0.03	7.28	0.13

Sample	Locality	Carbonate phases	Method	$\delta^{13}C$ (‰)$_{VPDB}$	stdev	$\delta^{18}O$ (‰)$_{VSMOW}$	stdev
P11_CS_8	Mt. Hochwart	Dol aggregate	Micro-drilled	-10.02	0.04	7.79	0.08
P11_WS_1	Mt. Hochwart	Dol aggregate	Micro-drilled	-9.61	0.03	8.03	0.05
P11_WS_2	Mt. Hochwart	Dol aggregate	Micro-drilled	-9.95	0.03	6.94	0.05
P11_WS_3	Mt. Hochwart	Dol aggregate	Micro-drilled	-10.03	0.04	7.00	0.05
PL1.1	Malga Preghena	Cal veins	Carbonate in WR	-8.33	0.06	20.68	0.80
PL1.2	Malga Preghena	Unknown	Carbonate in WR	-3.88	0.03	15.58	0.05
PL1.3	Malga Preghena	Unknown	Carbonate in WR	-4.23	0.02	16.09	0.12
PL1.4	Malga Preghena	Unknown	Carbonate in WR	-6.01	0.07	16.02	0.05
PL1.5	Malga Preghena	Unknown	Carbonate in WR	-5.74	0.03	16.37	0.07
PL1.6	Malga Preghena	Cal-brc intergrowths	Carbonate in WR	-4.52	0.04	15.37	0.07
PL1.7	Malga Preghena	Not observed	Carbonate in WR	-5.55	0.06	15.66	0.09
PL1.8	Malga Preghena	Unknown	Carbonate in WR	-0.99	0.04	15.01	0.12
PL1.9	Malga Preghena	Cal-brc intergrowths	Carbonate in WR	-5.56	0.06	12.86	0.07
PL2.1	Malga Preghena	Unknown	Carbonate in WR	-3.71	0.05	19.51	0.03
PL2.2	Malga Preghena	Unknown	Carbonate in WR	-5.71	0.03	15.94	0.06
PL2.3	Malga Preghena	Unknown	Carbonate in WR	-6.21	0.04	17.46	0.06
PL2.4	Malga Preghena	Unknown	Carbonate in WR	-4.40	0.03	18.98	0.06
PRE1	Malga Preghena	Unknown	Carbonate in WR	-0.03	0.06	16.46	0.10
PRE2	Malga Preghena	Unknown	Carbonate in WR	-8.05	0.09	16.97	0.12
PRE-A	Malga Preghena	Cal veins	Carbonate in WR	-2.71	0.09	16.60	0.06
SB1	Schönboden	Not observed	Carbonate in WR	-8.91	0.13	17.11	0.13
SB2.1	Schönboden	Cal-brc intergrowths	Carbonate in WR	-8.38	0.04	15.20	0.04
SB2.2	Schönboden	Cal-brc intergrowths	Carbonate in WR	-9.24	0.05	14.33	0.07
SB3.1	Schönboden	Cal-brc intergrowths	Carbonate in WR	-8.53	0.04	13.49	0.04
SB3.2	Schönboden	Cal-brc intergrowths	Carbonate in WR	-10.69	0.04	13.73	0.05
SB3.3	Schönboden	Cal-brc intergrowths	Carbonate in WR	-9.98	0.05	15.95	0.06
SB3.4	Schönboden	Cal veins	Carbonate in WR	-13.40	0.05	15.82	0.06
SBB-C1	Schönboden	Unknown	Carbonate in WR	-10.95	0.09	14.18	0.14
SBB-C2	Schönboden	Unknown	Carbonate in WR	-11.47	0.06	14.69	0.06
SBB-F1	Schönboden	Unknown	Carbonate in WR	-12.61	0.05	14.26	0.05
SBB-F2	Schönboden	Unknown	Carbonate in WR	-10.29	0.06	14.96	0.08
MR141B	Samerbergalm	Dol grain in srp vein	Micro-drilled	-15.75	0.07	9.96	0.06
SBA1	Samerbergalm	Unknown	Carbonate in WR	-10.82	0.02	13.86	0.02
SBA2	Samerbergalm	Unknown	Carbonate in WR	-7.80	0.13	14.69	0.12
SBA3	Samerbergalm	Unknown	Carbonate in WR	-6.99	0.06	16.19	0.15
SBA4	Samerbergalm	Discrete dol	Carbonate in WR	-8.91	0.08	12.30	0.17
SBA5	Samerbergalm	Discrete dol	Carbonate in WR	-8.64	0.05	13.22	0.09
SBA6	Samerbergalm	Unknown	Carbonate in WR	-10.63	0.03	12.98	0.04
SBA7	Samerbergalm	Discrete dol	Carbonate in WR	-9.42	0.03	11.49	0.08
SBA8	Samerbergalm	Unknown	Carbonate in WR	-11.75	0.04	11.98	0.04
SBA9	Samerbergalm	Unknown	Carbonate in WR	-14.60	0.06	10.50	0.04
SGS2	Schöngrubspitz	Unknown	Carbonate in WR	-5.45	0.08	13.50	0.05
SGS3	Schöngrubspitz	Unknown	Carbonate in WR	-6.91	0.07	16.18	0.11
WG1	Walschgrube	Cal-brc intergrowths	Carbonate in WR	-11.60	0.04	14.86	0.05
WG2	Walschgrube	Cal-brc intergrowths	Carbonate in WR	-10.61	0.07	15.91	0.06
WG3	Walschgrube	Unknown	Carbonate in WR	-10.61	0.04	16.92	0.09
WG4	Walschgrube	Not observed	Carbonate in WR	-11.69	0.10	14.28	0.09
WG5	Walschgrube	Not observed	Carbonate in WR	-11.72	0.14	17.79	0.15
WG6	Walschgrube	Unknown	Carbonate in WR	-11.22	0.03	12.76	0.04
WG8	Walschgrube	Unknown	Carbonate in WR	-11.35	0.05	15.96	0.06
WG9	Walschgrube	Cal-brc intergrowths	Carbonate in WR	-11.61	0.04	16.93	0.07
WG11	Walschgrube	Unknown	Carbonate in WR	-10.04	0.02	15.97	0.04
Mineral abbreviations after Whitney & Evans (2010)							

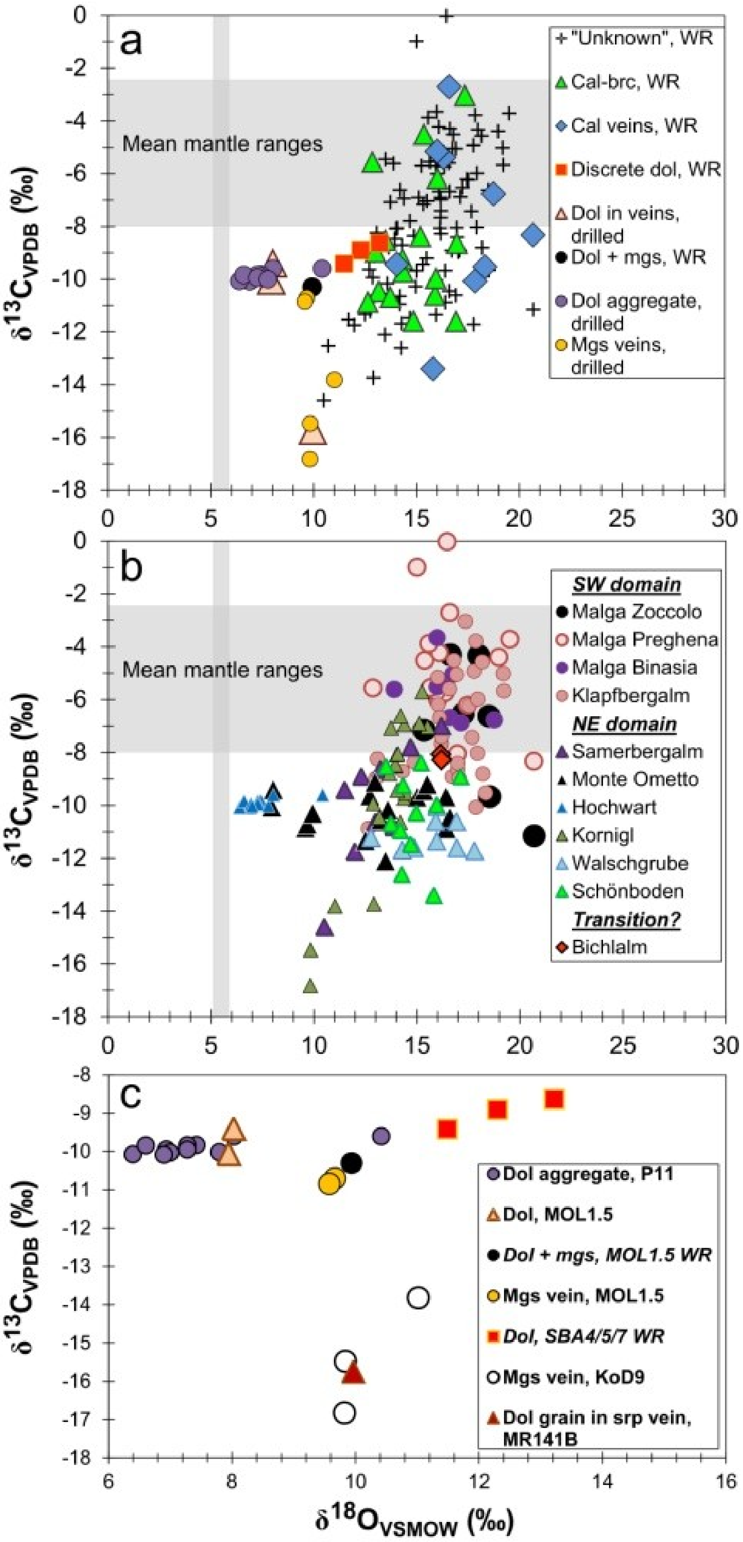

Figure 5.8. $\delta^{13}C$ and $\delta^{18}O$ for carbonates in whole-rock peridotites from the Ulten Zone. (a) The stable-isotope composition of carbonates in samples with unknown carbonate contents, of calcite-brucite intergrowths (Cal-brc), calcite veins (Cal veins), discrete interstitial dolomite (Discrete dol), dolomite grains in amphibole and serpentine veins (Dol in veins), interstitial dolomite + magnesite in the coarse-grained protogranular sample MOL1.5 (Dol + mgs), the micro-drilled dolomite aggregate in the fine-grained garnet-amphibole peridotite VM25P11 (Dol aggregate), micro-drilled magnesite veins crosscutting the peridotite matrix (Mgs veins). Mean mantle ranges for $\delta^{13}C$ and $\delta^{18}O$ are shown for comparison ($\delta^{13}C$ from ~8‰ to ~2.5‰, Shirey et al., 2013; $\delta^{18}O$ ca. +5.5‰ ± 0.4‰, Mattey et al., 1994). The stable isotopic composition of the carbonates is highly variable and $\delta^{18}O$ is generally more positive relative to the main mantle range, whereas the carbonate's $\delta^{13}C$ ranges from values overlapping the main mantle range to more negative values. The high variability of the stable-isotope composition is displayed by all carbonates and the different carbonate types do not show a clear link to distinct stable isotopic compositions. (b) The stable-isotope composition of all carbonates as shown in (a), but grouped according to the peridotite sample locality in the Ulten Zone. The carbonates from peridotites from localities located in the southwest (SW) of the Ulten Zone display $\delta^{13}C$ largely overlapping with the notional main mantle range, whereas carbonates from peridotites from localities in the northeast (NE) display mainly more negative $\delta^{13}C$. The $\delta^{18}O$ of the SW carbonates are in general slightly more positive relative to the carbonates from the NE Ulten Zone. The stable isotopic composition of the carbonates thus distinguishes the Ulten Zone in a SW domain and a NE domain. (c) The stable-isotope composition of distinct micro-drilled carbonate phases and carbonates in whole-rock samples as illustrated in (a), the carbonate contents of which is clearly defined by petrographic observations and which contain a single carbonate phase. Mineral abbreviations after Whitney & Evans (2010).

5.6 Discussion

5.6.1 Implications for the metasomatic stages during the UZ evolution

This paper presents a novel and integrated petrographic-petrologic-geochemical study of C concentrations in ultramafic rocks from the UZ, in oxidized/carbonate and reduced forms (potentially graphite, but possibly organic in origin) and the stable-isotope compositions of whole-rock and micro-drilled carbonates. The occurrence of dolomites in these rocks has been discussed previously (Rampone & Morten, 2001; Braga & Sapienza, 2007; Sapienza et al., 2009; Förster et al., 2017), but C concentrations and the stable-isotope compositions have not been reported. We will discuss our new data in the context of the different metasomatic stages in the UZ evolution that lead to the crystallization of the several carbonate phases (summarized in section 5.3; Förster et al., 2017).

The formation of interstitial matrix dolomite together with amphibole and apatite in fine-grained recrystallized hydrated peridotites has been attributed to peridotite interaction with C-bearing aqueous fluids at garnet stability (section 5.3; summarized in Förster et al., 2017). These aqueous fluids were interpreted to transport incompatible trace elements, such as LREE and LILE, into the fine-grained peridotites, reflected by the enrichment of this metasomatic type in these elements (e.g. Morten and Obata, 1990; Godard et al., 1996; Rampone and Morten, 2001; Scambelluri et al., 2006; Sapienza et al., 2009). Accordingly, the concentrations of LREE and LILE in UZ peridotites are controlled by the different metasomatic events which are recorded by the petrographic/mineralogic peridotite types. Thus, if fine-grained recrystallized garnet-amphibole peridotites were subjected to enrichment in C, LREE and LILE by the same metasomatic process, one would expect elevated C concentrations in this peridotite type and low C concentrations in coarse-grained peridotites that were largely prevented from enrichment in the incompatible elements. Accordingly, fine-grained garnet-amphibole peridotites show a correlation between oxidized C and LREE and LILE (Figure 5.9a,b), but it is noteworthy that also coarse-grained peridotites can contain high C concentrations (Figure 5.9). This indicates that the introduction of C was not closely coupled with the assumed main metasomatic event and was attributed to additional metasomatic processes. As postulated by Förster et al. (2017), carbonate formation in UZ peridotites occurred during the entire UZ history from the mantle wedge to exhumation and record a variety of metasomatic processes. Additionally, the observation of different C specifications, oxidized and reduced C, shows that not only carbonates play a role in the C cycle in the UZ. The origin and nature of C and implications on the C-mobilizing metasomatic processes affecting the UZ lithologies will be discussed in the following two sections.

5.6.2 Constraints on carbon-mobilizing processes in the UZ

The overall C and O isotopic composition in carbonates is highly variable, but relative to the notional main mantle ranges, $\delta^{13}C$ is generally lighter and $\delta^{18}O$ generally heavier, indicating the involvement of crustal agents in the metasomatic carbonate-forming processes. However, the link between the carbonate stable-isotope composition and the provenance of the peridotites in the UZ (Figure 5.8b) is clearly visible and also is slightly mirrored by the whole-rock C-isotope composition and C concentrations (Figure 5.7b). The samples with the highest total C concentration derive from the NE domain and it is important to note that the magnesite veins occur in samples from the NE domain only. In terms of all other carbonate types and the present peridotite types, the UZ cannot be distinguished in a NE and a SW domain. Thus, the isotopic discrimination must be a result of regionally differing metasomatic processes and/or the involvement of isotopically different metasomatic agents.

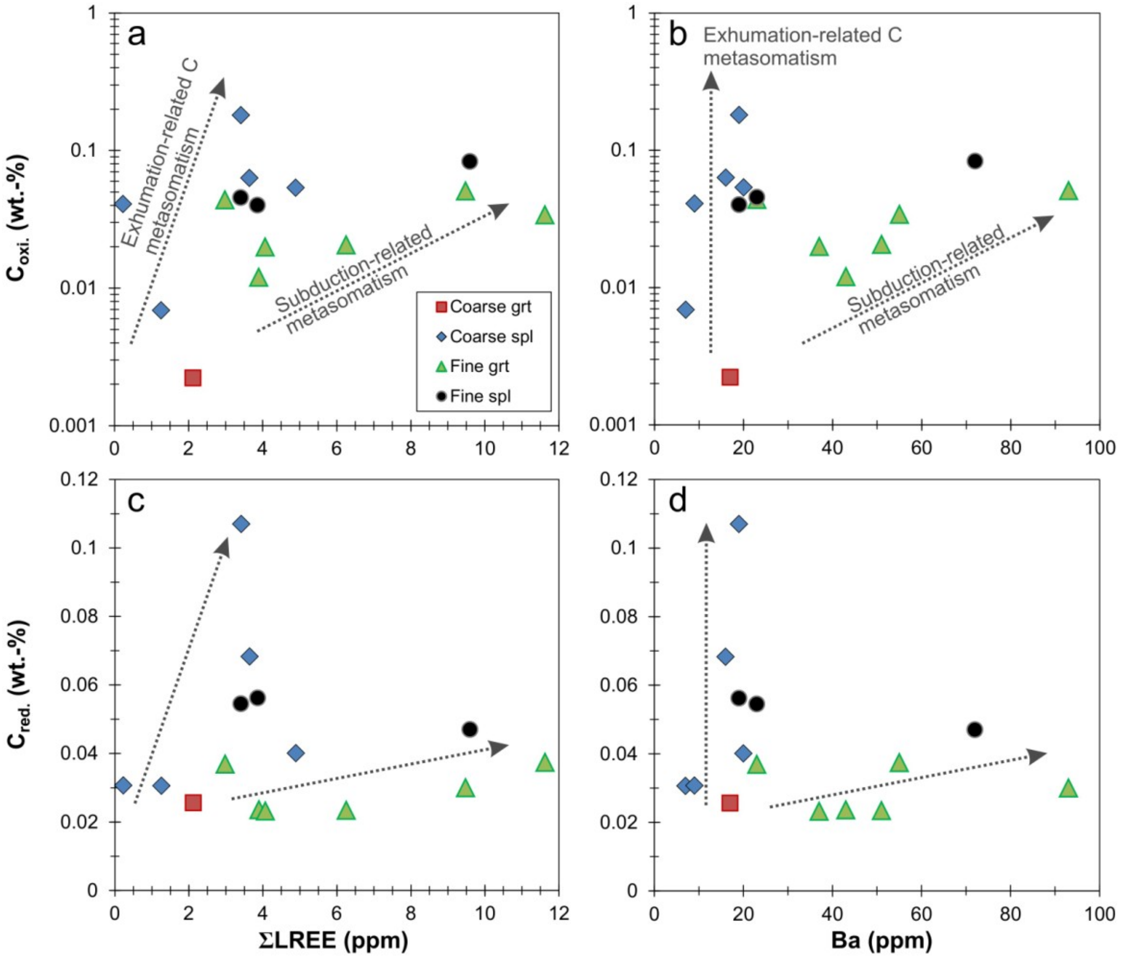

Figure 5.9. Comparison of concentrations of (a) oxidized C and (b) reduced C with ΣLREE and Ba in the different petrographic types of Ulten Zone peridotites (coarse-grained vs. fine-grained, spinel-bearing vs. garnet-bearing). In contrast to coarse-grained peridotites, the fine-grained recrystallized garnet-amphibole peridotites reflect strong enrichment in LREE and LILE (e.g. Ba), which has been attributed to crustal metasomatism owing to interaction with slab-derived aqueous fluids during recrystallization of peridotites at garnet-facies conditions (arrow labeled "Subduction-related metasomatism"; e.g. Morten and Obata, 1990; Godard et al., 1996; Rampone and Morten, 2001; Scambelluri et al., 2006). These aqueous fluids were C-bearing and fluid-rock interaction lead to the formation of dolomite together with amphibole and apatite (summarized in Förster et al., 2017). However, also coarse-grained peridotites contain carbonates which are rather of exhumation-related origin and formed from local C-bearing aqueous fluids (arrow labeled "Exhumation-related C metasomatism"). The enrichment of incompatible trace elements and modal metasomatism is unrelated to the location of the peridotites in the UZ, i.e. no correlation between this crustal metasomatism and the two UZ domains (NE domain and SE domain) is observed. Both fine-grained peridotites and coarse-grained peridotites can contain reduced C, the introduction of which can be attributed to additional metasomatic processes. Mineral abbreviations after Whitney & Evans (2010).

Two possible (end-member) scenarios may explain this observation: (1) Initially carbonate formed in the mantle wedge and/or close to the slab-mantle interface from a metasomatic agent derived from deeper parts of the subduction zone or from a "mantle source", resulting in a mantle-like carbonate $\delta^{13}C$. New carbonate generations were formed during subsequent and ongoing fluid-rock interaction related to continental subduction and exhumation. The mantle-$\delta^{13}C$ was stronger overprinted by "metasedimentary" $\delta^{13}C$ from slab-derived C in the NE domain, resulting in more negative $\delta^{13}C$; (2) The dolomites formed from slab-derived aqueous fluids during/after peridotite incorporation in the crustal slab and initially had "metasedimentary" δ^{13}C. During subsequent exhumation, the peridotites from the SW domain were mechanically mixed with an ancient ophiolitic suite that had been dismembered in an orogenic prism and derived from a former pre-Variscan oceanic mantle (Susini & Martin, 1996; Martin et al., 1998). Fluid-assisted interaction of the SW peridotites with this suite, which contains ophicarbonates, drove the carbonates in the SW domain to less negative δ^{13}C, which plot coincidentally in the notional main mantle range.

Scenario (1) is supported by the (rare) occurrence of carbonates in primary spinel (Förster et al., 2017), indicating that a first dolomite generation formed in the high-temperature spinel stage from subduction-related mafic melts which derived from deeper parts of the subduction zone (Scambelluri et al., 2006) and must have carried a C component (Förster et al., 2017). The origin of these melts is yet not fully constrained, but they presumably carried recycled crustal components (Scambelluri et al., 2006). Dolomites which formed from these melts inherited their mantle-like δ^{13}C. Subsequent fluid-mediated interaction of the peridotites with the subducted metapelites prompted formation of a new generation of dolomite during ongoing garnet formation and also later during exhumation. These new dolomite generations inherited the more negative δ^{13}C from the crust-derived C. In conclusion, this would mean that the crustal overprint was stronger in the NE domain and no or very rare new carbonates with crustal signature formed in the SW domain, whereas primary dolomite was preserved, in spite of intense fluid-peridotite interaction. However, since fluid-mediated metasomatic overprint, mirrored by highly abundant amphibole occurrence, affected all (fine-grained garnet-amphibole) peridotites across the entire UZ consistently, this scenario does not seem to be a plausible explanation for the isotopic difference of the two domains.

In scenario (2), primary carbonate formation in the high-temperature spinel stage was largely overprinted by the formation of new dolomite from C-bearing aqueous fluids released from the crustal slab in the entire UZ, starting at garnet-facies conditions and progressing on the exhumation path. The newly formed dolomite inherited a crust-like δ^{13}C, what is reflected by the C isotopic signature of the carbonates from the NE domain. In contrast, the SW domain of the UZ was mechanically mixed with an ancient ophiolitic orogenic prism (Susini & Martin, 1996) during its ascent to lower-crustal levels. This is based on the field evidence that the SW domain of the UZ is tectonically embedded in a series of metamorphic rocks containing ultramafic slices that consist of chlorite ± amphibole ± carbonate-bearing serpentinite and partly serpentinized harzburgite and dunite, located in the southwestern portion of the Ulten unit (Cresta Camucina, Cima Mezzana and the locality Cogni, Figure 5.10; Susini & Martin, 1996). Ultramafic rocks consisting of serpentinites, ophicalcites and calc-silicate rocks occur also in the Tonale unit in the southeast of the Ulten unit and these rocks have been suggested to represent a dismembered ophiolitic suite (Martin et al., 1998). Similarly, the southwestern part of the Ulten unit has been suggested to represent portions of an ancient subducted slab of old oceanic lithosphere pre-dating the Variscan continental collision (Susini & Martin, 1996; Martin et al., 1998). In several studies on natural samples from various localities from the Alps and Apennines it has been demonstrated that ophicarbonates have δ^{13}C of ca. 0 ± 4‰ (Clerc et al., 2014; Collins et al., 2015; Scambelluri et al., 2016). As a result of mechanical mixing and rock-rock interaction mediated by a C-bearing fluid inheriting the C isotopic ratio of the ophicarbonates in the southwestern Ulten unit, the δ^{13}C of the carbonates in the SW domain of the UZ may have been driven to less negative values. In this case, the "mantle-like" δ^{13}C of the SW domain would be misleading and would record isotopic mixing instead of displaying a pristine mantle signature. Due to the greater distance of the NE domain to the ophiolitic suites, the NE carbonates were not subjected to this process and retained the "crust-like" stable isotopic character.

Supportive of scenario (2) is the observation by Marocchi et al. (2011) who analyzed the intra-grain isotopic zoning of boron in tourmaline from hybrid peridotite-crust contact rocks ("blackwalls") from Mt. Hochwart (NE domain) and from Malga Preghena (SW domain): tourmalines from those localities can be distinguished in terms of their opposing boron isotope intra-grain zoning what has been interpreted to evidence tourmaline growth from fluids of at least two different reservoirs (Marocchi et al., 2011).

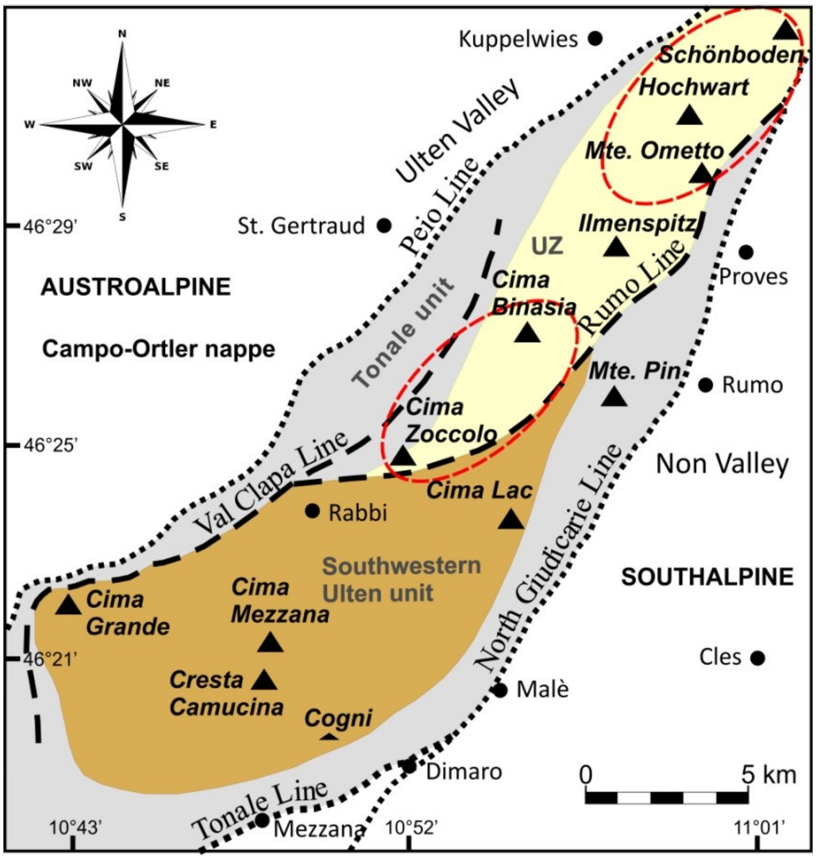

Figure 5.10. Map of the Tonale nappe located between the Peio Line, the Tonale Line and the North Giudicarie Line in the Austroalpine, composed of the Tonale unit and the Ulten unit. The Ulten unit is subdivided into a northeastern part, the Ulten Zone (UZ), and a southwestern area (Southwestern Ulten unit). The UZ is characterized by high-grade metamorphic basement rocks containing bodies of ultramafic rocks (peridotites ± pyroxenites), whereas the southwestern Ulten unit is composed of lower grade crustal rocks which are partly associated with serpentinized peridotites and ophiolites (Cresta Camucina, Cima Mezzana and the locality Cogni; Susini & Martin, 1996). The stippled ovals show the subdivision of the Ulten Zone in a northeastern (NE) and a southwestern (SW) domain. The two domains can be distinguished by the stable-isotope (C and O) composition of carbonates in Ulten Zone ultramafic rocks. Figure redrawn after Godard et al. (1996) and Susini & Martin (1996). In other maps (e.g. Martin et al., 1998), the southwestern area of the Ulten unit extends up to the Tonale and the North Giudicarie Lines, including the Mte. Pin area.

These authors conclude that, in the case for rocks at Mt. Hochwart, a fluid locally derived from the country-rock gneisses, and subsequently an externally derived fluid, presumably originated in the subducting slab, caused the formation of tourmaline. The opposite chronology is exhibited by the Malga Preghena tourmaline which initially grew from the slab-related fluid and mirrors the later growth from locally derived fluids. It has been demonstrated (Marocchi et al., 2009; 2011) that the hybrid contact zones formed at 0.5-0.7 GPa and 660-700°C during exhumation of the UZ crust-peridotite mélange, conditions which are in agreement with mechanical mixing of the ascending mélange with a dismembered ophiolitic suite at crustal levels. In this case, the clear isotopic discrimination of the two UZ domains could be explained by exhumation-related fluid infiltration in the SW domain, involving a fluid with an isotopically mixed signature resulting from mixing of the crust-derived fluid with an external ophicarbonate-derived fluid. Whether the ophicarbonate-derived fluid is sourced in the involved rock suites or derives from external sources and migrates through the exhumation mélange remains matter of debate. Carbonates from the SW domain define a trend to increasing concentration of oxidized C with less negative $\delta^{13}C$, whereas carbonates from the NE domain exhibit more negative $\delta^{13}C$ with increasing concentration of oxidized C (Figure 5.11a).

Although weaker, these trends are also displayed by the whole-rock $\delta^{13}C$ (Figure 5.7b), which is probably largely dictated by the carbonate $\delta^{13}C$. A similar trend, such as demonstrated by the SW carbonates was previously reported in Bianchini & Natali (2017) for mantle xenoliths and was interpreted to reflect a mantle origin of C related to partial melting. This process and Rayleigh-type C fractionation liberated liquids with less negative $\delta^{13}C$, leaving residual components with progressively more negative $\delta^{13}C$ (Bianchini & Natali, 2017 and references therein). Such a mechanism could explain the trend of the SW carbonates in case of scenario (1). However, as discussed above, this scenario seems not to be a viable mechanism in the UZ. The trend displayed by the SW carbonates rather indicates fluid-mediated late-stage enrichment in oxidized C with changing $\delta^{13}C$: in the peridotites containing dolomite with initially crust-related (more negative) $\delta^{13}C$, exhumation-related carbonates formed with progressively less negative $\delta^{13}C$. Accordingly, the opposite trend, defined by the NE carbonates, indicates progressive influx of oxidized C derived from the crustal host rocks. The relationship between the concentration of oxidized C and $\delta^{18}O$ (Figure 5.11b) is less distinctive regarding the two UZ domains. A general trend to less positive $\delta^{18}O$ with increasing $C_{oxi.}$ can be observed but the reason of this trend is to date unclear. In summary, our findings show that the spatial position of portions in an exhumation association can affect the lithologies' isotopic signature, and fluid-involved mechanical mixing of rock suites during exhumation is capable to promote element transfer and must be considered as a process that plays a role in the element cycle and mass transfer in collisional settings.

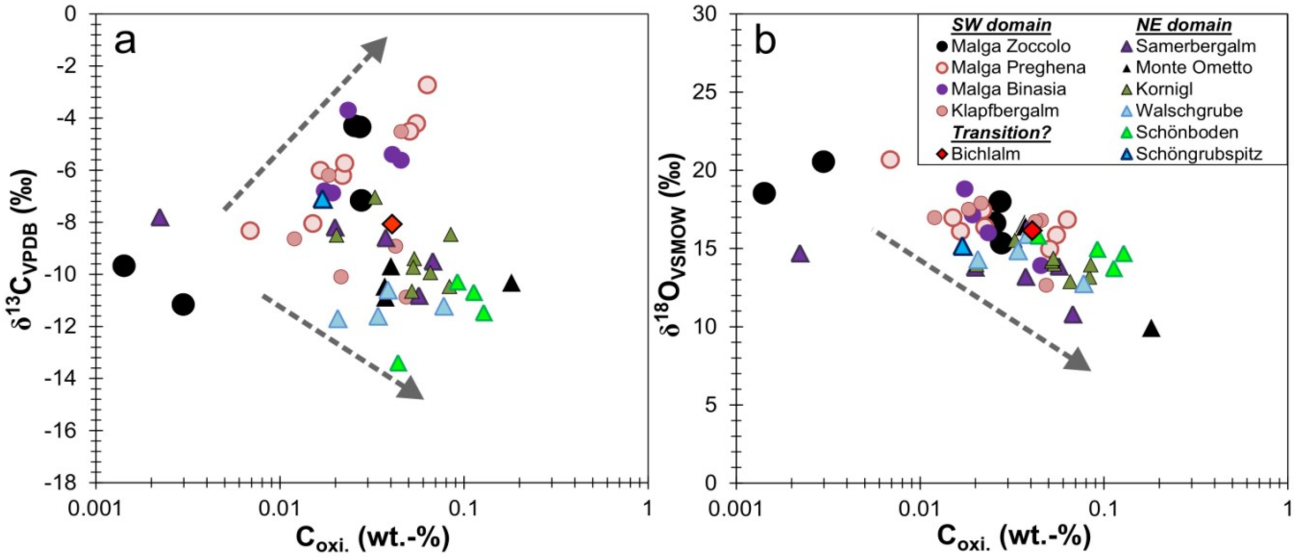

Figure 5.11. Relationship between the concentration of oxidized C (carbonate C, $C_{oxi.}$) and the stable-isotope compositions of carbonates ($\delta^{13}C$ and $\delta^{18}O$). (a) Two trends are displayed by the $C_{oxi.}$ vs. $\delta^{13}C$. The more $C_{oxi.}$ samples from the SW domain in the Ulten Zone contain, the less negative is the $\delta^{13}C$ of the carbonates. For samples from the NE domain, increasing $C_{oxi.}$ is coupled with more negative $\delta^{13}C$. (b) For $\delta^{18}O$, all samples, unrelated to the two UZ domains, define one trend. The $\delta^{18}O$ becomes more negative with increasing $C_{oxi.}$ concentration.

5.6.3 Carbon forms and carbon origin in UZ peridotites

5.6.3.1 Origin and nature of carbonate fluid sources

Matrix dolomites and dolomite veins formed from C-bearing aqueous fluid/s released by the crustal slab in the entire retrograde history of the UZ, starting from garnet-facies to subsurface conditions. Dolomites in textural equilibrium with amphibole have similar $\delta^{13}C$ (from -11 to -9‰; Figure 5.8c) and may indicate dolomite formation together with hydrous phases from the same COH-fluid. The narrow inter-grain variability of $\delta^{13}C$ displayed by these dolomites may show that dolomite formed from an isotopically similar (or identical) source and/or reflects similar C fractionation processes. However, the stable isotopic composition of the drilled crystals of the dolomite aggregate may give more detailed insights into the growth conditions of the dolomite and the source of C. The single drilled spots in the aggregate do not show significant variability in $\delta^{13}C$ (ca. -10‰; Figure 5.8c). Since C solubility in the surrounding mantle minerals is negligible low (Shcheka et al., 2006), C fractionation between dolomite and the peridotite minerals can be ruled out. Instead, fractionation could occur only between the growing dolomite and the fluid. Progressive formation of the single crystals of the dolomite aggregate from the migrating fluid would result in inter-grain isotopic variability, as the $\delta^{13}C$ of the residual fluid would change. However, the inter-grain C isotopic homogeneity may show that the C isotopic values of the single crystals initially displayed closed-system fractionation but were subjected to subsequent isotopic homogenization. It cannot be clearly identified whether the dolomite formed vein-like in an isotopically open system with Rayleigh fractionation during fluid percolation or whether the C from the incoming fluid was completely consumed by dolomite precipitation and subjected to close-system fractionation. Assuming the latter, the aggregate's $\delta^{13}C$ would reflect the initial C isotopic composition of the fluid. As the notional main range of mantle $\delta^{13}C$ ranges from -8‰ to -2.5‰ (Shirey et al., 2013), the lower dolomite $\delta^{13}C$ evidence the crustal origin of the aqueous fluid. In this context it must be noted that the aggregate derives from Mt. Hochwart, a peridotite locality in the NE domain of the UZ, which probably did not experience major interaction with fluids that were sourced outside of the gneiss+migmatite-peridotite mélange (see previous section). The crust-derived fluid responsible for dolomite formation was likely a COH-fluid generated by partial melting of the orthogneiss on the prograde metamorphic path of the continental slab (see section 3; Hauzenberger et al., 1996; Rampone & Morten, 2001). Whole-rock C isotopic compositions of gneisses and migmatites in the UZ range from $\delta^{13}C$ of -33‰ to -25‰ (Table 5.2) and are probably mainly attributed to graphite that was observed in the crustal rocks (pers. comment, R. Braga). However, similar C-isotope compositions were reported for gneisses from the orogenic Dabie-Sulu terrane (Zheng et al., 2003) and are inherited from the gneissic precursor protoliths which underwent meteoric-hydrothermal alteration prior to involvement in the subducting continental plate (Zheng et al., 2003). Such a pre-subduction scenario could be true also for the gneisses in the UZ, as it was discussed that partial melting of the gneisses occurred under water oversaturated conditions in the presence of water that was transported into the subduction zone by the crustal slab (Tumiati et al., 2007). During migmatization of the gneisses on a prograde decompressional metamorphic path (Tumiati et al., 2003), the migmatites would have inherited the light C isotopic composition of the gneiss, driving the residual aqueous fluid to less negative $\delta^{13}C$, what is preserved in the dolomite aggregate, assuming that it represents the initial fluid composition. Although the time of dolomite formation is largely unconstrained, in the context of the new observations that peridotite emplacement into the crustal host rocks occurred at low-*P*-*T* at ca. 333 Ma (thesis chapter 3), the age of a zircon (ca. 334 Ma; thesis chapter 3) containing dolomite ± apatite inclusions in a fine-grained garnet-amphibole peridotite indicates that at least some dolomite formed during exhumation.

The similar $\delta^{13}C$ displayed by the magnesite vein in the coarse-grained peridotite (MOL1.5) and the above discussed dolomites in textural equilibrium with amphibole in other samples (ca. -10 to -9‰), may be the result of the same fluid-assisted metasomatic stage. In contrast, the C isotopic compositions displayed by the distinct magnesite vein in sample KoD9 ($\delta^{13}C$ ca. -17 to -14‰) and by the dolomite grains in a serpentine vein in sample MR141B (-15.7‰) are significantly lower. This discrepancy may be explained by the probable late-stage serpentinization-related origin of the these carbonates: the magnesite vein in KoD9 is in textural contact with serpentine veins in a serpentinized peridotite and the dolomite grains in MR141B are situated within a distinct serpentine vein crosscutting the peridotite matrix (Förster et al., 2017). This could mean that these carbonates precipitated from the serpentinizing migrating fluid which had a different isotopic composition compared to the earlier carbonate-forming fluid. On the other hand, the magnesite veins may have formed at higher-temperature conditions and persisted metastably during serpentinization (Förster et al., 2017). If so, the magnesite vein in KoD9 may have the same origin as the other magnesite veins but were later subjected to serpentinization-related isotope fractionation. Accordingly, the UZ magnesite veins display slightly higher $\delta^{18}O$ but clearly more negative $\delta^{13}C$ compared to primary magnesite from UHP-garnet peridotites from the Sulu terrane, indicating magnesite formation during carbonatitic magmatism in the mantle wedge (Zhang et al., 2007). Thus, the more negative $\delta^{13}C$ of the UZ magnesite and its textural occurrence as crosscutting veins corroborates the crustal origin of the C and the formation of magnesite from C-rich aqueous fluids at late stages in the UZ history, especially in the NE domain.

In general, the high stable-isotope variability of carbonates in peridotites containing calcite-brucite intergrowths as a dolomite-breakdown product (Förster et al., 2017) mirrors open-system isotope fractionation during peridotite-fluid interaction probably at the serpentinization stage on the UZ exhumation path. The breakdown of dolomite not only results in the formation of the calcite-brucite intergrowths but also enables the liberation of a C species into the percolating serpentinizing fluid (Förster et al., 2017). The large range of stable isotopic compositions of these samples is therefore probably a result of open-system isotope fractionation between the residual calcite and the fluid. Additionally it must be noted that in these samples a mixed carbonate content is present (calcite ± dolomite) due to various degrees of dolomite breakdown and relict dolomite may be present. The general variable O isotopic compositions of the carbonates can be explained by diffusion-controlled isotope exchange between the carbonates and the surrounding peridotite minerals. The O isotopic compositions of the carbonates is generally heavier than reported isotopic values for olivine, pyroxene and amphibole ($\delta^{18}O$ ca. +5 to +6‰; Chazot et al., 1997), corroborating the crustal character of the source fluid.

5.6.3.2 Implications for the origin of reduced carbon in UZ peridotites

Comparison of the C isotopic compositions of the whole-rock peridotites and the carbonates shows that the whole-rock $\delta^{13}C$ is generally slightly more negative (Tables 5.2, 5.3; Figure 5.12). This is true for almost all samples where $\delta^{13}C$ data of both whole rock and carbonates are available and indicates that, besides the carbonates, one and/or other C-trapping species occur/s in the UZ peridotites, which lower/s the whole-rock C isotopic signature. Such a species may be graphite and/or reduced compounds. Indeed, while no C-bearing phases other than carbonates were observed during petrographic investigations, reduced C was detected in the peridotites, even in similar concentrations as oxidized C, i.e. carbonate C (Figure 5.6). Fine-grained peridotites and coarse-grained spinel peridotites display a ratio of reduced and oxidized C around unity, whereas the one garnet-bearing coarse-grained peridotite and two pyroxenitic samples show a ten-fold higher ratio. A general positive correlation between reduced and oxidized C in the studied samples is recognizable. Reduced C compounds can be brought to mantle depths via subduction of metasediments and can be oxidized via redox reactions and then be retained in the mantle (e.g. Yang et al., 2001; Deines, 2002; Dasgupta & Hirschmann, 2010; Manning et al., 2013; Sverjensky et al., 2014; Duncan & Dasgupta, 2017 and references therein). In this context, it may be that the slight positive correlation indicates carbonate formation in the peridotites as a result of oxidation of subducted reduced C during crust-peridotite interaction. The oxidation of reduced C is strictly coupled to the present oxidation state in the system and it has been shown that the fine-grained garnet-amphibole peridotites from the UZ record relatively high O fugacities (FMQ to FMQ+2; Malaspina & Tumiati, 2012), what would promote the formation of carbonate from subducted reduced compounds.

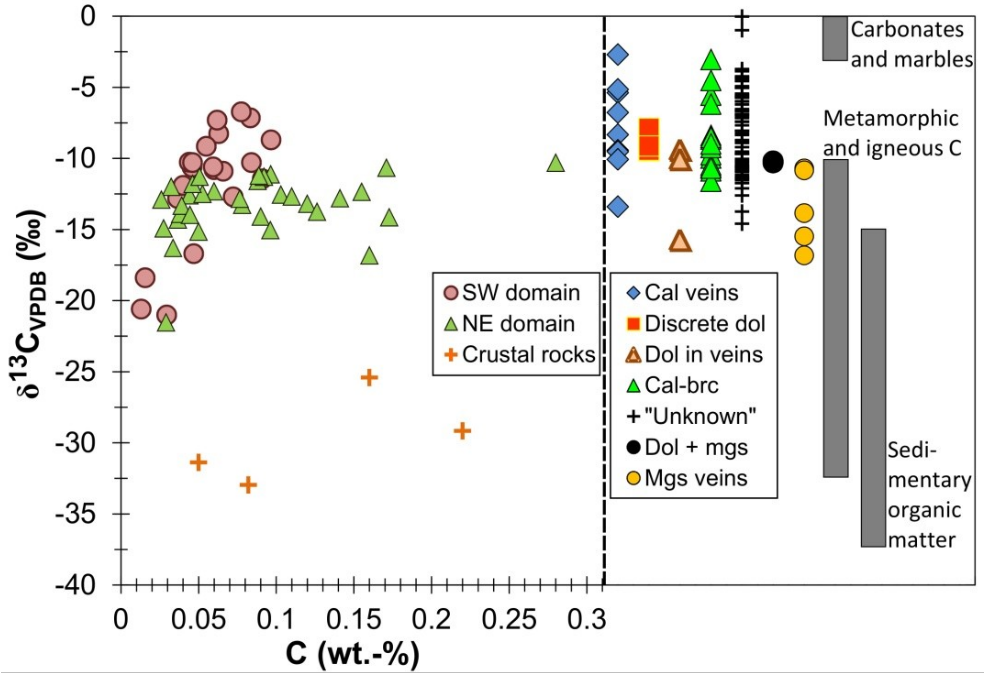

Figure 5.12. Total C concentration and $\delta^{13}C$ in whole rocks (as in Figure 5.7) and $\delta^{13}C$ in carbonate phases in peridotites (as in Figure 5.8) from the Ulten Zone. The columns encompass the $\delta^{13}C$ ranges of the indicated reservoirs (Des Marais, 2001) which may represent subducted materials.

However, the high $C_{red.}/C_{oxi.}$ ratio in the garnet-bearing coarse-grained peridotite could argue against a redox-related carbonate formation and may show that oxidation of introduced crust-derived reduced C was hampered by more reduced conditions. If so, this peridotite would record a more reduced environment in the mantle wedge and it would also mean that continental slabs are capable of carrying reduced compounds into the mantle. However, graphite-saturated slab melts are relatively incapable of transporting CO_2 and reduced C is quite immobile in subduction zones (Duncan & Dasgupta, 2017). On the other hand, it has been demonstrated that both oxidized and reduced C can be transported as ionic species in subduction fluids and that C solubility increases in aqueous solutions with increasing alkali contents (Manning et al., 2013; Sverjensky et al., 2014). However, both oxidized and reduced C occur as dissolved ionic species in eclogitic fluids, but not in fluids in equilibrium with peridotites (Sverjensky et al., 2014). In summary, slab-derived organic compounds would probably be subjected to oxidation and carbonate formation in the UZ peridotites, thus, the occurrence of reduced C may be rather explained by retrograde processes during ascent of the peridotites to crustal levels. In this context, several experiments and studies on natural samples of serpentinized peridotites from various geologic settings show that methane and other hydrocarbons can form as a result of abiotic reduction of dissolved CO_2 or other C compounds by reaction with H_2 produced during serpentinization (e.g. Berndt et al., 1996; Horita & Berndt, 1999; Jones et al., 2010; Wang et al., 2014; Miller et al., 2016; Neubeck et al., 2016; Etiope, 2017 and references therein). These studies report that the abiotic synthesis of organic compounds through near-surface serpentinization of ultramafic rocks is a widespread process. For the UZ this could mean that during serpentinization-induced dolomite breakdown in fine-grained garnet-amphibole peridotites the dissolved CO_2 in the migrating aqueous fluid was subjected to redox processes, resulting in the synthesis of abiotic organic compounds. In this way, the fluid could carry reduced compounds also into initially carbonate-free peridotites. This is in agreement with the elevated $C_{red.}/C_{oxi.}$ ratio of the pyroxenitic samples (Figure 5.6a), which are cm-thick foliated veins crosscutting the peridotites and crystallized from initially probably C-poor local melts. Late-stage fluid-mediated introduction of reduced C compounds after pyroxenite formation would thus also explain the light whole-rock $\delta^{13}C$ of these largely carbonate-free samples. Furthermore, serpentinization-related transport of C would also explain the occurrence of newly-formed calcite veinlets in the serpentine mesh texture of some coarse-grained initially carbonate-free peridotites and pyroxenitic samples (Förster et al., 2017). Although the origin of reduced C in the UZ peridotites remains largely enigmatic, formation of organic compounds during late stages in the UZ evolution through serpentinization-mediated dolomite breakdown seems a viable process.

5.7 Summary and conclusions

The study of C contents and stable isotopes of whole-rocks and carbonates in UZ ultramafic rocks provide insights into C-mobilizing processes in a collisional setting. Our findings suggest that C was brought to upper mantle levels in the form of graphite in a continental slab and was deposited in carbonates in ultramafic mantle-derived rocks via multi-stage fluid-rock interaction and ultimately recycled to crustal levels during exhumation of the orogenic crust-peridotite association:

1) Carbon concentrations and C- and O-isotope compositions are independent of the petrographic type of the peridotites. Carbon fixation in these rocks is not strictly coupled to the suggested main metasomatic event that led to enrichment in LILE and LREE in recrystallized garnet-amphibole peridotites. Rather, in accordance with the conclusions of Förster et al. (2017), various mechanisms were responsible for C introduction into these rocks during the entire history of the UZ.
2) The relatively low $\delta^{13}C$ and high $\delta^{18}O$ of dolomites may reflect the isotopic composition of the C-bearing aqueous fluid likely generated during migmatization of the adjacent host gneisses (e.g. Rampone & Morten, 2001). The high variability of carbonate $\delta^{13}C$ and $\delta^{18}O$ is probably the result of various fluid-rock interactions and isotope fractionation, including the serpentinization-related dolomite breakdown and the formation of calcite-brucite intergrowths (Förster et al., 2017).
3) Carbonate stable-isotope compositions distinguish the UZ in a NE and a SW domain. Carbonates of the SW domain mainly display less negative $\delta^{13}C$ and more positive $\delta^{18}O$ relative to the carbonates of the NE domain. We suggest that, during the late stages of exhumation, tectonic uplift of the UZ crust-peridotite mélange to midcrustal levels (Ranalli et al., 2005), the SW domain was mechanically mixed with an ancient ophiolitic orogenic prism (Susini & Martin, 1996) that remained from a former oceanic slab. The peridotites in the SW domain interacted with fluids deriving from this ophiolitic suite, resulting in a carbonate-$\delta^{13}C$ shift to less negative values. The peridotites from the NE domain remained largely unaffected by this process.
4) The occurrence of reduced C may be attributed to abiotic synthesis of organic compounds through near-surface serpentinization of the ultramafic rocks, during which dissolved CO_2 in the migrating aqueous fluid, derived from dolomite breakdown, may have been subjected to redox processes.

Our results bear on the understanding of the C cycle in continental subduction settings, thus contributing to the current debate on the global C cycle. Carbon can be efficiently transported into wedge-derived peridotites via fluid-rock interaction and presumably at in part precipitated as carbonates due to redox processes. However, during exhumation of the carbonated mantle rocks and ongoing fluid-rock interaction on the retrograde path, some of this C is transferred back to the surface. Moreover, the fluid-mediated introduction of C into wedge-derived peridotites seems to be a local process, largely restricted to direct crust-peridotite interaction short time before and during/after peridotite incorporation into the host crustal rocks and is therefore not a viable mechanism to carry C deep into the mantle wedge. This implies that non-UH*P* collisional settings, such as the UZ, are not adequate loci to promote long-term C storage in the mantle. According to the conclusions of Sapienza et al. (2009), C transport from crust to mantle and C long-term storage in the mantle could be promoted at deeper subduction levels, when C-bearing melts (carbonatites and/or C-bearing silicate melts) can be generated and migrate into the mantle wedge.

With the analytical technique that we applied for the stable-isotope study, we obtained the C and O isotopic composition of all carbonates present in the peridotite samples. That means that the stable isotope results of samples with mixed carbonate contents, where different carbonate phases possibly derive from different metasomatic stages, are not feasible to resolve the isotopic composition of carbonates from individual metasomatic stages. In order to unravel individual carbonate-forming events and to understand the C sources during these processes, it would be necessary to analyze the isotopic ratios of single carbonate phases in the UZ peridotites. With this approach it will be possible not only to resolve different metasomatic processes during peak-metamorphic conditions and exhumation but also to understand the sources of C at high-temperature conditions in the mantle wedge.

5.8 References

1. Alt, J.C., Garrido, C.J., Shanks III, W.C., Turchyn, A., Padrón-Navarta, J.A., Sánchez-Vizcaíno, V.L., Gómez Pugnaire, M.T., Marchesi, C. (2012). Recycling of water, carbon, and sulfur during subduction of serpentinites: a stable isotope study of Cerro del Almirez, Spain. Earth and Planetary Science Letters 327-328, 50-60.
2. Bebout, G.E. (1996). Volatile transfer and recycling at convergent margins: mass-balance and insights from high-P/T metamorphic rocks. In: G.E. Bebout, D.W. Scholl, S.H. Kirby and J.P. Platt (Eds.). Subduction top to bottom. American Geophysical Union, Washington, D.C., 96, 179-193.
3. Berndt, M.E., Allen, D.E., Seyfried, Jr., W.E. (1996). Reduction of CO_2 during serpentinization of olivine at 300 °C and 500 bar. Geology 24, 351-354.
4. Bianchini, G., Natali, C. (2017). Carbon elemental and isotopic composition in mantle xenoliths from Spain: Insights on sources and petrogenetic processes. Lithos 272-273, 84-91.
5. Braga, R., Sapienza, G.T. (2007). The retrograde evolution of a dolomite-bearing hydrous peridotite from the Ulten Zone (Italian Alps). GeoActa 6, 37-45.
6. Canil, D. (1990). Experimental study bearing on the absence of carbonate in mantle-derived xenoliths. Geology 18, 1011-1013.
7. Carswell, D.A., Van Roermund, H.L.M. (2005). On multi-phase mineral inclusions associated with microdiamond formation in mantle-derived peridotite lens at Bardane on Fjørtoft, west Norway. European Journal of Mineralogy 17, 31-42.
8. Chazot, G., Lowry, D., Menzies, M., Mattey, D. (1997). Oxygen isotopic composition of hydrous and anhydrous mantle peridotites. Geochimica et Cosmochimica Acta 61, 161-169.
9. Clerc, C., Boulvais, P., Lagabrielle, Y., de Saint Blanquat, M. (2014). Ophicalcites from the northern Pyrenean belt: a field, petrographic and stable isotope study. International Journal of Earth Sciences (Geologische Rundschau) 103, 141-163.
10. Collins, N.C., Bebout, G.E., Angiboust, S., Agard, P., Scambelluri, M., Crispini, L., John, T. (2015). Subduction zone metamorphic pathway for deep carbon cycling: II. Evidence from HP/UHP metabasaltic rocks and ophicarbonates. Chemical Geology 412, 132-150.
11. Cook-Kollars, J., Bebout, G.E., Collins, N.C., Angiboust, S., Agard, P. (2014). Subduction zone metamorphic pathway for deep carbon cycling: I. Evidence from HP/UHP metasedimentary rocks, Italian Alps. Chemical Geology 386, 31-48.

12. Das Sharma, S., Patil, D.T., Gopalan, K. (2002). Temperature dependence of oxygen isotope fractionation of CO_2 from magnesite-phosphoric acid reaction. Geochimica et Cosmochimica Acta 66, 589-593.
13. Dasgupta, R., Hirschmann, M.M. (2006). Melting in the Earth's deep upper mantle caused by carbon dioxide. Nature 440, 659-662.
14. Dasgupta, R., Hirschmann, M.M. (2010). The deep carbon cycle and melting in the Earth's interior. Earth and Planetary Science Letters 298, 1-13.
15. Deines, P. (2002). The carbon isotope geochemistry of mantle xenoliths. Earth-Science Reviews 58, 247-278.
16. Del Moro, A., Martin, S., Prosser, G. (1999). Migmatites of the Ulten Zone (NE Italy), a record of melt transfer in deep crust. Journal of Petrology 40, 1803-1826.
17. Des Marais, D.J. (2001). Isotopic evolution of the biogeochemical carbon cycle during the Precambrian. In: J.W. Valley, D.R. Cole (Eds.). Stable isotope geochemistry. Reviews in Mineralogy and Geochemistry, Mineralogical Society of America and the Geochemical Society, Washington, D.C., 43, 555-578.
18. Ducea, M.N., Saleeby, J., Morrison, J., Valencia, V.A. (2005). Subducted carbonates, metasomatism of mantle wedges, and possible connections to diamond formation: an example from California. American Mineralogist 90, 864-870.
19. Duncan, M.S., Dasgupta, R. (2017). Rise of Earth's atmospheric oxygen controlled by efficient subduction of organic carbon. Nature Geoscience 10, 387-392.
20. Eggler, D.H., Kushiro, I., Holloway, J.R. (1979). Free energies of decarbonation reactions at mantle pressures: I. Stability of the assemblage forsterite-enstatite-magnesite in the system $MgO\text{-}SiO_2\text{-}CO_2\text{-}H_2O$ to 60 kbar. American Mineralogist 64, 288-293.
21. Etiope, G. (2017). Abiotic methane in continental serpentinization sites: an overview. Procedia Earth and Planetary Science 17, 9-12.
22. Förster, B., Braga, R., Aulbach, S., Lo Pò, D., Bargossi, G.M., Mair, V. (2017). A petrographic study of carbonate phases in the Ulten Zone ultramafic rocks: insights into carbonation in the mantle wedge and exhumation-related decarbonation. Ofioliti 42, 105-127.
23. Ghosh, S., Ohtani, E., Litasov, K.D., Terasaki, H. (2009). Solidus of carbonated peridotite from 10 to 20 GPa and origin of magnesiocarbonatite melt in the Earth's deep mantle. Chemical Geology 262, 17-28.
24. Godard, G., Martin, S., Prosser, G., Kiénast, J.R., Morten, L. (1996). Variscan migmatites, eclogites and garnet-peridotites of the Ulten Zone, Eastern Austroalpine system. Tectonophysics 259, 313-341.
25. Green, D.H., Wallace, M.E. (1988). Mantle metasomatism by ephemeral carbonatite melts. Nature 336, 459-462.
26. Green, T.H., Adam, J., Sie, S.H. (1992). Trace element partitioning between silicate minerals and carbonatite at 25 kbar and application to mantle metasomatism. Mineralogy and Petrology 46, 179-184.
27. Hauzenberger, C.A., Höller, W., Hoinkes, G. (1996). Transition from eclogite to amphibolite-facies metamorphism in the Austroalpine Ulten Zone. Mineralogy and Petrology 58, 111-130.
28. Horita, J., Berndt, M.E. (1999). Abiogenic methane formation and isotopic fractionation under hydrothermal conditions. Science 285, 1055-1057.
29. Ionov, D.A., Dupuy, C., O'Reilly, S.Y., Kopylova, M.G., Genshaft, Y.S. (1993). Carbonated peridotite xenoliths from Spitsbergen: implications for trace element signature of mantle carbonate metasomatism. Earth and Planetary Science Letters 119, 283-297.
30. Ionov, D.A., O'Reilly, S.Y., Genshaft, Y.S., Kopylova, M.G. (1996). Carbonate-bearing mantle peridotite xenoliths from Spitsbergen: phase relationships, mineral compositions and trace-element residence. Contributions to Mineralogy and Petrology 125, 375-392.

31. Isshiki, M., Irifune, T., Hirose, K., Ono, S., Ohishi, Y., Watanuki, T., Nishibori, E., Takata, M., Sakata, M. (2004). Stability of magnesite and its high-pressure form in the lowermost mantle. Nature 427, 60-63.
32. Jones, L.C., Rosenbauer, R., Goldsmith, J.I., Oze, C. (2010). Carbonate control of H_2 and CH_4 production in serpentinization systems at elevated P-Ts. Geophysical Research Letters 37, L14306
33. Keppler, H., Wiedenbeck, M., Shcheka, S.S. (2003). Carbon solubility in olivine and the mode of carbon storage in the Earth’s mantle. Nature 424, 414-416.
34. Kelemen, P.B., Manning, C.E. (2015). Reevaluating carbon fluxes in subduction zones, what goes down, mostly comes up. Proceedings of the National Academy of Science 112, E3997-E4006.
35. Kerrick, D.M., Connolly, J.A.D. (1998). Subduction of ophicarbonates and recycling of CO_2 and H_2O. Geology 26, 375-378.
36. Kushiro, I. (1975). Carbonate-silicate reactions at high pressures and possible presence of dolomite and magnesite in the upper mantle. Earth and Planetary Science Letters 28, 116-120.
37. Malaspina, N., Scambelluri, M., Poli, S., Van Roermund, H.L.M., Langenhorst, F. (2010). The oxidation state of mantle wedge majoritic garnet websterites metasomatised by C-bearing subduction fluids. Earth and Planetary Science Letters 298, 417-426.
38. Malaspina, N., Tumiati, S. (2012). The role of C-O-H and oxygen fugacity in subduction-zone garnet peridotites. European Journal of Mineralogy 24, 607-618.
39. Manning, C.E., Shock, E.L., Sverjensky, D.A. (2013). The chemistry of carbon in aqueous fluids at crustal and upper-mantle conditions: Experimental and theoretical constraints. Reviews in Mineralogy and Geochemistry 75, 108-148.
40. Marocchi, M., Hermann, J., Morten, L. (2007). Evidence for multi-stage metasomatism of chlorite-amphibole peridotites (Ulten Zone, Italy): constraints from trace element compositions of hydrous phases. Lithos 99, 85-104.
41. Marocchi, M., Mair, V., Tropper, P., Bargossi, G.M. (2009). Metasomatic reaction bands at the Mt. Hochwart gneiss-peridotite contact (Ulten Zone, Italy): insights into fluid-rock interaction in subduction zones. Mineralogy and Petrology 95, 251-272.
42. Marocchi, M., Hermann, J., Tropper, P., Bargossi, G.M., Mair, V. (2010). Amphibole and phlogopite in “hybrid” metasomatic bands monitor trace element transfer at the interface between felsic and ultramafic rocks (Eastern Alps, Italy). Lithos 117, 135-148.
43. Marocchi, M., Marschall, H.R., Konzett, J., Tropper, P., Ludwig, T., Mair, V., Bargossi, G.M. (2011). Metasomatic tourmaline in hybrid contact-bands between gneiss and peridotite in the Ulten Zone of the Eastern Italian Alps: chemistry and boron isotopic composition. Canadian Mineralogist 49, 245-261.
44. Martin, S., Morten, L., Prosser, G. (1993). Metamorphic and structural evolution of the Spl- to Grt-peridotites and surrounding basement rocks from the Nonsberg area. In: L. Morten (Ed.). Italian eclogites and related rocks. Rendiconti dell’Accademia Nazionale Quaranta 13, 237-251.
45. Martin, S., Godard, G., Prosser, G., Schiavo, A., Bernoulli, D., Ranalli, G. (1998). Evolution of the deep crust at the junction Austroalpine/Southalpine: the Tonale Nappe. Memorie di Scienze Geologiche (Padova) 50, 3-50.
46. Mattey, D., Lowry, D., Macpherson, C. (1994). Oxygen isotope composition of mantle peridotite. Earth and Planetary Science Letters 128, 231-241.
47. Miller, H.M., Matter, J.M., Kelemen, P., Ellison, E.T., Conrad, M.E., Fierer, N., Ruchala, T., Tominaga, M., Templeton, A.S. (2016). Modern water/rock reactions in Oman hyperalkaline peridotite aquifers and implications for microbial habitability. Geochimica et Cosmochimica Acta 179, 217-241.
48. Molina, J.F., Poli, S. (2000). Carbonate stability and fluid compositions in subducted oceanic crust: an experimental study on H_2O-CO_2-bearing basalts. Earth and Planetary Science Letters 176, 295-310.
49. Morten, L., Bargossi, G.M., Landini Bargossi, F. (1976). Notizie preliminari sulle metamorfiti della Val di Rumo, Val di Non, Trento. Mineralogica et Petrographica Acta 21, 137-144.

50. Morten, L., Obata, M. (1983). Possible high-temperature origin of pyroxenite lenses within garnet peridotite, Northern Italy. Bulletin de Minéralogie 106, 775-780.
51. Morten, L., Obata, M. (1990). Rare earth abundances in the eastern Alpine peridotites, Nonsberg area, Northern Italy. European Journal of Mineralogy 2, 643-653.
52. Morten, L., Trommsdorff, V. (2003). Metamorphism and textures of dry and hydrous garnet peridotites. In: D.A. Carswell, R. Compagnoni (Eds.). Ultrahigh pressure metamorphism. EMU Notes in Mineralogy, Eötvös University Press, Budapest, 443-466.
53. Neubeck, A., Nguyen, D.T., Etiope, G. (2016). Low-temperature dunite hydration: evaluating CH_4 and H_2 production from H_2O and CO_2. Geofluids 16, 408-420.
54. Nimis, P., Morten, L. (2000). P-T evolution of “crustal” garnet peridotites and included pyroxenites from Nonsberg area (Upper Austroalpine), NE Italy: from the wedge to the slab. Journal of Geodynamics 30, 93-115.
55. Obata, M., Morten, L. (1987). Transformation of spinel lherzolite to garnet lherzolite in ultramafic lenses of the Austridic Crystalline Complex, Northern Italy. Journal of Petrology 28, 599-623.
56. Poli, S., Franzolin, E., Fumagalli, P., Crottini, A. (2009). The transport of carbon and hydrogen in subducted oceanic crust: an experimental study to 5 GPa. Earth and Planetary Science Letters 278, 350-360.
57. Poli, S. (2015). Carbon mobilized at shallow depths in subduction zones by carbonatitic liquids. Nature Geoscience, 8, 633-636.
58. Rampone, E., Morten, L. (2001). Records of crustal metasomatism in the garnet peridotites of the Ulten Zone (Upper Austroalpine, Eastern Alps). Journal of Petrology 42, 207-219.
59. Ranalli, G., Martin, S., Mahatsente, R. (2005). Continental subduction and exhumation: an example from the Ulten Unit, Tonale Nappe, Eastern Austroalpine. In: D. Gapais, J.P. Brun, P.R. Cobbold (Eds.). Deformation mechanisms, rheology and tectonics: from minerals to lithosphere. Geological Society of London Special Publications 243, 159-174.
60. Sapienza, G.T., Scambelluri, M., Braga, R. (2009). Dolomite-bearing orogenic garnet peridotites witness fluid-mediated carbon recycling in a mantle wedge (Ulten Zone, Eastern Alps, Italy). Contributions to Mineralogy and Petrology 158, 401-420.
61. Scambelluri, M., Philippot, P. (2001). Deep fluids in subduction zones. Lithos 55, 213-227.
62. Scambelluri, M., Hermann, J., Morten, L., Rampone, E. (2006). Melt- versus fluid-induced metasomatism in spinel to garnet wedge peridotites (Ulten Zone, Eastern Italian Alps): clues from trace element and Li abundances. Contributions to Mineralogy and Petrology 151, 372-394.
63. Scambelluri, M., Pettke, T., Van Roermund, H.L.M. (2008). Majoritic garnets monitor deep subduction fluid flow and mantle dynamics. Geology 36, 59-62.
64. Scambelluri, M., Bebout, G.E., Belmonte, D., Gilio, M., Campomenosi, N., Collins, N., Crispini, L. (2016). Carbonation of subduction-zone serpentinite (high-pressure ophicarbonate; Ligurian Western Alps) and implications for the deep carbon cycling. Earth and Planetary Science Letters 441, 155-166.
65. Shcheka, S.S., Wiedenbeck, M., Frost, D.J., Keppler, H. (2006). Carbon solubility in mantle minerals. Earth and Planetary Science Letters 245, 730-742.
66. Shirey, S.B., Cartigny, P., Frost, D.J., Keshav, S., Nestila, F., Nimis, P., Pearson, D.G., Sobolev, N.V., Walter, M.J. (2013). Diamonds and the geology of mantle carbon. Reviews in Mineralogy and Geochemistry 75, 355-421.
67. Smart, K.A., Tappe, S., Stern, R.A., Webb, S.J., Ashwal, L.D. (2016). Early Archaean tectonics and mantle redox recorded in Witwatersand diamonds. Nature Geoscience 9, 255-259.
68. Stachel, T., Harris, J.W. (2009). Formation of diamond in the Earth’s mantle. Journal of Physics – Condensed Matter 21
69. Susini, S., Martin, S. (1996). Microstrutture nelle peridotiti della Serie d’Ultimo (Austroalpino superiore, Alpi Orientali). Atti Ticinesi di Scienze della Terra 4, 47-63.

70. Sverjensky, D.A., Stagno, V., Huang, F. (2014). Important role for organic carbon in subduction-zone fluids in the deep carbon cycle. Nature Geoscience 7, 909-913.
71. Tumiati, S., Thöni, M., Nimis, P., Martin, S., Mair, V. (2003). Mantle-crust interactions during Variscan subduction in the Eastern Alps (Nonsberg-Ulten zone): geochronology and new petrological constraints. Earth and Planetary Science Letters 210, 509-526.
72. Tumiati, S., Godard, G., Martin, S., Nimis, P., Mair, V., Boyer, B. (2005). Dissakisite-(La) from the Ulten zone peridotite (Italian Eastern Alps): a new end-member of the epidote group. American Mineralogist 90, 1177-1185.
73. Tumiati, S., Godard, G., Martin, S., Klötzli, U., Monticelli, D. (2007). Fluid-controlled crustal metasomatism within a high-pressure subducted mélange (Mt. Hochwart, Eastern Italian Alps). Lithos 94, 148-167.
74. Tumiati, S., Fumagalli, P., Tiraboschi, C., Poli, S. (2013). An experimental study on COH-bearing peridotite up to 3.2 GPa and implications for crust-mantle recycling. Journal of Petrology 54, 453-479.
75. Wang, X.B., Ouyang, Z.Y., Zhuo, S.G., Zhang, M.F., Zheng, G.D., Wang, Y.L. (2014). Serpentinization, abiogenic organic compounds, and deep life. Science China – Earth Sciences 57, 878-887.
76. Whitney, D.L., Evans, B.W. (2010). Abbreviations for names of rock-forming minerals. American Mineralogist 95, 185-187.
77. Wyllie, P.J., Huang, W.L. (1975). Peridotite, kimberlite, and carbonatite explained in the system CaO-MgO-SiO_2-CO_2. Geology 3, 621-624.
78. Wyllie, P.J., Huang, W.L., Otto, J., Byrnes, A.P. (1983). Carbonation of peridotites and decarbonation of siliceous dolomites represented in the system CaO-MgO-SiO_2-CO_2 to 30 kbar. Tectonophysics 100, 359-388.
79. Yang, J., Godard, G., Kienast, J.-R., Lu, Y., Sun, J. (1993). Ultrahigh-pressure (60 kbar) magnesite-bearing garnet peridotites from Northeastern Jiangsu, China. Journal of Geology 101, 541-554.
80. Yang, X.-Y., Zheng, Y.-F., Liu, D., Dai, J. (2001). Chemical and carbon isotope compositions of fluid inclusions in peridotite xenoliths and eclogites from eastern China: Geodynamic implications. Physics and Chemistry of the Earth 26, 705-718.
81. Zanetti, A., Mazzucchelli, M., Rivalenti, G., Vannucci, R. (1999). The Finero phlogopite-peridotite massif: an example of subduction-related metasomatism. Contributions to Mineralogy and Petrology 134, 107-122.
82. Zhang, R.Y., Li, T., Rumble, D., Yui, T.-F., Li, L., Yang, J.S., Pan, Y., Liou, J.G. (2007). Multiple metasomatism in Sulu ultrahigh-P garnet peridotite constrained by petrological and geochemical investigations. Journal of Metamorphic Geology 25, 149-164.
83. Zheng, Y.-F., Gong, B., Zhao, Z.-F., Fu, B., Li, Y.-L. (2003). Two types of gneisses associated with eclogite at Shuanghe in the Dabie Sulu terrane: carbon isotope, zircon U-Pb dating and oxygen isotope. Lithos 70, 321-343.

6 Summary and conclusions

This PhD work deals with the orogenic peridotites from the Ulten Zone (UZ) in the Italian Eastern Alps. These peridotites are portions from a former mantle wedge, which were involved in a continental subduction zone in the course of the Variscan orogeny in the Late Paleozoic, subsequently incorporated in the crustal slab during exhumation and ultimately exhumed in a crust-mantle mélange. The UZ peridotites are exposed at the surface as lenses often up to hundreds of meters in length, embedded in foliated high-grade metamorphic crustal basement (Obata & Morten, 1987; Godard et al., 1996). Due to weak overprint during the Alpine orogeny (Godard et al., 1996; Hauzenberger et al., 1996), the complex pre-Alpine tectono-metamorphic evolution of these peridotites has been preserved and is recorded by mineral parageneses and geochemical characteristics. Subduction zones in continental collisional settings are key loci where various petrogenetic processes, involving melts and fluids, promote fundamental mass exchange between crust and mantle and contribute to the long-term cycling of elements between the earth's reservoirs.

Therefore, the orogenic UZ peridotites are valuable samples for studying the element cycling from crust to mantle (and back) in a continental collisional setting. In particular, this PhD study aimed to shed light on the various melt-mediated and fluid-mediated processes acting upon the mantle wedge and a crust-mantle mélange subjected to subduction and exhumation. In the current debate on the global carbon cycle, the study focused on the origin and nature of carbon-mobilizing metasomatic agents involved in the recycling of carbon from crust to mantle.

In order to approach these aims, new samples from multiple peridotite localities across the entire UZ were collected during field work and examined regarding their petrography and geochemistry. A comprehensive petrographic study focused on the characterization of different petrographic peridotite types and on the occurrence of carbonate phases in the UZ peridotites. In addition to analyses of whole-rock major- and trace elements, the concentrations of total carbon as well as of both oxidized and reduced carbon in the UZ peridotites were analyzed. A multi-isotope study on whole-rocks provided the first combined analysis of the radiogenic isotopes Nd, Sr, Hf and Pb as well as the first analyses of the carbon-isotope composition in UZ peridotites. The occurrence metasomatic accessory minerals (zircon and carbonates) allowed geochemical and geochronological analyses of zircon as well as analyses of stable isotopes (carbon and oxygen) in carbonates.

The results of this integrated study obtained by petrographic, elemental and isotopic analyses, provide new insights into the multi-stage evolution of the UZ peridotites, including melt-mediated and fluid-mediated metasomatic processes, and ultimately contribute to the understanding of the geodynamics and mass transfer in a continental collisional setting:

6.1 Constraints on geodynamics and the sequence of events from subduction to exhumation

The new results help better constrain the sequence of events in the evolution of the peridotites in the UZ geodynamic setting. After a high-temperature spinel stage in the mantle wedge (stage 1, Figure 6.1) (Scambelluri et al., 2006), the peridotites experienced temperature decrease and concomitant pressure increase due to corner flow towards the slab-mantle interface, reaching garnet stability and maximum pressure of ca. 2.0 GPa at ca. 900°C (stage 2, Figure 6.1). These *P-T* conditions are inferred from the occurrence of dolomite in fine-grained garnet-amphibole peridotites in combination with the lack of high-pressure magnesite. The transition from spinel peridotites to garnet peridotites occurred in the mantle wedge and subsequently, the peridotites started an exhumation path in the mantle wedge close to the slab-mantle interface. This is inferred from the ca. 333 Ma age obtained from zircons in peridotites and in a phlogopitite rocks from the hybrid crust-peridotite contact zone, indicating that the formation of the contacts occurred at ca. 333 Ma as a result of peridotite insertion into the crustal host rocks at low-P-T conditions (stage 3, Figure 6.1). The fluid responsible for the formation of the hydrous contact zones was presumably a residual fluid released by leucosome crystallization. At this stage, the exhumation mélange consisting of crustal rocks and peridotites reached lower crustal levels and during this event and/or during subsequent serpentinization (stage 4, Figure 6.1), some portions of peridotites were mechanically mixed with different adjacent lithologies residing at crustal levels.

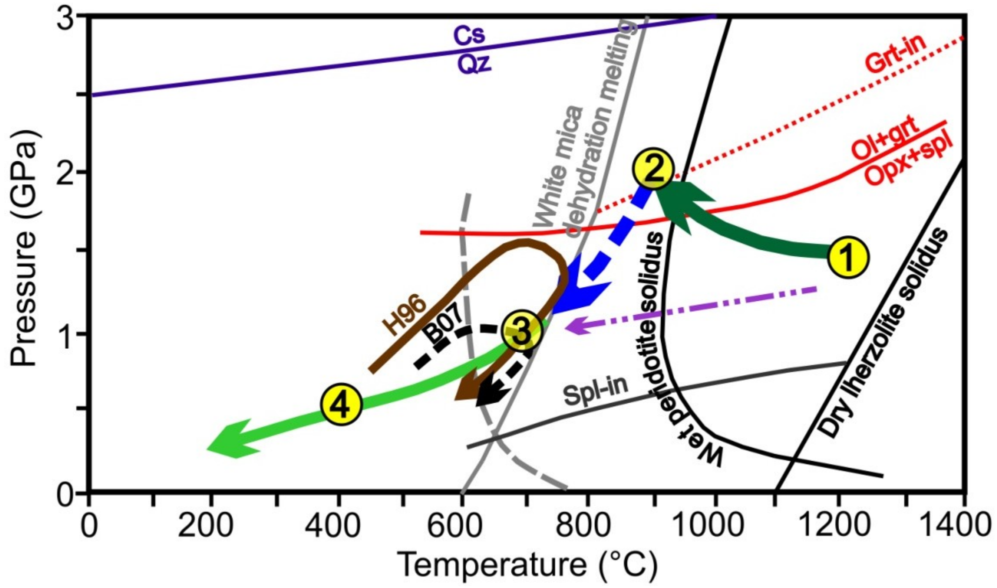

Figure 6.1. Pressure-Temperature (P-T) evolution for Ulten Zone peridotites inferred from the results of this PhD study, based on previous results from Nimis & Morten (2000), Tumiati et al. (2003), Scambelluri et al. (2006), Marocchi et al. (2007, 2009, 2010) and Sapienza et al. (2009). Dark green thick full arrow marks peridotite P-T paths starting at stage 1 (spinel stage) at high temperatures, reaching garnet stability at maximum $P \approx 2.0$ GPa at $T = 900$°C (stage 2). Blue thick stippled arrow marks P-T decrease of garnet peridotites on a retrograde exhumation path in the mantle wedge. Insertion of peridotites into crustal host rocks occurs during exhumation at low-P-T conditions at ca. 333 Ma (stage 3), concomitant to development of the contact zones between peridotites and crustal host rocks. Green full arrow marks the common exhumation path of the crust-peridotite association starting at stage 3. Stage 4 marks possible P-T conditions for the serpentinization stage of the peridotites. Purple stippled-dotted line indicates path of chlorite peridotites which possibly never equilibrated at garnet-facies conditions (Marocchi et al., 2007). Proposed P-T paths for crustal rocks: H96 (Hauzenberger et al., 1996) and B07 (Braga et al., 2007a). Red stippled garnet-in curve as in Marocchi et al. (2009), full red curve opx+spl → ol+grt as in Tumiati et al. (2003). Gray stippled line indicates the solidus for H_2O-saturated metapelites. Mineral abbreviations after Whitney & Evans (2010).

This is evidenced by different carbon-isotope compositions in carbonates, which distinguish the UZ in a northeastern (NE) and a southwestern (SW) domain. Carbonates from the NE domain display a more negative carbon-isotope signature (δ^{13}C from -16.8‰ to -5.7‰) than carbonates in the SW domain (δ^{13}C from -11.1‰ to -0.03‰). The latter is connected to the southwestern part of the Ulten unit, which comprises carbonate-bearing rocks dismembered from an ancient oceanic slab (e.g. Susini & Martin, 1996). Mechanical mixing of the SW domain with these rocks during tectonic uplift and exhumation and fluid-mediated interaction is suggested to have resulted in the different carbon isotopic composition.

These new findings show that previous suggestions on the geodynamic history of the UZ must be reconsidered and that the UZ cannot be considered as an example for deep subduction as previously thought.

6.2 Constraints on mechanisms of element cycling

Various melt-mediated and fluid-mediated processes acting upon the UZ peridotites promote element transfer in the mantle wedge and between crust and mantle, resulting in decoupling of major-element and trace-element compositions in these peridotites. Based on whole-rock elemental and isotopic data, the following main processes are suggested:

1) The protoliths of the UZ peridotites derive from a primitive-mantle portion which was subjected to melt depletion during the assembly of the supercontinent Rodinia in the Proterozoic. This is inferred from Hf and Nd T_{CHUR} model ages of > 1 Ga, obtained from peridotites with depleted major-element compositions and with depleted Hf- and Nd-isotope compositions.
2) The peridotite protoliths experienced refertilization at the time of the onset of the Variscan orogeny, displayed by a Sm-Nd isochron age of 409 ± 38 Ma which marks the timing of isotopic re-equilibration after the Proterozoic partial melting event. Refertilization was the result of protolith interaction with metasomatic liquids, possibly mafic melts, which rose up from deeper parts of a subduction zone and carried recycled crustal components into the overlying hot supra-subduction zone mantle wedge. All UZ peridotites display radiogenic Pb isotopic compositions with a signature of mixed recycled crustal components in the mantle source.
3) After transport closer to the slab-mantle interface during the subduction of a continental slab in the course of the Variscan orogeny, the peridotites experienced multi-stage interaction with aqueous fluids derived from the crustal slab. These fluids were released during migmatization of the crustal rocks and were enriched in the most incompatible trace elements, such as LREE and LILE, U. Interaction with such crust-derived aqueous fluids is evidenced by the formation of amphibole and peridotite enrichment in the most incompatible trace elements which is also reflected by substantial addition of unradiogenic Nd and radiogenic Sr, as shown by the majority of the UZ peridotites. This process marks a first stage of crustal metasomatism which affected the UZ peridotites during residence in the mantle wedge, and accompanied the beginning exhumation of the peridotites, indicating that crust-derived elements can be carried into the mantle wedge through fluid-mediated metasomatism.
4) The peridotites were incorporated in the crustal host rocks on the exhumation path at ca. 333 Ma and were subjected to a second stage of crustal metasomatism by aqueous fluids liberated after leucosome crystallization at low pressures and temperatures (ca. 600-700°C, from Ti-in-zircon thermometry). These fluids carried HFSE from the crustal rocks to the peridotites, evidenced by zircon growth in peridotites and a phlogopitite from the crust-peridotite contact. Interaction with fluids enriched in HFSE at this stage may also account for the elevated HFSE concentrations in fine-grained hydrated peridotites relatively to coarse-grained peridotites which could largely escape hydration. The coupled addition of radiogenic Sr and unradiogenic Hf at this stage, as observed in UZ peridotites, indicates that crust-derived fluids marked by radiogenic Sr compositions are capable of mobilizing HFSE.

6.3 Constraints on the carbon cycle during crust-mantle interaction

The UZ peridotites contain different carbonate minerals (dolomite, magnesite, calcite) which can be linked to individual stages in the peridotite evolution, indicating multi-stage carbonation and exhumation-related dolomite breakdown. Dolomite inclusions in primary spinel in coarse-grained peridotites provide evidence that the melts responsible for refertilization of peridotite protoliths in the mantle wedge (see section 6.2) contained a carbon component. Since these melts likely derived from deeper parts of the subduction zone and carried crustal components, the occurrence of dolomite inclusions in spinel testifies to carbon recycling from the crustal slab into the mantle wedge. Dolomite is the major carbonate phase in little-serpentinized fine-grained garnet-amphibole peridotites and formed there from crust-derived COH-fluids simultaneously with amphibole and apatite during the high-pressure garnet-facies stage. At this stage, the peridotites likely resided close to the slab-mantle interface, indicating that crust-derived aqueous fluids can transport carbon from the slab to the associated mantle portion. However, the efficiency of such fluids to carry crust-derived carbon deeper inside the mantle wedge remains unconstrained. Ongoing ingress of crustal carbon-bearing fluids after the high-pressure event, likely during exhumation of the peridotites, is documented by the local occurrence of dolomite in veins crosscutting the peridotite matrix and of retrograde magnesite. Importantly, serpentinized fine-grained garnet-amphibole peridotites contain intergrowths of calcite and brucite, which form as products of serpentinization-induced dedolomitization according to the chemical reaction $CaMg(CO_3)_2 + H_2O \rightarrow CaCO_3 + Mg(OH)_2 + CO_2$. The dissolved carbon species released into the migrating serpentinizing fluid possibly accounts for the precipitation of calcite in veins in the serpentine mesh texture, as well as for abiotic synthesis of reduced carbon via redox reactions (e.g. Berndt et al., 1996; Etiope, 2017). In addition to carbon in carbonates (concentration of oxidized carbon from 0.0014 to 0.1810 wt. %), all UZ peridotites contain reduced carbon (0.0164 to 0.1240 wt. %) and the total carbon concentration ranges from 0.0130 to 0.2800 wt. %, implying the capability of mantle wedge-derived rocks to store crust-derived carbon. However, the release of a carbon species testifies to decarbonation at the serpentinization stage during exhumation and shows that carbon, which was once transported to deeper levels in the subduction zone, can be ultimately brought back to crustal levels. This suggests that subduction zones in continental collisional settings are not only responsible for carbon transport to mantle depths and there for carbon introduction into the mantle, but contribute also to the return of carbon from mantle depths to the crust.

6.4 References

1. Berndt, M.E., Allen, D.E., Seyfried, Jr., W.E. (1996). Reduction of CO_2 during serpentinization of olivine at 300 °C and 500 bar. Geology 24, 351-354.
2. Etiope, G. (2017). Abiotic methane in continental serpentinization sites: an overview. Procedia Earth and Planetary Science 17, 9-12.
3. Godard, G., Martin, S., Prosser, G., Kiénast, J.R., Morten, L. (1996). Variscan migmatites, eclogites and garnet-peridotites of the Ulten zone, Eastern Austroalpine system. Tectonophysics 259, 313-341.
4. Hauzenberger, C.A., Höller, W., Hoinkes, G. (1996). Transition from eclogite to amphibolite-facies metamorphism in the Austroalpine Ulten Zone. Mineralogy and Petrology 58, 111-130.
5. Nimis, P., Morten, L. (2000). P-T evolution of "crustal" garnet peridotites and included pyroxenites from Nonsberg area (Upper Austroalpine), NE Italy: from the wedge to the slab. Journal of Geodynamics 30, 93-115.
6. Marocchi, M., Hermann, J., Morten, L. (2007). Evidence for multi-stage metasomatism of chlorite-amphibole peridotites (Ulten Zone, Italy): Constraints from trace element compositions of hydrous phases. Lithos 99, 85-104.
7. Marocchi, M., Mair, V., Tropper, P., Bargossi, G.M. (2009). Metasomatic reaction bands at the Mt. Hochwart gneiss-peridotite contact (Ulten Zone, Italy): insights into fluid-rock interaction in subduction zones. Mineralogy and Petrology 95, 251-272.
8. Marocchi, M., Hermann, J., Tropper, P., Bargossi, G.M., Mair, V. (2010). Amphibole and phlogopite in "hybrid" metasomatic bands monitor trace element transfer at the interface between felsic and ultramafic rocks (Eastern Alps, Italy). Lithos 117, 135-148.
9. Obata, M., Morten, L. (1987). Transformation of spinel lherzolite to garnet lherzolite in ultramafic lenses of the Austridic Crystalline Complex, Northern Italy. Journal of Petrology 28, 599-623.
10. Sapienza, G.T., Scambelluri, M., Braga, R. (2009). Dolomite-bearing orogenic garnet peridotites witness fluid-mediated carbon recycling in a mantle wedge (Ulten Zone, Eastern Alps, Italy). Contributions to Mineralogy and Petrology 158, 401-420.

11. Scambelluri, M., Hermann, J., Morten, L., Rampone, E. (2006). Melt- versus fluid-induced metasomatism in spinel to garnet wedge peridotites (Ulten Zone, Eastern Italian Alps): clues from trace element and Li abundances. Contributions to Mineralogy and Petrology 151, 372-394.
12. Susini, S., Martin, S. (1996). Microstrutture nelle peridotiti della Serie d'Ultimo (Austroalpino superiore, Alpi Orientali). Atti Ticinesi di Scienze della Terra 4, 47-63.
13. Tumiati, S., Susini, S., Thöni, M., Nimis, P., Martin, S., Mair, V. (2003). Mantle-crust interactions during Variscan subduction in the Eastern Alps (Nonsberg-Ulten zone): geochronology and new petrological constraints. Earth and Planetary Science Letters 210, 509-526.
14. Whitney, D.L., Evans, B.W. (2010). Abbreviations for names of rock-forming minerals. American Mineralogist 95, 185-187.

Appendix

Table A1 Sample locality and petrographic characteristics of Ulten Zone peridotites from the new sample set.

Sample/type	Locality	Texture	Porphyro-clasts	Grt / pseudomorphs after grt	Alteration degree
Coarse-grained spl peridotites					
Ko2C (Ko2a)	Kornigl	transitional from protogranular to porphyroclastic			high
KoB4	Kornigl	porphyroclastic			high
KoD12	Kornigl	protogranular-granoblastic			medium
KoD4	Kornigl	transitional from protogranular to porphyroclastic			medium
KoD8	Kornigl	protogranular-granoblastic, fine grains in between coarse grains: recrystallized parts			medium
KoDb1	Kornigl	transitional from protogranular to porphyroclastic			high
MBS1	Malga Binasia	transitional from protogranular to porphyroclastic			medium
MBS2	Malga Binasia	protogranular-granoblastic			medium
MBS3C	Malga Binasia	transitional from protogranular to porphyroclastic			medium
MBS8	Malga Binasia	transitional from protogranular to porphyroclastic			medium
MOL1.1C	Monte Ometto	transitional from protogranular to porphyroclastic			medium
MOL1.5	Monte Ometto	protogranular-granoblastic, fine grains in between coarse grains: recrystallized parts			low
MOL2.4	Monte Ometto	porphyroclastic			high
MZS1.2	Malga Zoccolo	protogranular-granoblastic, fine grains in between coarse grains: recrystallized parts			medium
MZS3.1	Malga Zoccolo	protogranular-granoblastic, fine grains in between coarse grains: recrystallized parts			medium
MZS3.2	Malga Zoccolo	granoblastic-porphyroclastic, mylonitic			low
PL1.1	Malga Preghena	protogranular-granoblastic, fine grains in between coarse grains: recrystallized parts			high
PL1.4	Malga Preghena	porphyroclastic			medium
PL2.3	Malga Preghena	transitional from protogranular to porphyroclastic			high
PL2.5C	Malga Preghena	transitional from protogranular to porphyroclastic			na
PL2.2	Malga Preghena	granoblastic-porphyroclastic, mylonitic		Pseudomorphs after grt	high
PRE1	Malga Preghena	protogranular-granoblastic, fine grains in between coarse grains: recrystallized parts			medium
PRE-A	Malga Preghena	protogranular-granoblastic, fine grains in between coarse grains: recrystallized parts			high
SBB1C	Schönboden	porphyroclastic			high
SBB2C (SBB-C2)	Schönboden	porphyroclastic			high
Coarse-grained grt peridotites					
SBA2	Samerbergalm	protogranular-granoblastic		Grt	low
SBA3	Samerbergalm	protogranular-granoblastic		Grt	low

Sample/type	Locality	Texture	Porphyro-clasts	Grt / pseudomorphs after grt	Alteration degree
Fine-grained grt-amp peridotites					
KBA6	Klapfbergalm	granoblastic-porphyroclastic, mylonitic	Grt	Grt with thin kelyphite rim	low
KBA7	Klapfbergalm	granoblastic-porphyroclastic, mylonitic	Grt	Grt with thin kelyphite rim	medium
KBA8	Klapfbergalm	granoblastic-porphyroclastic, mylonitic	Grt, opx	Grt with thin kelyphite rim	low
KBA9	Klapfbergalm	granoblastic-porphyroclastic, mylonitic	Grt	Grt with thin kelyphite rim	low
KL1.2-3	Klapfbergalm	granoblastic-porphyroclastic, mylonitic	Grt	Grt with kely rim + blasts of kely after Grt	low
KL1.3b	Klapfbergalm	granoblastic-porphyroclastic, mylonitic	Grt	Grt with kely rim + blasts of kely after Grt	low
KL1.3c	Klapfbergalm	granoblastic-porphyroclastic, mylonitic	Grt	Grt with kely rim + blasts of kely after Grt	low
KL1.6	Klapfbergalm	granoblastic-porphyroclastic, mylonitic	Grt	Grt with kely rim + blasts of kely after Grt	low
KL2.4-2b	Klapfbergalm	granoblastic-porphyroclastic, mylonitic	Grt	Grt with kely rim + blasts of kely after Grt	high
PL1.10	Malga Preghena	decussate-porphyroclastic, mylonitic	Grt	Grt with thin kelyphite rim	high
PL1.2	Malga Preghena	granoblastic-porphyroclastic, mylonitic	Grt	Grt with thin kelyphite rim	high
PL1.3	Malga Preghena	granoblastic-porphyroclastic, mylonitic	Grt	Grt with thin kelyphite rim	high
PL1.6	Malga Preghena	granoblastic-porphyroclastic, mylonitic	Grt	Grt with thin kelyphite rim	high
PL1.7a	Malga Preghena	granoblastic-porphyroclastic, mylonitic	Grt	Grt with kely rim + blasts of kely after Grt	low
PL1.7b	Malga Preghena		Grt		low
PL1.9	Malga Preghena	granoblastic-porphyroclastic, mylonitic	Grt	Grt with kely rim + blasts of kely after Grt	medium
SB1	Schönboden	granoblastic-porphyroclastic, mylonitic	Grt	Grt with thin kelyphite rim	medium
SB2.1	Schönboden	granoblastic-porphyroclastic, mylonitic	Grt	Grt with thin kelyphite rim	high
SB2.2	Schönboden	granoblastic-porphyroclastic, mylonitic	Grt, opx	Grt with thin kelyphite rim	high
SB3.1	Schönboden	granoblastic-porphyroclastic, mylonitic	Grt, opx	Grt	high
SB3.2	Schönboden	granoblastic-porphyroclastic, mylonitic	Grt	Grt	high
SB3.3	Schönboden	granoblastic-porphyroclastic, mylonitic	Grt	Grt with thin kelyphite rim	high
SB3.4	Schönboden	granoblastic-porphyroclastic, mylonitic	Grt, opx	Grt	medium
SB3.5	Schönboden	granoblastic-porphyroclastic, mylonitic	Grt, opx	Grt with thin kelyphite rim	na
SB3.6	Schönboden	granoblastic-porphyroclastic, mylonitic	Grt, opx	Grt with thin kelyphite rim	na
SBA4	Samerbergalm	granoblastic-porphyroclastic, mylonitic	Grt	Grt with thin kelyphite rim	low
SBA5	Samerbergalm	granoblastic-porphyroclastic, mylonitic	Grt, opx	Grt with thin kelyphite rim	low
SBA7	Samerbergalm	granoblastic-porphyroclastic, mylonitic	Grt	Grt	low
WG1	Walschgrube	granoblastic-porphyroclastic, mylonitic	Grt	Grt with kely rim + blasts of kely after Grt	high
WG2	Walschgrube	granoblastic-porphyroclastic, mylonitic	Grt	Grt with thin kelyphite rim	medium
WG4	Walschgrube	granoblastic-porphyroclastic, mylonitic	Grt	Grt with kely rim + blasts of kely after Grt	low
WG5	Walschgrube	granoblastic-porphyroclastic, mylonitic	Grt	Grt with kely rim + blasts of kely after Grt	low
WG7	Walschgrube	granoblastic-porphyroclastic, mylonitic	Grt	Grt with kely rim +	na

Sample/type	Locality	Texture	Porphyro-clasts	Grt / pseudomorphs after grt	Alteration degree
				blasts of kely after Grt	
WG9b	Walschgrube	granoblastic-porphyroclastic, mylonitic	Grt	Grt with kely rim + blasts of kely after Grt	high
WG9c	Walschgrube				high
WG11	Walschgrube	granoblastic(-porphyroclastic)	Grt	Grt with kely rim + blasts of kely after Grt	high
Fine-grained peridotites					
BAL1.1	Bichlalm	granoblastic, mylonitic			na
BAL1.2	Bichlalm	granoblastic(-porphyroclastic), mylonitic			medium
BAL1.3	Bichlalm	granoblastic-porphyroclastic, mylonitic	Opx	Pseudomorphs after grt	low
BAL1.4	Bichlalm	granoblastic-porphyroclastic, mylonitic			na
BAL2.1	Bichlalm	granoblastic-porphyroclastic, mylonitic		Pseudomorphs after grt	na
BAL2.2	Bichlalm	decussate, mylonitic		Pseudomorphs after grt	high
BAL2.3	Bichlalm	granoblastic-porphyroclastic, mylonitic		Pseudomorphs after grt	na
BAL2.4	Bichlalm	granoblastic-decussate, mylonitic			na
KBA4	Klapfbergalm	granoblastic-porphyroclastic, mylonitic	Opx		na
KBA5	Klapfbergalm	granoblastic, mylonitic		Pseudomorphs after grt	low
KL1.2-1	Klapfbergalm	granoblastic-porphyroclastic, mylonitic		Pseudomorphs after grt	low
KL1.4-1	Klapfbergalm	granoblastic-porphyroclastic, mylonitic		Pseudomorphs after grt	low
KL1.7-2	Klapfbergalm	granoblastic-porphyroclastic, mylonitic		Pseudomorphs after grt	medium
KL1.8	Klapfbergalm	granoblastic(-porphyroclastic)		Pseudomorphs after grt	medium
KL1.1	Klapfbergalm	granoblastic(-porphyroclastic), mylonitic		Pseudomorphs after grt	high
KL1.3a	Klapfbergalm	granoblastic-porphyroclastic, mylonitic		Pseudomorphs after grt	medium
KL1.5	Klapfbergalm	granoblastic(-porphyroclastic), mylonitic			high
KL1.9	Klapfbergalm	granoblastic(-porphyroclastic), mylonitic			medium
KL1b-1	Klapfbergalm	granoblastic-porphyroclastic, mylonitic	Opx?		na
KL1b-2	Klapfbergalm	granoblastic(-porphyroclastic)		Pseudomorphs after grt	medium
KL2.2	Klapfbergalm	granoblastic, mylonitic		Pseudomorphs after grt	medium
KL2.3	Klapfbergalm	granoblastic-porphyroclastic, mylonitic			medium
KL2.4	Klapfbergalm	granoblastic(-porphyroclastic), mylonitic			high
KL2.4-1	Klapfbergalm	granoblastic(-porphyroclastic), mylonitic			high
KL2.4-2a	Klapfbergalm	granoblastic, mylonitic			high
KLa2	Klapfbergalm	granoblastic-porphyroclastic, mylonitic	Opx		na
KLb	Klapfbergalm	porphyroclastic		Pseudomorphs after grt	high
Ko1	Kornigl	granoblastic(-porphyroclastic), mylonitic			high
Ko2F (Ko2b, Ko2c)	Kornigl	granoblastic(-porphyroclastic), mylonitic			high
Ko3	Kornigl	granoblastic(-porphyroclastic), mylonitic			high
Ko4	Kornigl	granoblastic			high
KoB1	Kornigl	granoblastic-porphyroclastic, mylonitic	Opx		high
KoB2	Kornigl	granoblastic(-porphyroclastic), mylonitic			high
KoB3	Kornigl	granoblastic(-porphyroclastic), mylonitic			high
KoD1	Kornigl	granoblastic(-porphyroclastic), mylonitic			medium
KoD9	Kornigl	granoblastic(-porphyroclastic), mylonitic			na
KoD10	Kornigl	granoblastic-porphyroclastic, mylonitic	Opx		high
KoD11	Kornigl	granoblastic-porphyroclastic, mylonitic	Opx		high
KoD13	Kornigl	granoblastic(-porphyroclastic), mylonitic			medium
KoD14	Kornigl	granoblastic			high
KoD15	Kornigl	granoblastic(-porphyroclastic), mylonitic			medium
KoD2	Kornigl	granoblastic-porphyroclastic, mylonitic			medium
KoD3	Kornigl	granoblastic-porphyroclastic, mylonitic	Opx		medium
KoD5	Kornigl	granoblastic-porphyroclastic, mylonitic	Opx		high
KoD6	Kornigl	granoblastic(-porphyroclastic), mylonitic			high
KoD7	Kornigl	granoblastic(-porphyroclastic), mylonitic			high
KoDb2 (medium-grained)	Kornigl	transitional from protogranular to porphyroclastic		Pseudomorphs after grt	high
MBS3F	Malga Binasia	granoblastic(-porphyroclastic), mylonitic		Pseudomorphs after grt	medium

Sample/type	Locality	Texture	Porphyro-clasts	Grt / pseudomorphs after grt	Alteration degree
MBS3TZ	Malga Binasia	granoblastic-porphyroclastic, mylonitic	Opx	Pseudomorphs after grt	medium
MBS4	Malga Binasia	granoblastic, mylonitic			na
MBS5	Malga Binasia	granoblastic-porphyroclastic, mylonitic	Opx		medium
MBS6	Malga Binasia	granoblastic(-porphyroclastic), mylonitic			medium
MBS7	Malga Binasia	granoblastic-porphyroclastic, mylonitic	Opx		medium
MBS9	Malga Binasia	granoblastic-porphyroclastic, mylonitic			na
MM300	Malga Masa Murada/Lavazzee valley	granoblastic-porphyroclastic, mylonitic	Opx		low
MOL1.1F1	Monte Ometto	granoblastic, mylonitic			medium
MOL1.1F2	Monte Ometto	granoblastic-porphyroclastic, mylonitic			medium
MOL1.2	Monte Ometto	granoblastic, mylonitic			medium
MOL1.3	Monte Ometto	granoblastic, mylonitic			medium
MOL1.6	Monte Ometto	granoblastic-porphyroclastic, mylonitic			na
MOL1.7	Monte Ometto	granoblastic-porphyroclastic, mylonitic			low
MOL1.8	Monte Ometto	granoblastic-porphyroclastic, mylonitic			medium
MOL1.9	Monte Ometto	granoblastic-porphyroclastic, mylonitic			high
MOL2.1	Monte Ometto	granoblastic-porphyroclastic, mylonitic			medium
MOL2.2	Monte Ometto	granoblastic-porphyroclastic, mylonitic			medium
MOL2.3	Monte Ometto	granoblastic-porphyroclastic, mylonitic			high
MZS1.1	Malga Zoccolo	granoblastic(-porphyroclastic), mylonitic			low
MZS1.4 dark part	Malga Zoccolo	granoblastic(-porphyroclastic), mylonitic			medium
MZS2	Malga Zoccolo	granoblastic-porphyroclastic, mylonitic			na
PL1.5	Malga Preghena	granoblastic(-porphyroclastic), mylonitic			medium
PL2.5F	Malga Preghena	granoblastic-porphyroclastic, mylonitic			na
PL2.1a	Malga Preghena	granoblastic, mylonitic			high
PL2.1b	Malga Preghena	granoblastic(-porphyroclastic), mylonitic			high
PL2.4	Malga Preghena	granoblastic			high
PRE2	Malga Preghena	granoblastic-porphyroclastic, mylonitic			medium
SBA1	Samerbergalm	granoblastic-porphyroclastic, mylonitic	Ol, opx	Pseudomorphs after grt	low
SBA6	Samerbergalm	granoblastic-porphyroclastic, mylonitic			low
SBA9	Samerbergalm	granoblastic-porphyroclastic, mylonitic	Ol/opx?		medium
SBB1F	Schönboden	granoblastic-porphyroclastic, mylonitic		Pseudomorphs after grt	high
SBB2F (SBB2F1, SBB2F2)	Schönboden	granoblastic-porphyroclastic, mylonitic	Opx	Pseudomorphs after grt	high
SGS1	Schöngrubspitz	granoblastic-porphyroclastic, mylonitic			high
SGS2	Schöngrubspitz	granoblastic-porphyroclastic, mylonitic			high
SGS3	Schöngrubspitz	granoblastic-porphyroclastic, mylonitic	Opx		high
SGS4	Schöngrubspitz	granoblastic-porphyroclastic, mylonitic			high
WG10	Walschgrube	granoblastic-porphyroclastic	Opx		na
WG3	Walschgrube	granoblastic(-porphyroclastic), mylonitic		Pseudomorphs after grt	medium
WG6	Walschgrube	granoblastic(-porphyroclastic), mylonitic			medium
WG8	Walschgrube	granoblastic(-porphyroclastic), mylonitic			medium
WG9a	Walschgrube	granoblastic(-porphyroclastic), mylonitic			high
Pyroxenitic-amphibolized samples					
MOL1.7a dark part	Monte Ometto	decussate, mylonitic			
MOL1.7a green part	Monte Ometto	decussate, mylonitic			
MOL1.4 dark part	Monte Ometto	decussate-porphyroclastic, mylonitic			
MOL1.4 green part	Monte Ometto	decussate-granoblastic, mylonitic			
MZS1.3	Malga Zoccolo	granoblastic, mylonitic			
MZS1.4 green part	Malga Zoccolo	granoblastic, mylonitic			
MZS1.5	Malga Zoccolo	granoblastic, mylonitic			
MZS1.6	Malga Zoccolo	granoblastic(-porphyroclastic), mylonitic			
SBA8	Samerbergalm	granoblastic(-porphyroclastic), mylonitic			

Mineral abbreviations after Whitney & Evans (2010).

na: not available.

Table A2 List of new samples from the field campaign and performed analyses in this PhD work.

Sample	Section type	Backing piece	Thick section		Whole-rock powder				
			SEM	Zircon U-Pb geochronology and geochemistry	WR major and trace elements	WR radiogenic isotopes	WR oxidized and reduced carbon	WR C concentration and C-isotopes	Carbonate C- and O-isotopes
BAL1.1	thick section	x							
BAL1.2	thick section	x					x		x
BAL1.3	thick section	x							x
BAL1.4	thick section	x							
BAL2.1	thick section	x							
BAL2.2	polished thick section	x							x
BAL2.3	thick section	x							
BAL2.4	thick section	x							
KBA1	-	-							x
KBA2	-	-							x
KBA4	thick section	x							
KBA5	thick section	x							x
KBA6	polished thick section	x	x				x	x	x
KBA7	thick section	x							x
KBA8	polished thick section	x	x		x		x	x	x
KBA9	polished thick section	x	x						x
KL1.1	thick section	x							x
KL1.2-1	thick section	x			x				x
KL1.2-2	-	-							x
KL1.2-3	polished thick section	x 2x	x						x
KL1.2-4	-	-							x
KL1.3a	(polished?) thick section	x	x						KL1.3 peri.
KL1.3b	polished thick section	x	x						and
KL1.3c	polished thick section	x	x						KL1.3 vein
KL1.4-1	thick section	x							x
KL1.4-2	-	-							x
KL1.5	thick section	x					x	x	x
KL1.6	polished thick section	x	x				x	x	x
KL1.7-1	-	-							x
KL1.7-2	polished thick section	x	x				x		x
KL1.8	thick section	x							x
KL1.9	thick section	x							x
KL1b-1	thick section	x							
KL1b-2	thick section	x							x
KL2.2	polished 1 mm section	x	x		x				
KL2.3	thick section	x					x		x
KL2.4	thick section	x							x
KL2.4-1	thick section	x							x
KL2.4-2a	thick section	x							KL2.4-2

Sample	Section type	Backing piece	Thick section		Whole-rock powder				
			SEM	Zircon U-Pb geochronology and geochemistry	WR major and trace elements	WR radiogenic isotopes	WR oxidized and reduced carbon	WR C concentration and C-isotopes	Carbonate C- and O-isotopes
KL2.4-2b	polished thick section	x	x						
KL2.4-3	-	-							x
KLa2	thick section	x							
KLb	thick section	x							x
Ko1	thick section	x							x
Ko2C (Ko2a)	polished 1 mm section 3x (one rather fine)	x	x		x		x	x	x
Ko2F (Ko2b, Ko2c)	thick section	x			x		x	x	x
Ko3	thick section	x					x		x
Ko4	thick section	x							x
KoB1	thick section	x					x		x
KoB2	thick section	x							x
KoB3	thick section	x							x
KoB4	-	x							x
KoD1	thick section	x							x
KoD2	thick section	x							x
KoD3	thick section	x							x
KoD4	polished thick section	x	x				x		x
KoD5	thick section	x							
KoD6	thick section	x							x
KoD7	thick section	x							
KoD8	-	x							x
KoD9	polished 1 mm section	x	x						
KoD10	thick section	x							x
KoD11	thick section	x							x
KoD12	-	x					x	x	x
KoD13	thick section	x							
KoD14	thick section	x							x
KoD15	thick section	x					x	x	x
KoDb1	-	x							
KoDb2	polished thick section	x	x				x		x
MBS1	polished thick section	x	x				x		x
MBS2	polished thick section	x	x		x	x	x	x	x
MBS3C	-	x							x
MBS3F	thick section	x					x		x
MBS3TZ	polished thick section	x	x						
MBS4	thick section	x							
MBS5	thick section	x							x
MBS6	thick section	x			x	x	x	x	x
MBS7	thick section	x							x
MBS8	polished thick section	x	x				x		x
MBS9	thick section	x							
MM-300D	two parts in one thick section	x							x
MM-300G									x

Sample	Section type	Backing piece	Thick section		Whole-rock powder				
			SEM	Zircon U-Pb geochronology and geochemistry	WR major and trace elements	WR radiogenic isotopes	WR oxidized and reduced carbon	WR C concentration and C-isotopes	Carbonate C- and O-isotopes
MOL1.1C	thick section	x 2x					x		x
MOL1.1F1	thick section	x					x		MOL1.1
MOL1.1F2	thick section	x							
MOL1.2	thick section	x							x
MOL1.3	thick section	x			x		x	x	x
MOL1.4 dark part	thick section / polished thick section	x							x
MOL1.4 green part									
MOL1.5	polished 1 mm section	x	x		x	x	x	x	x
MOL1.6	thick section	x							
MOL1.7	thick section	x							x
MOL1.7a dark part	thick section / polished thick section	x							
MOL1.7a green part									
MOL1.8	thick section	x							x
MOL1.9	thick section	x							x
MOL2.1	thick section	x							x
MOL2.2	thick section	x							x
MOL2.3	thick section	x							x
MOL2.4	polished thick section	x							x
MZS1.1	thick section	x					x	x	x
MZS1.2	polished thick section	x	x				x		x
MZS1.3	thick section / polished thick section	x					x		x
MZS1.4 dark part	thick section	x							x
MZS1.4 green part									
MZS1.5	thick section	x					x		x
MZS1.6	thick section / polished thick section	x							
MZS2	thick section	x							
MZS3.1	-	x					x	x	x
MZS3.2	thick section	x							x
PL1.1	polished thick section	x	x		x		x	x	x
PL1.2	thick section	x							x
PL1.3	thick section	x					x		x
PL1.4	-	x					x		x
PL1.5	thick section	x					x		x
PL1.6	polished thick section	x	x	x	x		x	x	x
PL1.7a	polished thick section	x	x						PL1.7
PL1.7b	polished thick section	x	x						
PL1.8	-	x							x
PL1.9	polished	x	x						x

Sample	Section type	Backing piece	Thick section		Whole-rock powder				
			SEM	Zircon U-Pb geochronology and geochemistry	WR major and trace elements	WR radiogenic isotopes	WR oxidized and reduced carbon	WR C concentration and C-isotopes	Carbonate C- and O-isotopes
	thick section								
PL1.10	polished thick section	x							x
PL2.1a	thick section	x							PL2.1
PL2.1b	thick section	x							
PL2.2	thick section	x							x
PL2.3	-	x					x		x
PL2.4	thick section	x							x
PL2.5C	-	x 2x							
PL2.5F	thick section	x							
PRE1	-	x							x
PRE2	thick section	x					x		x
PRE-A	polished thick section	x	x		x		x		x
SB1	polished thick section	x	x						x
SB2.1	polished thick section	x	x						x
SB2.2	polished thick section	x	x						x
SB3.1	polished thick section	x	x						x
SB3.2	polished thick section	x	x				x		x
SB3.3	polished thick section	x	x						x
SB3.4	polished thick section	x	x		x		x	x	x
SB3.5	-	x							
SB3.6	-	x							
SBB1C	thick section	x							SBB-C1
SBB1F	thick section	x							SBB-F1
SBB2C	thick section	x					SBB-C2		SBB-C2
SBB2F1	thick section	x							
SBB2F2	thick section / polished thick section	x	x	x			SBB-F2		
SBA1	thick section	x					x		x
SBA2	polished thick section	x	x		x		x	x	x
SBA3	polished thick section	x	x						x
SBA4	polished thick section	x	x		x	x	x	x	x
SBA5	polished thick section	x	x				x		x
SBA6	thick section	x							x
SBA7	polished thick section	x	x				x	x	x
SBA8	thick section / polished thick section	x							x
SBA9	thick section	x							x
SGS1	thick section	x							
SGS2	thick section	x							x
SGS3	thick section	x							x
SGS4	thick section	x							

Sample	Section type	Backing piece	Thick section		Whole-rock powder				
			SEM	Zircon U-Pb geochronology and geochemistry	WR major and trace elements	WR radiogenic isotopes	WR oxidized and reduced carbon	WR C concentration and C-isotopes	Carbonate C- and O-isotopes
WG1	polished 1 mm section	x	x		x		x		x
WG2	polished thick section	x	x				x	x	x
WG3	thick section	x							x
WG4	polished thick section	x	x		x	x	x	x	x
WG5	polished thick section	x	x						x
WG6	thick section	x					x		x
WG7	polished thick section	x	x						
WG8	thick section	x							x
WG9a	thick section	x							WG9
WG9b	polished thick section	x	x						
WG9c	polished thick section	x	x						
WG10	thick section	x							
WG11	thick section	x							x

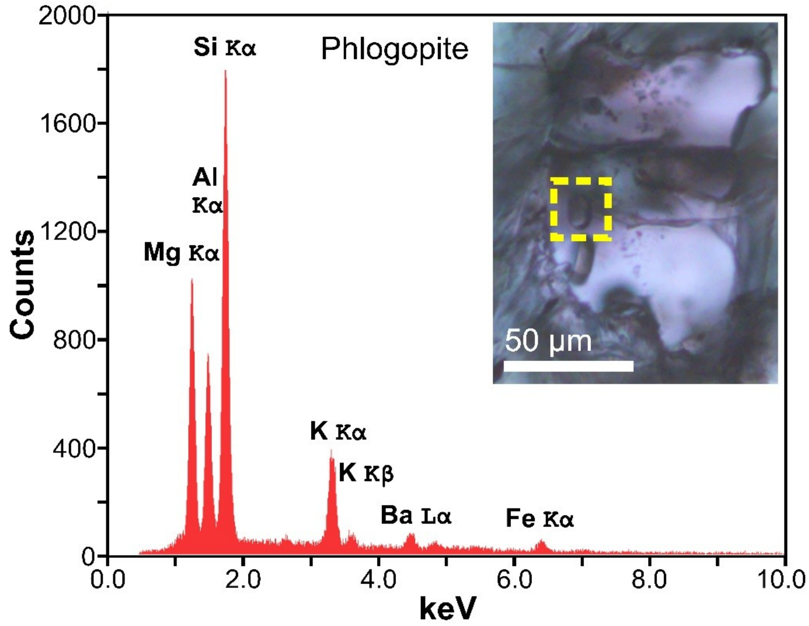

Figure A1. Microphotograph and EDS spectra of the phlogopite inclusion in zircon in the peridotite sample SBB2F. The label in the photograph marks the analyzed inclusion that was exposed on the surface of the thin section.

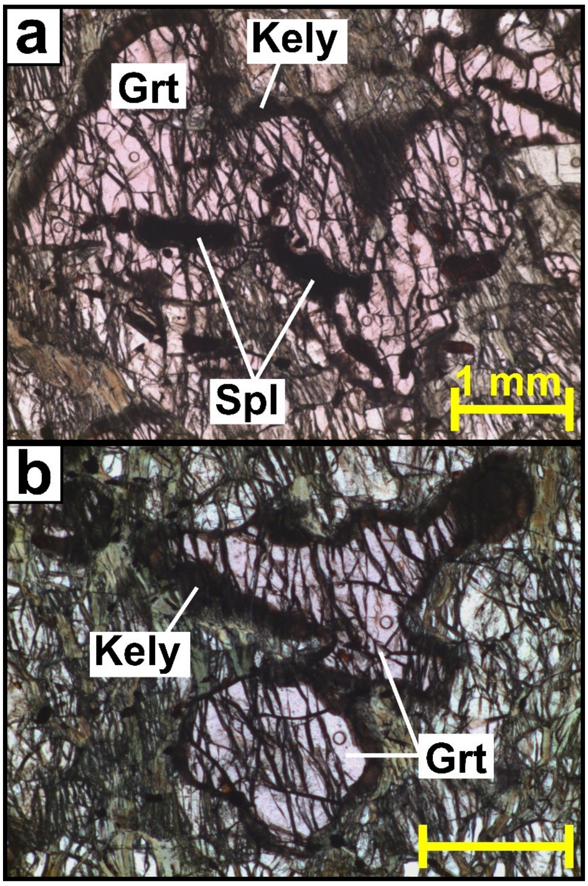

Figure A2. Photomicrographs of garnets in the fine-grained peridotite PL1.6. (a) Large garnet porphyroclast (~6 mm) surrounding vermicular spinel, with kelyphite corona. (b) Medium-sized garnets (Grt1 and Grt2) without any inclusions, with kelyphite corona. Grt: garnet, spl: spinel, kely: kelyphite. Scale bar denotes 1 mm.

Table A3. Bulk-rock major element and trace element composition of zircon-bearing Ulten Zone peridotites and phlogopitite from the crust-peridotite contact zone.

Sample:	PL1.6	VM25P10A	detection limit	NB103*
wt. %				
SiO_2	42.2	44.16	0.01	43.93
TiO_2	0.061	0.033	0.001	0.7
Al_2O_3	2.91	2.36	0.01	14.29
Fe_2O_3	2.29	1.46	0.01	
FeO	5.3	6.6	0.1	
MnO	0.126	0.131	0.001	0.05
MgO	38.07	39.68	0.01	20.63
CaO	2.85	2.21	0.01	3.98
Na_2O	0.19	0.16	0.01	0.54
K_2O	0.05	0.03	0.01	6.27
P_2O_5	0.02	<dl	0.01	0.18
LOI	5.08	0.25		2.94
Sum	99.15	97.07		100.58
$Fe_2O_3^{total}$	8.19	8.83	0.01	7.07
ppm				
Sc	14	12	1	
V	66	57	5	89.15
Cr	2290	2780	20	860.5
Co	95	110	1	69.35
Ni	1560	2250	20	1167
Cu	30	20	10	3.86
Zn	50	50	30	170.5
Ga	2	2	1	23.35
Ge	0.8	1.2	0.5	0.864
Rb	1	2	1	258.7
Sr	39	23	2	15.08
Y	1.9	1.6	0.5	7.314
Zr	13	7	1	66.99
Nb	<dl	0.7	0.2	11.31
Cs	0.2	0.2	0.1	11.82
Ba	93	49	2	1082
La	2.18	2.06	0.05	4.363
Ce	4.26	3.71	0.05	12.11
Pr	0.49	0.39	0.01	1.916
Nd	1.77	1.44	0.05	9.09
Sm	0.38	0.26	0.01	2.579
Eu	0.098	0.061	0.005	0.717
Gd	0.3	0.14	0.01	2.281
Tb	0.05	0.03	0.01	0.302
Dy	0.33	0.23	0.01	1.494
Ho	0.07	0.05	0.01	0.247
Er	0.21	0.21	0.01	0.614
Tm	0.034	0.033	0.005	0.083
Yb	0.24	0.21	0.01	0.501
Lu	0.035	0.031	0.002	0.072
Hf	0.3	0.3	0.1	2.047
Ta	0.02	0.31	0.01	1.304
Th	0.58	0.43	0.05	0.528
U	0.17	0.17	0.01	0.739

*Data from Marocchi et al. (2009; sample labeled NB101B_03); total iron as $Fe_2O_3^{total}$, included in sum.

Detailed information about analytical techniques is reported on the laboratory website www.actlabs.com for the analytical package “4Lithores”.

Table A4. Trace element concentrations (ppm) of garnets in the zircon-bearing garnet-amphibole peridotite PL1.6.

Group:	Group 1			Group 2		Group 3			Group 4			Standard	
Grt grain:	Grt1	Grt2	Grt5	Grt3	BigGrt-1	BigGrt-2	BigGrt-3	Grt4	BigGrt-4	BigGrt-5	BigGrt-6		
Domain:	Medium-sized grt close to rim			Small grt	Large grt rim	Large grt close to rim		Small grt core	Large grt rim		Large grt close to rim	avg BIR	avg dl
Mg	210178	225234	190635	188681	175129	189707	187617	200266	185393	190178	180117	91710	19.90
Si	246538	250687	210098	217270	204178	226671	227337	248897	225144	232976	219174	242034	76.14
Ca	47146	47146	41566	41056	40854	40854	40854	41499	43771	43771	41232	94626	210.73
Sc	214	173	163	132	114	104	106	101	66	74	69	39.07	0.41
Ti	324	362	284	212	223	220	204	396	486	393	390	7182	1.77
V	104	114	100	88	109	118	104	140	144	131	120	344	0.09
Cr	12192	10175	10659	8511	12843	9798	8871	13553	9702	11113	10954	12107	3.64
Mn	5425	5061	4105	5139	5383	5356	5346	5334	4807	5198	4714	1578	0.70
Rb	<dl	<dl	<dl	<dl	1.05*	<dl	<dl	<dl	<dl	<dl	<dl	0.25	0.11
Sr	<dl	<dl	<dl	<dl	3.98	<dl	1.57	0.27	<dl	<dl	0.23	104	0.23
Y	43.11	37.59	37.47	24.63	20.69	15.04	17.18	15.20	10.04	9.97	7.68	11.13	0.05
Zr	42.43	21.21	37.67	10.35	11.23	10.62	12.55	3.63	5.49	4.69	3.36	10.43	0.31
Nb	0.07	0.05	0.07	0.05	0.05	0.04	0.04	0.06	0.05	0.08	0.08	0.56	0.02
Cs	<dl	<dl	<dl	<dl	0.27*	<dl	<dl	<dl	<dl	<dl	<dl	0.28	0.06
Ba	<dl	<dl	<dl	<dl	15.28*	<dl	0.47	<dl	<dl	0.52	<dl	6.23	0.39
La	<dl	<dl	<dl	<dl	<dl	<dl	<dl	<dl	<dl	<dl	<dl	0.55	0.04
Ce	0.21	0.34	0.14	0.12	0.08	0.07	0.05	0.12	0.24	0.21	0.22	1.84	0.04
Pr	0.11	0.13	0.09	0.05	0.04	0.03	0.02	0.05	0.12	0.11	0.10	0.33	0.02
Nd	1.44	1.53	1.45	0.63	0.54	0.52	0.36	0.55	1.74	1.30	1.22	2.19	0.08
Sm	1.60	1.42	1.77	0.62	0.62	0.68	0.41	0.46	1.21	0.85	0.69	20.98	0.08
Eu	0.75	0.53	0.84	0.33	0.30	0.30	0.29	0.32	0.40	0.37	0.31	0.46	0.03
Gd	2.76	2.37	2.77	1.44	1.27	1.03	0.80	0.89	1.15	1.27	0.76	63.70	0.24
Tb	0.78	0.58	0.75	0.38	0.35	0.30	0.31	0.28	0.24	0.24	0.15	0.24	0.03
Dy	7.08	5.77	5.78	3.79	3.28	2.09	2.62	2.65	1.66	1.71	1.22	1.99	0.07
Ho	1.66	1.38	1.37	0.87	0.80	0.57	0.65	0.54	0.36	0.40	0.28	0.41	0.01
Er	5.30	4.46	4.01	2.92	2.56	1.64	2.06	1.75	1.27	1.07	1.01	1.15	0.05
Tm	0.89	0.73	0.57	0.44	0.42	0.26	0.31	0.27	0.18	0.16	0.15	10.49	0.01
Yb	5.84	5.53	4.10	3.41	3.02	2.08	2.20	2.06	1.29	1.06	1.19	1.33	0.06
Lu	0.89	0.83	0.50	0.47	0.44	0.25	0.29	0.30	0.17	0.18	0.14	0.16	0.01
Hf	0.41	0.16	0.53	0.09	<dl	0.08	0.08	<dl	<dl	0.07	<dl	0.39	0.07
Ta	<dl	<dl	<dl	<dl	<dl	<dl	<dl	<dl	<dl	<dl	<dl	0.027	0.025
Pb	<dl	<dl	<dl	<dl	1.189*	0.097	0.606	0.072	0.088	0.127	0.875	110	0.068
Th	0.011	0.043	<dl	0.011	0.020	0.017	0.015	0.009	0.016	0.010	0.007	0.024	0.007
U	0.030	0.191	0.009	0.087	0.077	0.095	0.093	0.056	0.158	0.097	0.069	0.018	0.004

*unrealistic high values for garnet, probably derived from inclusions/fractures

Mineral abbreviations after Whitney & Evans (2010)

Table A5. Comparison of U-Pb ages of zircons in ultramafic (peridotites and pyroxenites), crustal (migmatites) and contact rocks from the Ulten Zone.

Rock type / sample	Locality	Reference	Zircon analyses	Age (Ma)
Peridotite				
PL1.6	Malga Preghena	This study	*in-situ*	333±2 & 236±8
VM25P10A	Hochwart/Vedetta Alta	This study	*in-situ*	334±3
SBB2	Schönboden	This study	*in-situ*	Intercepts at 320.0±6.9 & 2299±1100
Grt-amp peridotite	Seefeldalm	Gebauer & Grünenfelder (1979)	single zircons	
Pyroxenite				
Grt-amp websterite MO9	Seefeldalm	Gebauer & Grünenfelder (1979)	single zircons	336
Grt-amp clinopyroxenite ULG6	Seefeldalm	Gebauer & Grünenfelder (1979)	single zircons	332
Migmatite				
from orthogneiss	Cima Binasia ridge	Hauzenberger et al. (1993)	single zircons	ca. 470 and ca. 365
migmatite-related leucosome A4319	Hochwart/Vedetta Alta	Tumiati et al. (2007)	single zircons; secondary electron multiplier in ion counting mode MS	Concordant ages: 560, 502, 576; discordant age: 661
Contact zone (gneiss-peridotite)				
Phlogopitite				
NB103	Hochwart/Vedetta Alta	This study	*in-situ*	333±3
Amphibolite (phl-bearing)				
A4452	Hochwart/Vedetta Alta	Tumiati et al. (2007)	single zircons; secondary electron multiplier in ion counting mode MS	333.3±2.4
Mineral abbreviations after Whitney & Evans (2010)				

Table A6. Petrographic description of Ulten Zone peridotites from different localities, with particular attention to their carbonate content.

Sample/textural type	Locality	Texture	Carbonates	Apatite	Serpent.[1]	Comments
Coarse-grained						
Ko2a	Kornigl	transitional from protogranular to porphyroclastic	Cal veins	-	yes	
KoD4	Kornigl	transitional from protogranular to porphyroclastic	Mgs vein	-	yes	
MBS1	Malga Binasia	transitional from protogranular to porphyroclastic	Cal veins, cal veins in cpx	-	yes	
MBS2	Malga Binasia	protogranular-granoblastic	Cal(+dol) veins, ± cal-brc	-	little	
MOL1.5	Monte Ometto	protogranular-granoblastic + fine-grained recrystallized parts	Mgs vein, interstitial dol + mgs, dol crystal in amp vein	-	-	
MZS1.2	Malga Zoccolo	protogranular-granoblastic + fine-grained recrystallized parts	Cal veins, cal veins in cpx	-	yes	
PL1.1	Malga Preghena	protogranular-granoblastic + fine-grained recrystallized parts	Cal veins, cal veins in spl	-	yes	
PRE-A	Malga Preghena	protogranular-granoblastic + fine-grained recrystallized parts	Cal veins, cal veins in cpx	-	yes	
Fine-grained (grt-free)						
KL1.7-2	Klapfbergalm	granoblastic-porphyroclastic, mylonitic	Cal veins	-	yes	blasts of kely/amp/chl after grt
KL1-3a	Klapfbergalm	granoblastic-porphyroclastic, mylonitic	Cal-brc	yes	yes	blasts of kely/amp/chl after grt
KL2.2	Klapfbergalm	granoblastic, mylonitic	Cal-brc	?	yes	highly amphibolized, blasts of kely/amp/chl after grt
Ko2b, Ko2c	Kornigl	granoblastic-porphyroclastic, mylonitic	Cal veins, cal veins in amp	?	yes	
KoD9	Kornigl	granoblastic-porphyroclastic, mylonitic	Mgs vein	?	yes	highly amphibolized
KoDb2 (medium-grained)	Kornigl	transitional from protogranular to porphyroclastic	Cal-brc vein, cal veins, cal veins in cpx and spl	?	yes	blasts of kely/amp/chl after grt
MBS3TZ	Malga Binasia	granoblastic-porphyroclastic, mylonitic	Cal vein	?	yes	highly amphibolized, blasts of kely/amp/chl after grt
MR141B	Samerbergalm	granoblastic-porphyroclastic, mylonitic	Dol grains in serpentine vein	?	yes	
SBB2F	Schönboden	granoblastic-porphyroclastic, mylonitic	Dol crystal related to mgs aggregate, mgs veins, dol veinlets, cal veinlets	yes	yes	
Fine-grained grt-bearing						
KBA8	Klapfbergalm	granoblastic-	Cal-brc, cal-brc in grt,	?	little	

Sample/textural type	Locality	Texture	Carbonates	Apatite	Serpent.[1]	Comments
		porphyroclastic, mylonitic	cal+srp in grt, cal veins in grt, cal veins			
KL1.2-3	Klapfbergalm	granoblastic-porphyroclastic, mylonitic	Cal-brc, dol grains in matrix, dol in ap	yes	little	
KL1.3c	Klapfbergalm	granoblastic-porphyroclastic, mylonitic	Cal-brc	yes	little	
KL1.6	Klapfbergalm	granoblastic-porphyroclastic, mylonitic	Dol vein + cal-brc	yes	little	
KL2.4-2b	Klapfbergalm	granoblastic-porphyroclastic, mylonitic	Cal-brc, dol in spl in grt, cal-brc in ms incl. in spl	?	yes	
PL1-6	Malga Preghena	granoblastic-porphyroclastic, mylonitic	Cal-brc	?	yes	
PL1-9	Malga Preghena	granoblastic-porphyroclastic, mylonitic	Cal-brc, cal-brc in ms incl. in spl, cal+srp in ms incl. in spl, cal veins	yes	yes	
SB2-1	Schönboden	granoblastic-porphyroclastic, mylonitic	Cal-brc, cal veins	?	yes	
SB2-2	Schönboden	granoblastic-porphyroclastic, mylonitic	Cal-brc, cal-brc veinlet, cal(+dol) veins	yes	yes	
SB3-1	Schönboden	granoblastic-porphyroclastic, mylonitic	Cal-brc, cal veins, cal veins in amp and grt	yes	yes	
SB3-2	Schönboden	granoblastic-porphyroclastic, mylonitic	Cal-brc, cal(+dol) veins, dol in serpentinized parts, cal veins in amp and grt	yes	yes	
SB3-3	Schönboden	granoblastic-porphyroclastic, mylonitic	Cal-brc, cal veins	?	yes	
SB3-4	Schönboden	granoblastic-porphyroclastic, mylonitic	Dol in ol, cal veins	-	yes	
SBA4	Samerbergalm	granoblastic-porphyroclastic, mylonitic	Dol grains in matrix	yes	-	
SBA5	Samerbergalm	granoblastic-porphyroclastic, mylonitic	Dol grains in matrix, dol in amp and ol	yes	-	
SBA7	Samerbergalm	granoblastic-porphyroclastic, mylonitic	Dol grains in matrix, dol in ol	yes	-	
VM25P10A	Hochwart	granoblastic-porphyroclastic, mylonitic	Dol grains in matrix, dol in amp and zrn, dol in grt pseudomorph	yes	little	
VM25P10B	Hochwart	granoblastic-porphyroclastic, mylonitic	Dol in amp coronas around grt, part of ms incl. in grt, band of interstitial dol	yes	-	
VM25P10C	Hochwart	granoblastic-porphyroclastic, mylonitic	Dol grains in matrix, dol in amp, dol in kely around grt, dol in serpentinized parts	?	little	
VM25P11	Hochwart	granoblastic-porphyroclastic, mylonitic	Dol grains in matrix, dol in amp and ol, dol as part of grt pseudomorph, polycrystalline dol aggregate, dol in serpentinized parts	yes	little	
WG1	Walschgrube	granoblastic-	Cal-brc, cal+dol veins,	yes	yes	

Sample/textural type	Locality	Texture	Carbonates	Apatite	Serpent.[1]	Comments
		porphyroclastic, mylonitic	dol in serpentinized parts			
WG2	Walschgrube	granoblastic-porphyroclastic, mylonitic	Cal-brc, cal veins	yes	yes	
WG7	Walschgrube	granoblastic-porphyroclastic, mylonitic	Cal-brc, cal-brc in spl in grt, cal-brc in grt	yes	yes	highly amphibolized, veins of fibrous amp
WG9b, WG9c	Walschgrube	granoblastic-porphyroclastic, mylonitic	Cal-brc, cal-brc in ms incl. in spl, cal veins	?	yes	

[1] Serpent.: serpentinization

Mineral abbreviations after Whitney and Evans (2010): Cal: calcite; mgs: magnesite; brc: brucite; dol: dolomite; amp: amphibole; grt: garnet; ol: olivine; cpx: clinopyroxene; spl: spinel; srp: serpentine; ap: apatite; chl: chlorite

Other abbreviations: kely: kelyphite; ms incl.: multi-phase solid inclusion

Table A7 Summary of various carbonate phases and their textural setting in different microstructural types of Ulten Zone peridotites.

Textural type / sample names	Carbonate phase						
	Interstitial dolomite	Dolomite inclusions	Dolomite veins	Grains / patches of calcite-brucite intergrowths	Inclusions of calcite-brucite intergrowths	Calcite veins	Magnesite
Coarse-grained protogranular							
MOL1.5	Anhedral with curvilinear grain boundaries in contact with silicate minerals, spatially related with amp, partly associated with mgs (Figure 4.5e,f)						Distinct vein (≈500 µm in thickness) with frayed grain boundaries
Ko2a, MBS1, MBS2, MZS1.2, PL1.1, PRE-A						Associated with srp veins (Figure 11c)	
MBS1, MZS1.2, PRE-A						Crosscutting cpx	
MBS2			Associated with mag ± cal ± (secondary) srp(/chl?) cross-cutting pre-existing srp mesh texture	Rarely in srp mesh texture			
Ko2c						Crosscutting amp	
PL1.1						Crosscutting spl (Figure 4.11d)	
KoD4							Veins, associated with srp veins (Figure 4.11f)
Fine-grained non-serpentinized grt-amp peridotites							
SBA4, SBA5, SBA7, KL1.2-3, VM25P10C, VM25P11	Disseminated in matrix, often associated with ap, amp, grt (Figure 4.3)						
KL1.2-3		In ap (Figure 4.4a)					
SBA5, VM25P10C, VM25P11		In amp (Figure 4.4b)					
SBA5, SBA7, VM25P11		In ol (Figure 4.4c)					

Textual type / sample names	Carbonate phase						
	Interstitial dolomite	Dolomite inclusions	Dolomite veins	Grains / patches of calcite-brucite intergrowths	Inclusions of calcite-brucite intergrowths	Calcite veins	Magnesite
VM25P10B	In spl-free amp coronas around grt together with opx; in band (vein-like?) in textural association with amp (Figure 4.5b)	Part of multi-phase solid inclusion in coarse grt (Figure 4.4e)					
VM25P10C	In contact with kely around grt; with frayed boundaries located within srp veins cross-cutting the matrix						
VM25P11	Part of grt pseudomorph together with kely, cal, chl; lenticular polycrystalline aggregate (≈5 cm in length; Figure 4.6a); located within rare srp veins cross-cutting the matrix						
KL1.6			Consisting of aggregates of interstitial anhedral dol (up to 400 µm) cross-cutting the peridotite matrix; partly texturally associated with amp (Figure 4.5c,d), contains patches of cal-brc intergrowths	Situated within dol vein (Figure 4.5c,d)			
Fine-grained non-serpentinized amp-bearing peridotite with grt pseudomorphs							
VM25P10A	Disseminated in matrix; together with amp and spl as grt pseudomorph (Figure 4.5a)	In amp (Figure 4.4b); anhedral with curvilinear boundaries spatially associated with ap as lobate inclusion in zrn (Figure 4.4d)					
Fine-grained serpentinized grt-amp peridotites							

Textural type / sample names	Carbonate phase						
	Interstitial dolomite	Dolomite inclusions	Dolomite veins	Grains / patches of calcite-brucite intergrowths	Inclusions of calcite-brucite intergrowths	Calcite veins	Magnesite
KBA8, KL1.3c, KL2.4-2b, PL1.6, PL1.9, SB2-1, SB2-2, SB3-1, SB3-2, SB3-3, WG1, WG2, WG7, WG9b, WG9c				With frayed boundaries, commonly located within serpentinized parts of the peridotites, often contoured by Fe-oxide and often textural relation to cal veinlets (Figure 4.9a-f)			
SB3-2, WG1	Rarely, situated within srp mesh texture (Figure 4.7c)						
SB2-2, SB3-2, WG1,			Associated with mag ± cal ± (secondary) srp(/chl?) cross-cutting pre-existing srp mesh texture (Figure 4.7a)				
KBA8, SB3-1, SB3-2						Cross-cutting amp and grt	
KBA8, SB2-1, SB2-2, SB3-1, SB3-2, SB3-4, WG1, WG2, WG9b, WG9c						Associated with srp veins (Figure 4.11c)	
SB3-4		In ol (Figure 4.4f)					
KL2.4-2b		In spl hosted in grt (Figure 4.8a)					
KL2.4-2b, PL1.9, WG9b					Part of multi-phase solid inclusion in spl (Figure 4.8c)		
WG7					In spl hosted in grt (Figure 4.8b)		
KBA8, WG7					In grt, occasionally touching spl and/or related to srp (Figure 4.8d,e)		
KBA8, PL1.9						Cal + srp intergrowths hosted in grt, related to srp vein and as part of	

Textural type / sample names	Carbonate phase						
	Interstitial dolomite	Dolomite inclusions	Dolomite veins	Grains / patches of calcite-brucite intergrowths	Inclusions of calcite-brucite intergrowths	Calcite veins	Magnesite
						multi-phase solid inclusion in spl	
<u>Fine-grained serpentinized peridotite</u>							
MR141B	Situated in secondary srp vein (≈3 mm in thickness, Figure 4.7b)						
SBB2F	Well-preserved idiomorphic crystal (≈150 µm in length), texturally closely related with mgs aggregate, which is crosscut by thin dol veinlets (≈10 µm, Figure 4.7d-f)						Aggregate with rippled grain boundaries, closely related to dol grain, residing within secondary srp (Figure 4.7d-f); veins situated within srp veins
KL1.3a, KL2.2, KoDb2				Grains with frayed boundaries, commonly located within serpentinized parts of the peridotites, often contoured by Fe-oxide and often textural relation to cal veinlets (Figure 4.9a-f)			
KoDb2				Vein (≈150 µm in thickness) located within srp vein, cross-cutting peridotite matrix, interlaced with srp and mag (Figure 4.11a,b)		Cross-cutting cpx and spl (Figure 4.11d)	
KL1.7-2, Ko2b, Ko2c, KoDb2, MBS3TZ, SBB2F						Associated with srp veins (Figure 4.11c)	
KoD9							Distinct vein with frayed grain boundaries (≈2 mm in thickness, Figure 4.11e)

Mineral abbreviations after Whitney and Evans (2010)

Acknowledgments

This thesis is not only the outcome of my research activities throughout the last three years, but also it represents an important step and a special time in my life. Living and working in another country has been a very interesting and exciting time and I am glad to have gained this experience, combining it with PhD studies.

First of all, I would like to thank my supervisors Roberto Braga and Sonja Aulbach for offering me the possibility to go to Bologna. It was just in the right moment when Sonja told me that Roberto was looking for a PhD student.

I would like to thank Roberto for accepting me as a PhD student and for introducing me to the exciting and challenging world of the Ulten Zone. The field work in the Ulten Zone mountains, set in this beautiful landscape, was one of the best parts of my work. Roberto also introduced me to the world of Italian geoscience research, enabling me to get to know many new people and to create new connections. Many thanks go to Roberto also for helping me with "administrative" stuff regarding my stay in Italy, from opening an Italian bank account to assisting me picking up my car from a depository!

A big thank goes to Sonja for the guidance over the years, being always available for "remote support", from wherever in the world she was being around. She helped improve my writings and was teaching me with constructive criticisms and most of all with her unbeatable expertise in geochemistry and petrology!

Thanks to Gianluca Bianchini and Claudio Natali at the University of Ferrara for friendly collaboration and enthusiasm to study the carbon content in the Ulten peridotites. The trips to Ferrara were always a pleasure.

Thank you to Gray Bebout for accepting me as a visiting researcher at Lehigh University to work in his stable-isotope lab, but also for offering me to join geologic field trips with his students. These were great moments, providing me the possibility to travel around some nice parts of the US where I had not been before. A lot of appreciation goes to Bruce Idleman who gave valuable advice for the work in the stable-isotope lab and at the electron microscope.

Thanks also to Dmitri Ionov for offering me the possibility to spend a three-month research stay at the University of Montpellier in order to conduct analyses of radiogenic isotopes. Many thanks to Delphine Bosch for working with me in the clean lab and for some nice conversations during the chemical separation process as well as thanks to Olivier Bruguier for the support during the analyses on zircons.

I am very grateful to the people at ISA, the Institute of Advanced Studies, at the University of Bologna for granting me the ISA PhD Fellowship. Having this fellowship did not only provide me a place to live in Bologna, but also gave me the chance to meet other PhD students from all over the world. Our meetings and social activities with the ISA group have been inspiring and joyful moments. Many thanks to our coordinator Barbara Cimatti for her enthusiasm in managing ISA and in organizing many nice events and activities for the ISA group. I am also thankful that ISA provided me the possibility to attend Italian classes.

Nevertheless, I am very glad to have met many other members of the geoscience department in Bologna, especially other PhD students and post-docs who have become my friends.

A big thank goes to my family for support and advice at all times and in all situations and for their belief in me. Their visits in Bologna were precious moments and I enjoyed a lot spending time with them in the place which has been my home in the last three years.

Finally, I am grateful to Alessandra Montanini from the University of Parma and Peter Tropper from the University of Innsbruck for evaluating my PhD thesis and for their constructive criticisms and valuable comments.